2017

# Strategies for Optimal Control of the Current and Rotation Profiles in the DIII-D Tokamak

William P. Wehner
*Lehigh University*

# Strategies for Optimal Control of the Current and Rotation Profiles in the DIII-D Tokamak

by

William P. Wehner

Presented to the Graduate and Research Committee
of Lehigh University
in Candidacy for the Degree of
Doctor of Philosophy
in
Mechanical Engineering

Lehigh University
August 2017

**Final Dissertation Signature Sheet**

Approved and recommended for acceptance as a dissertation in partial fulfillment of the requirements for the degree of Doctor of Philosophy.

**Date**

**Professor Eugenio Schuster**, Dissertation Advisor

**Accepted Date**

Committee Members:

**Professor Mayuresh V. Kothare**

**Professor Arnold H. Kritz**

**Professor Sudhakar Neti**

**Professor Alparslan Oztekin**

# Acknowledgements

To the many who have contributed to this work you have my sincerest thanks. It would not have been possible without you. First and foremost I would like to express a deep gratitude to my thesis advisor, Professor Eugenio Schuster, for introducing me to wonderful world of tokamak controls research, for guiding me through the many challenges, for setting up the necessary resources, and for connecting me with the right people to make it all come together.

To my dissertation committee members at Lehigh University, Professor Mayuresh V. Kothare, Professor Arnold H. Kritz, Dr. Tariq Rafiq, Professor Sudhaker Neti, and Professor Alparslan Oztekin, thank you for your support during the completion of my dissertation work.

To my fellow colleagues and alumni of the Lehigh Plasma Controls Group, Dr. Justin Barton, Dr. Mark D. Boyer, Dr. Zeki Ilhan, Dr. Wenyu Shi, Hexiang Wang, and Dr. Menno Lauret, thank you for your assistance, collaboration, and most of all for your friendship. I wish you all the best.

Special thanks to the DIII-D National Fusion Facility team at General Atomics, especially Robert D. Johnson for his endless patience in assisting me with the implementation of control algorithms in the DIII-D plasma control system. Thank you to Dr. David A. Humphreys for believing in and supporting this work. Thank you to Dr. John R. Ferron, Dr. Michael L Walker, and Dr. Tim C. Luce for answering the many questions along the way, and thank you to Dr. Al W. Hyatt, Dr. Francesca Turco, and Benjamin G. Penaflor for assistance with carrying out tokamak experiments.

Thank you to my friend, Stephanie Lynn Bolmer, for encouragement and support.

# Contents

# List of Tables

# List of Figures

# Abstract

The tokamak is currently the most promising device for realizing commercially-viable fusion energy production. The device uses magnetic fields to confine a circulating ring of hydrogen in the plasma state, i.e. a cloud of hydrogen ions and electrons. When sufficiently heated the hydrogen ions can overcome the electrostatic forces and fuse together, providing an overwhelmingly abundant energy source. However, stable, high-performance operation of a tokamak requires several plasma control problems to be handled simultaneously. Moreover, the complex physics which governs the tokamak plasma evolution must be studied and understood to make correct choices in controller design. In this thesis, two key control issues are studied intensely, namely the optimization and control of the plasma current profile and control of the plasma rotation (or flow).

In order to maximize performance, it is preferable that tokamaks achieve advanced scenarios (AT) characterized by good plasma confinement, improved magnetohydrodynamic stability, and a largely non-inductively driven plasma current. A key element to the development of AT scenarios is the optimization of the spatial distribution of the current profile. Also, research has shown that the plasma rotation can stabilize the tokamak plasma against degradations in the desired magnetohydrodynamic equilibrium.

In this thesis, new model-based control approaches for the current profile and rotation profile are developed to allow experimental exploration of advanced tokamak scenarios. Methods for separate control of both the current profile and rotation profile are developed. The advanced model-based control methods presented in this thesis have contributed to the understanding of tokamak profile control and in some cases they have been successfully validated experimentally in the DIII-D tokamak.

# Chapter 1

# Introduction

This chapter begins with a review of basic nuclear fusion concepts and the experimental fusion reactor known as the tokamak. The initiated fusion sciences reader is advised to skip to Section 1.5.

## 1.1 Nuclear Fusion

A fusion reaction involves the literal fusing of two lightweight nuclei to produce a heavier product. Generally, the total mass of the products is slightly lower than the total mass of the reactants. The mass defect, i.e. the missing mass, is converted to energy in an amount determined by the law, $E = \Delta mc^2$, where $\Delta m$ is the mass defect. However, in order to obtain fusion reactions, particles must be heated to extremely high temperatures. At low energies, the Coulomb repulsion between like-charged nuclei deflects the particles away from each other, preventing fusion. When the particles are fast enough, i.e. the collisions between particles are energetic enough or equivalently the temperature of the particles is high enough, they can overcome the Coulomb barrier, at which point the short range nuclear force overwhelms the electrostatic force and the particles fuse together. The Coulomb barrier between singly charged ions is roughly 380 keV. However, due to an effect known as quantum mechanical tunneling, the particles can with small probability "tunnel" through the coulomb barrier at energies around 10-20 keV, as illustrated

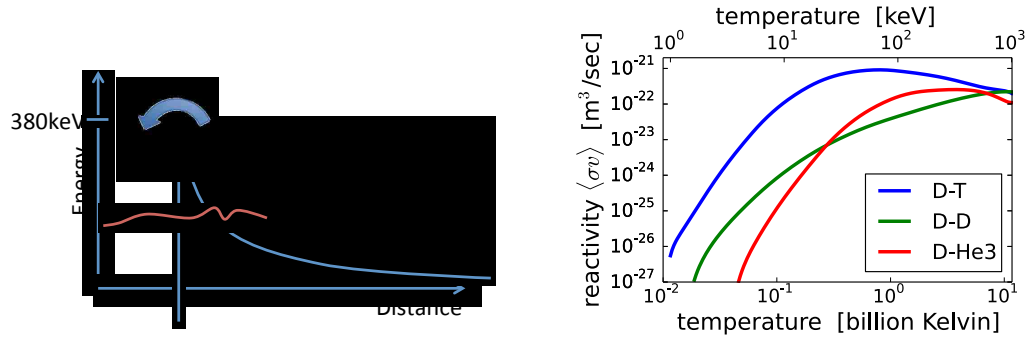


(a) Particle collisions can tunnel through the Coulomb barrier at energies around 10-20 keV.

(b) The reactivity (probability) of various types of fusion reactions: Deuterium-Tritium (D-T), Deuterium-Deuterium (D-D), Deuterium-Helium (D-He3).

**Figure 1.1:** The Coulomb barrier of the D-T reaction is an extremely high 380 keV, but, with some probability, the particles can tunnel through the barrier at 10-20 keV.

in Figure 1.1(a). At the temperatures required for fusion (10s of keV equivalently 100s of millions of degrees Kelvin), matter can only exist in the plasma state, i.e. when electrons are dislocated from their nuclei. Thus, fusion science is inherently connected to the study of plasma physics.

### 1.1.1 The Promise of Fusion

Imagine a world powered by a safe, clean, and virtually limitless fuel source such as water. It may sound fanciful, but that is in fact the world promised by a commercially viable fusion power plant.

The likelihood of fusion reactions can be described by a parameter called the reactivity, which is quantified by the cross section[1] times velocity averaged over the velocity distribution function. The deuterium-tritium (D-T) fusion reaction,

$$^2\mathrm{D} + {}^3\mathrm{T} \rightarrow {}^4\mathrm{He}\ (3.57\mathrm{MeV}) + {}^1\mathrm{n}\ (14.06\mathrm{MeV}) \tag{1.1}$$

is the easiest to produce because it has the largest reactivity as compared to other

[1]The cross-section $\sigma$ measured in units of areas characterizes the probability that a nuclear reaction will occur

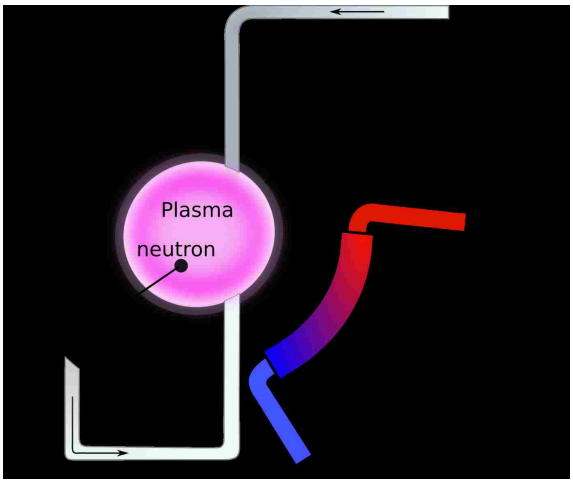


**Figure 1.2:** A fusion breeder reactor schematic. Energetic neutrons react with the surrounding lithium to produce tritium, which is pumped back into the confinement vessel to sustain further fusion reactions.

potential reactions (see Figure 1.1(b)). Deuterium is a stable hydrogen isotope which makes up 0.014% of hydrogenic atoms in ocean water, or approximately 1.6 grams per liter. Tritium does not exist in nature as it is radioactive and short-lived with a lifespan of about 12.5 years, but fortunately it can be produced from lithium, which can be mined or found in ocean water in an amount of 0.15 grams/$m^3$.

It is anticipated that a fusion reactor will produce the necessary tritium fuel from lithium. Tritium is a product of the reaction between an energetic neutron and $Li^6$ (Lithium-six),

$$n + Li^6 \rightarrow T + He + 4.8MeV.$$

along with Helium and 4.8 MeV of energy. Since energetic neutrons are a product of the D-T reaction, they can be used to "breed" the tritium fuel in a reactor. The concept breeder-reactor is illustrated in Figure 1.2, where the plasma confinement vessel is surrounded by a blanket of lithium. As fusion reactions occur, neutrons escape the confinement vessel and enter the blanket, at which point some neutrons react with the lithium to produce tritium. Also, significant heat is produced as neutrons strike the lithium blanket, which can be used to generate steam in a heat exchanger; in turn, the steam drives turbines for the production of electricity.

The real potential of fusion power becomes sharply apparent when comparing the specific energy (energy density) of the D-T reaction to that of conventional fossil fuels. For example, coal has a specific energy of 30 MJ/kg, oil 50 MJ/kg, fission (U-235) represents a giant leap forward to 85 million MJ/kg, but the D-T reaction brings about an incredible energy density of 350 million MJ/kg, more than 10 million times the energy density of coal.

Furthermore, nuclear fusion is incredibly safe. Unlike nuclear fission (the splitting of heavy nuclei into lighter nuclei), fusion does not involve a chain reaction, and the amount of fuel in a large, production-scale reactor would only be around a few grams. Even in the worst case scenario involving complete destruction of the machine, the small amount of radioactive material leaked would be no cause for concern to neighboring residents.

### 1.1.2 The Fusion Triple Product (Requirement for Energy Production)

In this section, some definitions are introduced in order to establish the necessary conditions on various plasma parameters (density, temperature, and confinement) for net energy production in a D-T plasma. Consider, for example, a purely hydrogenic plasma made up of equal parts deuterium and tritium ($n_{\mathrm{D}} = n_{\mathrm{T}} = n/2$), where $n$ is the density of the electrons. To obtain the fusion power density of the entire plasma, we start with the fusion power density for a particular relative velocity of the D-T collision,

$$P_F(v) = \underbrace{n_D n_T \sigma_{\mathrm{DT}}(v) v}_{\#\text{ reactions/s/volume}} \times \underbrace{E_{\mathrm{DT}}}_{\text{energy of reaction}},$$

where $E_{\mathrm{DT}}$ is the energy released from a D-T fusion reaction. If we assume a Maxwellian velocity distribution for each of the plasma species and integrate over the velocity, we can obtain the average energy density of the plasma

$$P_F = \langle P_F(v) \rangle = \frac{1}{4} n^2 \langle \sigma v \rangle_{\mathrm{DT}} E_{\mathrm{DT}}.$$

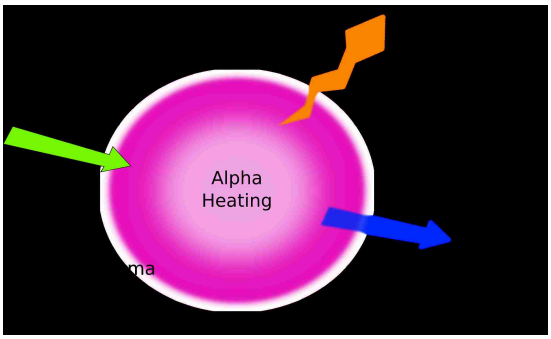


**Figure 1.3:** Example burning plasma in steady state. Alpha heating is the energy associated with the alpha particle, i.e. the Helium product of reaction (1.1.1).

Assume the plasma has reached steady state, in which case the power injected into the plasma plus the power produced from reactions must be equal to the power expelled from various types of losses as in Figure 1.3,

$$P_{\text{in}} + P_{\alpha} = P_{\text{rad}} + P_{\text{dl}}. \tag{1.2}$$

The power associated with alpha particle (Helium product of reaction (1.1.1)), $P_{\alpha}$, remains in the plasma after a reaction. The losses include that from radiation, $P_{\text{rad}}$, and the direct losses, $P_{\text{dl}}$, from convection and conduction. The direct losses can be characterized by the plasma energy confinement time, $\tau_E$, i.e. the characteristic time over which energy is transported outside the plasma. If we assume equipartition between the ions and electrons, which have an energy of $3k_BT/2$ each, where $k_B$ is Boltzmann's constant[2], then the direct power losses per unit volume are given by

$$P_{\text{dl}} = \frac{\text{energy/volume}}{\tau_E} = \frac{3nT}{\tau_E}.$$

The fusion gain, $Q$, is defined as the ratio of fusion power to input power, i.e.

$$Q = \frac{\text{Fusion Power}}{\text{Input Power}} = \frac{P_{\text{fus}}}{P_{\text{in}}},$$

where $P_{\text{fus}}$ is the total power produced by D-T fusion reactions including that associated with the neutrons and alpha particles of (1.1), i.e. $P_{\text{fus}} = P_{\alpha} + P_{\text{neut}}$.

[2]If temperature and energy are both measured in eV, the Boltzmann's constant $k_B = 1$.

At temperatures high enough for a significant number of fusion reactions, the direct losses will dominate over radiative losses. Therefore, at steady state the input power is approximately equal to the direct losses minus the alpha particle power, $P_{\rm in} = P_{\rm dl} - P_\alpha$, and the fusion gain can be written as

$$Q = \frac{P_{\rm fus}}{P_{\rm dl} - P_\alpha} = \frac{\frac{1}{4}n^2\langle\sigma v\rangle_{\rm DT}E_{\rm DT}}{\frac{3nT}{\tau_E} - \frac{1}{4}n^2\langle\sigma v\rangle_{\rm DT}E_\alpha},$$

where $E_\alpha$ is the alpha particle energy associated with the D-T reaction.

Alternatively, writing the input power in terms of the fusion power ($P_{\rm in} = P_{\rm fus}/Q$) we can obtain a constraint on the plasma parameters (density, temperature, and confinement time) required for a desired fusion power gain $Q$. Substituting $P_{\rm in} = P_{\rm fus}/Q$, $P_{\rm rad} \approx 0$, and $P_{\rm dl} = 3nT/\tau_E$, the power balance per unit volume (1.2), can be written as

$$\begin{aligned} P_\alpha + \frac{P_{\rm fus}}{Q} &= \frac{3nT}{\tau_E}, \\ P_{\rm fus}\left(\frac{P_\alpha}{P_{\rm DT}} + \frac{1}{Q}\right) &= \frac{3nT}{\tau_E}, \\ \left(\frac{1}{4}n^2\langle\sigma v\rangle_{\rm DT}E_{\rm DT}\right)\left(\frac{E_{\rm alpha}}{E_{\rm DT}} + \frac{1}{Q}\right) &= \frac{3nT}{\tau_E}, \end{aligned}$$

and, finally, obtaining

$$n\tau_E = \frac{12T/\langle\sigma v\rangle_{\rm DT}}{E_{\rm DT}\left(\frac{E_\alpha}{E_{\rm DT}} + \frac{1}{Q}\right)}. \tag{1.3}$$

From the expression (1.3) we can obtain the **necessary conditions for net energy production in a burning plasma**. In the range of temperatures typical for tokamaks (10-20 keV), the D-T reactivity can be approximated as

$$\langle\sigma v\rangle_{\rm DT} \approx 1.4 \times 10^{-24}T^2 \ ({\rm m}^3\ {\rm s}^{-1}), \tag{1.4}$$

where the D-T reaction energies are $E_{\rm DT} = 17.59$ MeV, and $E_\alpha = 3.56$ MeV. To reach break-even energy production, $Q = 1$, it is required from (1.3) and (1.4), that

$$n\tau_E T|_{\rm break\ even} \cong 10^{21} \ ({\rm keV\ m\text{-}3\ s}). \tag{1.5}$$

In theory it is possible to sustain the plasma with zero auxiliary input power, in which case the plasma is sustained solely by alpha particle heating, and the fusion gain $Q \to \infty$. This condition called "ignition," requires

$$n\tau_E T|_{\text{ignition}} = 6\, n\tau_E T|_{\text{break even}}\,. \tag{1.6}$$

Of course, imperfect energy conversion efficiencies will imply even more demanding constraints on density, temperature, and confinement for a desired fusion gain.

The term $n\tau_E T$ is called the fusion triple product and expression (1.5) is referred to as the Lawson Criterion [1]. Maximizing this quantity is the primary objective of experimental fusion reactors.

## 1.2 The Tokamak

The most promising approach to develop a production-scale fusion power plant is the tokamak. Charged particles are bound in tight orbits around magnetic field lines thanks to the very strong Lorentz force, $F = \hat{q}(v \times B)$, where $\hat{q}$ is the particle's charge, $v$ is the particle's velocity, and $B$ is the magnetic field strength. Taking advantage of the Lorentz force, numerous approaches have been explored to confine hot plasmas with magnetic fields for the purposes of sustaining controlled fusion reactions. The токамак (a Russian acronym for toroidal chamber with magnetic coils) curves a cylindrical magnetic field into a torus. The construction of a tokamak involves wrapping a set of coils poloidally around a toroidal vacuum vessel to produce a toroidal magnetic field as shown in Figure 1.4. However, a purely toroidal field is insufficient to confine the plasma because forces arising due to the radial decay of the toroidal field[3] act on the ions and electrons in different directions leading to charge separation. The resulting electric field subsequently forces the plasma column to drift into the wall of the confining structure. To counteract the charge separation, a poloidal field is introduced. The combined poloidal + toroidal magnetic field lines wind helically around the torus as shown in Figure 1.4. As the particles travel

[3]The toroidal field is inversely proportional to the major radius, $B_\phi \propto 1/R$, where $R$ is the major radius (see Figure 1.5).

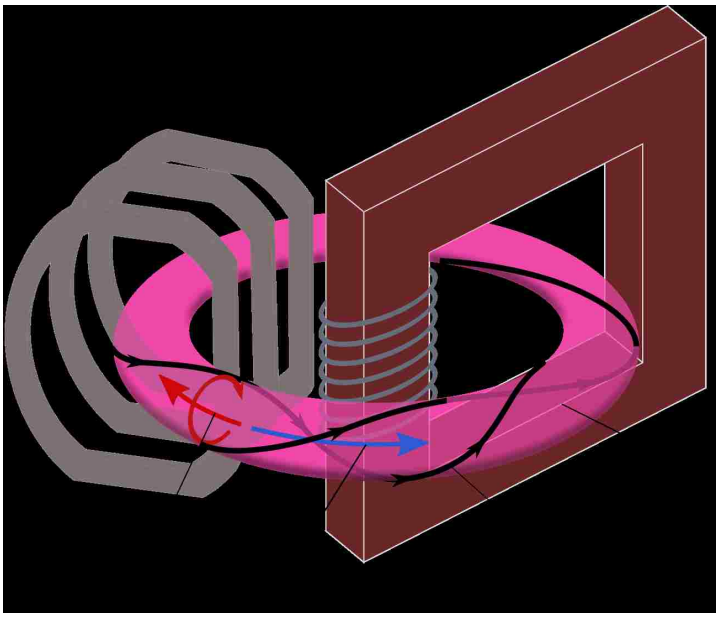

**Figure 1.4:** The tokamak: toroidal field coils wrap poloidally around the plasma torus and provide the primary toroidal field which confines the plasma. The plasma current, typically induced by a transformer effect, provides an additional poloidal field, resulting in a helical field structure.

around the plasma column in the poloidal direction, the particles sample regions of the plasma with opposite drift directions, and, on average, the drift is cancelled out. Since the plasma can also carry electrical currents, a tokamak produces the poloidal field by driving current in the plasma along the toroidal direction. Typically, the main plasma current is induced by a transformer action, where the central coil acts as the transformer primary and the plasma itself acts as the secondary.

The tokamak plasma geometry is essentially a torus (donut) in shape. The toroidal angle, $\phi$, lies in a plane parallel to the torus, and the poloidal angle, $\theta$, lies in a plane associated with a vertical cross-section of the plasma as shown in Figure 1.5. Two coordinate systems are typically used to describe the tokamak geometry, the quasi-cartesian coordinate system defined by $(R, Z, \phi)$, and the quasi-cylindrical coordinate system defined by $(\rho, \theta, \phi)$. These coordinate systems will be useful in the development of first-principles-based models of the current profile and rotation profile evolutions. The major radius of the tokamak is $R_0$, the minor radius is $a$, and the aspect ratio is $A = R_0/a$. For conventional tokamaks, the aspect ratio

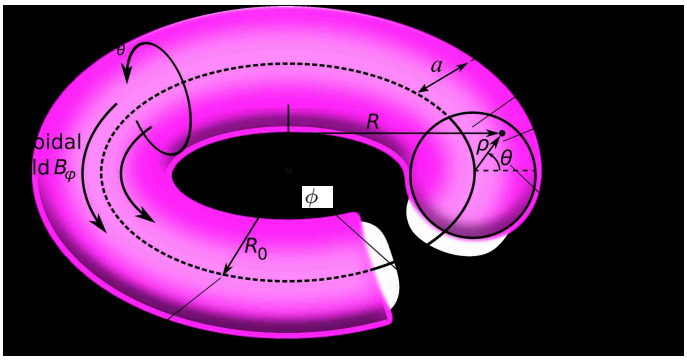


**Figure 1.5:** The tokamak geometry and coordinate system.

is about 3.5.

Research into tokamaks began in the 1960s at the Kurchatov institute in Russia. Today, there are about 40 tokamaks in operation worldwide. The largest, JET, has demonstrated power production of about 16 MW from D-T fusion with transient $Q$ values in the range of 0.6-0.9. The future of tokamak research is now focused around the ITER tokamak ("The Way" in Latin), which is expected to be completed in the 2020s [2] and will be able to produced sustained power production around $Q = 5-10$ for $\approx 1000$ seconds.

For stable tokamak plasmas, a hard limit on density exists (the Greenwald density limit), therefore, the primary goal of tokamak research is to maximize the energy confinement time. For various reasons described in the following sections, both the current profile and rotation profile play an important role in improving the confinement of tokamaks. Therefore, control of these parameters is becoming increasingly important in the tokamak research community.

### 1.2.1 Heating and Current Drive Systems

During the ramp-up phase much of the plasma current required for the poloidal magnetic field is driven inductively by a transformer action. The induced plasma current also heats the plasma due to resistive heating. However, the temperatures that can be reached by ohmic heating alone are insufficient to initiate a burning

plasma, therefore alternative heating sources are necessary. Besides ohmic heating, auxiliary heating sources generally fall into one of two categories; 1) injection of highly energetic neutrals, which heat the plasma through collisions between the energetic particles and the plasma particles; 2) injection of radio-frequency (RF) waves, whereby a wave is coupled to the plasma at a frequency resonant with a category of particles in the plasma and, therefore, capable of transferring energy to those particles.

### Ohmic Heating and Current Drive

Ohmic heating is the heating of a plasma by an electrical current. The current is generated by swinging the flux in the transformer coil, i.e. running a current through the coil, to produce an electromotive force in the plasma ring, which in turns drives a current in the plasma. The portion of the total plasma current that is driven by the transformer effect is referred to as the ohmic current throughout this work. Since the plasma resistivity is known to scale approximately with temperature as $\eta \propto T_{\mathrm{e}}^{-3/2}$, where $\eta$ is the plasma resistivity and $T_{\mathrm{e}}$ is the electron temperature, we can make a couple of observations about the ohmic current. First, the current driven by a transformer effect is given by

$$I_{\mathrm{p}} = -\frac{1}{R_{\mathrm{p}}} \underbrace{\frac{d\phi^{\mathrm{trans}}}{dt}}_{\substack{\text{Transformer} \\ \text{Flux Swing}}},$$

where $I_{\mathrm{p}}$ is the total plasma current and $R_{\mathrm{p}}$ is the average plasma resistance. The ohmic heating power is given by

$$P_{\mathrm{ohm}} = R_{\mathrm{p}} I_{\mathrm{p}}^2 \sim \eta j_\phi^2 \sim T_{\mathrm{e}}^{-3/2},$$

where $j_\phi$ is the toroidal current. Therefore the heating effect of the plasma current becomes progressively more and more inefficient as the plasma temperature increases. Above temperatures of about 1 keV, the ohmic heating effect is essentially absent. This implies alternative heating sources are required to reach temperatures necessary for fusion. Second, since the temperature profile is peaked at the plasma

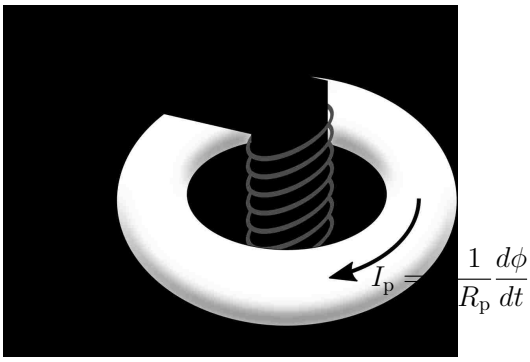


(a) Transformer

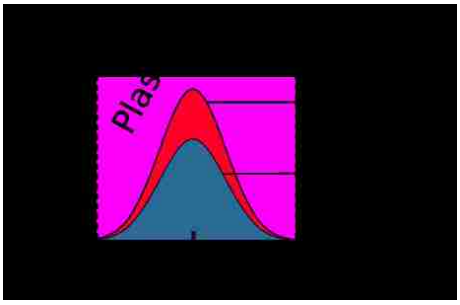


(b) Ohmic Current Profile Shape

**Figure 1.6:** Ohmic current driven by flux swing of transformer. Since the resistivity is proportional to temperature, and the temperature is peaked in the plasma center the ohmic current will also be peaked in the plasma center.

center, the resistivity will be smallest at the center, and therefore the ohmic current will also be peaked at the plasma center as shown in Figure 1.6(b). As will be described in the following sections, centrally peaked current profiles are not desirable for high plasma performance implying a need for alternative sources that can drive current off-axis.

Because the ohmic current is driven by a flux swing, which is inherently limited by the maximum current limit of the ohmic coil, inductive current drive is necessary limited in duration. This is the primary reason that tokamaks are operated in short pulses. Non-inductive current drive sources can, in principle, lengthen the pulse of tokamaks to indefinite operation, and can also be used to locally modify the current profile.

### Neutral Beam Injection

Neutral beam injection (NBI) consists of injecting highly energetic neutral particles into the plasma. The neutral particles become ionized once they enter the plasma and transfer their energy and momentum to the existing plasma particles via collisions.

A schematic of a simplified neutral beam system is shown in Figure 1.7. First a source of neutral gas flows into the neutral beam injector, the neutral gas is then

converted into positive ions by an arc discharge, for example. The newly created ions are then accelerated by a set of electrostatic grids. The beam of highly energetic ions is then passed through a neutralization chamber, which is essentially a large box filled with a low density neutral gas. As the ions pass through the neutral gas, some of the ions experience a charge exchange with the neutral atoms, obtaining an electron and thus neutralizing the positive ion. Of course, only a fraction of the ions will be neutralized so the remaining charged particles are defected into an ion dump, which must be actively cooled. Once neutralized, the high energy particles are free to pass through the deflector and the confining magnetic field into the tokamak plasma.

NBI systems typically function as the auxiliary heating work horse in many present-day tokamaks. If the beams are aligned tangentially with the plasma torus, they can also provide momentum drive and current drive to the plasma. Varying the alignment of the beam with the plasma allows the application of different current and torque input profiles enabling current and rotation profile control. However, their are a few drawbacks associated with NBI; *i)* the power deposition profile is not very localized which limits their effectiveness for profile control, *ii)* the large size of the of the neutral beam implies the need for a large opening in the plasma chamber which can lead to concerns associated with neutron leakage from a reactor device, *iii)* the present-day technology has a low electrical efficiency which presents a problem for a commercial device. Substantial research efforts including the use of negative ions to improve the efficiency of NBI devices is on going [3].

### Radio Frequency (RF) Waves

Radio frequency waves can be used to heat the plasma by an effect known as cyclotron absorption or drive current by an effect known as Landau absorption. In any case, the wave is generated by different systems according to frequency (tetrodes or diacrodes for ion cyclotron frequency, klystrons for hybrid frequency, gyrotrons for electron cyclotron frequency), then is propagated to the tokamak by carefully scaled transmission lines (wave guides), and then is coupled to the plasma by means of an

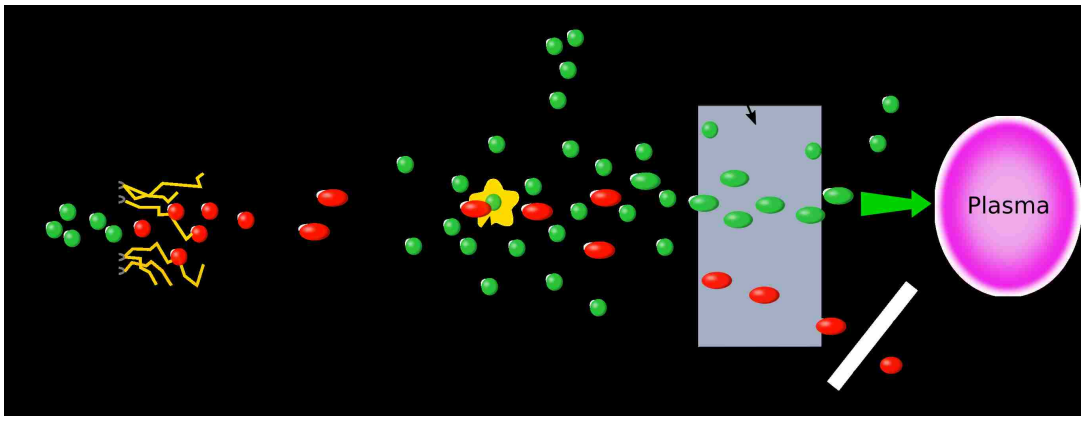


**Figure 1.7:** Neutral beam injector schematic.

antenna, placed inside the vacuum chamber. Apart from the material problems posed by these sensitive electro-technical systems, the difficulty consists in coupling the wave to the plasma, involving complex physical processes and requiring proper control of the plasma edge.

## 1.3 Tokamak Parameters of Interest

The plasma toroidal $\beta$, defined as the ratio of kinetic pressure to magnetic pressure,

$$\beta = \frac{\langle p \rangle}{B_{\phi,0}^2/2\mu_0}, \tag{1.7}$$

represents a measure of confinement efficiency, where $\langle p \rangle$ is the volume averaged plasma pressure, $B_{\phi,0}$ is the vacuum toroidal field strength at the magnetic axis, and $\mu_0$ is the vacuum permeability. Normalizing the plasma $\beta$ to the total plasma current, $I_\mathrm{p}$, we obtain a parameter that is often used as a heuristic for plasma stability,

$$\beta_N = \beta[\%]\frac{a[\mathrm{m}]B_{\phi,0}[\mathrm{T}]}{I_\mathrm{p}[\mathrm{MA}]}. \tag{1.8}$$

The maximum $\beta_N$ that can be obtained before instigating a complete collapse of the plasma is given by the TROYON limit, which is generally around $\beta_N \leq 3.5$ for most conventional tokamaks [4]. The DIII-D tokamak, which is the tokamak of primary

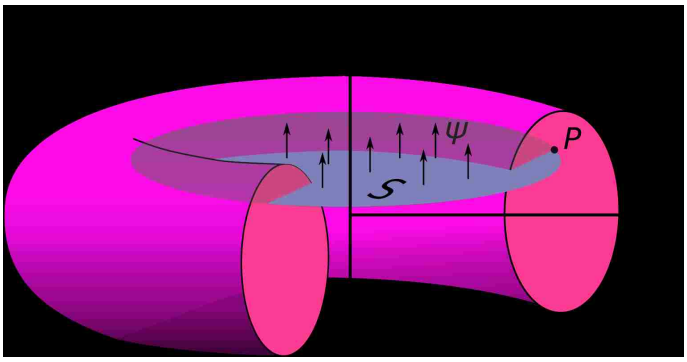


**Figure 1.8:** The poloidal flux definition.

focus throughout this work, has been able to exceed the TROYON limit ($\beta_N \sim 4$) by using highly triangular shaped plasma.

A quantity closely related to the current profile is the safety factor profile, $q$. The safety factor

$$q = \frac{\partial \Phi}{\partial \Psi}$$

is a measure of the pitch of the helical magnetic field lines, where $\Phi$ is the toroidal field component and $\Psi$ is the poloidal field component. A tokamak discharge operates at constant toroidal field, thus the $q$ profile is considered in most cases to be purely a function of the poloidal field. Since the poloidal field is dominated by the toroidal current density distribution (the current profile), the $q$ profile is connected in a one-to-one relationship to the current profile. It is in fact common to refer to $q$ profile and current profile interchangeably.

To model the $q$ profile evolution it will be important to define the poloidal magnetic flux. As is illustrated in Figure 1.8, the poloidal magnetic flux, $\Psi$, at a point $P$ in the cross section of the plasma (i.e., poloidal cross section) is the total flux through the surface $S$ bounded by the toroidal ring passing through $P$, i.e., $\Psi = \int_S \frac{1}{2\pi} B_\mathrm{p} d\mathrm{S}$. As mentioned above the $q$ profile can be expressed as a function of the poloidal magnetic field or equivalently of the poloidal flux, i.e., $q = q(\Psi)$.

## 1.4 Tokamak Confinement Modes and Operating Scenarios

Experiments conducted on the ASDEX tokamak in the early eighties led to the discovery of the H-mode (for "High Confinement"), which provided for a near doubling of the confinement time over what was then the more standard operating mode now called L-mode (for "Low Confinement"). The H-mode is obtained by injecting a sufficient amount of power into the plasma until the appearance of an edge transport barrier (ETB), which is characterized by a steep pressure gradient towards the edge of the plasma. In contrast, the L-mode plasma shows a pressure profile which decays at a smooth rate towards the plasma edge as shown in Figure 1.9(a).

In a standard H-mode discharge most of the current is driven by inductive means, which translates to a monotonic $q$ profile, with $q$ near 1 at the plasma center, see Figure 1.9(b). Today, the H-mode, is solidly established, and research is well underway on alternative scenarios called *advanced tokamak scenarios*. The tokamak operating scenario is for the most part defined by the pressure and $q$ profiles. We can obtain an advanced scenario by introducing a significant fraction of non-inductive current off-axis. Slowly increasing the non-inductive, off-axis current, the first operating scenario observed is the *hybrid* scenario, which is characterized by a flat zero magnetic sheared $q$ profile near the plasma center. For a toroidal magnetic confinement device, the magnetic shear is given by

$$s = \frac{\rho}{q}\frac{dq}{d\rho}. \tag{1.9}$$

High values of magnetic shear provide stability, since the radial extension of $q$ values where MHD modes can become unstable is reduced. Negative shear also provides stability because convective cells, generated by curvature-driven instabilities, are sheared apart as the field lines twist around the torus [5]. Increasing the non-inductive current fraction further results in a negative sheared $q$ profile, which characterizes the advanced scenario. Strongly negative sheared $q$ profiles are correlated with the appearance of internal transport barriers (ITB), a strong pressure gradient in the core, providing a region of significantly reduced transport in the plasma center

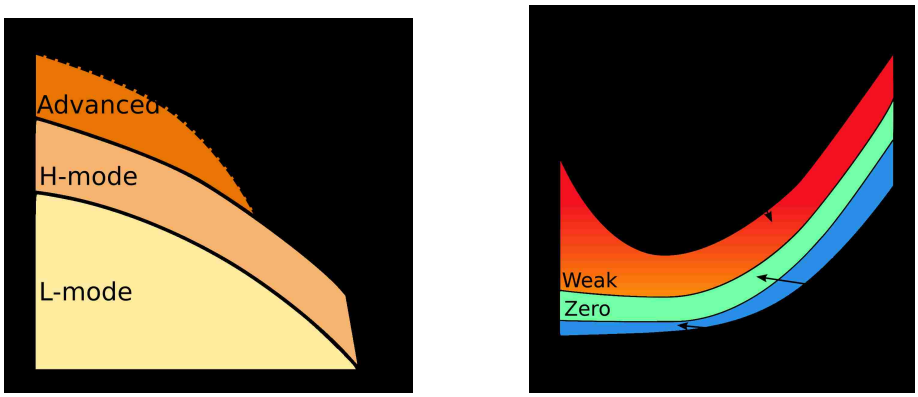


(a) Confinement modes characterized by pressure profile.

(b) Operating scenarios characterized by $q$ profile.

**Figure 1.9:** Tokamak confinement modes and operating scenarios.

(see Figure 1.9).

The steep gradient in the plasma pressure profile associated with advanced scenarios also corresponds to a large amount of off-axis bootstrap current reducing the needs for auxiliary current drive sources. In principle, if all the current can be driven non-inductively, the ohmic current drive could be eliminated therefore enabling continuous or non-pulsed operation of the machine.

The advanced tokamak scenario is highly promising, but requires sophisticated control solutions to actively shape the current profile distribution during the discharge.

## 1.5 Current Profile Control

Control and optimization of the plasma current profile shape is key to improving tokamak performance. This is largely due to the effects of the $q$ profile on transport and plasma heat confinement. For example, optimizing the $q$ profile to obtain low magnetic shear across a large volume of the plasma core, i.e. the hybrid scenario described in Section 1.4, has achieved improved confinement and higher $\beta$ limits (improved stability against deleterious MHD) relative to the standard inductive H-mode [6, 7]. This is partly due to the absence of large sawteeth which can trigger

NTMs and partially due to a reduction in radial transport that is accompanied by triggering internal transport barriers (ITB). Furthermore, the increased central pressure associated with a sheared magnetic profile drives bootstrap current aiding in the access of steady-state plasmas, i.e. plasmas composed of 100% non-inductive current, which are most likely required for reactor-grade devices. An extensive body of research on the connection between current profile shape and plasma performance in terms of stability, transport, and steady-state potential exists in the literature, see [8–11] for a review.

The standard method to obtain an advanced tokamak scenario characterized involves a fast current ramp-up with early heating [12]. The ohmically driven current is initially focused towards the plasma edge and the early heating slows the diffusion of the current into the plasma center. The induced off-axis current can be replaced by non-inductive current driven from auxiliary sources or bootstrap current, to prevent the $q$ profile from relaxing to a standard monotonic profile. A careful timing of the current ramp and application of auxiliary sources is necessary to guide the plasma through a stable operating space and avoid instigating MHD activity. Maintaing good profile development on a reliable shot-to-shot basis requires sophisticated current profile control algorithms.

## 1.6 Rotation Profile Control

In a tokamak, each individual particle has its own velocity. The net sum of velocities of a particle species, hydrogen ions for example, is the fluid velocity of that species. The fluid velocity can be separated into components parallel and perpendicular to the flux surfaces. Fluid velocity perpendicular to a flux surface is called convection, and fluid velocity parallel to the flux surface is called rotation [13]. The toroidal shape of a tokamak produces strong poloidal rotation damping [14], therefore the toroidal rotation is usually of much more importance to plasma stability and performance.

It is generally accepted that plasma rotation can contribute to both stability

and confinement in tokamak plasmas. The confinement in a tokamak is governed by the radial transport of energy from the plasma center to the plasma edge. A large part of this transport is driven by turbulence, which is substantially reduced by rotational shear. The role of the so-called $E \times B$ rotation shear in enhancing energy confinement by suppressing turbulence is now well established theoretically [15] and experimentally [16].

Plasma toroidal rotation, or its shear, has also been recognized as a stabilizing mechanism for deleterious magnetohydrodynamic (MHD) instabilities such as the neoclassical tearing mode (NTM) [17–19] and the resistive wall mode (RWM) [20, 21]. If not suppressed, such MHD instabilities would otherwise limit the achievable $\beta$. NTMs and RWMs undesirably reshape the confining magnetic field lines. Ideally, a plasma will be confined in a set of perfectly nested magnetic-flux surfaces. However, sources of free energy in the plasma or external deviations in the confining magnetic field, error fields, can break up and reconnect the flux surfaces with deformed magnetic topology, a process known as a tearing mode. Error fields are static, and as a result, the tearing modes they excite do not move. Tearing modes, however, have to rotate with the plasma velocity. In rotating plasmas, the tendency of error fields to drive tearing modes is suppressed. The RWM, a non-axisymmetric phenomena in tokamaks, is a form of plasma kink instability. In a kink mode, the entire plasma configuration deforms in a helically symmetric manner. RWMs occur in plasmas with a high plasma energy density. When they lock, i.e. when they do not move with respect to the vessel wall, RWMs can cause a disruption (a catastrophic loss of plasma energy to the confining wall). Like tearing modes, the magnetic topology of RWMs is suppressed in rotating plasmas. It has been shown that the critical rotation speed for RWM stabilization is indeed a function of the rotation profile shape, implying a radially distributed stabilizing mechanism [22].

Torques on the plasma, i.e. sources of toroidal angular momentum include neutral beam injection (NBI) and the non-axisymmetric magnetic fields (NRMF) generated by a set of coils adjacent to the plasma.

NBI is the dominant source of momentum (and therefore rotation) in present-day tokamaks [23, 24]. Mature numerical codes, such as TRANSP [25], are now

routinely used to compute the NBI sources of momentum and energy. NBI also enables a technique known as charge exchange spectroscopy [26], which is used to measure the rotation across the plasma radius.

Ambient or purposely imposed non-axisymmetric magnetic fields (NRMF) (perturbations from the perfectly symmetric tokamak field configuration) create a drag force on the plasma rotation, an effect known as neoclassical toroidal viscosity (NTV) [27, 28]. Theoretically, this can be understood in terms of increased radial transport resulting from nonuniformity of the magnetic field caused by the nonaxisymmetric fields [29]. Recent experiments have observed that static NRMF fields tend to drag the rotation to a negative offset [30, 31], allowing spin-up of rotation in the counter-current direction. Plasma acceleration has also been achieved using rapidly rotating resonant fields [32], creating a "forward drag".

## 1.7 Experimental Fusion Devices Considered in this Work

### 1.7.1 The DIII-D Tokamak

The DIII-D tokamak pioneered the distinctive D shape plasma, now the standard for most tokamak operation around the world, shown in Figure 1.10(a). The D shape was found to suppress a variety of instabilities and therefore vastly improve the plasma confinement. The NBI system at DIII-D consists of four beam-lines, each of which has two ion sources in parallel. Each ion source can inject a maximum of around 2.0 MW of power into the plasma. Of the eight ion sources, four are configured to inject in the co-current direction (in the same direction as the plasma current) aligned with the magnetic axis, two beams are configured to drive co-current with alignment 16.5° off-axis, and the last two beams are configured to inject counter-current (opposite to the plasma current direction) with on-axis alignment. The configuration of each beam type is shown in Figure 1.10(b). Additionally, DIII-D is equipped with six gyrotrons which can be configured for electron heating

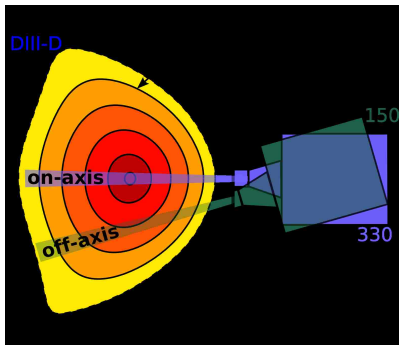


(a) Direction of on-axis vs off-axis NBI deposition. The DIII-D plasma shape has a very D like shape, improving access to high confinement operating regimes.

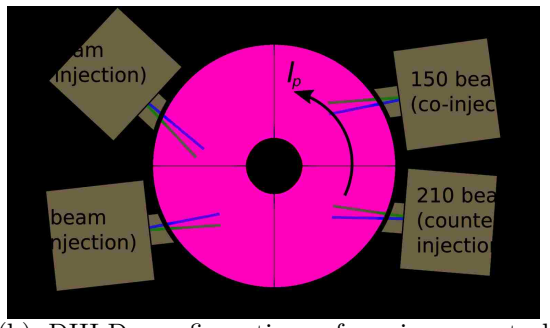


(b) DIII-D configuration of various neutral beam injectors relative to the plasma current direction.

**Figure 1.10:** DIII-D NBI configuration.

or current drive. The discharge length of the DIII-D tokamak is about 6 seconds, which is about 5 times the resistive diffusion time. Combined with the long discharge time and the assortment of auxiliary current drive sources, DIII-D makes for a good test bed for current profile control algorithms.

### 1.7.2 The Spherical Torus and NSTX-U

A spherical torus (ST) [33–35] differs from a conventional tokamak in that it has a much smaller aspect ratio (major radius/minor radius) of $A = R_0/a < 2$ compared to 3.5-5 for typical tokamaks. Whereas a conventional tokamak plasma is much like a donut in shape, the ST plasma resembles a cored apple, see Figure 1.11(a). As the aspect ratio shrinks, the qualitative structure of the field lines is altered as illustrated in Figure 1.11(b). In a tokamak the toroidal field is much stronger than the poloidal field, whereas the ST poloidal field is of comparable or greater strength than the toroidal field in the plasma out-board region. At the in-board region, however, a stronger toroidal field and relatively short toroidal circumference compared to the poloidal circumference, results in a qualitatively different field line structure. The net result is that the edge safety factor $q$ can be raised to $\approx 10$ in the ST plasma [34]. Comparatively, the tokamak requires an edge $q$ around 3-5

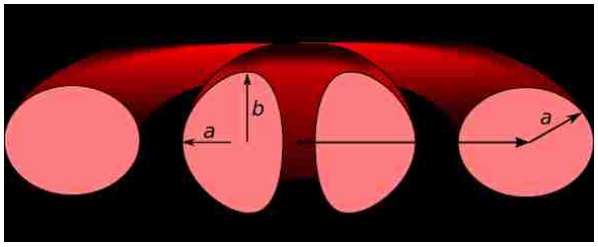


(a) The spherical torus is characterized by a larger aspect ratio ($A = R_0/a$) and larger elongation ($\kappa = b/a$) than that of a conventional tokamak.

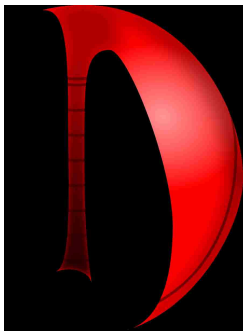

(b) Due to the large aspect ratio and elongation, the ST field lines spend more time on the in-board side of the machine.

**Figure 1.11:** Tokamak vs spherical torus.

to permit interesting plasma $\beta$ values. The higher safety factor provides improved stability of large-scale MHD modes in the plasma.

The improved stability of the ST can be understood from the increased $\beta$ limit associated with lower aspect ratio and higher elongation. The critical $\beta$ limit is given by

$$\beta_{\text{crit}} \approx 5\langle B_N \rangle \left( \frac{1+\kappa^2}{2} \right) \frac{1}{Aq^\star}$$

where $\langle B_N \rangle$ is a constant and $q^\star$ is the modified cylindrical safety factor [36]. Due to the low aspect ratio, $A$, and large elongation, $\kappa$ in the ST, the plasma $\beta$ can exceed that of a standard tokamak by an order of magnitude. The improved stability of the ST is due to the fact that particles spend an increased portion of their orbit on the in-board side of the device, see Figure 1.11(b), where they experience convex lines of magnetic force as opposed to concave on the out-board side of the device. It is theorized that field line curvature associated with convex magnetic force is beneficial to plasma stability [34].

The ST approach is economically attractive because it discards components from the inner side of the plasma: no in-board blanket or shield, no in-board poloidal coil, and the field coils are inherently much smaller on account of the compact plasma shape. However there is a downside to the compactness: little room is left for a central solenoid, which means the ST will have to rely on little to no inductive

current drive. This presents a significant challenge especially during the plasma startup and current ramp-up phases of the discharge.

Methods for non-inductive startup have included lower hybrid (LH) current [37] RF assistance [38], and helicity injection [39]. Initial progress towards the design of non-inductive current ramp-up scenarios in the National Spherical Torus Experiment Upgrade (NSTX-U) has been made through the use of TRANSP predictive simulations [40]. The strategy involves, first, ramping the plasma current with high harmonic fast waves (HHFW) to about 400 kA, and then further ramping to 900 kA with neutral beam injection (NBI). However, the early ramping of neutral beams and application of HHFW leads to an undesirably peaked current profile making the plasma unstable to ballooning modes. It is expected that careful control and optimization of the density and current profiles through the ramp-up phase will be necessary to ensure robust, reliable current ramp-up. Recently completed upgrades to NSTX-U including 3 additional large tangency radius NBI, see Figure 1.12, will enable sufficient current drive for 100% non-inductive scenarios and control of the current profile.

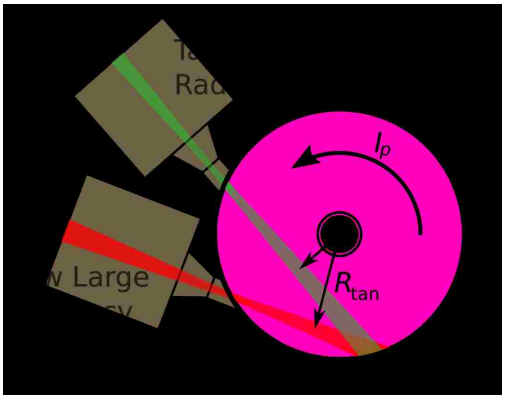


**Figure 1.12:** Recently upgraded NSTX-U includes three additional NBI at large tangency radii.

## 1.8 Dissertation Outline

The dissertation is organized as follows:

– Chapter 2: **Data-Driven Modeling of Current Profile and $\beta_N$ Evolution**

A control-oriented, linear model of the poloidal magnetic flux profile, which is directly related to the current profile, and normalized beta, $\beta_N$, evolution is developed based on experimental data from the DIII-D tokamak. Dedicated system-identification experiments have been carried out to generate data for the development of this model. The data-driven model, which is both device-specific and scenario-specific, describes the response of the poloidal flux profile the inductive current drive as well as the auxiliary heating and current drive systems during the flat-top phase of a H-mode discharge in DIII-D.

– Chapter 3: **First-Principles Based Modeling of the Current Profile and Rotation Profile Evolution**

Simplified physics-based models of the current profile and rotation profile evolution are presented that are suitable for control design. The models combine first principles laws with correlations of various plasma parameters specific to the particular scenario and machine to be controlled. These models are used for the development of real-time optimal control strategies in later chapters as well as simulation testing of the proposed control strategies.

– Chapter 4: **Feedforward Control Design via Nonlinear Optimization**

In this chapter, feedforward control solutions for reaching target $q$ profiles during the ramp-up phase of the tokamak discharge are developed. The control problem is formulated as a nonlinear optimization problem, and designed so as to produce a control strategy that the steers the tokamak plasma to the desired target $q$ profile while avoiding plasma stability limits.

– Chapters 5 and 6: **Feedback Control Design for the Current Profile Evolution**

In these chapters, the feedforward control strategy of Chapter 4 is combined with feedback control to mitigate deviations from the desired target current

profile evolution. Various approaches to feedback control are considered, each with increasing complexity until arriving at a model predictive control strategy that combines current profile control with plasma stored energy control. Constraints are imbedded into the control design actions so as to avoid violation of plasma stability limits. Numerous experiments demonstrating the effectiveness of the combined feedforward + feedback control approach are presented.

– Chapter 7: **Feedback Control Design for the Rotation Profile Evolution**

  Two feedback control approaches suitable for regulating the combined rotation profile and plasma stored energy evolution are considered. The first, a state feedback control approach, presents a simple solution for profile control, and, the second, a model predictive control approach allows the introduction of various types of constraints to provide a control approach that can regulate the profile while avoiding plasma stability limits or adapted to a variety of control objectives.

– Chapter 8: **TRANSP-Based Optimization for Non-inductive Ramp-up**

  In this chapter, the TRANSP code is combined with an optimization routine to aid the design of open-loop control strategies in tokamaks. The particular case of non-inductive ramp-up in NSTX-U is considered as an example problem.

– Chapter 9: **Conclusions and Future Work**

  This chapter summarizes the contributions of the dissertation and discusses possible directions for further research.

# Chapter 2

# Data-Driven Modeling of Current Profile and $\beta_N$ Evolution

In this chapter a data-driven model for the evolution of the poloidal magnetic flux profile, which is directly related to the safety factor profile (equivalently the current profile), and the normalized plasma beta, $\beta_N$, is constructed for the DIII-D tokamak based on experimental data. Mathematical modeling of plasma transport phenomena with sufficient complexity to capture the dominant dynamics is critical for plasma control design. Transport theories (classical, neoclassical and anomalous) even under restrictive assumptions, produce strongly nonlinear models based on partial differential equations (PDEs). The complexity of these first-principles models needs to be reduced for control design since it is very challenging, if not impossible, to synthesize compact and reliable control strategies based on these complicated mathematical models. During this control-oriented model reduction process there is always a trade-off between the simplicity of the model and both its physics accuracy and its range of validity, which will of course be reflected in the model-based controller performance and capability. First-principles modeling provides the freedom of arbitrarily handling this trade-off and deciding on the level of complexity and accuracy of the model. If, however, model simplicity is preferred over model accuracy

and range of validity, data-driven modeling techniques, including system identification [41] and data assimilation [42], emerge as an alternative to first-principles modeling and have the potential to obtain low-complexity, linear, dynamic models useful for the design of local regulators that are effective around an equilibrium.

Data-driven modeling techniques have been successfully used in the past to model plasma transport dynamics for active control design in tokamaks [43]. System identification using input/output data has been used to model the current profile dynamics in ASDEX Upgrade [44]. In the JET tokamak [45], a two-time-scale linear model has been used to describe the dynamics of the magnetic and kinetic profiles around certain quasi-steady-state trajectories, where system matrices can be identified from experimental data. In low confinement (L-mode) discharges of the JT-60U tokamak [46], diffusive and non-diffusive coefficients of the momentum transport equation of the toroidal rotation profile dynamics have been estimated from transient data obtained by modulating the momentum source.

This chapter is organized as follows. In Section 2.1, a model structure suitable for system identification is derived. In Section 2.2, the system identification procedure used to obtain the identified model is described. Finally, in Section 2.3, a statement of conclusions is made.

## 2.1 Model Structure

The poloidal magnetic flux at the plasma edge evolves according to $\partial\Psi_{\text{edge}}/\partial t = -V_{\text{loop}}$, where $V_{\text{loop}}$ is the externally applied loop voltage. Since the poloidal magnetic flux will therefore not reach a stationary[1] if the applied loop voltage is nonzero, we instead consider the poloidal magnetic flux relative to its boundary value. Let $\psi$ be the poloidal magnetic flux per radian, i.e. $\psi = \Psi/2\pi$, and $\bar{\psi}$ be the value of $\psi$ relative to the boundary value, i.e. $\bar{\psi} = \psi(\hat{\rho}, t) - \psi(1, t)$. With this change of variables, the boundary condition at the edge becomes, $\bar{\psi}(1, t) = 0$, allowing the profile to reach a stationary value for constant inputs.

[1] A stationary profile is one that is fixed in time.

The evolution of $\bar{\psi}$ is given by the magnetic diffusion equation [47, 48], which, with the assumption of a fixed cylindrical plasma shape, can be written as [49]

$$\frac{\partial \bar{\psi}}{\partial t} = c_1 \eta \frac{1}{\hat{\rho}} \frac{\partial}{\partial \hat{\rho}} \left( \hat{\rho} \frac{\partial \bar{\psi}}{\partial \hat{\rho}} \right) + c_2 j_{\mathrm{NI}} + \frac{1}{2\pi} V_{\mathrm{loop}}, \tag{2.1}$$

with boundary conditions $\partial \bar{\psi}/\partial \hat{\rho}(0,t) = 0$, $\bar{\psi}(1,t) = 0$, where $c_1$ and $c_2$ are constants associated with the plasma shape and the toroidal magnetic field configuration, and $j_{\mathrm{NI}}$ is the noninductive current density. The spatial coordinate, $\rho$, can be expressed in terms of the toroidal magnetic flux, $\Phi$, and the toroidal field strength at the plasma center, $B_{\phi,0}$, i.e. $\pi B_{\phi,0} \rho^2 = \Phi$. Normalized $\rho$, denoted by $\hat{\rho} \in [0,1]$, is defined as $\rho/\rho_b$, where $\rho_b$ is the value of $\rho$ at the last closed magnetic flux surface.

The evolution of the plasma electron temperature, $T_e$, is given by

$$\frac{3}{2} n_e \frac{\partial T_e}{\partial t} = c_3 \frac{1}{\hat{\rho}} \frac{\partial}{\partial \hat{\rho}} \left( \hat{\rho} n_e \chi_e \frac{\partial T_e}{\partial \hat{\rho}} \right) + Q_e, \tag{2.2}$$

with boundary conditions $\partial T_e/\partial \hat{\rho}(0,t) = 0$, $T_e(1,t) = T_{e,\mathrm{bdry}}$, where $n_e$ is the plasma electron density, $\chi_e$ is the electron heat diffusivity, and $Q_e$ is the total electron heating power density, and $T_{e,\mathrm{bdry}}$ is the electron temperature at the plasma boundary, which is assumed constant [50]. Since the plasma resistivity and the bootstrap current, which contributes to the noninductive current density, are both functions of the electron temperature, the dynamics of the poloidal magnetic flux are coupled to the dynamics of the electron temperature.

### 2.1.1 Linearization and Reduction to State Space Form by Galerkin Projection

Assuming the coupled system defined by (2.1) and (2.2) is linearized around a stationary equilibrium[2], we can introduce some unknown linear differential operators, $L_{\alpha,\beta}(\hat{\rho})$, where the first subscript denotes the equation linearized and the second subscript represents the deviation variable. The differential operators depend only

[2] An equilibrium state, referred to as the reference state, is defined as a state where the internal plasma parameters are stationary, i.e. no longer evolving in time.

on the variable $\hat{\rho}$ since the linearization is assumed to be obtained at a stationary equilibrium point. The linearized system can then be written as

$$\frac{\partial \hat{\bar{\psi}}}{\partial t}(\hat{\rho},t) = L_{\bar{\psi},\bar{\psi}}(\hat{\rho})\hat{\bar{\psi}}(\hat{\rho},t) + L_{\bar{\psi},T_e}(\hat{\rho})T_e(x,t) + \boldsymbol{L}_{\bar{\psi},\boldsymbol{u}}\boldsymbol{u}(t), \tag{2.3}$$

$$\frac{\partial \hat{T}_e}{\partial t}(\hat{\rho},t) = L_{T_e,\bar{\psi}}(\hat{\rho})\bar{\psi}(\hat{\rho},t) + L_{T_e,T_e}(\hat{\rho})\hat{T}_e(\hat{\rho},t) + \boldsymbol{L}_{T_e,\boldsymbol{u}}\boldsymbol{u}(t), \tag{2.4}$$

where $\hat{\bar{\psi}}$ and $\hat{T}_e$ represent the values of $\bar{\psi}$ and $T_e$, respectively, relative to their reference equilibrium values, i.e.

$$\begin{aligned} \hat{\bar{\psi}}(t) &= \bar{\psi}(t) - \bar{\psi}_{\text{ref}}, \\ \hat{T}_e(t) &= T_e(t) - T_{e,\text{ref}}. \end{aligned} \tag{2.5}$$

The input vector, $\boldsymbol{u}(t)$, represents the set of actuators relative to their reference values associated with the equilibrium of interest,

$$\boldsymbol{u}(t) = \begin{bmatrix} P_{\text{CO}}(t) - P_{\text{CO,ref}} \\ P_{\text{OA}}(t) - P_{\text{OA,ref}} \\ P_{\text{CT}}(t) - P_{\text{CT,ref}} \\ P_{\text{BAL}}(t) - P_{\text{BAL,ref}} \\ P_{\text{EC}}(t) - P_{\text{EC,ref}} \\ V_{\text{loop}}(t) - V_{\text{loop,ref}} \end{bmatrix} \tag{2.6}$$

where $P_{\text{CO}}$ is the co-current on-axis NBI power, $P_{\text{OA}}$ is the co-current off-axis NBI power, $P_{\text{CT}}$ is the counter-current on-axis NBI power, $P_{\text{BAL}}$ is the balanced NBI power, $P_{\text{EC}}$ is the total ECCD power, and $V_{\text{loop}}$ is the externally applied plasma loop voltage. The eight NBI sources at DIII-D have been reduced to a set of four actuators for simplicity by grouping the NBI with similar effects on the plasma. The $P_{\text{CO}}$ group consists of NBI sources 30L and 330L, the $P_{\text{OA}}$ group consists of NBI sources 150L and 150R, the $P_{\text{CT}}$ group consists of the NBI source 210R, and the $P_{\text{BAL}}$ (balanced) group consists of NBI sources 210L and 330R (see Figure 1.10(b)). The balanced group combines one counter-current NBI source with one co-current NBI source, with the purpose of creating an actuator that drives little current and

only heats the plasma. The last NBI source, 30R, is used for diagnostics and not considered as a control actuator.

The system defined by (2.3) and (2.4) represents the minimal distributed-parameter model one can possibly derive for the time evolution of the magnetic and kinetic profiles of the plasma. The profile $\hat{\bar{\psi}}$ and electron temperature $\hat{T}_e$ can be considered as state variables.

### Overview of Galerkin Projection

The continuously distributed spatial variables such as $\bar{\psi}(\hat{\rho}, t)$ are discretized by Galerkin projection, a process by which an infinite dimensional parameter is projected onto a set of trial basis functions. The Galerkin projection of a generic dynamical variable, $y(\hat{\rho}, t)$, reads:

$$y(\hat{\rho}, t) \approx \sum_{i=1}^{N} G_{y,i}(t) b_i(\hat{\rho}), \tag{2.7}$$

where $N$ is the number of coefficients, $b_i(\hat{\rho})$ are the basis functions, and $G_{y,i}(t)$ are called the Galerkin coefficients. A variety of basis functions could be chosen, for example, cubic splines or piece-wise linear functions. Most important is that the spatial derivatives of the basis functions match the spatial derivatives of the continuous dimensional variable at the boundaries, and the order of the functions is sufficient to calculate any relevant spatial derivatives [51].

The expansion coefficients, $G_{y,i}(t)$, are lumped together in a vector array denoted by the bold symbol $\boldsymbol{y}(t)$, i.e. $\boldsymbol{y}(t) = [G_{y,1}, G_{y,2}, \ldots, G_{y,N}]^T$. To determine the Galerkin coefficients, we multiply both sides of the expansion equation (2.7) with any basis function $b_j(\hat{\rho})$, $j = 1, 2, ...N$ and integrate over the spatial coordinate to obtain,

$$\int_0^1 y(\hat{\rho}, t) b_j(\hat{\rho}) d\hat{\rho} = \int_0^1 \left[ \sum_{i=1}^{N} G_{y,i}(t) b_i(\hat{\rho}) \right] b_j(\hat{\rho}) d\hat{\rho}, \tag{2.8}$$

for $j = 1, 2, ...N$. If the basis functions are orthonormal, i.e. $\int_0^1 b_i(\hat{\rho}) b_j(\hat{\rho}) d\hat{\rho} = \delta_{ij}$, then the coefficients $G_{y,i}$ can be computed explicitly. Otherwise the coefficients are

obtained by solving the linear system

$$\begin{bmatrix} \hat{y}_1 \\ \hat{y}_2 \\ \vdots \\ \hat{y}_N \end{bmatrix} = \begin{bmatrix} m_{11} & m_{12} & \dots & m_{1n} \\ m_{21} & m_{22} & \dots & m_{2n} \\ \vdots & \vdots & \ddots & \vdots \\ m_{n1} & m_{n2} & \dots & m_{nn} \end{bmatrix} \begin{bmatrix} G_{y,1} \\ G_{y,2} \\ \vdots \\ G_{y,N} \end{bmatrix}. \tag{2.9}$$

where $m_{ij}$ is the inner product of $b_i$ and $b_j$, i.e., $\int_0^1 b_i(\hat{\rho})b_j(\hat{\rho})d\hat{\rho}$ and $\hat{y}_j$ is the inner product between $y(\hat{\rho},t)$ and $b_j(\hat{\rho})$, i.e., $\hat{y}_j = \int_0^1 y(\hat{\rho},t)b_j(\hat{\rho})d\hat{\rho}$. It is simply assumed that by increasing the number of basis functions, the discrete approximation converges towards the infinite dimensional variable.

### Model Discretization by Galerkin Projection

To identify the differential operators of the distributed parameter model given by (2.3) and (2.4), we can reduce the model to a finite-dimensional state space representation by Galerkin projection. The resulting system can then be identified by conventional system identification techniques [41].

Multiplying the equations (2.3) and (2.4) by the an appropriate basis function set, labeled $a_j(\hat{\rho})$ for $j = 1, 2, \dots, N$, and integrating over the domain yields an ordinary differential equation system of the form

$$\mathbf{M}_{\bar{\psi}}\dot{\bar{\boldsymbol{\psi}}}(t) = \mathbf{A}_{\bar{\psi}\bar{\psi}}\bar{\boldsymbol{\psi}}(t) + \mathbf{A}_{\bar{\psi}T_e}\boldsymbol{T}_e(t) + \mathbf{B}_{\bar{\psi}\boldsymbol{u}}\boldsymbol{u}(t), \tag{2.10}$$

$$\mathbf{M}_{T_e}\dot{\boldsymbol{T}}_e(t) = \mathbf{A}_{T\bar{\psi}}\bar{\boldsymbol{\psi}}(t) + \mathbf{A}_{T_eT_e}\boldsymbol{T}_e(t) + \mathbf{B}_{T_e\boldsymbol{u}}\boldsymbol{u}(t), \tag{2.11}$$

where $\bar{\boldsymbol{\psi}}$ and $\boldsymbol{T}_e$ represent the Galerkin approximations of $\hat{\bar{\psi}}$ and $\hat{T}_e$, respectively. The matrices $\mathbf{M}_\alpha$ and $\mathbf{A}_{\alpha,\beta}$ have elements of the form

$$(\mathbf{M}_\alpha)_{i,j} = \int_0^1 a_i(\hat{\rho})a_j(\hat{\rho})d\hat{\rho}, \quad (\mathbf{A}_{\alpha\beta})_{i,j} = \int_0^1 a_i(\hat{\rho})L_{\alpha,\beta}(\hat{\rho})a_j(\hat{\rho})d\hat{\rho}, \tag{2.12}$$

and $\mathbf{B}_{\alpha\boldsymbol{u}}$ is a matrix whose *ith* row is given by

$$(\mathbf{B}_{\alpha\boldsymbol{u}})_i = \int_0^1 a_i(x)\boldsymbol{L}_{\alpha,\boldsymbol{u}}(x)d\hat{\rho}. \tag{2.13}$$

Finally, inverting the matrices $\mathbf{M}_\alpha$ results in the coupled linear system given by

$$\dot{\bar{\boldsymbol{\psi}}}(t) = \mathbf{A}_{11}\bar{\boldsymbol{\psi}}(t) + \mathbf{A}_{12}\boldsymbol{T}_e(t) + \mathbf{B}_1\boldsymbol{u}(t), \tag{2.14a}$$

$$\dot{\boldsymbol{T}}_e(t) = \mathbf{A}_{21}\bar{\boldsymbol{\psi}}(t) + \mathbf{A}_{22}\boldsymbol{T}_e(t) + \mathbf{B}_2\boldsymbol{u}(t). \tag{2.14b}$$

Noting that the plasma temperature evolves much faster than the poloidal magnetic flux diffusion time, we can approximate (2.14b) with its steady-state counterpart, $0 = \mathbf{A}_{21}\bar{\boldsymbol{\psi}}(t) + \mathbf{A}_{22}\boldsymbol{T}_e(t) + \mathbf{B}_2\boldsymbol{u}(t)$. This is a fair approximation given we are primarily interested in control of the magnetic profile. In this case, we can obtain a state space model given by

$$\dot{\bar{\boldsymbol{\psi}}} = \mathbf{A}_s\bar{\boldsymbol{\psi}} + \mathbf{B}_s\boldsymbol{u}, \tag{2.15a}$$

$$\boldsymbol{T}_e = \mathbf{C}_s\bar{\boldsymbol{\psi}} + \mathbf{D}_s\boldsymbol{u}, \tag{2.15b}$$

where $\bar{\boldsymbol{\psi}}$ arises as the system state and $\boldsymbol{T}_e$ arises as a system output. The matrices $\mathbf{A}_s$, $\mathbf{B}_s$, $\mathbf{C}_s$, and $\mathbf{D}_s$ are linked to original model (2.14a)-(2.14b) matrices by

$$\begin{aligned}
\mathbf{A}_s &= \mathbf{A}_{11} - \mathbf{A}_{12}\mathbf{A}_{22}^{-1}\mathbf{A}_{21}, \\
\mathbf{B}_s &= \mathbf{B}_1 - \mathbf{A}_{12}\mathbf{A}_{22}^{-1}\mathbf{B}_2, \\
\mathbf{C}_s &= -\mathbf{A}_{22}^{-1}\mathbf{A}_{21}, \\
\mathbf{D}_s &= -\mathbf{A}_{22}^{-1}\mathbf{B}_2.
\end{aligned} \tag{2.16}$$

The plasma $\beta_N$ is proportional to the volume averaged plasma energy divided by the total plasma current, i.e. $\beta_N \propto E/I_\mathrm{p}$, where the volume averaged plasma energy is defined as

$$E = \int_V \frac{3}{2}n_eT_e + \frac{3}{2}n_iT_idV, \tag{2.17}$$

where $V$ is the plasma volume, and the total plasma current is a function of the externally applied loop voltage, noninductive current drive sources, and bootstrap current. Therefore, assuming a constant plasma density and equilibrium between the electron and ion species ($T_e = T_i$), and noting the form of the linear temperature model given by (2.15b), a linearized model for $\beta_N$ can be written as

$$\hat{\beta}_N = \mathbf{C}_{s,\beta_N}\bar{\boldsymbol{\psi}} + \mathbf{D}_{s,\beta_N}\boldsymbol{u}, \tag{2.18}$$

where $\hat{\beta}_N$ represents $\beta_N$ relative to its reference value associated with the equilibrium state ($\hat{\beta}_N = \beta_N - \beta_{N,\text{ref}}$), and the row matrices $\mathbf{C}_{s,\beta_N}$, $\mathbf{D}_{s,\beta_N}$ are unknown and to be determined by system identification.

## 2.2 System Identification Procedure

### 2.2.1 Collecting Experiment Data For System Identification

To collect data for system identification, a number of discharges of an advanced tokamak (AT) scenario (i.e., at high plasma pressure relative to the magnetic field pressure) were run with identical ramp-up phases during the experimental campaign of 2009. The reference plasma state (equilibrium state) was that of a plasma current $I_p = 0.9$ MA AT scenario which had been optimized to combine non-inductive current fractions near unity with $3.5 < \beta_N < 3.9$, bootstrap current fractions larger than 65%, and $H_{98}(y, 2) = 1.5$ [52]. During flattop, various actuators were modulated around their reference values. Actuator modulations were applied from $t = 2.6$ s, i.e., after 1 s of 0.9 MA current flat top. Figures 2.1(a)-2.1(b) display some typical modulations of the system inputs and the resulting outputs.

The actuators include the neutral beam injectors, the electron cyclotron current drive, and the plasma surface loop voltage. The NBI were grouped by: co-injection beam power, counter-injection beam power, and balanced-injection beam power, where the co-injection means in the direction of plasma current, counter-injection is the opposing direction, and balanced-injection refers to equal co- and counter-injection power. All actuators were modulated individually in open loop according to predefined waveforms while the other actuators were kept constant and equal to those values used to produce the reference discharge. Starting in 2012, two of the co-injection neutral beam injectors were re-positioned to direct their beams at 16.5° off-axis, providing more current drive towards the center of the profile. Data from the 2012 campaign is used to include the effects of off-axis NBI.

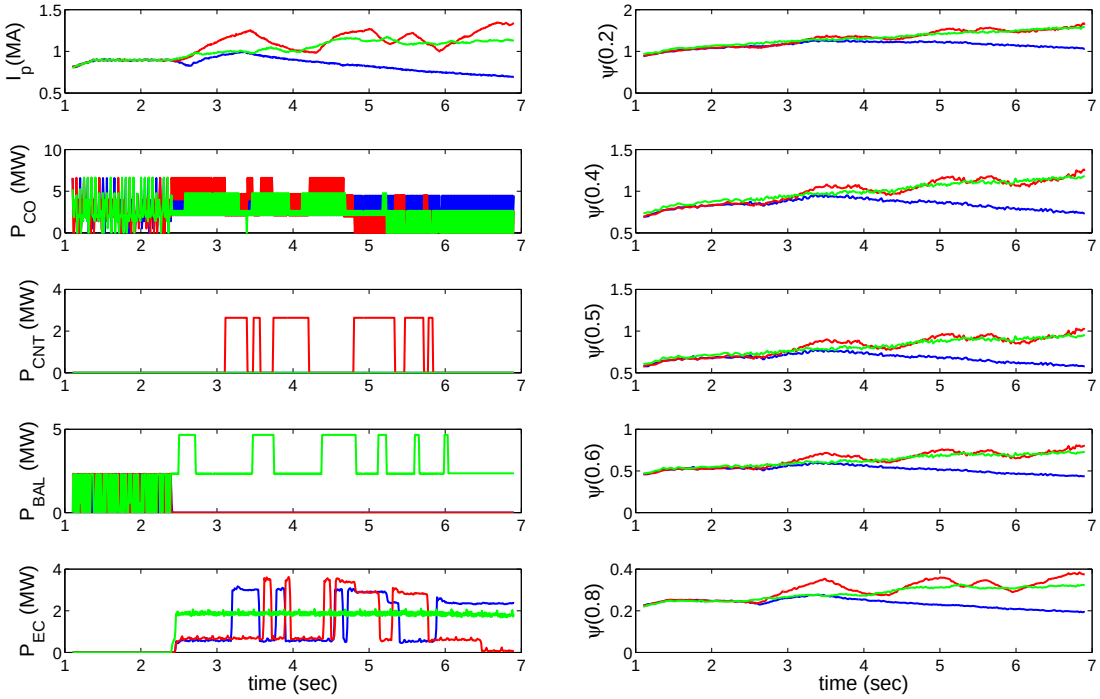


(a) (b)

**Figure 2.1:** Sample data for model identification. (a) Time evolution of $I_p$, $P_{CO}$, $P_{CNT}$, $P_{BAL}$, and $P_{EC}$ in DIII-D shots #140093 (blue), 140094 (red), and 140109 (green). (b) Time evolution of the magnetic profile, $\hat{\psi}$ for each shot.

### 2.2.2 Model Order Reduction

As described in Section 2.1, the model to be identified for the evolution of $\bar{\psi}$ and $\beta_N$ takes the form

$$\dot{\bar{\boldsymbol{\psi}}} = \mathbf{A}_s \bar{\boldsymbol{\psi}} + \mathbf{B}_s \boldsymbol{u}, \tag{2.19a}$$

$$\hat{\beta}_N = \mathbf{C}_{s,\beta_N} \bar{\boldsymbol{\psi}} + \mathbf{D}_{s,\beta_N} \boldsymbol{u}. \tag{2.19b}$$

First, the measured $\bar{\psi}$ profile data was projected onto 9 trial basis functions (cubic splines as shown in Figure 2.2) by Galerkin reduction, reducing the distributed data set to an approximate discrete data set of 9 points across the normalized plasma radius $\hat{\rho} = 0.1, 0.2, ..., 0.9$. However, if we attempt to identify a model of full order, i.e. an $\mathbf{A}_s$ matrix of dimension $9 \times 9$, the number of parameters becomes rather

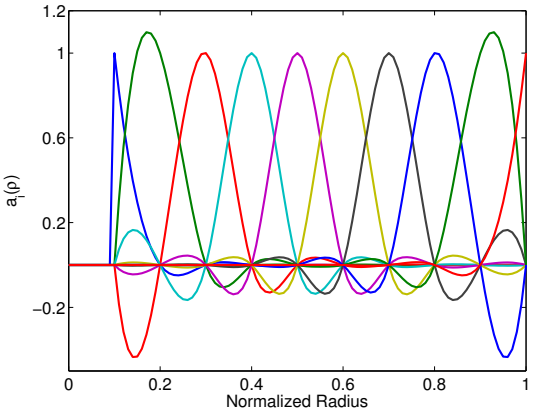


**Figure 2.2:** Cubic splines $a_i(\hat{\rho})$, used for the Galerkin reduction of $\hat{\psi}(\hat{\rho}, t)$.

large. When using noisy experimental data, the possible solutions become multiple and unstable to small changes in the data, and the identification algorithm cannot determine a consistent model. In order to find a model that applies to all 9 discrete points, the data set has to be projected onto an appropriate subspace of reduced order. Then we identify only the dynamics within this subspace and neglect the remaining dynamics.

From (2.19a), the steady state gain of $\bar{\boldsymbol{\psi}}$ is given by the static gain matrix

$$\mathbf{K}_{sg} = -\mathbf{A}_s^{-1}\mathbf{B}_s, \tag{2.20}$$

which represents the approximate steady state response of the $\bar{\psi}$ profile in response to a step input for each of the actuators. The static gain matrix can be used to determine an appropriate subspace for system identification, since it contains the most essential aspects of the model for control purposes, namely the steady state response. Singular value decomposition of the static gain matrix is used to determine its principal components, the most significant of which are used to form the subspace basis

$$\mathbf{K}_{sg} = \mathbf{W} \cdot \mathbf{\Sigma} \cdot \mathbf{V}^T, \tag{2.21}$$

$$= [W_1\ W_2\ \ldots\ W_{n_{\hat{\boldsymbol{\psi}}}}] \cdot \mathbf{\Sigma} \cdot [V_1\ V_2\ \ldots\ V_{n_{\boldsymbol{u}}}]^T. \tag{2.22}$$

The output vectors corresponding to the largest singular values are used as the subspace basis. For example, if we choose to identify a model with order 3, the

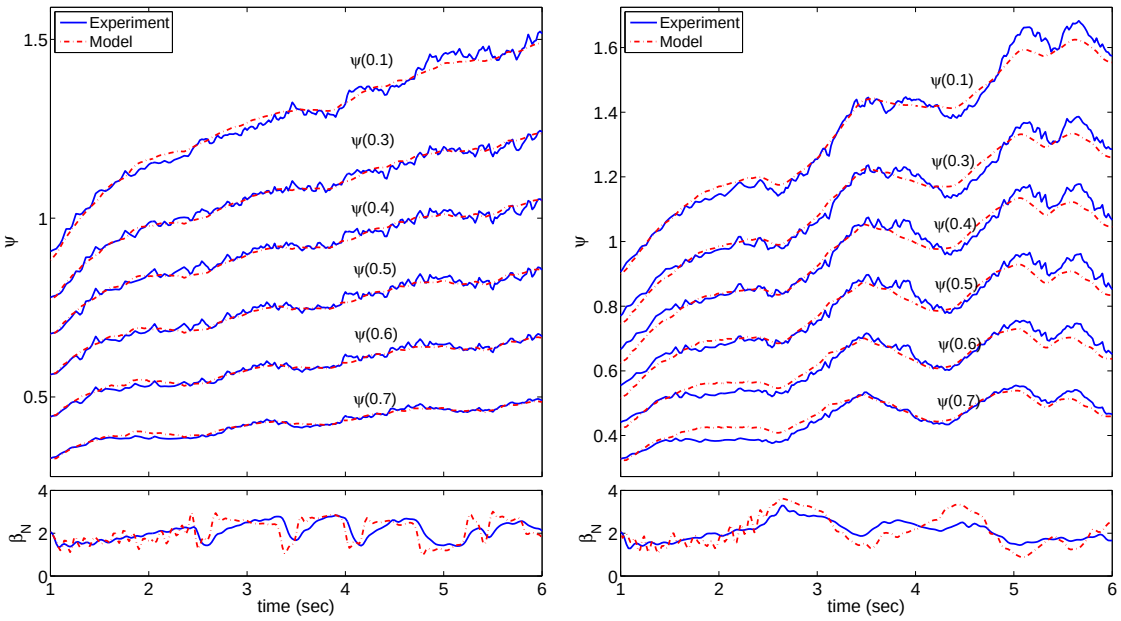


(a) Shot 140076 (training shot)

(b) Shot 140094 (test shot)

**Figure 2.3:** Comparison between measured (blue line) and estimated (red dash) of the $\hat{\psi}$ profile (Wb) and $\beta_N$ for training shot 140076 (data used in model identification) and test shot 140094 (data not used in model identification).

first three singular vectors, $W_1$, $W_2$, and $W_3$, would form the subspace basis. Thus, the data used for identification would capture the dominant characteristics of the system in steady state. A reduced order model of the form

$$\dot{\boldsymbol{X}}(t) = \mathbf{A}_s^r \boldsymbol{X}(t) + \mathbf{B}_s^r \boldsymbol{u}(t) \tag{2.23}$$

is then sought by system identification, where $\boldsymbol{X}(t)$ represents the reduced order state, determined by

$$\boldsymbol{X}(t) = \begin{bmatrix} W_1 & W_2 & W_3 \end{bmatrix}^T \psi(t) \triangleq \mathbf{W}_s^T \hat{\boldsymbol{\psi}}(t). \tag{2.24}$$

Once $\mathbf{A}_s^r$ and $\mathbf{B}_s^r$ have been identified, the system output equation which maps the state, $\boldsymbol{X}$, to the variable $\hat{\boldsymbol{\psi}}$ is assumed to be $\hat{\boldsymbol{\psi}}(t) = \mathbf{W}_s \boldsymbol{X}$.

The model is then identified using a step-wise approach, meaning parts of the model are identified in one step, then held constant to identify other parts of the

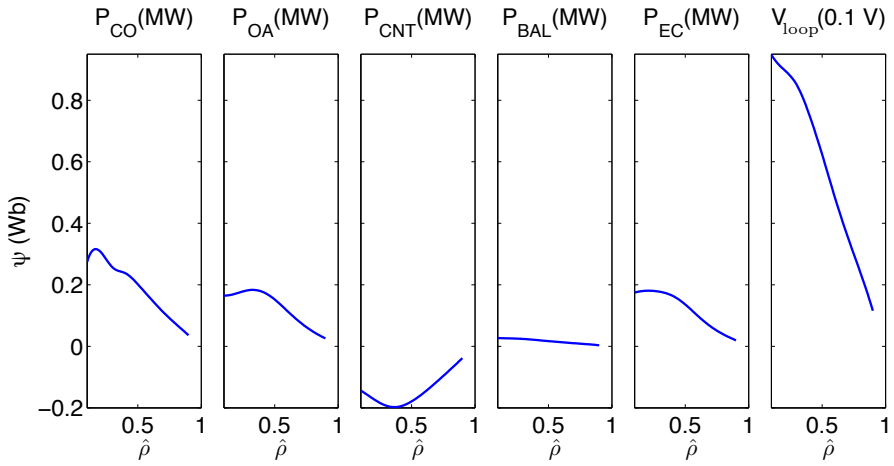


**Figure 2.4:** Model static gain matrix. The powers are the co-current NBI $P_{CO}$ (MW), off-axis co-current NBI $P_{OA}$ (MW), counter-current NBI $P_{CNT}$ (MW), balanced NBI $P_{BAL}$ (MW), electron cyclotron $P_{EC}$ (MW), and surface loop voltage $V_{surf}$ (0.1 V).

model, iterating back and forth until a suitable model is determined. The identification experiments, alternatively referred to as shots, used to generate the model were organized into various groups; one group for shots with little modulation, and one group for each set of shots with modulation in just one of the actuators. We start with the low modulation group to identify the free dynamics of the system, i.e. the matrix $\mathbf{A}_s^r$. Once the $\mathbf{A}_s^r$ matrix is determined, we identify the $\mathbf{B}_s^r$ matrix one column at a time using shots with only one modulated input corresponding to that $\mathbf{B}_s^r$ column. Then the static gain matrix is updated and the subspace basis is updated for subsequent iterations.

The identification process is carried out using the prediction error method [41] which calculates the matrices $\mathbf{A}_s^r$ and $\mathbf{B}_s^r$ by minimizing the norm $V_N(\mathbf{A}_s^r, \mathbf{B}_s^r)$, which for a least squares fit is defined as

$$V_N(\mathbf{A}_s^r, \mathbf{B}_s^r) = \frac{1}{N} \sum_{k=1}^{N} \epsilon^2(k) \tag{2.25}$$

where $\epsilon(k)$, called the prediction error, is the difference between the measured output and the predicted output at discrete time $k$ (see Appendix A.5). We begin the

identification considering only the data without off-axis NBI. To begin the identification of $\mathbf{A}_s^r$, a model and subspace of order 1 was chosen to identify the smallest eigenvalue, i.e. the longest characteristic time of the system. This eigenvalue was then held constant and the model order was increased to 2 to identify the next eigenvalue, this process was repeated up to order 4 using the shot group with low input modulation. Then we began with identification of the $\mathbf{B}_s^r$ matrix using the appropriate shot group for each column, while holding the eigenvalues of $\mathbf{A}_s^r$ constant. The identified model was found to have characteristic times of 5.88, 2.38, 1.05, and 0.19 seconds. This means that model orders above 4 have very fast transients with time constants less than 0.19 s, therefore they will not contribute much to the control design and a model of order 4 should be sufficient.

The off-axis NBI deliver a different current drive distribution from that of the on-axis co-injection beams used to identify the model, therefore they must be considered as a new actuator group. To account for this effect an additional column was added to the $\mathbf{B}_s^r$ matrix using various experiments from the early 2012 campaign with similar plasma scenarios to that of the open-loop system identification experiments carried out in 2009. Figure 2.3 displays an example of the typical fit between the experimental data and the identified model for one of the training shots 140076, i.e. a shot data used to inform the model identification algorithm, and test shot 140094, which was not used in the model identification. The fit between the original data $Y(t)$ and the reconstructed data $Y_m(t)$ is characterized by the parameter $f$,

$$f = 1 - \left[ \frac{\sum_{k=1}^{N} \left[ Y(t) - Y_m(t) \right]^2}{\sum_{k=1}^{N} \left[ Y(t) - \langle Y \rangle \right]} \right], \tag{2.26}$$

where $f = 1$ (100%) is a perfect fit and $f = 0$ corresponds to a reconstructed data set equal to the mean of the measured data, $\langle Y \rangle$. Fit parameters were between 60-80% for almost all shots and the worst matches were around 50%. While the model was identified using only data from the current flattop phase, i.e. after 2.5 s, it is noted that good fitting is achieved during much of the current ramp-up phase as well, i.e. $t = 1 - 2.5$ s.

For control purposes it is preferable to have a model that spans the whole profile

without an output equation, i.e. one in which the states represent the 9 discrete points of $\psi$ and the outputs are identically the states. The full order model can be achieved by using the subspace basis to expand $\mathbf{A}_s^r$ and $\mathbf{B}_s^r$ while imposing arbitrarily, large stable eigenvalues to the new eigenstates whose dynamics have not been identified. We refer to the new state equation matrices as $\mathbf{A}$ and $\mathbf{B}$:

$$\mathbf{A} = \mathbf{W}_s \mathbf{A}_s^r \mathbf{W}_s^T, \ \mathbf{B} = \mathbf{W}_s \mathbf{B}_s^r. \tag{2.27}$$

At this point we have obtained a state equation for the $\hat{\psi}$ profile of order 9 with 6 inputs, but have yet to consider $\beta_N$. The matrices $\mathbf{C}_{s,\beta_N}$ and $\mathbf{D}_{s,\beta_N}$ of (2.19b) are estimated in a similar manner as $\mathbf{A}_s^r$ and $\mathbf{B}_s^r$, first using the shots little input modulation to identify $\mathbf{C}_{s,\beta_N}$ and then identifying $\mathbf{D}_{s,\beta_N}$ column by column using shots with the corresponding input modulated. Figures 2.3(a) and 2.3(b) show a model fit comparison for $\beta_N$.

The final static gain matrix of the identified model can be represented as in Figure 2.4. In the figure, the steady-state response of the poloidal flux to unitary changes in the various inputs is plotted. The surface loop voltage has the greatest effect in manipulating the profile, the co-injection and counter-injection beams are the second most powerful, affecting the profile in different directions. The contradictory affects of co-injection and counter-injection beams agree with prior experiments considering neutral beam injection at different trajectories [53]. Both the balanced-injection beams and the gyrotrons lead to a small increase in the magnetic profile. The off-axis co-injection beam has a similar effect to the on-axis co-injection beam with the exception of reduced gain on the interior of the profile.

## 2.3 Conclusions

A simplified linear model for the evolution of the poloidal magnetic flux profile as well as $\beta_N$ in the DIII-D tokamak was obtained based on a semi-interactive system identification method. Reasonable model prediction of the magnetic profile evolution in response to modulations in the on-axis and off-axis neutral beam injector power, the total gyrotron power, and the surface loop voltage was achieved. The linear

model obtained in this chapter can be used to design controllers for the simultaneous regulation of current profile and $\beta_N$ evolution, which has been shown in closed-loop TRANSP simulations [54] and a single experimental test at DIII-D [55]. The model identification approach is straightforward and could be applied to other tokamaks or extended to other tokamak parameters important for plasma stability, such as the rotation profile evolution. While the modeling approach presented is limited in applicability to a certain plasma reference associated with the chosen plasma equilibrium state, in theory, the approach could be extended in applicability by identifying additional models around different operating points. This would enable current profile control in different scenarios (around different reference states) or control of the current profile during the ramp-up and ramp-down phases.

# Chapter 3

# First-Principles Based Modeling of the Current Profile and Rotation Profile Evolution

## 3.1 Introduction

In this chapter we describe control-oriented models based on first-principles laws to describe the evolution of the poloidal magnetic flux and the toroidal angular rotation. Naturally, the models must neglect some components of the underlying physics to be suitable for real-time control applications. First, we assume axisymmetric plasmas, i.e. no change along the toroidal angle, furthermore all quantities are averaged over flux surfaces to limit the complexity to only one spatial coordinate. Such models are often referred to as 1D within the physics community since the spatial dependence is limited to only the radial coordinate of the plasma. Still, with only these simplifications, the models remain overly complex for control design. They amount to partial differential equations (PDE) which are coupled nonlinearly to various plasma quantities. To further simplify the models, empirical scalings are used to approximate some of the plasma parameters.

As one might expect, since the tokamak's poloidal field is primarily generated

by the plasma current, the current profile can be expressed in terms of the poloidal magnetic flux profile. To model the poloidal magnetic flux evolution, we begin with the simplified 1D model referred to as the magnetic flux diffusion equation (MDE) [47, 48]. The MDE is a complicated partial differential equation which is coupled to the temperature of the plasma, as the resistivity depends intimately on the plasma temperature and in turn plays a significant role in the diffusion rate of plasma current. To simplify the model to a control-oriented form, the MDE can be combined with physics-based correlations for the electron temperature, plasma resistivity, and the efficiency of each of the current drive sources including neutral beam injection (NBI), electron cyclotron current drive (ECCD), and bootstrap current drive. In this chapter we describe each of the terms of the model and the model's overall qualitative behavior. The interested reader should examine [56–58] for the details associated with tailoring each of the parameters to specific operating scenarios in DIII-D tokamak.

In a similar fashion, modeling of the toroidal angular rotation evolution begins with the complete momentum balance equation assuming an axisymmetric plasma and taking flux surface averages of each of the spatially varying quantities involved [59, 60]. All but the most dominant contributions to the momentum balance equation are neglected and empirical scalings laws are used to approximate the plasma temperature, density, and momentum drive from various auxiliary sources.

It is important to note that the models considered in this work are only aimed at being sufficiently accurate for feedback control design purposes. Consequently, the models need only capture the dominant effects of the system dynamics because one of the main characteristics of feedback is the ability to deal with model uncertainties. At the same time the models must be sufficiently simple to be applicable for real-time model-based control solutions. It is, however, not entirely possible to assess whether the models contain sufficient accuracy for a successful control implementation until experimental tests of the controller are performed.

This chapter is organized as follows. The first-principles based control-oriented models for the current profile evolution and rotation profile evolution are described in Section 3.2 and Section 3.3, respectively; finally, in Section 3.4, a statement of

conclusions is made.

## 3.2 Modeling the Current Profile Dynamics

Let $\rho$ represent the radial coordinate of the plasma cross section. Since all the model parameters will be taken as flux surface averaged quantities, any flux surface constant quantity could be used to define $\rho$. We use the mean effective minor radius of the magnetic surface as $\rho$, i.e. $\pi B_{\phi,0}\rho^2 = \Phi$, where $\Phi$ is the toroidal magnetic flux and $B_{\phi,0}$ is the reference magnetic field at the magnetic axis of the tokamak. Normalizing $\rho$ by the mean effective minor radius of the last closed magnetic surface, $\rho_b$, we obtain a normalized spatial coordinate $\hat{\rho} = \rho/\rho_b \in [0, 1]$.

The toroidal current density profile $j(\hat{\rho}, t)$ is essentially prescribed by the poloidal magnetic flux profile, $\Psi(\hat{\rho}, t)$. To describe the evolution of poloidal magnetic flux, we start with the well known magnetic diffusion equation (MDE) [47, 48], which can be written as

$$\frac{\partial \psi}{\partial t} = \frac{\eta(T_\mathrm{e})}{\mu_0 \rho_\mathrm{b}^2 \hat{F}^2} \frac{1}{\hat{\rho}} \frac{\partial}{\partial \hat{\rho}} \left( \hat{\rho} \hat{F} \hat{G} \hat{H} \frac{\partial \psi}{\partial \hat{\rho}} \right) + R_0 \hat{H} \eta(T_\mathrm{e}) \frac{\langle \bar{j}_\mathrm{NI} \cdot \bar{B} \rangle}{B_{\phi,0}}. \tag{3.1}$$

Each of the terms involved in the MDE are briefly summarized for reference in Table 3.1, where $\psi$ is the poloidal stream function (related to poloidal magnetic flux by $\Psi = \frac{1}{2\pi}\psi$), $\eta$ is the plasma resistivity which depends on the electron temperature, $T_\mathrm{e}$, $\mu_0$ is the vacuum permeability, $\bar{j}_\mathrm{NI}$ represents the total non-inductively driven current density, $\bar{B}$ is the toroidal magnetic field, and $\langle \cdot \rangle$ denotes flux-surface average. The parameters $\hat{F}(\hat{\rho})$, $\hat{G}(\hat{\rho})$, and $\hat{H}(\hat{\rho})$ are associated with the magnetic geometry of plasma [57], and are given by

$$\hat{F}(\hat{\rho}) = \frac{R_0 B_{\phi,0}}{R B_\phi(R, Z)}, \quad \hat{G}(\hat{\rho}) = \langle R_0^2 |\Delta \rho|^2 / R^2 \rangle, \quad \hat{H}(\hat{\rho}) = \frac{\hat{F}}{\langle R_0^2 / R^2 \rangle}. \tag{3.2}$$

From (3.2), we can note the model assumes the magnetic geometry is fixed in time. For completion, the MDE is combined with the boundary conditions given by symmetry at the plasma center and a forcing function at the plasma edge,

$$\left. \frac{\partial \psi}{\partial \hat{\rho}} \right|_{\hat{\rho}=0} = 0, \qquad \left. \frac{\partial \psi}{\partial \hat{\rho}} \right|_{\hat{\rho}=1} = -\frac{\mu_0}{2\pi} \frac{R_0}{\hat{G}|_{\hat{\rho}=1} \hat{H}|_{\hat{\rho}=1}} I_\mathrm{p}(t), \tag{3.3}$$

where $I_{\rm p}(t)$ is the total plasma current.

A simplified model for the electron temperature can be obtained by first considering the plasma internal energy, i.e. the volume averaged energy density over the plasma volume, which is given by

$$E = \int_V \left( \frac{3}{2} n_{\rm e}(\hat{\rho},t) T_{\rm e}(\hat{\rho},t) + \frac{3}{2} n_{\rm i}(\hat{\rho},t) T_{\rm i}(\hat{\rho},t) \right) dV, \tag{3.4}$$

where $n_{\rm e}(\hat{\rho},t)$ and $T_{\rm e}(\hat{\rho},t)$ are the electron density and temperature profiles, and $n_{\rm i}(\hat{\rho},t)$ and $T_{\rm i}(\hat{\rho},t)$ are the ion density and temperature profiles. Under the assumption of fixed magnetic geometry, the plasma stored energy evolution can be well approximated by the 0D (zero-dimensional) energy balance equation,

$$\frac{dE}{dt} = -\frac{E}{\tau_E} + P_{\rm tot}, \tag{3.5}$$

where $\tau_E$ is a the global energy confinement time, and the total absorbed power, $P_{\rm tot}$ is equal to the auxiliary power injected into the plasma by NBI and ECRH, $P_{\rm aux} = \sum_{\xi=1}^{n_{\rm NBI}} P_{{\rm NBI},\xi} + P_{\rm EC}$, plus the power from the ohmic coil, $P_{\rm ohm}$, minus the radiative power, $P_{\rm rad}$,

$$P_{\rm tot} = P_{\rm aux} + P_{\rm ohm} - P_{\rm rad}. \tag{3.6}$$

Based on experimental data from numerous machines, scaling approximations for the energy confinement time have been developed for specific tokamak operating scenarios [61, 62]. In general the confinement time scales with total plasma current, total absorbed power, line averaged electron density, and other parameters which are always assumed fixed in this work. For example, in a typical DIII-D H-mode plasma, the confinement time can be approximated by the IPB98(y,2) scaling law [61],

$$\tau_E = 0.0562 H_{H98(y,2)} B_{\phi,0}^{0.15} R^{1.39} \kappa^{0.78} a^{0.58} M^{0.19} I_{\rm p}^{0.93} \bar{n}_{\rm e}^{0.41} P_{\rm tot}^{-0.69}, \tag{3.7}$$

where $H_{H98(y,2)}$ is the energy confinement enhancement factor, $a$ is the plasma minor radius, $M$ is the average ion mass, and $\kappa$ is the plasma elongation. In this work, $I_{\rm p}$, $P_{\rm tot}$, and $\bar{n}_e$ are treated as control parameters, and the remaining terms involved in (3.7) associated with the plasma geometry and magnetic equilibrium are assumed to be fixed.

Because the thermal diffusion time is much faster than the current diffusion time, the temperature is always in quasi-equilibrium on the time-scale of current diffusion. Therefore, the temporal dynamics of the electron temperature can be neglected in the development of a model relevant to current profile control. At steady state, the energy dynamics (3.5) and the expression (3.4) provide a relation for volume averaged temperature,

$$\langle T_{\rm e}\rangle = \frac{P_{\rm tot}\tau_E}{3\langle n_{\rm e}\rangle V} \tag{3.8}$$

where we have assumed, as an approximation, equilibrium in the electron and ion species, i.e. $n_{\rm e} = n_{\rm i}$ and $T_{\rm e} = T_{\rm i}$. Noting from (3.7) that a typical confinement time scaling law takes the form $\tau_E \propto I_{\rm p}^{\gamma_s}\bar{n}_{\rm e}^{\epsilon_s}P_{\rm tot}^{\zeta_s}$, the volume average temperature at steady state can be written as

$$\langle T_{\rm e}\rangle \propto I_{\rm p}^{\gamma_s}\langle\bar{n}_{\rm e}\rangle^{\epsilon_s-1}P_{\rm tot}^{1+\zeta_s}. \tag{3.9}$$

The form of this expression suggests a potential static map electron temperature model

$$T_{\rm e}(\hat{\rho},t) = k_{T_{\rm e}}(\hat{\rho})T_{\rm e}^{\rm prof}(\hat{\rho})\frac{I_{\rm p}(t)\sqrt{P_{\rm tot}(t)}}{\bar{n}_{\rm e}(t)}, \tag{3.10}$$

where the scalings on plasma current, line averaged density, and total absorbed power ($\gamma_s = 1$, $\epsilon_s = -0.5$ and $\zeta_s = 0$) are chosen according to the Goldston scaling law [62]. The reference profile, $T_{\rm e}^{\rm prof}(\hat{\rho})$ describes the experimentally measured shape of the temperature and the profile $k_{T_{\rm e}}(\hat{\rho})$ is introduced to normalize the model.

By a simplified Spitzer model, the plasma resistivity $\eta(T_{\rm e})$ scales with the electron temperature according to

$$\eta(\hat{\rho},t) = \frac{k_{\rm sp}Z_{\rm eff}}{T_{\rm e}^{3/2}(\hat{\rho},t)}, \tag{3.11}$$

where $k_{\rm sp}$ is a constant normalizing profile and $Z_{\rm eff}$ is the approximate effective charge of the ions, assumed to be constant. The electron density is modeled by

$$n_{\rm e}(\hat{\rho},t) = n_{\rm e}^{\rm prof}(\hat{\rho})\bar{n}_{\rm e}(t), \tag{3.12}$$

where $n_{\rm e}^{\rm prof}(\hat{\rho})$ is a reference electron density profile, and $\bar{n}_{\rm e}$ is the line-averaged electron density. This model implies that the control action only weakly affects the

| Parameter | Units | Description |
|---|---|---|
| $\rho = \sqrt{\Phi/\pi B_{\phi,0}}$ | m | Radius term: Square root of normalized toroidal flux |
| $\hat{\rho}$ | – | Normalized radius $\hat{\rho} = \rho/\rho_b$ |
| $R_0$ | m | Major radius of magnetic axis |
| $\Phi$ | Wb | Toroidal flux |
| $\Psi$ | Wb | Poloidal flux |
| $\psi$ | Wb/rad | Stream function ($\psi = \Psi/2\pi$) |
| $\eta(\hat{\rho}, t)$ | $\Omega$ m | Plasma resistivity |
| $\bar{j}_{\mathrm{NI}}(\hat{\rho}, t)$ | A m$^{-2}$ | Non-inductive current drive |
| $B_{\phi,0}$ | T | Cacuum toroidal field at $R_0$ |
| $n_{\mathrm{e}}(\hat{\rho}, t)$, $n_{\mathrm{i}}(\hat{\rho}, t)$ | #/m$^3$ | Electron and ion density |
| $T_{\mathrm{e}}(\hat{\rho}, t)$, $T_{\mathrm{i}}(\hat{\rho}, t)$ | keV | Electron and ion temperature |
| $\hat{F}(\hat{\rho})$, $\hat{G}(\hat{\rho})$, $\hat{H}(\hat{\rho})$ | – | Geometric factors |
| $Z_{\mathrm{eff}}$ | – | Effective average charge of ions in the plasma |

**Table 3.1:** Parameters associated with the magnetic diffusion equation (MDE).

radial distribution of the electron density, which is a valid assumption assuming the plasma remains in a single confinement mode.

Contributions to the non-inductive current drive include the bootstrap current and that produced by auxiliary sources such as ECCD and NBI,

$$\frac{\langle \bar{j}_{\mathrm{NI}} \cdot \bar{B} \rangle}{B_{\phi,0}} = \frac{\langle \bar{j}_{\mathrm{EC}} \cdot \bar{B} \rangle}{B_{\phi,0}} + \sum_{\xi=1}^{n_{\mathrm{NBI}}} \frac{\langle \bar{j}_{\mathrm{NBI},\xi} \cdot \bar{B} \rangle}{B_{\phi,0}} + \frac{\langle \bar{j}_{\mathrm{BS}} \cdot \bar{B} \rangle}{B_{\phi,0}} \tag{3.13}$$

where $\bar{j}_{\mathrm{EC}}$ is the total non-inductive current generated by the gyrotrons, $\bar{j}_{\mathrm{NBI},\xi}$ is the non-inductive current generated by the $\xi^{\mathrm{th}}$ NBI system ($\xi = 1, 2, \ldots, n_{\mathrm{NBI}}$), and $\bar{j}_{\mathrm{BS}}$ is that produced by the bootstrap effect. While there are multiple ECCD sources (gyrotrons) at DIII-D, we choose to model the ECCD contribution as a single block since all the control formulations considered in later chapters will assume the gyrotrons function as a group. For the gyrotrons and NBI systems, the non-inductive current drive contribution is modeled as a function of the electron temperature, electron density, and system power

$$\frac{\langle \bar{j}_{\mathrm{EC}} \cdot \bar{B} \rangle}{B_{\phi,0}} = j_{\mathrm{EC}}^{\mathrm{prof}} \frac{T_{\mathrm{e}}}{\bar{n}_{\mathrm{e}}} P_{\mathrm{EC}}, \tag{3.14}$$

$$\frac{\langle \bar{j}_{\mathrm{NBI},\xi} \cdot \bar{B} \rangle}{B_{\phi,0}} = j^{\mathrm{prof}}_{\mathrm{NBI},\xi} \frac{\sqrt{T_{\mathrm{e}}}}{\bar{n}_{\mathrm{e}}} P_{\mathrm{NBI},\xi}, \tag{3.15}$$

where $j^{\mathrm{prof}}_{\mathrm{EC}}(\hat{\rho})$ and $j^{\mathrm{prof}}_{\mathrm{NBI},\xi}(\hat{\rho},t)$ are reference profiles describing the current drive deposition shapes of the ECCD and individual NBI systems. The bootstrap current contribution is modeled using the well known Sauter Law [63, 64]. Assuming equilibrium in the electron and ion species, i.e. $n_{\mathrm{e}} = n_{\mathrm{i}}$ and $T_{\mathrm{e}} = T_{\mathrm{i}}$, we have

$$\frac{< \bar{j}_{bs} \cdot \bar{B} >}{B_{\phi,0}} = \frac{R_0}{\hat{F}(\hat{\rho})} \frac{1}{\partial\psi/\partial\hat{\rho}} \left[ 2\mathcal{L}_{31} T_e \frac{\partial n_e}{\partial\hat{\rho}} + (2\mathcal{L}_{31} + \mathcal{L}_{32} + \alpha\mathcal{L}_{34})\, n_e \frac{\partial T_e}{\partial\hat{\rho}} \right], \tag{3.16}$$

where the coefficients $\mathcal{L}_{31}$, $\mathcal{L}_{32}$, $\mathcal{L}_{34}$, and $\alpha$ depend on the equilibrium and collisionality (degree to which plasma behavior is dominated by collisions) of the plasma. The bootstrap current is primarily driven by the radial pressure gradient, which is evident from the contribution of the terms $T_{\mathrm{e}} \frac{\partial n_{\mathrm{e}}}{\partial\hat{\rho}}$ and $n_{\mathrm{e}} \frac{\partial T_{\mathrm{e}}}{\partial\hat{\rho}}$ in (3.16). Because the plasma density and temperature profiles of L-mode scenarios do not exhibit a steep gradients at the plasma edge (see Section 1.4), the bootstrap current fraction will be relatively small as compared to H-mode scenarios.

### 3.2.1 Output Quantities Important for Control

From knowledge of the flux profile, $\psi(\hat{\rho},t)$, and the plasma stored energy various quantities related to the magnetic configuration of the plasma can be calculated. Most important of which are the safety factor profile $q$ and the normalized plasma $\beta$ ($\beta_N$) as these quantities are directly associated with the desired plasma operating scenario and are often used as a heuristic for avoiding unstable plasmas. The safety factor, a quantity related to the toroidal current density, is given by $q(\rho,t) = -d\Phi/d\Psi$. This expression can be written as

$$q(\hat{\rho},t) = \frac{d\Phi}{d\Psi} = -\frac{d\Phi}{2\pi d\psi} = -\frac{B_{\phi,0}\rho_{\mathrm{b}}^2\hat{\rho}}{\partial\psi/\partial\hat{\rho}}, \tag{3.17}$$

where in the last expression we have used the assumption of a large aspect ratio ($R_0/a > 3.5$) typical of conventional tokamaks such as DIII-D. The normalized plasma beta, $\beta_N$, is related to the volume-averaged plasma stored energy, $E$, and is

defined as

$$\beta_N = \beta_t[\%]\frac{aB_{\phi,0}}{I_{\rm p}[MA]}, \quad \beta_t = \frac{p}{B_{\phi,0}^2/2\mu_0} = \frac{(2/3)(E/V_{\rm p})}{B_{\phi,0}^2/2\mu_0}, \tag{3.18}$$

where $\beta_t$ is the toroidal plasma beta, $a$ is the plasma minor radius, $I_{\rm p}$ is the total plasma current, $p$ is the volume-averaged plasma kinetic pressure, $\mu_0$ is the vacuum magnetic permeability, and $V_{\rm p}$ is the total plasma volume.

Below we list other output quantities of interest, some of which have already been mentioned in previous sections, but are listed here again for convenience.

- Toroidal current density (A/m$^2$) [65]:

$$j_{\rm tor}(\hat{\rho},t) = -\frac{1}{\mu_0\rho_b^2 R_0\hat{H}}\frac{\partial}{\partial\hat{\rho}}\left(\hat{\rho}\hat{G}\hat{H}\frac{\partial\psi}{\partial\hat{\rho}}\right) \tag{3.19}$$

- Rotational transform, i.e. inverse safety factor:

$$\iota(\hat{\rho},t) = \frac{1}{q} = -\frac{1}{B_{\phi,0}\rho_{\rm b}^2\hat{\rho}}\frac{\partial\psi}{\partial\hat{\rho}} \tag{3.20}$$

- Magnetic shear:

$$s(\hat{\rho},t) = \frac{\hat{\rho}}{q}\frac{dq}{d\hat{\rho}} \tag{3.21}$$

- Toroidal plasma loop voltage (V):

$$U_{\rm p}(\hat{\rho},t) = \frac{\partial\psi}{\partial t} \tag{3.22}$$

- Spatial derivative of plasma loop voltage (V/m):

$$g_{\rm ss}(\hat{\rho},t) = \frac{\partial U_{\rm p}}{\partial\hat{\rho}} \tag{3.23}$$

- Ohmic power density (W/m$^3$) and total ohmic power (W):

$$Q_{\rm ohm}(\hat{\rho},t) = j_{\rm tor}(\hat{\rho},t)^2\eta(\hat{\rho},t), \qquad P_{\rm ohm} = \int_V Q_{\rm ohm}dV \tag{3.24}$$

- Power loss density ($\mathrm{W/m^3}$) due to Bremsstrahlung radiation [1] and total radiative power (W) where $k_{\mathrm{brem}} = 5.5{\times}10^{-37}\ \mathrm{Wm^3}/\sqrt{keV}$ is the Bremsstrahlung radiation coefficient:

$$Q_{\mathrm{rad}} = k_{\mathrm{brem}} Z_{\mathrm{eff}} n_e(\hat{\rho},t)^2 \sqrt{T_e(\hat{\rho},t)}, \qquad P_{\mathrm{rad}} = \int_V Q_{\mathrm{rad}} dV \tag{3.25}$$

A number of related quantities may be computed such as the bootstrap current fraction $I_{\mathrm{bs}}/I_{\mathrm{p}}$ and driven current fraction from auxiliary sources $I_{\mathrm{aux}}/I_{\mathrm{p}}$. From the plasma loop voltage profile we can define the conditions for a stationary plasma. A stationary plasma is typically described by a flat loop voltage profile. We use the term "stationary state" to avoid confusion with the conventional terminology "steady state", which refers to a loop voltage profile identically equal to zero. In a stationary state the loop voltage profile is flat but not necessarily zero. Stationarity essentially means the plasma is no longer evolving but some of the current is provided by inductive means. The fusion science community typically reserves the term steady-state to describe a stationary plasma in which all the current is driven by non-inductive sources. In principle, a purely non-inductive discharge could continue indefinitely, hence the description steady-state.

### 3.2.2 Qualitative Effects of Various Actuators

The first and most effectual actuator is the total plasma current, which is regulated by the main ohmic coil (central solenoid) through a transformer effect. By controlling the total current inside the plasma, the internal current profile can be modified through resistive diffusion. Also, since the plasma is slightly resistive, some of the plasma current is dissipated into heat. The plasma resistivity scales inversely with the plasma electron temperature, therefore, as the temperature increases the resistive diffusion decreases, which tends to freeze the current profile evolution. The NBI system at DIII-D consists of four beam-lines, each of which has two ion sources in parallel (see Figure 1.10(b)). Each ion source can inject a maximum power around 2.2 MW into the plasma. Currently, of the eight ion sources, four are configured to inject in the co-current direction (same direction as plasma current) aligned with

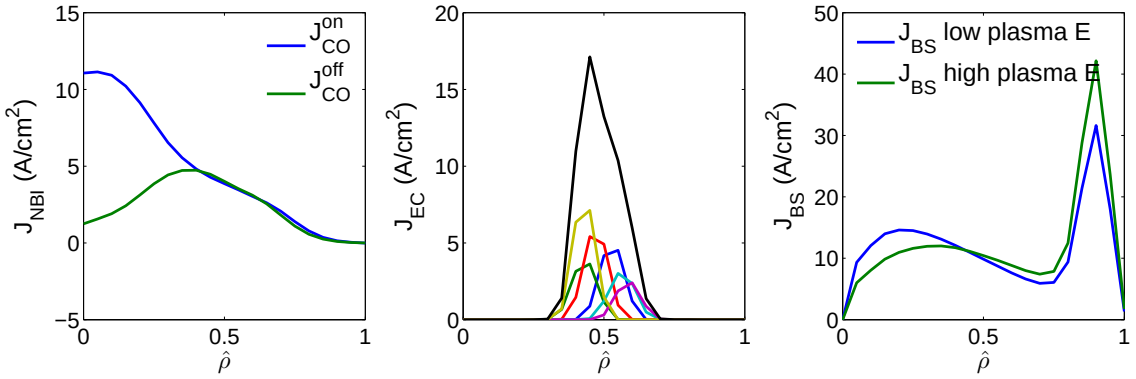


**Figure 3.1:** Left: Current deposition profiles for the co-current on-axis (CO) group and the co-current off-axis (OA) group. Middle: Current deposition profiles for the individual gyrotrons (colored) and the sum total EC (black). Group deposition profiles are the average of the individual beam deposition profiles associated with the group. Right: Bootstrap current drive density profile at low energy (blue) and high energy (green). The bootstrap current increases at the plasma edge and decreases at the plasma center with increasing energy.

the magnetic axis, referred to as co-current on-axis beams (CO-on). Two beams are configured to drive co-current with alignment 16.5° off-axis, referred to as co-current off-axis beams (CO-off). The last two beams are configured to inject counter-current (opposite the plasma current) with on-axis alignment, referred to as counter-current on-axis beams. The ECCD system is composed of six radio-frequency (RF) wave generators (gyrotrons), which drive current and heat the plasma. The gyrotrons can inject a maximum of 0.5 MW each (3 MW in total) for a pulse length of 3 s. The final actuator is the line averaged electron density, which is controlled by gas-feed and pellet launchers.

The typical driven current density profiles of the neutral beam groups and gyrotrons can be seen in Figure 3.1. Of the NBI; the CO-on group drives positive current (co-current direction) mostly near the plasma center and the CO-off group drives current towards the middle of the profile, and the CNT group drives negative current (counter-current direction) towards the plasma center (not shown). The ECCD group is configured to generate a sharply localized current drive toward the mid section of the plasma. Notice that the CO-on group appears to be far more

efficient at driving current than the CO-off group. This is because the total cross-sectional area is much smaller towards the center of plasma than around the middle. Thus while the current drive density is higher for the CO-on beams relative to the CO-off beams, the total driven current is about the same.

It can be shown that the value of $q$ on a flux surface is inversely proportional to the plasma current enclosed by that flux surface. Hence, increasing (or decreasing) the current flow inside a flux surface reduces (or raises) $q$ on that surface. Assuming the total plasma current is held constant by the ohmic coil, we can see from Figure 3.1, that injecting CO-on power modifies the current distribution towards the plasma center, i.e. an increase in current flow at the center and a corresponding decrease of current flow at the edge. Similarly, injecting CO-off power modifies the current distribution away from the plasma center. The bootstrap current distribution is plotted in Figure 3.1. An increase in plasma energy enhances the bootstrap current drive at the plasma edge and reduces it at the plasma center.

## 3.3 Modeling the Toroidal Rotation Dynamics

In this section we consider the spatial and temporal evolution of the toroidal angular rotation profile in response to the various actuators including neutral beam injection (NBI), electron cyclotron resonance heating (ECRH), and non-resonant magnetic field fields (NRMF). A complete treatment of the parabolic partial differential equation that describes the toroidal angular momentum, $P_\phi = m_\mathrm{i} n_\mathrm{i} \langle R^2 \rangle \Omega_\phi$, (mass density times angular rotation) can be found in [59, 60]. Assuming each ion species has the same angular bulk velocity and neglecting the momentum associated with the electrons, the momentum conservation equation for a fixed straight

| Parameter | units | Description |
|---|---|---|
| $\rho = \sqrt{\Phi/\pi B_{\phi,0}}$ | m | Radius term: Square root of normalized toroidal flux |
| $\hat{\rho}$ | – | Normalized radius $\hat{\rho} = \rho/\rho_b$ |
| $\Omega_\phi(\hat{\rho}, t)$ | krad/s | Toroidal angular velocity ($V_\phi = R\Omega_\phi$) |
| $V(\hat{\rho}, t)$ | $1/\mathrm{m}^3$ | Plasma volume |
| $m_\mathrm{i}$ | kg | Ion mass |
| $n_\mathrm{i}(\hat{\rho}, t)$ | $\#/\mathrm{m}^3$ | Ion density |
| $R_0$ | m | Major radius of magnetic axis |
| $\hat{H}(\hat{\rho})$ | – | Geometric factor |
| $\eta_\mathrm{NBI}(\hat{\rho}, t)$ | $\mathrm{N\ m/m}^3$ | Total NBI input torque density |
| $\eta_\mathrm{NRMF}(\hat{\rho}, t)$ | $\mathrm{N\ m/m}^3$ | Total NRMF input torque density |
| $\chi_\phi(\hat{\rho}, t)$ | $\mathrm{m}^2/\mathrm{s}$ | Effective momentum diffusivity |
| $P_\phi = m_\mathrm{i} n_\mathrm{i} \langle R^2 \rangle \Omega_\phi$ | $\mathrm{N\ m\ s/m}^3$ | Angular Momentum Density |

**Table 3.2:** Parameters associated with the momentum diffusion equation (3.26).

cylindrical plasma can be written as

$$\begin{aligned}\frac{\partial}{\partial t}P_\phi =& \sum_i n_i m_i \langle R^2 \rangle \frac{\partial \Omega_\phi}{\partial t} + \Omega_\phi \langle R^2 \rangle \sum_i m_i \frac{\partial n_i}{\partial t} \\ &+ \sum_i n_i m_i \Omega_\phi \frac{\partial \langle R^2 \rangle}{\partial t} + \sum_i n_i m_i \langle R^2 \rangle \Omega_\phi \left( \frac{\partial V}{\partial \hat{\rho}} \right)^{-1} \frac{\partial}{\partial t} \frac{\partial V}{\partial \hat{\rho}} = \\ &\underbrace{\sum_j \eta_j}_{\text{Torque sources}} + \underbrace{\left( \frac{\partial V}{\partial \hat{\rho}} \right)^{-1} \frac{\partial}{\partial \hat{\rho}} \left[ \frac{\partial V}{\partial \hat{\rho}} \sum_i n_i m_i \chi_\phi \langle R^2 (\nabla \hat{\rho})^2 \rangle \frac{\partial \Omega_\phi}{\partial \hat{\rho}} \right]}_{\text{Momentum loss due to viscous dissipation}} \\ &\underbrace{- \left( \frac{\partial V}{\partial \hat{\rho}} \right)^{-1} \frac{\partial}{\partial \hat{\rho}} \left[ \frac{\partial V}{\partial \hat{\rho}} \sum_i n_i m_i \Omega_\phi \langle R^2 (\nabla \hat{\rho})^2 \rangle \frac{\nu_\rho}{|\nabla \hat{\rho}|} \right]}_{\text{Momentum loss due to convection}} \\ &\underbrace{- \sum_i n_i m_i \langle R^2 \rangle \Omega_\phi \left( \frac{1}{\tau_{\phi cx}} \right)}_{\text{Momentum loss due to charge exchange}} .\end{aligned} \tag{3.26}$$

To reduce the modeling complexity of the rotation profile evolution we make the following simplifying assumptions:, *i)* the plasma shape is fixed, *ii)* the plasma ions can be modeled as a single fluid species, *iii)* the momentum transport is purely diffusive, i.e. the momentum loss due to convection and viscous dissipation can

be lumped together into a single effective diffusion term, *iv)* the momentum loss due to charge exchange is relatively small compared to that from viscous dissipation, and *v)* the dominant torque sources are from NBI and NRMF. With these assumptions (3.26) reduces to

$$n_{\mathrm{i}} m_{\mathrm{i}} \langle R^2 \rangle \frac{\partial \Omega_\phi}{\partial t} + m_{\mathrm{i}} \langle R^2 \rangle \Omega_\phi \frac{\partial n_{\mathrm{i}}}{\partial t} = \eta_{\mathrm{NBI}} + \eta_{\mathrm{NRMF}} + \frac{1}{\hat{\rho}\hat{H}} \frac{\partial}{\partial \hat{\rho}} \left[ \hat{\rho}\hat{H} n_{\mathrm{i}} m_{\mathrm{i}} \chi_\phi \langle R^2 \left( \nabla \hat{\rho} \right)^2 \rangle \frac{\partial \Omega_\phi}{\partial \hat{\rho}} \right], \tag{3.27}$$

where $m_{\mathrm{i}}$ and $n_{\mathrm{i}}$, are, respectively, the single fluid ion mass and ion density, $\chi_\phi$ is the effective angular momentum diffusivity coefficient, $\eta_{(\cdot)}$ represents the local torque density from NBI and NRMF sources, the operator $\langle \cdot \rangle$ stands for flux surface average, $R$ is the major radius of the plasma, and $\hat{H}$ is a spatial geometric factor specific to the magnetic configuration[1] (see Appendix A.4). The boundary conditions are determined from symmetry at the plasma center and an assumed no slip condition[2] at the plasma edge,

$$\left. \frac{\partial \Omega_\phi}{\partial \hat{\rho}} \right|_{\hat{\rho}=0} = 0, \qquad \Omega_\phi|_{\hat{\rho}=1} = 0. \tag{3.28}$$

In a similar fashion as that described in Section 3.2, the model for toroidal angular rotation evolution is transformed to a more control-oriented form by combining it with scenario-specific empirical correlations relating the ion density, ion temperature, and driven torque from various auxiliary sources. Assuming rotation control is limited to the H-mode regime, the control action employed to regulate the line-averaged ion density can be fairly approximated as only weakly affecting the radial distribution of the ions. Therefore, the ion density $n_{\mathrm{i}}(\hat{\rho}, t)$ is modeled as

$$n_{\mathrm{i}}(\hat{\rho}, t) = n_{\mathrm{i}}^{\mathrm{prof}}(\hat{\rho}) \bar{n}_{\mathrm{i}}(t), \tag{3.29}$$

where $n_{\mathrm{i}}^{\mathrm{prof}}(\hat{\rho})$ is a reference profile, and $\bar{n}_{\mathrm{i}}$ is the line averaged ion density. Following the approach of Section 3.2, the ion temperature profile evolution can be modeled

[1] Same as that used in the poloidal flux evolution model

[2] The rotation at the edge is not necessarily zero but very small compared to the bulk rotation for typical H-mode, NBI heated plasmas.

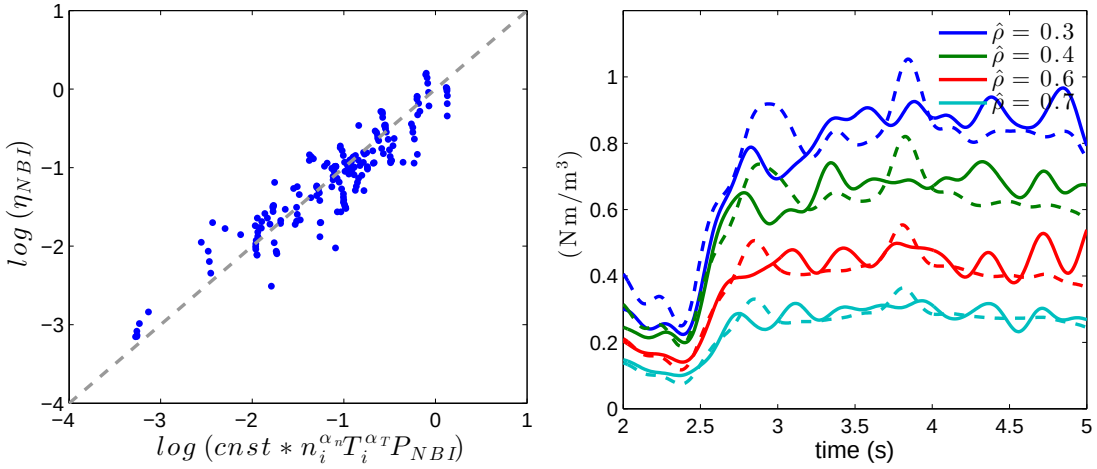


**Figure 3.2:** NBI torque estimated by the scaling model (3.31) in comparison to that calculated by NUBEAM for DIII-D shot 147634. The linear regression trend line compared to a small sampling of estimation data set (left) and comparison of torque estimate as predicted by (3.31) to that predicted by NUBEAM (right).

according to the scaling law [66],

$$T_{\mathrm{i}}(\hat{\rho},t) = k_{T_{\mathrm{i}}} T_{\mathrm{i}}^{\mathrm{prof}}(\hat{\rho}) \frac{I_{\mathrm{p}}(t)\sqrt{P_{\mathrm{tot}}(t)}}{\bar{n}_{\mathrm{i}}(t)}, \tag{3.30}$$

where $k_{T_{\mathrm{i}}}$ is a constant, $T_{\mathrm{i}}^{\mathrm{prof}}(\hat{\rho})$ is a reference ion temperature profile, $I_{\mathrm{p}}(t)$ is the total plasma current, and $P_{\mathrm{tot}}(t)$ is the total power absorbed by the plasma. Again, as in Section 3.2, the total absorbed power is defined as the auxiliary power injected into the plasma by NBI and ECRH, plus the ohmically driven power, $P_{\mathrm{ohm}}$, minus the radiative power, $P_{\mathrm{rad}}$, i.e., $P_{\mathrm{tot}} = P_{\mathrm{ohm}} + P_{\mathrm{aux}} - P_{\mathrm{rad}}$. The ohmic and radiative powers are functions of the poloidal flux and electron temperature and density as described in Section 3.2.1.

To model the torque density deposited by each neutral beam, we propose the scaling law,

$$\eta_{\mathrm{NBI},\xi}(\hat{\rho},t) = \eta_{\mathrm{NBI},\xi}^{\mathrm{prof}}(\hat{\rho}) n_{\mathrm{i}}(\hat{\rho},t)^{\alpha_n} T_{\mathrm{i}}(\hat{\rho},t)^{\alpha_T} P_{\mathrm{NBI},\xi}(t), \tag{3.31}$$

where $P_{\mathrm{NBI},\xi}(t)$ is the power for each neutral beam line, $\eta_{\mathrm{NBI},\xi}^{\mathrm{prof}}(\hat{\rho})$ is the torque density reference profile for each beam, and $k_{\mathrm{NBI},\xi}$ is a constant. The label $\xi =$

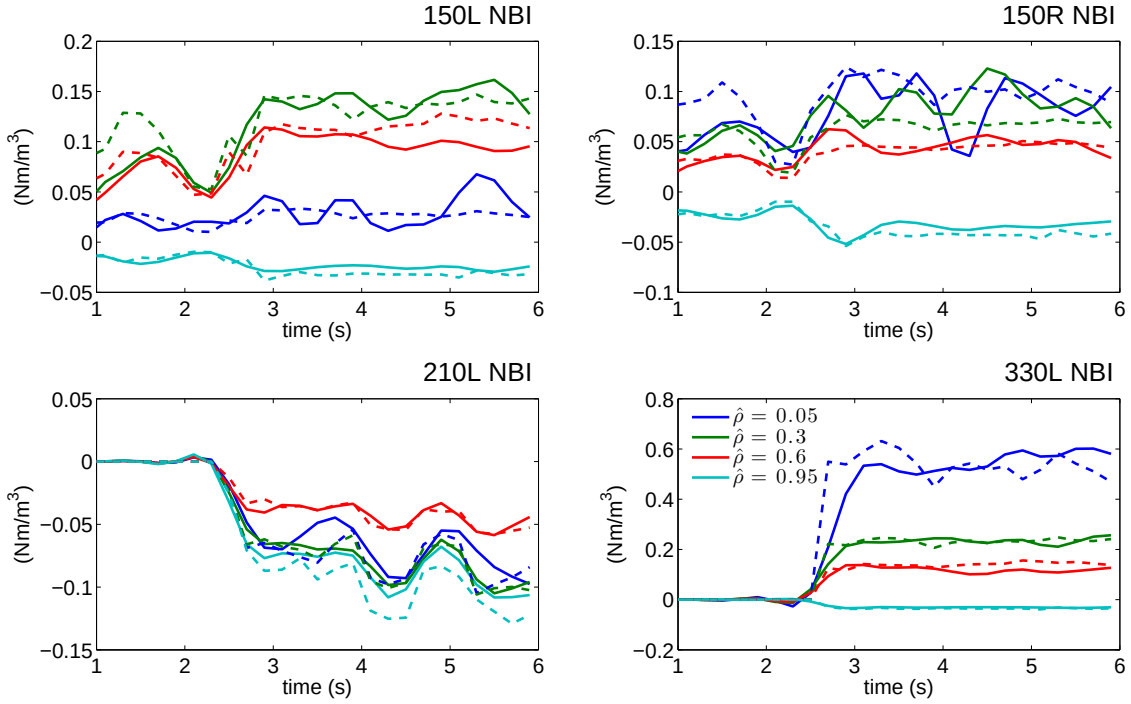


**Figure 3.3:** Comparison of NBI torque density modeled with (3.31) (dashed line) and TRANSP NUBEAM package (solid line) for shot 147634.

$1, \ldots, n_{\text{NBI}}$ is used to index the individual NBIs. The scalings $\alpha_n = 1.5$ and $\alpha_T = -0.5$ are determined by a linear regression fit to data based on DIII-D shots 147634, 154358, 154691, 146419. A comparison of the model fit, NBI torque density produced by (3.31) to that produced by the NUBEAM package is shown in Figure 3.2. On the left, a small sampling of the observed data-set is plotted over the model trend line to demonstrate the near one-to-one correspondence between the scaling model (3.31) and physical data, and on the right, the total torque density computed by NUBEAM as compared to the scaling model estimate is plotted. Additionally, in Figure 3.3, we plot the torque estimate for several of the individual NBI.

The NRMF torque density is dependent on the collisionality regime of the plasma, and thus dependent on plasma temperature and density. We make use

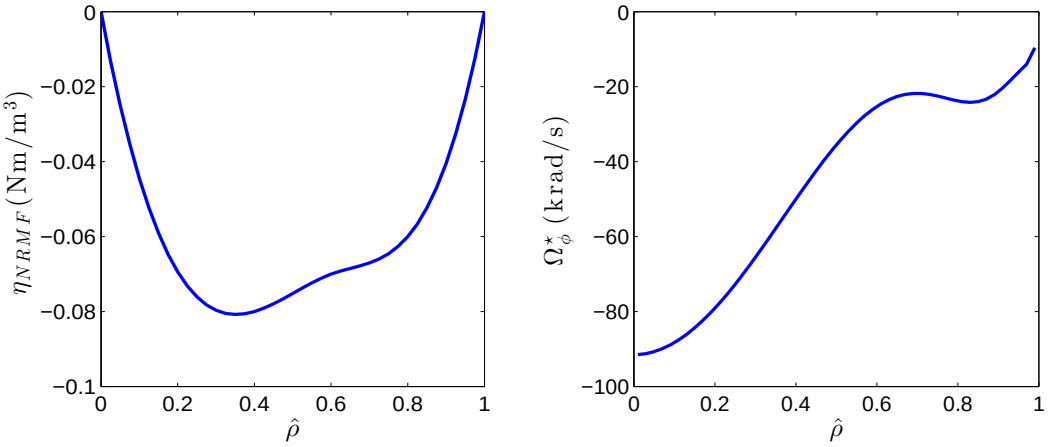


**Figure 3.4:** The NRMF torque density reference profile, $\eta^{\text{prof}}_{\text{NR}}$, (left) and the offset rotation $\Omega^{\star}(\hat{\rho})$ of (3.32) (right). As can be seen by the shape of the reference profile, the NRMF torque density is deposited primarily off-axis and has a dragging effect on the plasma rotation.

of the model reported in [67, 68],

$$\begin{aligned}\eta_{\text{NRMF}}(\hat{\rho},t) = \eta^{\text{prof}}_{\text{NRMF}}(\hat{\rho})\left(\Omega_{\phi}(\hat{\rho},t) - \Omega^{*}_{\phi}(\hat{\rho})\right) \\ \times\ n_{\text{i}}(\hat{\rho},t)^{\beta_n} T_{\text{i}}(\hat{\rho},t)^{\beta_T} \omega_E(\hat{\rho})^{\beta_\omega} I_{\text{NRMF}}(t)^2,\end{aligned} \tag{3.32}$$

where $I_{\text{NRMF}}(t)$ is the current in the perturbation field coils, $\Omega^{*}_{\phi}(\hat{\rho})$ is an offset rotation, $\omega_E(\hat{\rho})$ is the toroidal component of the $E \times B$ drift velocity, $\eta^{\text{prof}}_{\text{NR}}(\hat{\rho})$ is a reference profile, $k^{\text{prof}}_{\text{NR}}(\hat{\rho})$ is a constant scaling profile, and the scalings determined by linear regression fit to data, are given by $\beta_n = 3.6$, $\beta_T = 2.6$, and $\beta_\omega = -0.6$ [68]. The profile for $\Omega^{\star}$ plotted in Figure 3.4(b) is assumed to be constant; it can be determined from shot 131408. During this shot an applied NRMF field had no effect on the velocity profile implying the NRMF torque was zero, and thus the plasma velocity during that shot must have been equal to the offset velocity.

The parameters $\langle R^2\rangle(\hat{\rho})$, $\langle R^2(\nabla\hat{\rho})^2\rangle(\hat{\rho})$, and $\hat{H}(\hat{\rho})$ do not change significantly during the plasma current flattop phase of a discharge, thus we elect to approximate them as fixed spatial profiles. The profiles are obtained from a TRANSP simulation of DIII-D shot 147634. The selected profiles for each parameter are shown in Figure. 3.5. As can be seen, the profiles do not change significantly during

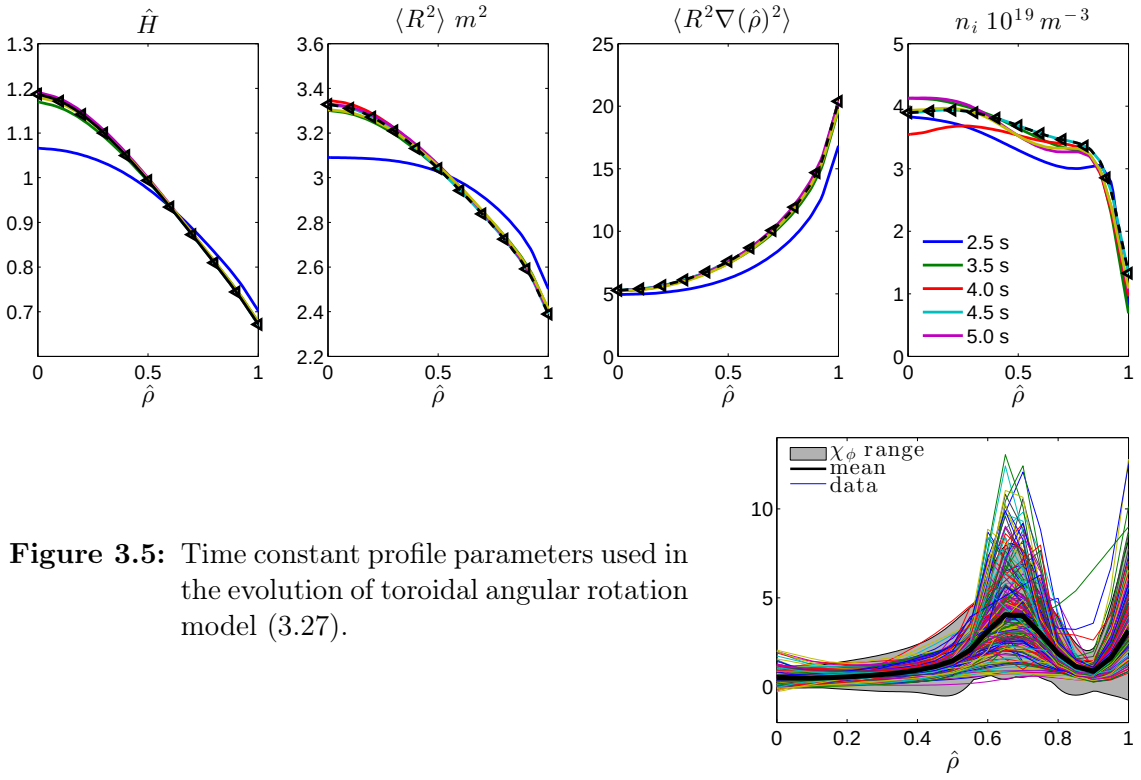


**Figure 3.5:** Time constant profile parameters used in the evolution of toroidal angular rotation model (3.27).

the discharge after 3.5 s, i.e. during flattop. Thus, the chosen parameter profiles are sufficient for modeling during the current flattop of the plasma discharge. Modeling of the effective diffusivity term, $\chi_\phi$, which is partly composed of turbulent effects, is not considered in this work. Instead, we select a constant nominal profile shape based on the time average of the measured diffusivity from DIII-D shot 147634 as shown in Figure 3.5. In the control development sections that follow, variations of $\chi_\phi$ from the nominal profile will be modeled as an uncertainty.

The rotation profile control strategies considered in later chapters often incorporate control of the plasma stored energy in combination with rotation, in which case the plasma stored energy is modeled by (3.4). Note that the ohmic power, which enters into the expression for total absorbed power, $P_{\text{tot}}$, is a function of the poloidal magnetic flux profile, therefore the rotation profile evolution is coupled to the poloidal magnetic flux evolution.

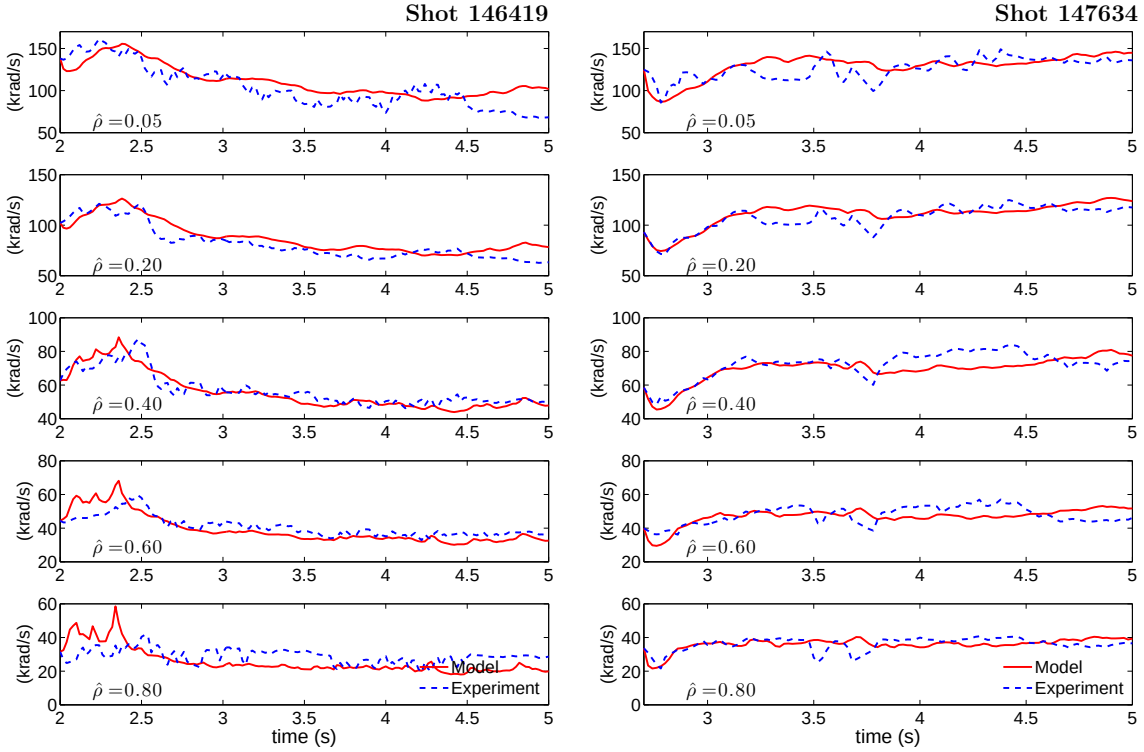


**Figure 3.6:** Comparison of modeled toroidal rotation evolution and experimental data. (Left) DIII-D shot 146419. (Right) DIII-D shot 147634. In both cases their is no NRFM torque contribution.

### 3.3.1 Comparison Between Model-Predicted Toroidal Rotation Evolution and Experimental Data

In Figure 3.6 a comparison between the model-predicted toroidal rotation evolution given by (3.27) and two experimental DIII-D H-mode discharges is shown. In both cases the discharges involve only torque contributions from NBI and no NRMF. The model captures most of the trend of the rotation evolution. The primary shortcoming of the model is due to the assumed constant shape of the diffusivity term, $\chi_\phi$ (see Figure 3.5). In actuality, $\chi_\phi$ varies substantially throughout the discharge, but unfortunately due its complex and anomalous behavior, dynamic models for $\chi_\phi$ are not yet available. However, it is important to note again that the model needs only capture the dominant effects of the system dynamics because one of the main characteristics of feedback is the ability to deal with model uncertainties. In the

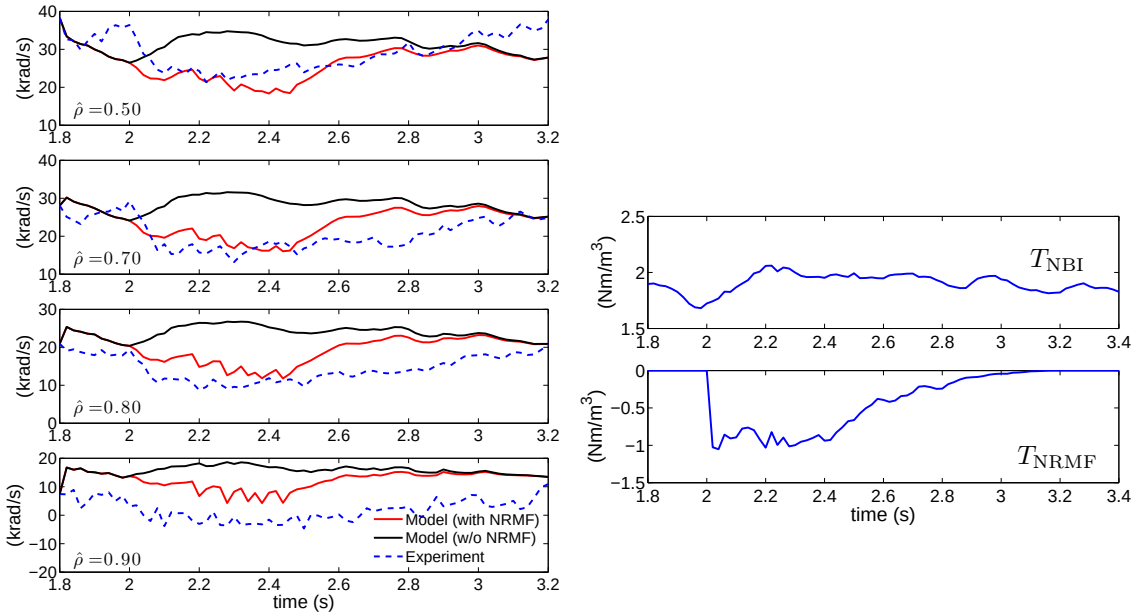


**Figure 3.7:** Comparison of modeled toroidal rotation evolution and experimental data for DIII-D shot 131320 which includes torque sources from both NBI and NRMF. The values $T_{\mathrm{NBI}}$ and $T_{\mathrm{NRMF}}$ represent the volume integrated torque densities, i.e., $T_{\mathrm{NBI}} = \int_V \eta_{\mathrm{NBI}} dV$ and $T_{\mathrm{NRMF}} = \int_V \eta_{\mathrm{NRMF}} dV$.

second case, Figure 3.7, we consider a DIII-D shot with applied torque sources from both NRMF and NBI. In this plot, the modeled rotation evolution is shown with and without including the torque contribution from NRMF given by (3.32). While again the model prediction is only approximate, it is clear that the NRMF torque model greatly improves the model-predicted evolution of the rotation profile.

## 3.4 Conclusion

First-principles, physics-based models for the evolution of the current profile and the rotation profile were described. These models were combined with scenario-specific correlations for the plasma temperature, density, and sources (current drive or torque) to develop simplified models suitable for real-time control strategies. In the following chapters these models will be used for the design and simulation testing of various control strategies. Since the models can be tailored to different

scenarios and to different tokamaks by adjusting the model parameters, the model-based control approaches described in the forthcoming chapters, which are design specifically for the DIII-D tokamak, can still be applied to other tokamaks with little modification.

# Chapter 4

# Feedforward Control Design via Nonlinear Optimization

## 4.1 Introduction

For reasons described in Section 1.5, control of the current profile (or equivalently $q$ profile) is crucial for sustaining stable, high performance operation of tokamaks. Present-day tokamak operation typically relies on "scenario planning", i.e. preprogramming a set of auxiliary current drive and heating powers according to semi-empirical laws to obtain a desired $q$ profile. This process often relies on extensive experience gained during operation of a particular machine as well as numerous trial-and-error attempts. In this chapter, the model describing the poloidal flux evolution of Section 3.2 is used to formulate the scenario planning task as an optimal control problem with the aim of improving shot-to-shot reproducibility of target current profiles, and retiring the long trial-and-error periods currently devoted by experimentalists to manually adjusting actuator waveforms.

We consider the control objective of achieving the best possible matching of the target current profile at a specified time during the early flattop phase of the discharge. Such a matching problem can be formulated as a finite-time optimal control problem. Solutions to optimal control synthesis can be categorized into indirect

and direct methods, based on calculus of variations [48, 69] and nonlinear programming [70], respectively. Calculus of variations can be used in indirect methods to derive the optimality conditions for a given optimal control problem. These optimality conditions result in a two boundary value problem, which usually requires numerical computations for its solution. Indirect methods tend to be numerically unstable and are difficult to implement and initialize [71]. As an alternative approach, the system states and controls over the optimization period can be treated as independent variables in direct methods to reformulate the original optimal control problem as a finite-dimensional optimization problem, which can be solved numerically with good accuracy by modern nonlinear programming techniques such as sequential quadratic programming (SQP).

Prior works have considered feedforward current profile control optimization by numerical methods including extremum seeking [72] and SQP combined with low-dimensional models [73]. Extremum seeking does not require a model to perform optimization, it is essentially a black-box optimization method, and therefore the methods considered in [73] could potentially be used for scenario planning without designing a model. Instead real machine data would be used to perform the optimization. However, this would, of course, require a large number of real tokamak discharges dedicated to the optimization procedure. The feedforward control design considered in this chapter is originated from the dissertation efforts of J.E. Barton [56], and in this chapter Barton's work is extended with the inclusion of analytic gradients calculations. Not only do analytic gradient calculations greatly reduce the time necessary to solve the optimization problem, but also addresses issues associated with inaccurate finite difference approximations that creep in as the dynamics become more complicated. Additionally, because of the high dimension of the system dynamics associated with the current profile only a small number of control parameters could be incorporated into the optimization problem when using finite differences to compute gradients. With explicit gradient calculations, it becomes practical to solve for optimal feedforward control solutions with many more control updates.

This chapter is organized as follows. In Section 4.2, the dynamic model of the

current profile described in Chapter 3 is re-introduced in a form more tractable for control design. Using finite difference approximations to the spatial derivatives, the governing infinite dimensional PDE is approximated by a finite dimensional system of ordinary differential equations to enable the synthesis of optimal control solutions. Section 4.3 describes the formulation of the open-loop optimal control problem as a finite-dimensional nonlinear optimization problem, and Section 4.4 describes the particular form of the optimal control problem for current profile control in the DIII-D tokamak. In Section 4.5, specific examples of the optimal control synthesis are presented for both L-mode and H-mode DIII-D discharges, and the chapter is closed in Section 4.6 with a statement of conclusions.

## 4.2 Reduced Order Modeling

In Chapter 3, a first-principles-based model (3.1) was described for the evolution of the poloidal magnetic flux profile (equivalently the current profile), which was simplified for applicability to model-based control design techniques. For convenience of control design, we can separate the time-varying and spatially-varying parameters of the model (3.1) to obtain

$$\begin{aligned}\frac{\partial \psi}{\partial t}(\hat{\rho},t) =& \frac{f_\eta}{\hat{\rho}}\frac{\partial}{\partial \hat{\rho}}\left(\hat{\rho} D_\psi \frac{\partial \psi}{\partial \hat{\rho}}\right) u_\eta(t) + \sum_{\xi=1}^{n_{\rm NBI}} f_{{\rm NBI},\xi} u_{{\rm NBI},\xi}(t) \\ &+ f_{\rm EC} u_{\rm EC}(t) + f_{\rm BS}\left(\frac{\partial \psi}{\partial \hat{\rho}}\right)^{-1} u_{\rm BS}(t),\end{aligned} \tag{4.1}$$

with the boundary conditions,

$$\left.\frac{\partial \psi}{\partial \hat{\rho}}\right|_{\hat{\rho}=0} = 0 \quad \text{and} \quad \left.\frac{\partial \psi}{\partial \hat{\rho}}\right|_{\hat{\rho}=1} = k_{I_{\rm p}} I_{\rm p}(t). \tag{4.2}$$

The functions $f_{(\cdot)}(\hat{\rho})$ capture the spatial dependence of the various parameters of the model (3.1), which are given by

$$\begin{aligned}
D_\psi(\hat{\rho}) &= \hat{F}\hat{G}\hat{H}, \\
f_\eta(\hat{\rho}) &= \frac{k_{\text{eff}} Z_{\text{eff}}}{\mu_0 \rho_b^2 k_{T_\text{e}}^{3/2} \hat{F}^2 \left(T_\text{e}^{\text{profile}}/n_\text{e}^{\text{profile}}\right)^{3/2}}, \\
f_{\text{EC}}(\hat{\rho}) &= \frac{k_{\text{eff}} Z_{\text{eff}} R_0 \hat{H} k_{\text{EC}} j_{\text{EC}}^{\text{profile}}}{k_{T_\text{e}}^{1/2} \left(T_\text{e}^{\text{profile}} n_\text{e}^{\text{profile}}\right)^{1/2}}, \\
f_{\text{NBI},\xi}(\hat{\rho}) &= \frac{k_{\text{eff}} Z_{\text{eff}} R_0 \hat{H} k_{\text{NBI},\xi} j_{\text{NBI},\xi}^{\text{profile}}}{k_{T_\text{e}}^{1/2} \left(T_\text{e}^{\text{profile}}\right)^{1/2}}, \qquad \text{for} \quad \xi = 1, 2, \ldots, n_{\text{NBI}}, \\
f_{\text{BS}}(\hat{\rho}) &= \left( k_{T_e} \left(2\mathcal{L}_{31} + \mathcal{L}_{32} + \alpha \mathcal{L}_{34}\right) \frac{dT_e^{\text{prof}}}{d\hat{\rho}} \right. \\
&\qquad \left. + 2\mathcal{L}_{31} k_{T_e} \frac{T_e^{\text{prof}}}{n_e^{\text{prof}}} \frac{dn_e^{\text{prof}}}{d\hat{\rho}} \right) \Bigg/ \frac{k_{Jev} R_0^2 \hat{H} k_{sp} Z_{eff}}{\hat{F}\left(k_{T_e} \frac{T_e^{\text{prof}}}{n_e^{\text{prof}}}\right)^{3/2}}, \\
k_{I_\text{p}} &= -\frac{\mu_0}{2\pi} \frac{R_0}{\hat{G}|_{\hat{\rho}=1} \hat{H}|_{\hat{\rho}=1}},
\end{aligned} \tag{4.3}$$

and $u_{(\cdot)}(t)$ are a set of nonlinear input functions of the form,

$$\begin{aligned}
u_\eta(t) &= \left( \frac{\bar{n}_\text{e}(t)}{I_\text{p}(t)\sqrt{P_{\text{tot}}(t)}} \right)^{3/2}, \\
u_{\text{EC}}(t) &= \left( \frac{1}{I_\text{p}(t)\sqrt{P_{\text{tot}}(t)}\bar{n}_\text{e}(t)} \right)^{1/2} P_{\text{EC}}(t), \\
u_{\text{NBI},\xi}(t) &= \left( \frac{1}{I_\text{p}(t)\sqrt{P_{\text{tot}}(t)}} \right)^{1/2} P_{\text{NBI},\xi}(t), \qquad \text{for} \quad \xi = 1, 2, \ldots, n_{\text{NBI}}, \\
u_{\text{BS}}(t) &= \left( \frac{\bar{n}_\text{e}(t)^3}{I_\text{p}(t)\sqrt{P_{\text{tot}}(t)}} \right)^{1/2}.
\end{aligned} \tag{4.4}$$

The form of these functions, $f_{(\cdot)}(\hat{\rho})$ and $u_{(\cdot)}(t)$, arise from the empirical correlations for plasma density, temperature, resistivity, and auxiliary current drive described in Section 3.2. The controls (4.4) admit diffusivity control, $u_\eta$, interior controls

from $u_{\mathrm{NBI},i}$ and $u_{\mathrm{EC}}$, and boundary control, $I_{\mathrm{p}}$. The control term labeled $u_{\mathrm{BS}}$ is associated with the bootstrap current drive, it can also be thought of as an interior control term.

As the $q$ profile depends inversely on the spatial derivative of the poloidal flux, we can introduce the terms $\theta$ and $\iota$ given by

$$\theta(\hat{\rho},t) \triangleq \frac{\partial \psi}{\partial \hat{\rho}}(\hat{\rho},t), \quad \iota(\hat{\rho},t) \triangleq \frac{1}{q(\hat{\rho},t)} = \frac{-\theta}{B_{\phi,0}\rho_{\mathrm{b}}^2 \hat{\rho}}, \tag{4.5}$$

which will be useful for control purposes. We can differentiate (4.1) in space to obtain an expression for the evolution of $\theta$,

$$\begin{aligned}\frac{\partial \theta}{\partial t} =& \frac{\partial}{\partial \hat{\rho}}\left\{\frac{f_\eta}{\hat{\rho}}\frac{\partial}{\partial \hat{\rho}}\left(\hat{\rho} D_\psi \frac{\partial \psi}{\partial \hat{\rho}}\right)\right\} u_\eta(t) + \sum_{\xi=1}^{n_{\mathrm{NBI}}} \frac{\partial f_{\mathrm{NBI},\xi}}{\partial \hat{\rho}} u_{\mathrm{NBI},\xi}(t) \\ &+ \frac{\partial f_{\mathrm{EC}}}{\partial \hat{\rho}} u_{\mathrm{EC}}(t) + \frac{\partial}{\partial \hat{\rho}}\left\{f_{\mathrm{BS}}\left(\frac{\partial \psi}{\partial \hat{\rho}}\right)^{-1}\right\} u_{\mathrm{BS}}(t),\end{aligned} \tag{4.6}$$

After carrying out the spatial derivatives, the model (4.6) reduces to

$$\begin{aligned}\frac{\partial \theta}{\partial t} =& h_0 u_\eta \theta'' + h_1 u_\eta \theta' + h_2 u_\eta \theta \\ &+ \sum_{\xi=1}^{n_{\mathrm{NBI}}} f'_{\mathrm{NBI},\xi} u_{\mathrm{NBI},\xi} + f'_{\mathrm{EC}} u_{\mathrm{EC}} + f'_{\mathrm{BS}} \frac{1}{\theta} u_{\mathrm{BS}} - f_{\mathrm{BS}} \frac{1}{\theta^2} \theta' u_{\mathrm{BS}},\end{aligned} \tag{4.7}$$

where $(\cdot)'$ denotes the spatial derivative, and the functions, $h_{(\cdot)}(\hat{\rho})$, introduced for compactness, can be written in terms of the functions $D_\psi(\hat{\rho})$ and $f_\eta(\hat{\rho})$,

$$\begin{aligned} h_0 &= f_\eta D_\psi, \\ h_1 &= f'_\eta D_\psi + f_\eta D_\psi \frac{1}{\hat{\rho}} + 2 f_\eta D'_\psi, \\ h_2 &= f'_\eta D'_\psi + f'_\eta D_\psi \frac{1}{\hat{\rho}} + f_\eta D'_\psi \frac{1}{\hat{\rho}} - f_\eta D_\psi \frac{1}{\hat{\rho}^2} + f_\eta D''_\psi. \end{aligned} \tag{4.8}$$

Thus, we can control $q$ indirectly be controlling either $\theta$ or $\iota$, and avoid the nonlinearity associated with the inverse of the spatial derivative of the poloidal magnetic flux in (3.17). Finally the boundary conditions (4.2) can be written in terms of $\theta$ as

$$\theta|_{\hat{\rho}=0} = 0, \quad \theta|_{\hat{\rho}=1} = -k_{I_{\mathrm{p}}} I_{\mathrm{p}}. \tag{4.9}$$

The system defined by (4.6) and (4.9) represents a PDE system for which it is very challenging and usually impossible to design optimal feedback control laws due to the infinite dimensionality of the system that arises from the continuous spatial domain. To transform the system to a finite dimensional state-space form, we first discretize the system in space using finite difference approximations to the spatial derivatives. Central difference spatial derivative approximations of $\mathrm{O}\big(\Delta\hat{\rho}^2\big)$ are used in the interior node region, $2 \leq i \leq (l-1)$ and forward and backward difference approximations of $\mathrm{O}\big(\Delta\hat{\rho}^2\big)$ at the boundary nodes $i = (1,\ l)$. The domain of interest, $\hat{\rho} = [0, 1]$, is truncated to $l$ evenly spaced nodes, separated by $\Delta\hat{\rho} = 1/(l-1)$ to obtain the finite-dimensional system,

$$\dot{\boldsymbol{\theta}} = \boldsymbol{f}_\theta(\boldsymbol{\theta}, \mathbf{u}), \quad \boldsymbol{\iota} = \mathbf{C}\boldsymbol{\theta}, \tag{4.10}$$

where the model state is $\boldsymbol{\theta} = [\theta_2, \theta_3, \ldots, \theta_{l-1}]^T$ (see Appendix A.1). The actuators represented by $\mathbf{u}$ include the nonlinear input functions of (4.4). Note that in addition to the non-inductive sources, we also have control of the total plasma current, $I_\mathrm{p}$, allowing control of the profile boundary. The total plasma current, represents the sum of non-inductive and inductive currents. It is assumed that a low level dedicated controller exists to regulate the tokamak central coil voltage to drive any missing current between the requested total current and the sum of non-inductive sources.

Alternatively, in some control cases we take the poloidal stream function relative to the boundary value, i.e. $\bar{\psi} = \psi - \psi_\mathrm{b}$ as the system state in which case we approximate the spatial derivatives of the system (4.1) and (4.2) with finite differences to obtain

$$\dot{\bar{\boldsymbol{\psi}}} = \boldsymbol{f}_{\bar{\psi}}(\bar{\boldsymbol{\psi}}, \mathbf{u}), \tag{4.11}$$

where the model state is $\bar{\boldsymbol{\psi}} = [\bar{\psi}_{\hat{\rho}=2}, \bar{\psi}_{\hat{\rho}=3}, \ldots, \bar{\psi}_{\hat{\rho}=l-1}]^T$.

## 4.3 Formulating the Feedforward Control Problem

The control problem is formulated as a trajectory optimization problem to search for a feasible path from the expected initial condition to the desired target. The

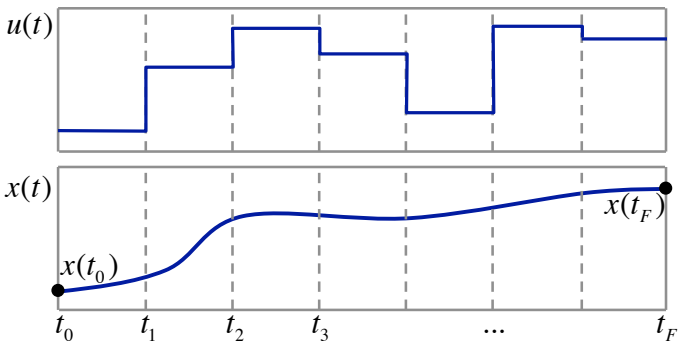


**Figure 4.1:** Discretized control sequence, $\mathbf{w} = [\mathbf{u}_0, \mathbf{u}_1, \ldots, \mathbf{u}_F]$ and output of integrator function $\mathbf{f}$, which maps $\mathbf{w}$, $\mathbf{x}_0$ and $t$ to $\mathbf{x}(t)$.

result comprises a sequence of feedforward (open-loop) control requests which steers the system state from some specified initial condition state to some desired state. Consider a dynamical system defined by

$$\dot{\mathbf{x}} = \boldsymbol{f}(\mathbf{x}, \mathbf{u}), \tag{4.12}$$

we can formulate the feedforward control design as an optimization problem of the form

$$\begin{aligned} \underset{\mathbf{u}(t)}{\text{minimize}} \quad & J(\mathbf{x}(t_F)) \\ \text{subject to} \quad & \dot{\mathbf{x}} = \boldsymbol{f}(\mathbf{x}, \mathbf{u}), \\ & \mathbf{x}(t_0) = \mathbf{x}_0, \\ & \mathbf{g}_{\text{in}}(\mathbf{x}(t), \mathbf{u}(t)) \leq 0, \\ & \mathbf{g}_{\text{eq}}(\mathbf{x}(t), \mathbf{u}(t)) = 0. \end{aligned} \tag{4.13}$$

This is often called a trajectory optimization problem because it involves the search for a state trajectory, $\mathbf{x}(t)$, that starts from the initial state, $\mathbf{x}_0$, and reaches some goal state at time $t_F$ quantified by the scalar function $J$. This state trajectory must be consistent with the system dynamics described by the equality constraint $\dot{\mathbf{x}} = \boldsymbol{f}(\mathbf{x}, \mathbf{u})$. Additionally, the optimization requires the state trajectory to avoid undesirable regions of the state space, which are quantified by the constraints, $\mathbf{g}_{\text{in}}$ and $\mathbf{g}_{\text{eq}}$. The undesirable regions of the state space are those regions of the tokamak operating space that are associated with MHD instabilities.

Problem (4.13) describes an infinite dimensional optimization problem on account of the fact that the optimization variables, $\mathbf{x}(t)$, and $\mathbf{u}(t)$, are defined on a continuous domain, $t \in [t_0, t_F]$. The most successful approach to solving an optimal control problem like (4.13) is to parameterize the problem with a finite set of decision variables, and then to solve it by using numerical optimization methods [71]. As illustrated in Figure 4.1, over a time grid $t_0, \ldots, t_F$, we discretize the control as a zero order hold

$$\mathbf{u}_k = \mathbf{u}(t \in [t_k, t_{k+1}]), \tag{4.14}$$

and then prescribe $\mathbf{x}$ as a function of $\mathbf{w} = [\mathbf{u}_0, \mathbf{u}_1, \ldots, \mathbf{u}_F]$, $\mathbf{x}_0$, and $t$ to obtain

$$\mathbf{x}(t) = \mathbf{F}(\mathbf{w}, \mathbf{x}_0, t) \equiv \mathbf{x}_0 + \int_{t_0}^{t} \boldsymbol{f}(\mathbf{x}(s), \mathbf{u}(s))ds. \tag{4.15}$$

The function $\mathbf{F}$ is an integrator function which depends on the choice of integration scheme used to simulate the system modeled by (4.12). With the use of (4.15), we can rewrite the original optimal control problem (4.13) as

$$\begin{aligned} \underset{\mathbf{w}}{\text{minimize}} \quad & J(\mathbf{F}(\mathbf{w}, \mathbf{x}_0, t_F)) \\ \text{subject to} \quad & \mathbf{g}_{\text{in}}(\mathbf{F}(\mathbf{w}, \mathbf{x}_0, t_i), \mathbf{u}_i) \leq 0, \text{ for } i = 0, 1, \ldots, F \\ & \mathbf{g}_{\text{eq}}(\mathbf{F}(\mathbf{w}, \mathbf{x}_0, t_i), \mathbf{u}_i) = 0, \text{ for } i = 0, 1, \ldots, F \end{aligned} \tag{4.16}$$

where we are now optimizing over a finite set of optimization variables defined by the feedforward control sequence $\mathbf{w}$[1]. Additionally, the constraints have been reduced to a finite number by evaluating $\mathbf{g}_{\text{eq}}$ and $\mathbf{g}_{\text{in}}$ only at the times $t_i$, for $i = 0, 1, \ldots F$.

First-order necessary conditions for optimality require solutions to the problem (4.16) to be feasible, i.e. to satisfy all the constraints, and to be a stationary point to the Lagrangian. By assuming for the moment that problem (4.16) includes only equality constraints, the Lagrangian can be written as $\mathcal{L} = J(\mathbf{w}) - \boldsymbol{\lambda}^T \mathbf{g}_{\text{eq}}(\mathbf{w})$, where $\boldsymbol{\lambda}$ is a Lagrange multiplier, and the first-order necessary conditions can be summarized as

$$\begin{bmatrix} \nabla J(\mathbf{w}) - \nabla \mathbf{g}_{\text{eq}}(\mathbf{w})\boldsymbol{\lambda} \\ \mathbf{g}_{\text{eq}}(\mathbf{w}) \end{bmatrix} = 0, \tag{4.17}$$

[1]Note that the state, $\mathbf{x}(t)$, has been solved away from the optimization problem with the use the integrator function $\mathbf{F}(\mathbf{u}_0, \mathbf{u}_1, \ldots, \mathbf{u}_F, \mathbf{x}_0, t) = \mathbf{x}(t)$.

where $\nabla$ represents $\partial/\partial\mathbf{w}$. We can proceed to search for a minimizer to the problem (4.16) by searching for points that satisfy (4.17). The natural approach is to solve the nonlinear equations (4.17) with Newton's method. Start with an initial guess, $(\mathbf{w}_k, \boldsymbol{\lambda}_k)$, of the optimal solution, $(\mathbf{w}^\star, \boldsymbol{\lambda}^\star)$, and make updates $(\mathbf{w}_{k+1}, \boldsymbol{\lambda}_{k+1}) = (\mathbf{w}_k, \boldsymbol{\lambda}_k) + (\Delta\mathbf{w}_k, \Delta\boldsymbol{\lambda}_k)$, where the update, $(\Delta\mathbf{w}_k, \Delta\boldsymbol{\lambda}_k)$ is determined by solving a linear approximation of (4.17), i.e. it is given by the Newton step,

$$\begin{bmatrix} \nabla^2_{\mathbf{ww}}\mathcal{L}(\mathbf{w}_k) & -\nabla\mathbf{g}_{\text{eq}}(\mathbf{w}_k) \\ \nabla\mathbf{g}_{\text{eq}}(\mathbf{w}_k)^T & 0 \end{bmatrix} \begin{bmatrix} \Delta\mathbf{w}_k \\ \Delta\boldsymbol{\lambda}_k \end{bmatrix} = \begin{bmatrix} -\nabla J(\mathbf{w}_k) + \nabla\mathbf{g}_{\text{eq}}(\mathbf{w}_k)\boldsymbol{\lambda}_k \\ -\mathbf{g}_{\text{eq}}(\mathbf{w}_k) \end{bmatrix}. \tag{4.18}$$

Sequential quadratic programming (SQP), the numerical optimization method used in this work, reformulates (4.18) as a quadratic optimization problem (quadratic program (QP))

$$\begin{aligned} \underset{\Delta\mathbf{w}_k}{\text{minimize}} \quad & J(\mathbf{w}_k) + \nabla J(\mathbf{w}_k)^T\Delta\mathbf{w}_k + \frac{1}{2}\Delta\mathbf{w}_k^T(\nabla^2_{\mathbf{ww}}\mathcal{L})\Delta\mathbf{w}_k, \\ \text{subject to} \quad & \mathbf{g}_{\text{eq}}(\mathbf{w}_k) + \nabla\mathbf{g}_{\text{eq}}{}^T(\mathbf{w}_k)\Delta\mathbf{w}_k = 0. \end{aligned} \tag{4.19}$$

It can be shown that the solution of (4.19) is also given by (4.18) [74]. While it is not possible to include inequality constraints into Newton's method because the optimality conditions associated with inequality constraints are non-smooth, they can be incorporated into (4.19) in the same form as the equality constraints. A complete description of the SQP method is provided in Appendix D.1.

Several techniques can be applied to find the gradients $\nabla J$, $\nabla\mathbf{g}_{\text{eq}}$, and $\nabla\mathbf{g}_{\text{in}}$, which include forward finite differences, forward sensitivity propagation, and the adjoint method (see [75] for a review of each one of them). The simplest method, forward finite differences, involves perturbing each element of $\mathbf{w}$ by a small amount and then computing each element of the gradient according to

$$\nabla J\big|_j = \frac{J(\mathbf{w} + \epsilon e_j) - J(\mathbf{w})}{\epsilon}. \tag{4.20}$$

If $n$ is the dimension of $\mathbf{w}$ then calculating gradients by this approach requires $n + 1$ evaluations of the cost function and constraints, which therefore requires $n+1$ evaluations of the function (4.15) at time $t = t_F$ or equivalently simulating the

system (4.12) from $t_0$ to $t_F$. If $n$ is large or the dynamics are difficult to integrate, for example stiff dynamics requiring implicit integration schemes, the finite difference calculation can be a lengthy process.

Forward sensitivity propagation involves propagating the sensitivity of the state along the trajectory to changes in each of the optimization variables. In order to carry out this method, first we need to decide on a discrete integration scheme to approximate the evolution of the system modeled by (4.12). Because the underlying dynamical model (3.1) (plasma current diffusion) is approximately a linear diffusion equation, an appropriate integration method is the backward (implicit) Euler method,

$$\mathbf{x}_{k+1} = \mathbf{x}_k + dt\boldsymbol{f}(\mathbf{x}_{k+1}, \mathbf{u}_{k+1}). \tag{4.21}$$

We require an implicit integration scheme as in (4.21) to handle the stiffness associated with the current diffusion dynamics (3.1), which arises due to the steep changes in the coefficient profiles around the boundary. The sensitivity of the state with respect to the optimization variables, $\mathbf{w}$, can be computed during the "forward simulation" of the dynamics. Taking partial derivatives of (4.21) with respect to $\mathbf{w}$, we obtain

$$\frac{\partial \mathbf{x}_{k+1}}{\partial \mathbf{w}} = \frac{\partial \mathbf{x}_k}{\partial \mathbf{w}} + dt\left(\left.\frac{\partial \boldsymbol{f}}{\partial \mathbf{x}}\right|_{\substack{\mathbf{x}_{k+1}\\ \mathbf{u}_{k+1}}} \frac{\partial \mathbf{x}_{k+1}}{\partial \mathbf{w}} + \left.\frac{\partial \boldsymbol{f}}{\partial \mathbf{u}}\right|_{\substack{\mathbf{x}_{k+1}\\ \mathbf{u}_{k+1}}} \frac{\partial \mathbf{u}_{k+1}}{\partial \mathbf{w}}\right). \tag{4.22}$$

Since the optimization variables include only the control values we have $\partial \mathbf{x}_0/\partial \mathbf{w} = 0$, $\partial \mathbf{u}_0/\partial \mathbf{w} = [\mathbf{I}, \mathbf{0}, \ldots, \mathbf{0}]$, $\partial \mathbf{u}_1/\partial \mathbf{w} = [\mathbf{0}, \mathbf{I}, \ldots, \mathbf{0}]$, etc. From (4.15), it can be seen that $\partial \mathbf{F}(\mathbf{w}, \mathbf{x}_0, t_k)/\partial \mathbf{w} = \partial \mathbf{x}_{k+1}/\partial \mathbf{w}$, which can be used in the chain rule to obtain gradients of both the cost function and each of the constraints. For example,

$$\nabla J = \frac{\partial J}{\partial \mathbf{w}} = \frac{\partial J}{\partial \mathbf{F}(\mathbf{w}, \mathbf{x}_0, t_F)} \frac{\partial \mathbf{F}(\mathbf{w}, \mathbf{x}_0, t_F)}{\partial \mathbf{w}} = \frac{\partial J}{\partial \mathbf{x}_{t_F}} \frac{\partial \mathbf{x}_{t_F}}{\partial \mathbf{w}}, \tag{4.23}$$

where $\mathbf{x}_{t_F}$ is found by propagating (4.22) forward. A complete description of the forward sensitivity calculation for general Runge-Kutta integration schemes is included in Appendix C.2.

The adjoint method allows for analytic calculations of the objective function, however, it cannot be applied directly to problems involving state constraints.

| Actuator | Rate Limit | Lower Limit | Upper Limit |
|---|---|---|---|
| $I_\mathrm{p}$ (Total Plasma Current) | $\pm 2$ MA/s | 0.3 MA | 1.5 MA |
| $\bar{n}_\mathrm{e}$ (Line Averaged Electron Density) | none | $1{\cdot}10^{19}/\mathrm{m}^3$ | $5{\cdot}10^{19}/\mathrm{m}^3$ |
| $P_{\mathrm{NBI},\xi}$ (NBI source) | none | 0 | 1.6 - 2.2 MW |
| $P_\mathrm{EC}$ (Total ECCD) | none | 0 | 3.0 MW |

**Table 4.1:** DIII-D actuator bounds and rate limits.

Rather one must use penalty methods to incorporate the state constraints; the constraints are included as additional terms to the cost function, and add a large penalty (cost) commensurate with the amount of constraint violation. This approach is not quite as accurate and it can be complicated to appropriately choose the penalty parameters. Ideally, the cost associated with the constraints must be high compared to cost of the primary objective, but making it too high can lead to numerical conditioning issues. Throughout this work we make use of the forward sensitivity propagation method to calculate gradients.

## 4.4 Cost Function and Constraints

The cost function $J$ consists in this case of a weighted sum of objectives associated with reaching the target $q$ profile, the target $\beta_N$ value, and a measure of stationarity,

$$\begin{aligned} J = &\left(\mathbf{q}(t_\mathrm{F}) - \mathbf{q}^\mathrm{t}\right)^T \mathbf{W}_q \left(\mathbf{q}(t_\mathrm{F}) - \mathbf{q}^\mathrm{t}\right) \\ &+ W_{\beta_N}(\beta_N(t_\mathrm{F}) - \beta_N^\mathrm{t})^2 + \mathbf{g}_\mathrm{ss}(t_\mathrm{F})^T \mathbf{W}_\mathrm{ss} \mathbf{g}_\mathrm{ss}(t_\mathrm{F}), \end{aligned} \tag{4.24}$$

where $\boldsymbol{q}^t$ represents the target $q$ profile, $\beta_N^\mathrm{t}$ represents the target $\beta_N$ value, and the terms $\mathbf{W}_q$, $W_{\beta_N}$ and $\mathbf{W}_\mathrm{ss}$ are cost weights. The term $\mathbf{g}_\mathrm{ss}$ represents the spatial derivative of the plasma loop voltage profile. The plasma stationarity is reached when the loop voltage profile is flat or equivalently when the spatial derivative is zero, i.e. $\mathbf{g}_\mathrm{ss} = 0$, (see Section 3.2.1).

The constraints include bounds and rate limits on the actuators as listed in Table 4.1, a limit on $q$,

$$q > 1, \tag{4.25}$$

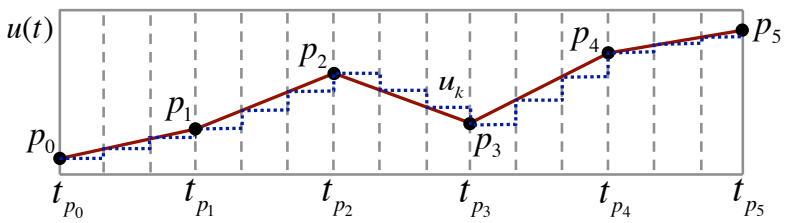


**Figure 4.2:** Feedforward control is parameterized by a piece-wise linear function described by $\mathbf{p} = [\mathbf{p}_1, \mathbf{p}_2, \ldots, \mathbf{p}_F]$.

to avoid the onset of sawtooth oscillations, a limit on density associated with the Greenwald density limit,

$$\bar{n}_e[10^{20}\mathrm{m}^{-3}] \leq \frac{I_\mathrm{p}[\mathrm{MA}]}{\pi a^2}, \tag{4.26}$$

and an upper bound on $\beta_N$ to avoid the onset of neoclassical tearing modes,

$$\beta_N \leq \beta_N^{\max}. \tag{4.27}$$

Each of the constraints (4.25)-(4.27) and cost function (4.24) can be written as a function of the state $\mathbf{x}$ and control $\mathbf{u}$, therefore the gradients can be obtained with the forward sensitivity propagation method described above.

### 4.4.1 Parameterizing the Input Function

The optimization problem as described above involves a set of optimization variables which includes the control variables at each time step $k$. This amounts to substantially large number of optimization variables making the problem difficult to solve. To reduce the complexity, sacrificing optimality to some extent, we choose to parameterize the control sequence $\mathbf{w}$ as a piecewise linear function, as illustrated in Figure 4.2. Thus the optimization variables $\mathbf{w}$ are reduced to the set $\mathbf{p} = [\mathbf{p}_0, \mathbf{p}_1, \ldots, \mathbf{p}_5]$, which has dimension 6 $\times$ (# of actuators considered for optimization).

## 4.5 Examples

### L-mode Discharges

First, we consider control during L-mode discharges with the goal of reaching a specified target at a specified time. Three different target $q$ profiles are considered, each with monotonically increasing $q$ profiles shown in Figure 4.3. The control is optimized over the period $t_{\text{opt}} \in [t_0, t_F] = [0.4, t_F]$ s, where $t_F$, the target time, is taken as a design parameter.

The optimization setup includes the following design choices. The control update times ($t_{P_i}$ of Figure 4.2) are selected as $t_{P_i} = [0.4, 0.5, 0.75, 1.0, \ldots, t_F]$. The initial control value at time $t_{P_0} = 0.4$ is fixed in accordance with the required powers for start-up conditions. The to be optimized inputs include the total plasma current, the off-axis co-current NBI (150L and 150R), and the on-axis co-current NBI (330L and 330R). The 30L and 30R NBI are dedicated to diagnostics, and the counter-current NBI are not used in order to avoid triggering locked-modes due to low torque, and therefore low rotation, plasmas. As the particle confinement in the plasma is strongly dependent on the value of the total plasma current, the line average electron density trajectory is chosen to be proportional to the total plasma current trajectory following the expression

$$n_e(t) \ \ [10^{19}\text{m}^{-3}] = 2.5 I_{\text{p}}(t) \ \ [\text{MA}]. \tag{4.28}$$

Finally, to avoid L-H transitions, a total auxiliary power limit was imposed as an optimization constraint. From experimental tests, the H-mode transition power was observed to approximately scale with the electron density according to

$$P_{\text{LH}} = 2\bar{n}_e^{3/4}. \tag{4.29}$$

Therefore the total auxiliary power is constrained according to

$$\sum_{\xi=1}^{n_{\text{NBI}}} P_{\text{NBI},\xi} + P_{\text{EC}} \leq P_{\text{LH}} \tag{4.30}$$

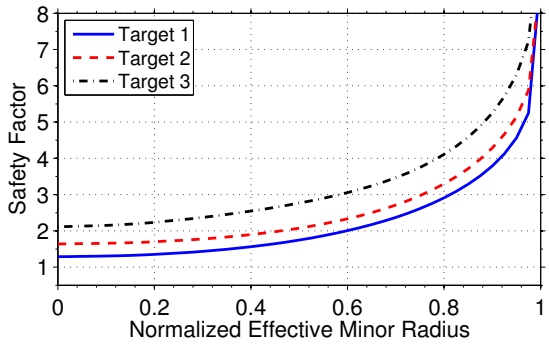


**Figure 4.3:** Target $q$ profiles for L-mode discharges. All targets are monotonically increasing with various values of $q_{\min}$ and $q_{95}$ to be obtained at target time $t_F$. **Target 1**: $q_{\min} = 1.3$, $q_{95} = 4.4$, **Target 2**: $q_{\min} = 1.65$, $q_{95} = 5.0$, and $t_F = 1.3$ s, and **Target 3**: $q_{\min} = 2.1$, $q_{95} = 6.2$, and $t_F = 1.5$ s.

The optimized control sequences for Target 1, 2, and 3, are displayed in Figures 4.4, 4.5, and 4.6, respectively. Qualitatively similar results can be noted in each case. The auxiliary heating scheme is characterized, initially, by little injected power (other than the power injected by the 30L-NBI required for diagnostics). Towards the end of the ramp-up phase, the off-axis NBI power (150L and 150R beamlines) is rapidly injected as required to setup the plasma state with off-axis current drive. This is required to achieve the desired $q$ value at the plasma center. Additional, NBI power is injected closer to the target time to raise the plasma temperature, which lowers the plasma resistivity, and in turn, slows the diffusion of current in an attempt to freeze the obtained $q$ profile as best as possible.

### H-mode Discharges

The optimization setup for H-modes discharges is very similar to that of L-mode discharges. The two primary changes include updating the model of the current profile dynamics (3.1) by tailoring the model parameters to H-mode discharges, and swapping the upper power limit (4.29) for a lower power limit to avoid back-transitions to L-mode.

The optimization is carried out over the time interval $t_{\text{opt}} = t \in [t_0, t_f] = [0.5, 3.0]$ s, and the control updates are parameterized by a first order hold as in Figure 4.2

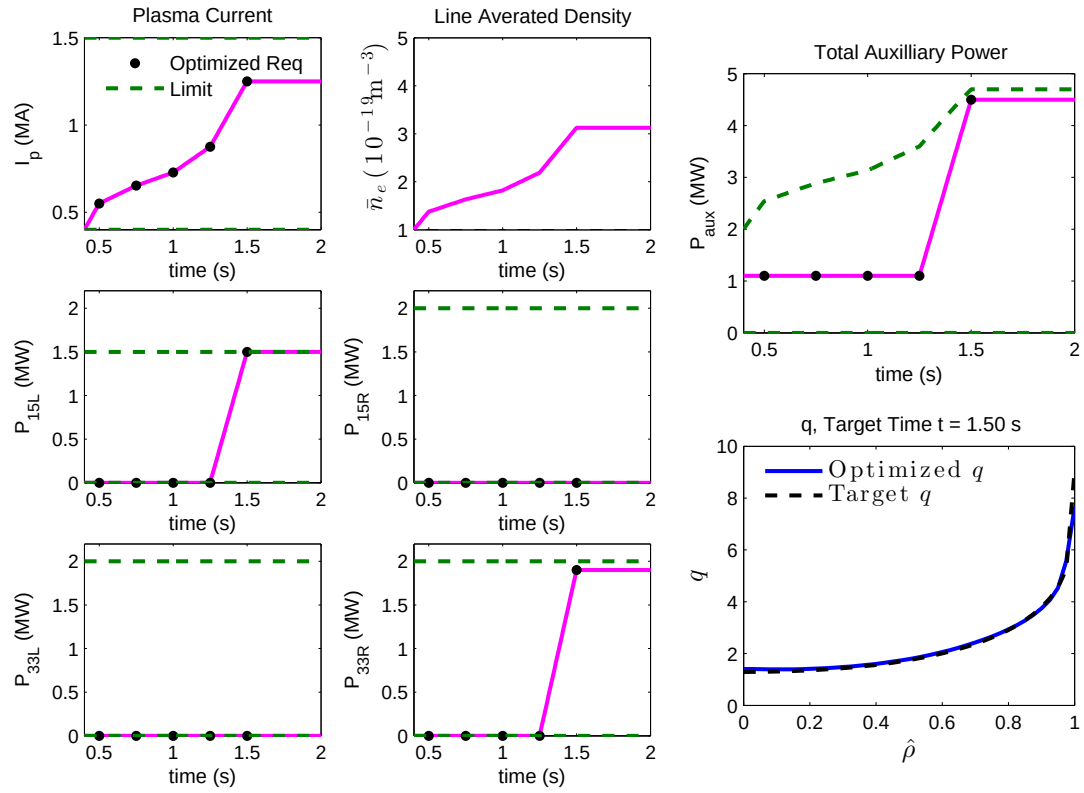


**Figure 4.4:** Optimized control sequence for Target 1 of Figure 4.3, where $t_F = 1.5$ s. The black dots represent the optimized control parameterization. The optimized 150R and 330L neutral beam injection powers are 0 MW (not shown). The total auxiliary power limit (green dash) of the upper right plot is associated with the L-H transition (4.29).

with time points $t_{P_i} = [0.5, 1.0, ..., 3.0]$ s. For simplicity the gyrotorns (ECCD sources) are controlled as group, therefore the total gyrotron power, $P_{\mathrm{EC}}$, is evenly distributed amongst the individual gyrotron launchers. Also, the ECCD power is restricted to be OFF during the time period $t \in [0.5, 2.0]$, since the DIII-D have a limited amount of total energy they can deliver during a plasma discharge. For diagnostics purposes, the 30L and 30R NBI are modulated to deliver a constant 1.1 MW to the plasma.

The target $q$ profile and target $\beta_N$ at the target time of 3.0 s are chosen from an experimental discharge, DIII-D shot 147634. Results of the optimization are shown

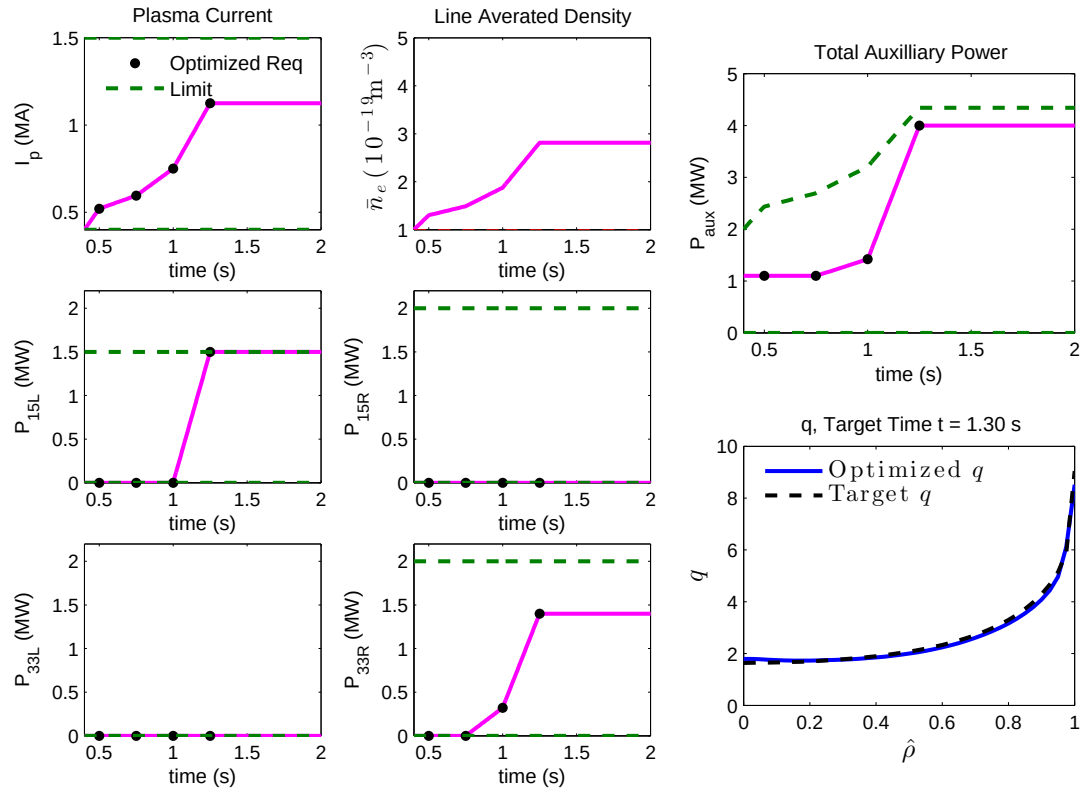


**Figure 4.5:** Optimized control sequence for Target 2 of Figure 4.3, where $t_F = 1.30$ s. The black dots represent the optimized control parameterization. The optimized 150R and 330L neutral beam injection powers are 0 MW (not shown). The L-H transition limit (4.29) is shown in the plot of total auxiliary power.

in Figure 4.7. To reach the target $\beta_N$ value of 3.5, almost all of the auxiliary power available is required. A preference to off-axis (150L and 150R) power over on-axis (330L and 330R) is found to help obtain the target $q$ profile in the center. Again, similar to the results of the L-mode discharges, the auxiliary power is ramped late, not only to obtain the target $\beta_N$, but also to help freeze in the target $q$ profile[2].

[2]Tests of the feedforward control results in real tokamak experiments will be presented in Chapter 5

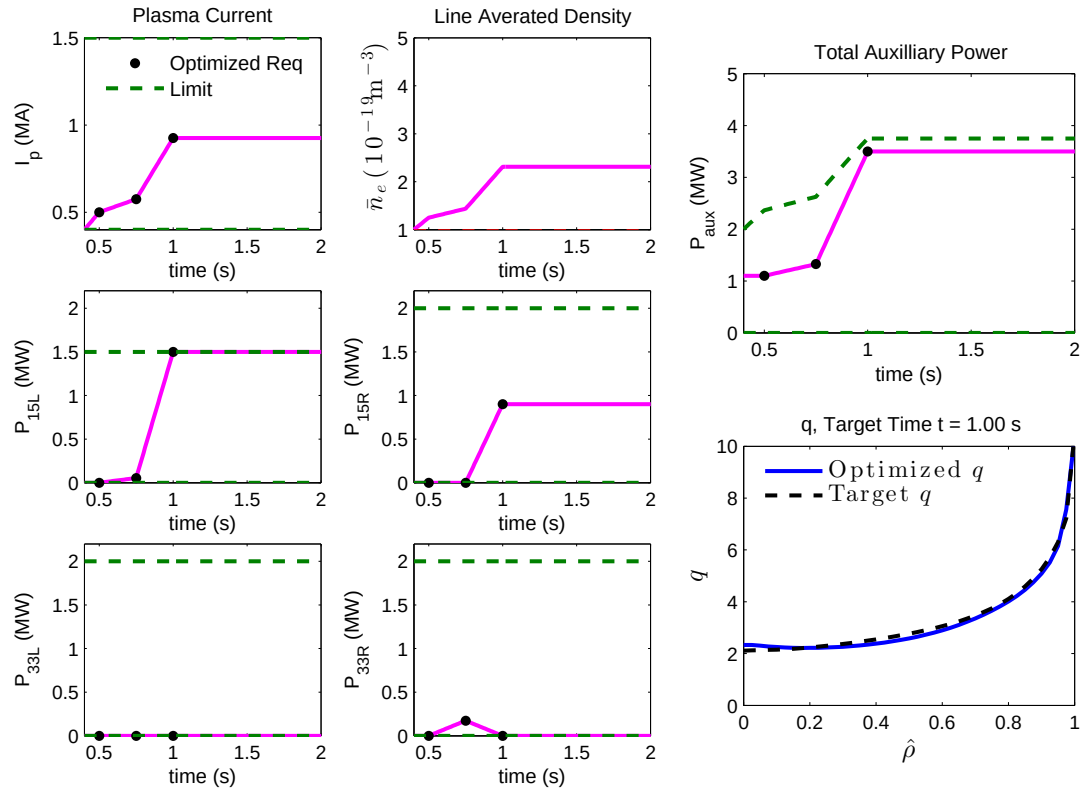


**Figure 4.6:** Optimized control sequence for Target 3 of Figure 4.3, where $t_F = 1.0$ s. The black dots represent the optimized control parameterization. The 30L neutral beam injection power is at a constant 1.1 MW for diagnostic purposes and the optimized 330L neutral beam injection power is 0 MW (not shown). The L-H transition limit (4.29) is shown in the plot of total auxiliary power.

## 4.6 Conclusions

This chapter considered numerical optimization to synthesize feedforward control solutions for the available actuators, in order to steer the plasma through the tokamak operating space to reach a target $q$ profile and $\beta_N$ value. The optimization was carried out subject to constraints associated with actuator limits, plasma state, and operating scenario constraints for both L-mode and H-mode discharges.

While results showed that the desired targets could successfully be achieved in simulations, it is anticipated that a feedforward control approach alone will be

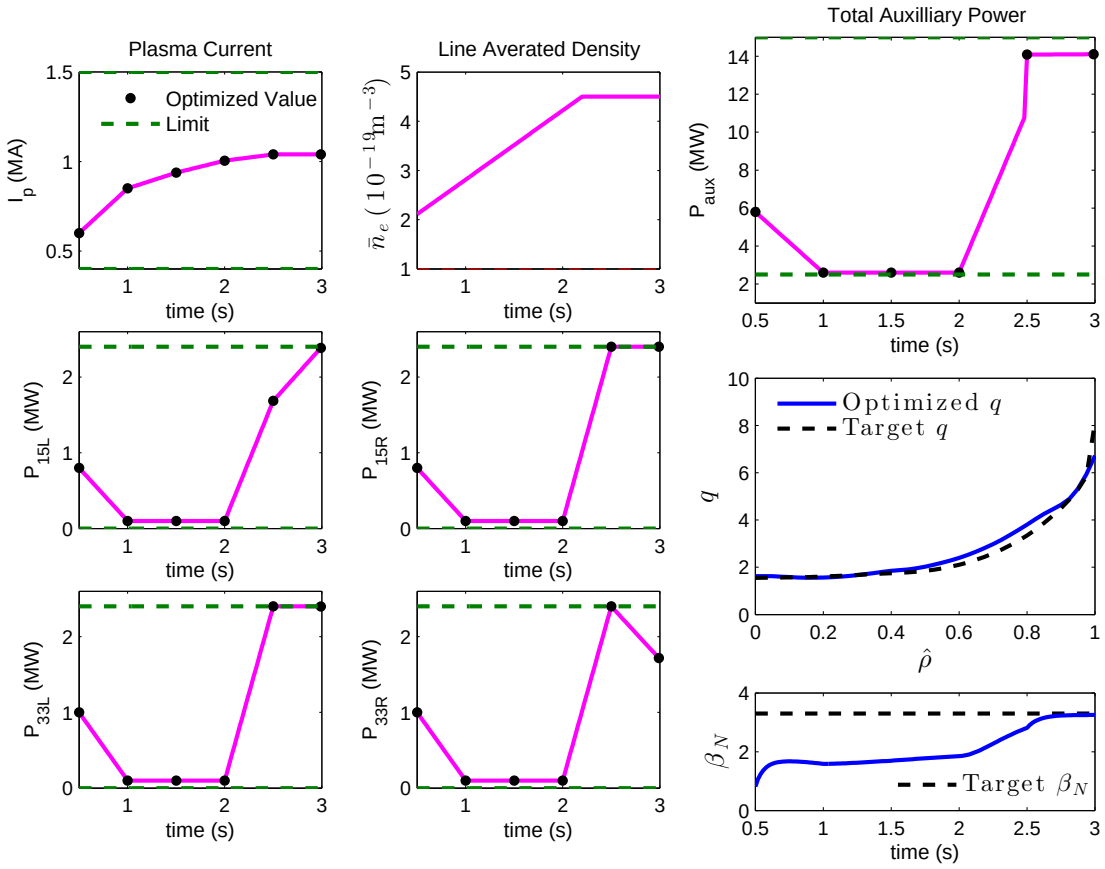


**Figure 4.7:** Optimized control sequence for an H-mode discharge. The time parameterization of the control sequence is $t_{P_i} = [0.5, 1.0, ..., 3.0]$. The density is obtained from a reference discharge (DIII-D shot 147634). The gyroton power (not shown) comes on full at 2.5 s.

insufficient to reliably reach the target due to mismatch between the model and real system. The next chapter will focus on combining the feedforward control with various feedback strategies.

# Chapter 5

# Feedback Control Design for the Current Profile Evolution via Linear Quadratic Integral

The following two chapters consider feedback control design for the current profile evolution. The first focuses on state feedback via a linear quadratic integral approach, and the second focuses on real-time model predictive control. In both cases, the feedback controller is designed so as to be combined with the feedforward control approach of the previous chapter. The state feedback control approach is easier to implement, since the primary control function is computed by a single matrix multiplication. The model predictive control approach allows for improved control performance, but involves substantial online computation. However, with efficient optimization techniques, the computation involved is shown to be fast enough to allow real-time applicability of the control approach.

## 5.1 Introduction

The first-principles-based model of the current profile evolution described in Chapter 3 was used in Chapter 4 to develop a feedforward (open-loop) control strategy

to reach a target current profile at a specified time during the discharge. If the initial conditions assumed in the feedforward control development could be guaranteed and the model fully and accurately described all of the underlying dynamics, we could simply apply the feedforward control strategy blindly and expect to see reliable achievement of the target current profile. However, reproducing the initial conditions assumed for the feedforward control problem is often difficult during real tokamak experiments. Residue in the tokamak walls, which can cause unexpected impurity concentrations, or actuator faults can often lead to different conditions during the plasma formation phase. Despite the difficulty in reproducing the desired initial conditions, imperfections in the system model due to un-modeled dynamics and unavoidable errors in the estimation of the various model parameters make it necessary to complement the feedforward control approach with feedback to correct for disturbances from the target trajectory.

In this chapter we explore several options for feedback control of the current profile evolution with each step increasing the complexity of the design approach. Throughout this chapter we consider only optimal control approaches based on linear quadratic formulations, i.e. linearized dynamics and quadratic cost functions. We begin with a control formulation that can be solved in closed form – the standard linear quadratic regulator (LQR) formulation. This approach produces an optimal feedback policy, which minimizes a quadratic penalty of the tracking error subject only to constraints associated with the system dynamics. In the next chapter, the control approach will be extended and refined with a numerical optimal control approach, which incorporates hard constraints on control actions to maintain plasma stability (model predictive control).

Each of the feedback control approaches developed in this chapter and the next were tested experimentally in the DIII-D tokamak. In some cases the experiments involved substantial development of newly coded control algorithms introduced to the DIII-D plasma control system (PCS)[1]. Some tests were performed in L-mode (low confinement) and some in H-mode (high confinement) discharges (see Section 1.4).

[1]The plasma control system (PCS) developed and maintained by General Atomics, San Diego, California is used to control the plasma during day-to-day operation of many tokamaks.

We begin with control of H-mode discharges with the objective of regulating the profile only during the flattop phase. The main purpose of these initial control tests is aimed at getting the profile control components of the PCS functioning properly and show some promise towards achieving control of the current profile experimentally.

While initial tests did show some success, the real intention of this work is to design profile controllers for the aid of tokamak experiments. The objective is to improve shot-to-shot reproducibility of the tokamak operating conditions in order to aid other plasma physics studies. Therefore the work progressed onto the goal of improving reproducibility of a target current profile at a specified time during the discharge. Starting first with more easy to control L-mode discharges, then extending the combined feedforward and feedback control approach to H-mode discharges. For each control test, we compare the results obtained with the combined feedback+feedforward approach to that of feedforward control alone. In general, we find that the addition of feedback control on top of the feedforward control is necessary for good profile tracking.

This chapter is organized as follows. In Section 5.2, we consider linear quadratic integral (LQI) feedback control of the plasma current profile through the flattop phase in H-mode discharges. In Section 5.3, the LQI control approach is considered again with the goal of obtaining a particular target at a specified time during both L-mode and H-mode discharges. Finally, conclusions are given in Section 5.4.

## 5.2 LQI Feedback for Current Profile Control

In this section, a multi-input-multi-output (MIMO) feedback controller based on the first-principles-driven model (4.11) is proposed for the regulation of the evolution of the poloidal magnetic flux profile and thus the current profile at DIII-D. For control design, we consider the poloidal stream function relative to the boundary value, i.e. $\bar{\psi} = \psi - \psi_{\mathrm{b}}$.

### 5.2.1 Model Order Reduction and Linearization

To facilitate control design, the model governing the evolution of $\bar{\psi}$ is reduced to a finite set of ordinary differential equations (ODEs) by using finite difference approximations to the spatial derivatives as mentioned in the previous section. Consider the reduced-order model (4.11), where the model state is $\bar{\boldsymbol{\psi}} = [\bar{\psi}_2, \bar{\psi}_3, ..., \bar{\psi}_{l-1}]^T$ and the model input includes the nonlinear input functions of (4.4), $\mathbf{u} = [u_\eta,\ u_{\mathrm{BS}},\ u_{\mathrm{CO}}^{\mathrm{on}},\ u_{\mathrm{CO}}^{\mathrm{off}},\ u_{\mathrm{EC}},\ I_{\mathrm{p}}]^T$. The NBI have been grouped together as on-axis co-current NBI (330L and 330R) and off-axis co-current NBI (150L and 150R) to obtain the nonlinear input functions

$$u_{\mathrm{CO}}^{\mathrm{on}} = \left(\frac{1}{I_{\mathrm{p}}(t)\sqrt{P_{\mathrm{tot}}(t)}}\right)^{1/2} \left(P_{\mathrm{NBI}}^{330L} + P_{\mathrm{NBI}}^{330R}\right), \tag{5.1}$$

$$u_{\mathrm{CO}}^{\mathrm{off}} = \left(\frac{1}{I_{\mathrm{p}}(t)\sqrt{P_{\mathrm{tot}}(t)}}\right)^{1/2} \left(P_{\mathrm{NBI}}^{150L} + P_{\mathrm{NBI}}^{150R}\right), \tag{5.2}$$

and the remaining input functions are given by (4.4). Let $\bar{\boldsymbol{\psi}}_{\mathrm{FF}}$ and $\mathbf{u}_{\mathrm{FF}}$ represent the feedforward trajectories of the states and inputs that satisfy

$$\dot{\bar{\boldsymbol{\psi}}}_{\mathrm{FF}} = \boldsymbol{f}(\bar{\boldsymbol{\psi}}_{\mathrm{FF}}, \mathbf{u}_{\mathrm{FF}}), \tag{5.3}$$

and let the variables $\mathbf{x} = \bar{\boldsymbol{\psi}} - \bar{\boldsymbol{\psi}}_{\mathrm{FF}}$ and $\mathbf{u}_{\mathrm{FB}} = \mathbf{u} - \mathbf{u}_{\mathrm{FF}}$ represent perturbations around the feedforward trajectory. Inserting the perturbation variables into a Taylor series approximation of (4.11) and ignoring second and higher order terms results in

$$\dot{\bar{\boldsymbol{\psi}}} = \boldsymbol{f}(\bar{\boldsymbol{\psi}}_{\mathrm{FF}}, \mathbf{u}_{\mathrm{FF}}) + \frac{\partial \boldsymbol{f}}{\partial \bar{\boldsymbol{\psi}}}(\bar{\boldsymbol{\psi}}_{\mathrm{FF}}, \mathbf{u}_{\mathrm{FF}})\mathbf{x} + \frac{\partial \boldsymbol{f}}{\partial \mathbf{u}}(\bar{\boldsymbol{\psi}}_{\mathrm{FF}}, \mathbf{u}_{\mathrm{FF}})\mathbf{u}_{\mathrm{FB}}, \tag{5.4}$$

from which we obtain the linear dynamics around the feedforward trajectory

$$\dot{\mathbf{x}} = \mathbf{A}_{\mathrm{FPD}}(t)\mathbf{x}(t) + \mathbf{B}_{\mathrm{FPD}}(t)\mathbf{u}_{\mathrm{FB}}(t), \tag{5.5}$$

where

$$\mathbf{A}_{\mathrm{FPD}} = \frac{\partial \boldsymbol{f}}{\partial \bar{\boldsymbol{\psi}}}(\bar{\boldsymbol{\psi}}_{\mathrm{FF}}, \mathbf{u}_{\mathrm{FF}}), \quad \mathbf{B}_{\mathrm{FPD}} = \frac{\partial \boldsymbol{f}}{\partial \mathbf{u}}(\bar{\boldsymbol{\psi}}_{\mathrm{FF}}, \mathbf{u}_{\mathrm{FF}}). \tag{5.6}$$

While it is possible to design an optimal state feedback controller for the time varying linear model (5.5), we choose to further approximate the model by linearizing around

a constant feedforward state and input, which is a reasonable approximation during the flattop current phase of the discharge. We can further simply the system to a time-invariant system, assuming that the profile is controlled without transitioning back to L-mode,

$$\dot{\mathbf{x}} = \mathbf{A}\mathbf{x} + \mathbf{B}\mathbf{u}_{\rm FB}, \tag{5.7}$$

where $\mathbf{A}$ and $\mathbf{B}$ are taken as $\mathbf{A}_{\rm FPD}(t_{\rm flattop})$ and $\mathbf{B}_{\rm FPD}(t_{\rm flattop})$ and $t_{\rm flattop}$ at the beginning of the current flattop of the discharge.

### 5.2.2 Singular Value Decomposition

For a requested target state, $\mathbf{x}_{\rm targ}$, let $\mathbf{x}_\infty^{ss}$ represent the closest stationary state[2] achievable according to the model. This can be determined from the pseudo-inverse, $\mathbf{K}_{\rm sg}^\dagger$, of the model static gain matrix $\mathbf{K}_{\rm sg} = -\mathbf{A}^{-1}\mathbf{B}$. The symbol † represents the Moore-Penrose pseudoinverse determined by singular value decomposition (SVD), i.e.

$$\mathbf{K}_{\rm sg} = \mathbf{W}\mathbf{\Sigma}\mathbf{V}^T, \quad \mathbf{K}_{\rm sg}^\dagger = \mathbf{V}\mathbf{\Sigma}^\dagger\mathbf{W}^T, \tag{5.8}$$

where $\mathbf{W}$ and $\mathbf{V}$ are unitary matrices, i.e. $\mathbf{W}\mathbf{W}^T = \mathbf{W}^T\mathbf{W} = \mathbf{I}$ and $\mathbf{V}^T\mathbf{V} = \mathbf{V}\mathbf{V}^T = \mathbf{I}$. The pseudoinverse of the diagonal matrix $\mathbf{\Sigma}$ is obtained by taking its transpose, $\mathbf{\Sigma}^T$, and then replacing each nonzero element with its reciprocal.

The input associated with the desired target is determined from the pseudo-inverse of the static gain matrix

$$\mathbf{u}_{\rm FB,\infty}^{ss} = \mathbf{K}_{\rm sg}^\dagger\mathbf{x}_{\rm targ} \tag{5.9}$$

which is used to determine the closest achievable stationary state given by

$$\mathbf{x}_\infty^{ss} = \mathbf{K}_{\rm sg}\mathbf{u}_{\rm FB,\infty}^{ss} = \mathbf{K}_{\rm sg}\mathbf{K}_{\rm sg}^\dagger\mathbf{x}_{\rm targ}. \tag{5.10}$$

[2]The term stationary state is used to refer to an equilibrium state in which the plasma parameters are no longer evolving, but some of the plasma current may be driven inductively. In the plasma physics community the term "steady state" is reserved to describe a plasma state that can be sustained without the need for an inductive current drive source.

Because several of the actuators have similar effects on the profile, the matrix $\mathbf{K}_{\rm sg} = \mathbf{W}\mathbf{\Sigma}\mathbf{V}^T$ is ill-conditioned, i.e. the ratio of the largest singular value to the smallest one is much larger than one. Therefore small deviations in the profile associated with the directions of the smaller singular values can result in unreasonably large control requests. Thus, we use a truncated (Tr) singular value expansion of the static gain matrix given by,

$$\mathbf{K}_{\rm sg,Tr} = \mathbf{W}_{\rm Tr}\mathbf{\Sigma}_{\rm Tr}\mathbf{V}_{\rm Tr}^T, \tag{5.11}$$

where the matrices $\mathbf{W}_{\rm Tr}$, $\mathbf{\Sigma}_{\rm Tr}$, and $\mathbf{V}_{\rm Tr}$ are the components of the SVD associated with the $n_{\rm SV}$ largest singular values,

$$\mathbf{W} = \begin{bmatrix}\mathbf{W}_{\rm Tr} & \mathbf{W}_{\rm n}\end{bmatrix},\ \mathbf{\Sigma} = \begin{bmatrix}\mathbf{\Sigma}_{\rm Tr} & 0\\ 0 & \mathbf{\Sigma}_{\rm n}\end{bmatrix},\ \mathbf{V} = \begin{bmatrix}\mathbf{V}_{\rm Tr} & \mathbf{V}_{\rm n}\end{bmatrix}, \tag{5.12}$$

and $\mathbf{W}_n$, $\mathbf{\Sigma}_n$, and $\mathbf{V}_n$ are the components associated with the smaller, neglected singular values. Therefore,

$$\mathbf{u}_{\rm FB,\infty}^{ss} \cong \mathbf{u}_{\rm FB,\infty} = \mathbf{K}_{\rm sg,Tr}^{\dagger}\mathbf{x}_{\rm targ}, \quad \mathbf{x}_{\infty}^{ss} \cong \mathbf{x}_{\infty} = \mathbf{K}_{\rm sg,Tr}\mathbf{K}_{\rm sg,Tr}^{\dagger}\mathbf{x}_{\rm targ}. \tag{5.13}$$

We use the theory of linear quadratic optimal control to obtain a control law which regulates the system to the closest achievable stationary state while minimizing the cost function

$$J = \int_0^{\infty} \left[\bar{\mathbf{x}}^T(t)\ \boldsymbol{\zeta}^T(t)\right] \mathbf{Q} \begin{bmatrix}\bar{\mathbf{x}}(t)\\ \boldsymbol{\zeta}(t)\end{bmatrix} + \bar{\mathbf{u}}^T(t)\mathbf{R}\bar{\mathbf{u}}(t)dt, \tag{5.14}$$

where $\bar{\mathbf{x}} = \mathbf{x} - \mathbf{x}_{\infty}$, $\bar{\mathbf{u}} = \mathbf{u}_{\rm FB} - \mathbf{u}_{\rm FB,\infty}$, $\mathbf{Q}$ positive semidefinite, $\mathbf{R}$ positive definite, and $\boldsymbol{\zeta}$ represents the integral states introduced for integral control. The added integral states are expressed as

$$\boldsymbol{\zeta} = \mathbf{K}_{\zeta}\int_0^t \bar{\mathbf{x}}(\tau)d\tau, \tag{5.15}$$

where $\mathbf{K}_{\zeta}$ is a design matrix.

**Choice of Matrix $K_\zeta$**

We can note that with the choice

$$\mathbf{K}_\zeta = \mathbf{W}_{\rm Tr}^T \tag{5.16}$$

we have $\mathbf{K}_\zeta \mathbf{K}_{\rm sg,Tr} \mathbf{K}_{\rm sg,Tr}^\dagger = \mathbf{K}_\zeta$, since

$$\left[\mathbf{W}_{\rm Tr}^T\right] \cdot \left[\mathbf{W}_{\rm Tr} \mathbf{\Sigma}_{\rm Tr} \mathbf{V}_{\rm Tr}^T\right] \cdot \left[\mathbf{V}_{\rm Tr} \mathbf{\Sigma}_{\rm Tr}^{-1} \mathbf{W}_{\rm Tr}^T\right] = \mathbf{W}_{\rm Tr}^T = \mathbf{K}_\zeta. \tag{5.17}$$

This ensures

$$\mathbf{K}_\zeta \mathbf{x}_{\rm targ} = \mathbf{K}_\zeta \mathbf{x}_\infty, \tag{5.18}$$

since

$$\mathbf{x}_\infty = \mathbf{K}_{\rm sg,Tr} \mathbf{u}_{\rm FB,\infty} = \mathbf{K}_{\rm sg,Tr} \mathbf{K}_{\rm sg,Tr}^\dagger \mathbf{x}_{\rm targ}. \tag{5.19}$$

Here, we have made use of the fact that $\mathbf{W}_{\rm Tr}^T \mathbf{W}_{\rm Tr} = \mathbf{I}$, and $\mathbf{V}_{\rm Tr}^T \mathbf{V}_{\rm Tr} = \mathbf{I}$, but $\mathbf{W}_{\rm Tr} \mathbf{W}_{\rm Tr}^T \neq \mathbf{I}$.

### 5.2.3 Proportional Plus Integral Control

Written in terms of the requested target ($\bar{\mathbf{x}}(t) = \mathbf{x}(t) - \mathbf{K}_{\rm sg,Tr} \mathbf{K}_{\rm sg,Tr}^\dagger \mathbf{x}_{\rm targ}(t)$), the control law that minimizes (5.14) reduces to a proportional plus integral controller of the form

$$\begin{aligned} \mathbf{u}_{\rm FB}(t) = \mathbf{u}_{\rm FB,\infty} &- \mathbf{K}_{\rm p} \left[\mathbf{x}(t) - \mathbf{K}_{\rm sg,Tr} \mathbf{K}_{\rm sg,Tr}^\dagger \mathbf{x}_{\rm targ}(t)\right] \\ &- \mathbf{K}_{\rm i} \mathbf{K}_\zeta \int_0^t \left[\mathbf{x}(\tau) - \mathbf{K}_{\rm sg,Tr} \mathbf{K}_{\rm sg,Tr}^\dagger \mathbf{x}_{\rm targ}(\tau)\right] d\tau, \end{aligned} \tag{5.20}$$

where the proportional gain, $\mathbf{K}_{\rm p}$, and integral gain, $\mathbf{K}_{\rm i}$, are given by

$$\begin{bmatrix} \mathbf{K}_{\rm p} & \mathbf{K}_{\rm i} \end{bmatrix} = \mathbf{R}^{-1} \hat{\mathbf{B}} \mathbf{S},$$

where $\mathbf{S} = \mathbf{S}^T$ is the unique positive semi-definite solution to the algebraic Ricatti equation,

$$\hat{\mathbf{A}}^T \mathbf{S} + \mathbf{S} \hat{\mathbf{A}} - \mathbf{S} \hat{\mathbf{B}} \mathbf{R}^{-1} \hat{\mathbf{B}}^T \mathbf{S} + \mathbf{Q} = 0,$$

and the system ($\hat{\mathbf{A}}$, $\hat{\mathbf{B}}$) is constructed by augmenting the model (5.7) with the integrator states, i.e.

$$\begin{bmatrix} \dot{\bar{\mathbf{x}}} \\ \dot{\boldsymbol{\zeta}} \end{bmatrix} = \underbrace{\begin{bmatrix} \mathbf{A} & 0 \\ \mathbf{K}_\zeta & 0 \end{bmatrix}}_{\hat{\mathbf{A}}} \begin{bmatrix} \bar{\mathbf{x}} \\ \boldsymbol{\zeta} \end{bmatrix} + \underbrace{\begin{bmatrix} \mathbf{B} \\ 0 \end{bmatrix}}_{\hat{\mathbf{B}}} \bar{\mathbf{u}}. \tag{5.21}$$

The design parameters include $\mathbf{K}_\zeta = \mathbf{W}_{\mathrm{Tr}}^T$, $\mathbf{Q}$ and $\mathbf{R}$. The state weighting matrix, $\mathbf{Q}$, is chosen as

$$\mathbf{Q} = \begin{bmatrix} \hat{\mathbf{Q}} & 0 \\ 0 & \alpha_\zeta^2 \mathbf{I}_{n_{\mathrm{SV}}} \end{bmatrix}, \tag{5.22}$$

where $\alpha_\zeta$ is a constant that weights the integrator states relative to the model states, $\hat{\mathbf{Q}}$ is the weighting on the model states and $\mathbf{R}$ is chosen diagonal.

### Anti-windup Compensator

Given the limited power of the available actuators and the aggressive control goals, actuator saturation is expected to be unavoidable. During the time when one or more actuators are saturated, the error signals between the current plasma state and the target state may not decrease causing the integral term of the controller to wind-up the errors and make ever larger requests on the actuators. When the error signals finally do reverse it may take a long time for the control request to reset to a value below the saturation. An anti-windup scheme, as shown in Figure 5.1, is therefore incorporated into the control architecture to avoid the integral wind-up

$$\mathbf{u}_{\mathrm{aw}} = \mathbf{G}_{\mathrm{windup}} \int_0^t \mathbf{u}_{\mathrm{sat}}(\tau) - \mathbf{u}_{\mathrm{req}}(\tau) d\tau. \tag{5.23}$$

When the actuators are not saturated, the anti-windup compensator becomes inactive and the value of $\mathbf{u}_{\mathrm{aw}}$ remains constant.

### Control Signal Transformation

During experiments and simulations, the outputs of the profile controller $\mathbf{u} = [u_\eta,\ u_{\mathrm{BS}},\ u_{\mathrm{CO}}^{\mathrm{on}},\ u_{\mathrm{CO}}^{\mathrm{off}},\ u_{\mathrm{EC}},\ I_{\mathrm{p}}]^T$ need to be converted to the physical actuators, $\bar{n}_{\mathrm{e}}$, $P_{\mathrm{CO}}^{\mathrm{on}}$,

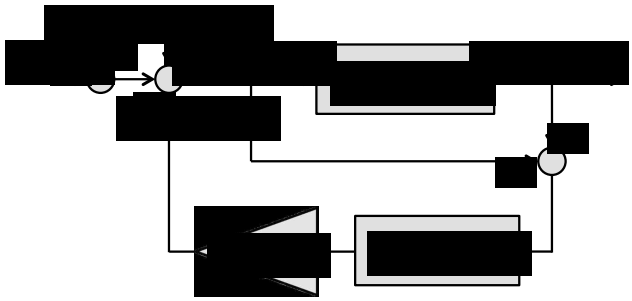

**Figure 5.1:** Anti-windup scheme: $u_{\rm FB}$ is the feedback control signal, $\mathbf{u}_{\rm FF}$ is the feedforward, $\mathbf{u}_{\rm d}$ is an added input disturbance, $\mathbf{u}_{\rm req}$ is the requested control, $\mathbf{u}_{\rm sat}$ is the saturated request, and $\mathbf{u}_{\rm aw}$ is the anti-windup compensation.

$P_{\rm CO}^{\rm off}$, $P_{\rm EC}$, and $I_{\rm p}$. Inverting the nonlinear transformations (4.4), we can obtain expressions for the physical actuators

$$\bar{n}_{\rm e} = \frac{u_{\rm BS}}{u_\eta^{1/3}}, \tag{5.24}$$

$$\hat{P}_{CO}^{\rm on} = \frac{u_{\rm CO}^{\rm on} u_{\rm BS}}{u_\eta^{2/3}}, \quad \hat{P}_{\rm CO}^{\rm on} = \frac{u_{\rm CO}^{\rm off} u_{\rm BS}}{u_\eta^{2/3}}, \tag{5.25}$$

$$\hat{P}_{\rm EC} = \frac{u_{\rm EC} u_{\rm BS}}{u_\eta^{2/3}}, \quad \text{and} \quad \hat{P}_{\rm tot} = \left( \frac{u_{\rm BS}}{u_\eta I_{\rm p}} \right)^2. \tag{5.26}$$

However, the inverse transformations (5.25)-(5.26) along with the constraint $\hat{P}_{\rm tot} = \hat{P}_{CO}^{\rm on} + \hat{P}_{\rm CO}^{\rm on} + \hat{P}_{\rm EC}$ form a set of over-constrained equations, all of which cannot be satisfied simultaneously. We desire to find the best approximation to the overdetermined system

$$\mathbf{X}_{\rm LS} \underbrace{\begin{bmatrix} P_{\rm CO}^{\rm on} & P_{\rm CO}^{\rm off} & P_{\rm EC} \end{bmatrix}^T}_{\mathbf{P}_{\rm req}} = \underbrace{\begin{bmatrix} \hat{P}_{CO}^{\rm on} & \hat{P}_{\rm CO}^{\rm on} & \hat{P}_{\rm EC} & \hat{P}_{\rm tot} \end{bmatrix}^T}_{\hat{\mathbf{P}}}, \tag{5.27}$$

where $P_{\rm req}$ represents the actuator power requests to be determined, $X_{\rm LS}$ is the $(4 \times 3)$ matrix

$$\mathbf{X}_{\rm LS} = \begin{bmatrix} 1 & & \\ & 1 & \\ & & 1 \\ 1 & 1 & 1 \end{bmatrix}, \tag{5.28}$$

We choose a weighted least squares approach to determine the actuator power requests,

$$\mathbf{P}_{\text{req}} = \arg\min_{\mathbf{P}_{\text{req}}} (\hat{\mathbf{P}} - \mathbf{X}_{\text{LS}}\mathbf{P}_{\text{req}})^T \mathbf{Q}_{\text{LS}} (\hat{\mathbf{P}} - \mathbf{X}_{\text{LS}}\mathbf{P}_{\text{req}}), \tag{5.29}$$

where $\mathbf{Q}_{\text{LS}}$ is a diagonal weighting matrix and the solution can be written as

$$\mathbf{P}_{\text{req}} = \left(\mathbf{Q}_{\text{LS}}\mathbf{X}_{\text{LS}}\right)^{\dagger} \mathbf{Q}_{\text{LS}}\hat{\mathbf{P}}. \tag{5.30}$$

In order to calculate the actuator saturation of Figure 5.1, the control signal $\mathbf{u}_{\text{req}}$ is first converted to the physical actuator requests by (5.29), the physical requests are saturated, and then the saturated values are used to calculate $\mathbf{u}_{\text{sat}}$ according to (4.4).

### Augmenting with energy control

During simulations it was discovered that the profile tracking performance could be improved by augmenting the controller with energy control. The energy control is incorporated by adding the energy equation (3.5) to the linearized model (5.7)

$$\begin{bmatrix} \dot{\mathbf{x}} \\ \dot{E} \end{bmatrix} = \begin{bmatrix} \mathbf{A} & 0 \\ 0 & -1/\tau_{\text{E}} \end{bmatrix} \begin{bmatrix} \mathbf{x} \\ E \end{bmatrix} + \begin{bmatrix} \mathbf{B} & 0 \\ 0 & 1 \end{bmatrix} \begin{bmatrix} \mathbf{u}_{\text{FB}} \\ P_{\text{tot,kin}} \end{bmatrix}, \tag{5.31}$$

and then proceeding with the control design as before in Section 5.2.3. Here we have introduced an additional control request on the total power, labeled $P_{\text{tot,kin}}$. Thus, we choose the physical actuator requests as the best least squares approximation to the overdetermined system

$$\begin{aligned} \mathbf{X}_{\text{LS,kin}} \begin{bmatrix} P_{\text{CO}}^{\text{on}} & P_{\text{CO}}^{\text{off}} & P_{\text{EC}} \end{bmatrix}^T = \\ \begin{bmatrix} \hat{P}_{CO}^{\text{on}} & \hat{P}_{\text{CO}}^{\text{on}} & \hat{P}_{\text{EC}} & \hat{P}_{\text{tot}} & \hat{P}_{\text{tot,kin}} \end{bmatrix}^T, \end{aligned} \tag{5.32}$$

where $\mathbf{X}_{\text{LS,kin}}$ is a matrix of the form

$$\mathbf{X}_{\text{LS,kin}} = \begin{bmatrix} 1 & & \\ & 1 & \\ & & 1 \\ 1 & 1 & 1 \\ 1 & 1 & 1 \end{bmatrix}. \tag{5.33}$$

### 5.2.4 Experimental Results

In this section, simulations and experimental results are presented to test the effectiveness of the feedback approach described above. To simplify matters the feedforward control design of Chapter 4 is not used in these initial tests. Instead the target profile is selected as the achieved profile from a previous DIII-D experiment (shot 154358). The feedforward inputs for the neutral beam groups and the plasma current are identical to the actuator commands of the target shot. However, a disturbance is introduced to the feedforward control by freezing the control commands of the target shot at 1.5 s, and reducing the EC power by 1/2. This is done in order to ensure that feedback control action is necessary to reproduce the target shot. In short, the objective is to show repeatability of previous shots.

The tuning problem consists of the selection of the diagonal elements of $\mathbf{Q}$ and $\mathbf{R}$ and the constant $\alpha_\zeta$ of (5.22) to regulate the profile as close as possible to the target. An experiment carried out at DIII-D (shot 154691) is shown in Figure 5.2, where we have attempted to control only the current profile ($\bar{\psi}$ profile) without using energy control. The feedforward and requested actuator powers are plotted in Figure 5.2(b), the measured and target $\bar{\psi}$ profiles, together with the internal energy, are plotted in Figure 5.2(a), and the measured and target $q$ profiles are plotted in Figure 5.2(c). During the experiment good profile regulation was maintained up to about 3.5 s. The profile controller attempted to correct the $q$ profile in the plasma center after 3.5 s by saturating the CO-off NBI and EC powers while turning off the CO-on power with the goal of modifying the current distribution away from the center. Recall from Figure 3.1 that the CO-on NBI drives current at the plasma center while the CO-off NBI and EC drive current away from the plasma center. Thus, assuming the total plasma current remains constant, decreasing CO-on NBI power while increasing CO-off NBI and EC power should modify the current distribution away from the plasma center resulting in an increase of $q$ at the center. However, the failure to maintain high energy in the the plasma (see Figure 5.2(a)), which is not feedback controlled, may have deteriorated the off-axis bootstrap current drive effect to a level that made the $q$ at the center remarkably more difficult to regulate in

spite of the efforts by the feedback controller. It is important to point out that the the oscillations in the delivered $I_p$ starting around 3.5 s (green line in Figure 5.2(b)) are not due to the profile control algorithm, as shown by the controller requested $I_p$ (red line in Figure 5.2(b)). The cause of these oscillations remains unclear but they may have contributed to a loss in energy confinement.

Anticipating that plasma energy regulation may be critical to maintain tight control of $q$ at the plasma center, closed-loop simulations were carried out combining current-profile and internal-energy control, the results of which are presented in Figure 5.3. The feedforward and requested actuator powers are plotted in Figure 5.3(b), the simulated and target $\bar{\psi}$ profiles and internal energy are plotted in Figure 5.3(a), and the measured and target $q$ profiles are plotted in Figure 5.3(c). The target profile is determined from the response of the nonlinear model (4.11) to the input values of shot 154358. Here, we are able to maintain good profile tracking throughout the simulation despite large input disturbances caused by holding the feedforward inputs constant after 1.5 s. The controller increases CO-on power starting around 1.5 s to push $q$ down towards the target at the plasma center. While the CO-on NBI group acts to regulate $q$, the CO-off power decreases between $t = 2$ s and $t = 2.5$ s to balance the internal energy at the target value of 0.8 MJ. After 2.5 s the CO-off and EC powers begin to increase to raise the internal energy up to the desired final value of approximately 1 MJ. The total plasma current is reduced slightly from its FF value to maintain tight control of $q$ at the plasma edge. Note that in both the experiment and the simulation the control design parameters are the same.

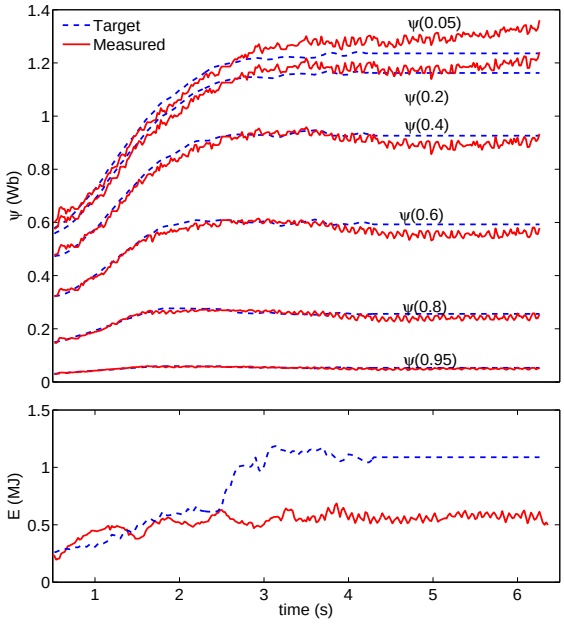


(a) $\bar{\psi}$ and internal energy $E$

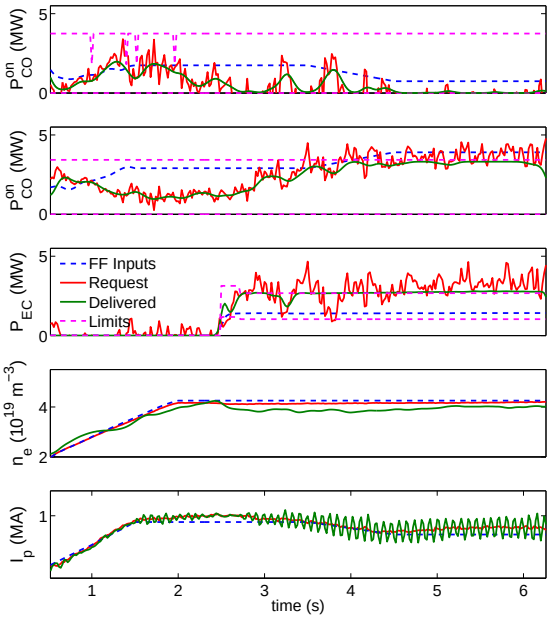


(b) Input powers

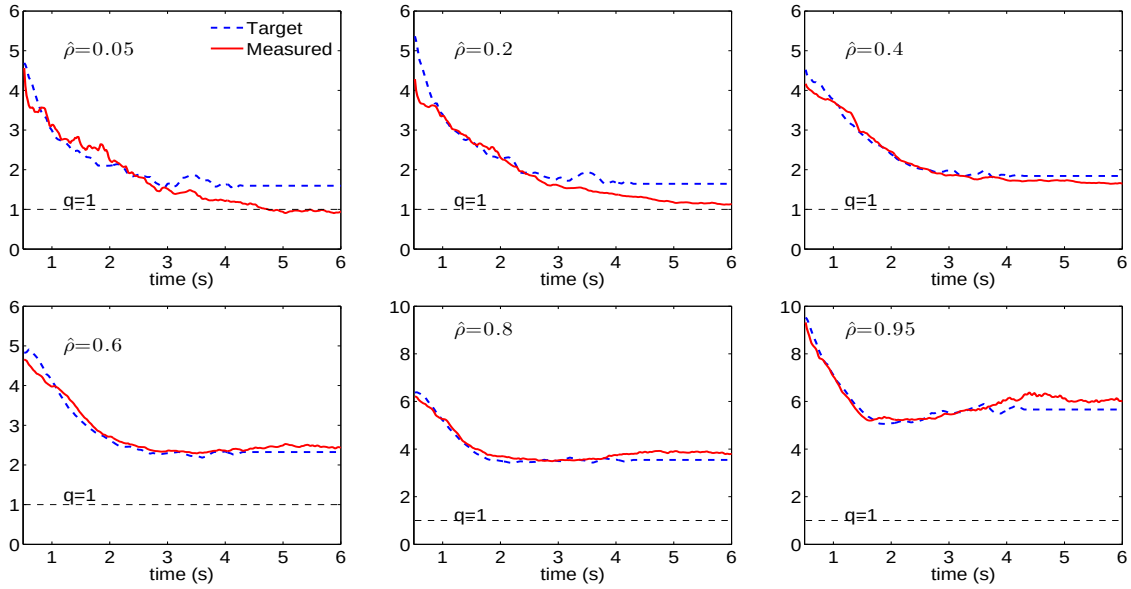


(c) Safety factor profile ($q$)

**Figure 5.2:** DIII-D shot 154619: Current profile control experiment.

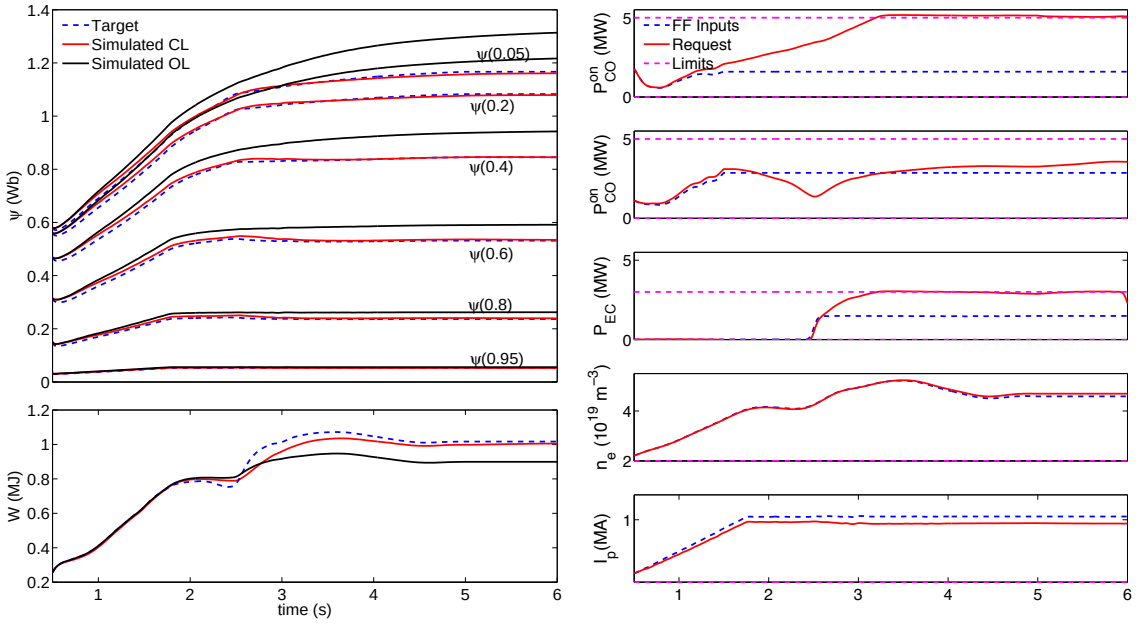


(a) $\bar{\psi}$ and internal energy $E$ (b) Input powers

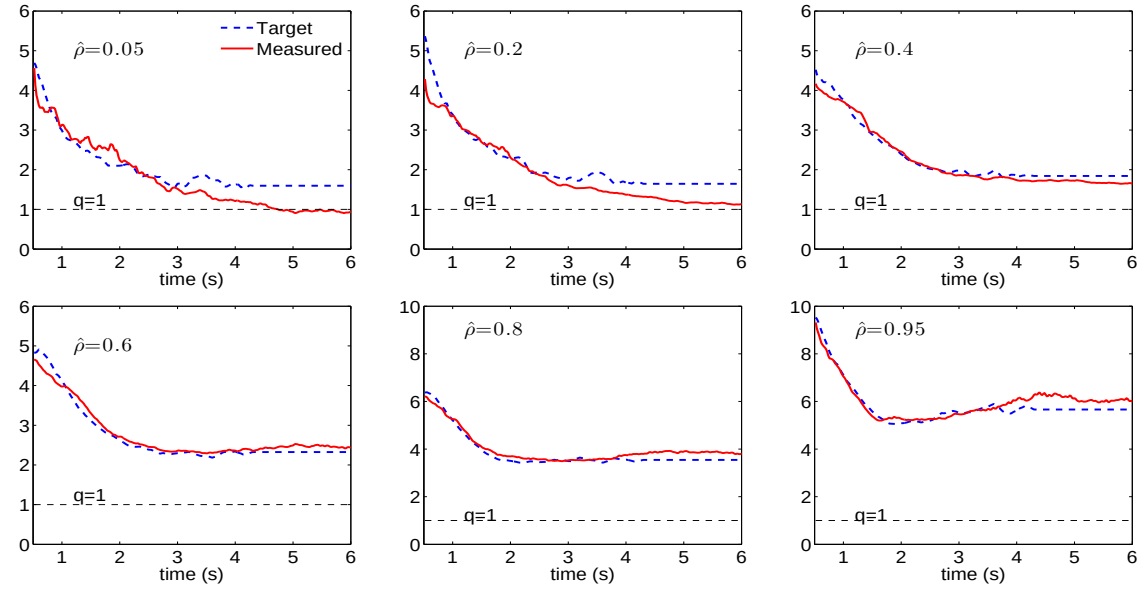


(c) Safety factor profile ($q$)

**Figure 5.3:** Simulation: Combined current profile and energy control.

## 5.3 LQI Feedback for Shot-to-Shot Reproducibility of Current Profiles

In this section we consider feedback control design based on linear quadratic integrator techniques for current profile control during L-mode discharges. The control approach is similar to that of Section 5.2 except the feedforward control will be based on the optimal feedforward control design of Chapter 4 rather than the actuator waveform of a previous shot. Also, we consider the control objective of reaching a particular target at a specified time, as opposed to regulating the current profile through the flattop phase as in the previous section. Since the bootstrap contribution is small in L-mode discharges, the main motivation for designing the control law in terms of the nonlinear input functions (4.4) is lost, so, instead we take the physical actuators as the system inputs. For convenience, the system considered for control is rewritten here,

$$\dot{\boldsymbol{\theta}} = \boldsymbol{f}_\theta(\boldsymbol{\theta}, \mathbf{u}), \quad \boldsymbol{\iota} = \mathbf{C}\boldsymbol{\theta}, \tag{5.34}$$

where the input is the set of physical actuators including the total plasma current, the line averaged density, the total ECCD power, and the individual NBI powers, i.e., $\mathbf{u} = [I_\mathrm{p}, \bar{n}_\mathrm{e}, P_\mathrm{EC}, P_{\mathrm{NBI},1}, \ldots,]$, the system state is $\boldsymbol{\theta} = [\theta_2, \theta_3, \ldots, \theta_{l-1}]^T$, and the system output is $\boldsymbol{\iota} = [\iota_2, \iota_3, \ldots, \iota_{l-1}]^T$, where $l$ represents an index over the discretized spatial domain as described in Appendix A.1.

The main purpose of the feedback controller described in this section is to aid the feedforward control of Chapter 4 to mitigate disturbances from the desired profile evolution, and, therefore, improve shot-to-shot repeatability of the feedforward control solution.

### 5.3.1 Model Linearization

Let $\mathbf{u}_\mathrm{FF}$, $\boldsymbol{\theta}_\mathrm{FF}$, and $\boldsymbol{\iota}_\mathrm{FF}$ represent the feedforward control sequence and corresponding state and output trajectories determined from the trajectory optimization approach described in Chapter 4. This set of feedforward controls and state and output trajectories necessarily satisfy the system dynamics, i.e. $\dot{\boldsymbol{\theta}}_\mathrm{FF} = \boldsymbol{f}_\theta(\boldsymbol{\theta}_\mathrm{FF}, \mathbf{u}_\mathrm{FF})$, $\boldsymbol{\iota}_\mathrm{FF} = \mathbf{C}\boldsymbol{\theta}_\mathrm{FF}$,

and let the variables $\tilde{\boldsymbol{\theta}} = \boldsymbol{\theta} - \boldsymbol{\theta}_{\mathrm{FF}}$, $\tilde{\boldsymbol{\iota}} = \boldsymbol{\iota} - \boldsymbol{\iota}_{\mathrm{FF}}$, and $\mathbf{u}_{\mathrm{FB}} = \mathbf{u} - \mathbf{u}_{\mathrm{FF}}$ represent perturbations around the feedforward trajectory. In a neighborhood of the feedforward trajectory we can approximate the dynamics of the system (5.34), with the linear system

$$\dot{\tilde{\boldsymbol{\theta}}} \approx \boldsymbol{f}_\theta(\boldsymbol{\theta}_{\mathrm{FF}}(t), \mathbf{u}_{\mathrm{FF}}(t)) + \left.\frac{\partial \boldsymbol{f}_\theta}{\partial \boldsymbol{\theta}}\right|_{\substack{\boldsymbol{\theta}_{\mathrm{FF}}(t) \\ \mathbf{u}_{\mathrm{FF}}(t)}} \tilde{\boldsymbol{\theta}} + \left.\frac{\partial \boldsymbol{f}_\theta}{\partial \mathbf{u}}\right|_{\substack{\boldsymbol{\theta}_{\mathrm{FF}}(t) \\ \mathbf{u}_{\mathrm{FF}}(t)}} \mathbf{u}_{\mathrm{FB}},$$

from which we obtain the time-varying linear dynamical system around the feedforward trajectory

$$\dot{\tilde{\boldsymbol{\theta}}} = \mathbf{A}_{\mathrm{FPD}}(t)\tilde{\boldsymbol{\theta}} + \mathbf{B}_{\mathrm{FPD}}(t)\mathbf{u}_{\mathrm{FB}}, \quad \tilde{\boldsymbol{\iota}} = \mathbf{C}\tilde{\boldsymbol{\theta}}, \tag{5.35}$$

where $\mathbf{A}_{\mathrm{FPD}} = \nabla_{\boldsymbol{\theta}} \boldsymbol{f}_\theta|_{\boldsymbol{\theta}_{\mathrm{FF}}, \mathbf{u}_{\mathrm{FF}}}$ and $\mathbf{B}_{\mathrm{FPD}} = \nabla_{\mathbf{u}} \boldsymbol{f}_\theta|_{\boldsymbol{\theta}_{\mathrm{FF}}, \mathbf{u}_{\mathrm{FF}}}$. Given that we have full state measurement and the outputs have a direct one-to-one correspondence with the states, we can eliminate the output function for simplicity of control design to write, $\dot{\mathbf{x}} = \bar{\mathbf{A}}_{\mathrm{FPD}}(t)\mathbf{x} + \bar{\mathbf{B}}_{\mathrm{FPD}}(t)\mathbf{u}_{\mathrm{FB}}$, wher $\mathbf{x} = \tilde{\boldsymbol{\iota}}$, $\bar{\mathbf{A}}_{\mathrm{FPD}}(t) = \mathbf{C}\mathbf{A}_{\mathrm{FPD}}(t)\mathbf{C}^{-1}$ and $\bar{\mathbf{B}}_{\mathrm{FPD}}(t) = \mathbf{C}\mathbf{B}_{\mathrm{FPD}}(t)$. For feedback design purposes we can further simply the system to a time-invariant system, which is an acceptable approximation assuming that the plasma remains in a single confinement regime,

$$\dot{\mathbf{x}} = \mathbf{A}\mathbf{x} + \mathbf{B}\mathbf{u}_{\mathrm{FB}}, \tag{5.36}$$

where $\mathbf{A}$ and $\mathbf{B}$ are taken as $\bar{\mathbf{A}}_{\mathrm{FPD}}(t_{\mathrm{targ}})$ and $\bar{\mathbf{B}}_{\mathrm{FPD}}(t_{\mathrm{targ}})$ and $t_{\mathrm{targ}}$ is the target time.

### 5.3.2 LQI Control Design

We begin the control design following the same strategy described in sections 5.2.2-5.2.3. However, of the available actuators only the NBI and total plasma current are controlled in feedback, and the remaining are controlled in feedforward only. The variables $\mathbf{x}_{\mathrm{targ}}$, $\mathbf{x}_\infty^{ss}$, $\tilde{\mathbf{u}}_{\mathrm{FB}}$ are defined in the same way.

### 5.3.3 Two-Loop LQI Controller

Via a two-loop feedback controller, the total plasma current is used to regulate the profile at the plasma edge and the NBI are used to regulate the interior profile.

This approach of focusing the total plasma current on edge regulation and NBI on interior regulation is well conceived when combined with optimized feedforward control, which provides not only a feedforward control action but also an optimal trajectory (path) to the target profile. The feedback controller simply has to follow the desired trajectory produced by the optimized trajectory design. To construct the two-loop controller, the feedback controlled inputs (NBI and total plasma current) of the system (5.36) are separated into the NBI powers, $\tilde{\mathbf{u}}_{\mathrm{NBI}}$, and the total plasma current, $\tilde{\mathbf{u}}_{I_\mathrm{p}}$,

$$\dot{\tilde{\mathbf{x}}} = \mathbf{A}\tilde{\mathbf{x}} + \begin{bmatrix}\mathbf{B}_{\mathrm{NBI}} & \mathbf{B}_{I_\mathrm{p}}\end{bmatrix}\begin{bmatrix}\tilde{\mathbf{u}}_{\mathrm{NBI}} \\ \tilde{\mathbf{u}}_{I_\mathrm{p}}\end{bmatrix}. \tag{5.37}$$

For the inner loop controller, we consider only the response of the edge value, to the total plasma current,

$$\begin{aligned}\dot{\tilde{\mathbf{x}}} =& \mathbf{A}\tilde{\mathbf{x}} + \mathbf{B}_{I_\mathrm{p}}\tilde{\mathbf{u}}_{I_\mathrm{p}}, \\ \tilde{x}_\mathrm{b} =& \mathbf{C}_{I_\mathrm{p}}\tilde{\mathbf{x}},\end{aligned} \tag{5.38}$$

where $\mathbf{C}_{I_\mathrm{p}} = [0, 0, ..., 1]$, and $\tilde{x}_\mathrm{b}$ is the value of $\tilde{\mathbf{x}}$ at the edge[3]. The controller is constructed by first augmenting the system (5.38) with the integrator state, $x_c = \mathbf{C}_{I_\mathrm{p}} \int \tilde{\mathbf{x}} dt$,

$$\begin{bmatrix}\dot{\tilde{\mathbf{x}}} \\ \dot{x}_c\end{bmatrix} = \begin{bmatrix}\mathbf{A} & 0 \\ \mathbf{C}_{I_\mathrm{p}} & 0\end{bmatrix}\begin{bmatrix}\tilde{\mathbf{x}} \\ x_c\end{bmatrix} + \begin{bmatrix}\mathbf{B}_{I_\mathrm{p}} \\ 0\end{bmatrix}\tilde{u}_{I_\mathrm{p}}, \tag{5.39}$$

and then by solving for the linear control policy, $\tilde{u}_{I_p} = -\mathbf{K}_{\mathrm{LQI}}[\tilde{\mathbf{x}}^T \; x_c]^T$, following the approach explained in sections 5.2.2-5.2.3. The gain matrix can be partitioned into $\mathbf{K}_{\mathrm{LQI}} = [\mathbf{K}_{\mathrm{P},\tilde{\mathbf{x}}} \; K_{\mathrm{I},x_c}]$, where $\mathbf{K}_{\mathrm{P},\tilde{\mathbf{x}}}$ are gains on the $\tilde{\mathbf{x}}$ and $K_{\mathrm{I},x_c}$ is the gain on the integrator state $x_c$. For a state space description of the controller, we have

$$\begin{aligned}\dot{x}_c =& 0x_c + \mathbf{C}_{I_\mathrm{p}}\tilde{\mathbf{x}}, \\ \tilde{u}_{I_\mathrm{p}} =& -\mathbf{K}_{\mathrm{P},\tilde{\mathbf{x}}}\tilde{\mathbf{x}} - K_{\mathrm{I},x_c}x_c.\end{aligned} \tag{5.40}$$

[3]The edge in this case is the flux surface at $\hat{\rho} = 0.95$.

Combining (5.40) with the plant (5.37), we close the inner loop to obtain,

$$\begin{bmatrix} \dot{\tilde{\mathbf{x}}} \\ \dot{x}_c \end{bmatrix} = \begin{bmatrix} \mathbf{A} - \mathbf{B}_{I_\mathrm{p}} \mathbf{K}_{\mathrm{P},\tilde{\mathbf{x}}} & -\mathbf{B}_{I_\mathrm{p}} K_{\mathrm{I},x_c} \\ \mathbf{C}_{I_p} & 0 \end{bmatrix} \begin{bmatrix} \tilde{\mathbf{x}} \\ x_c \end{bmatrix} + \begin{bmatrix} \mathbf{B}_{\mathrm{NBI}} \\ \mathbf{0} \end{bmatrix} \tilde{\mathbf{u}}_{\mathrm{NBI}}. \tag{5.41}$$

For the outer loop controller, again we proceed with LQI design, but now applied to the system (5.41). In this case, the inputs, which are solely the NBI, are used to control the interior profile shape. First, the system (5.41) is augmented with the integrator states, $\boldsymbol{\zeta} = \hat{\mathbf{K}}_\zeta \int \tilde{\mathbf{x}} dt$. Then, the open loop system augmented with integrator states can be written as

$$\begin{bmatrix} \dot{\tilde{\mathbf{x}}} \\ \dot{x}_c \\ \dot{\zeta} \end{bmatrix} \begin{bmatrix} \mathbf{A} - \mathbf{B}_{I_\mathrm{p}} \mathbf{K}_{\mathrm{P},\tilde{x}} & -\mathbf{B}_{I_\mathrm{p}} K_{\mathrm{I},x_c} & \mathbf{0} \\ \mathbf{C}_{I_p} & 0 & \mathbf{0} \\ \hat{\mathbf{K}}_{\boldsymbol{\zeta}} & 0 & \mathbf{0} \end{bmatrix} \begin{bmatrix} \tilde{\mathbf{x}} \\ x_c \\ \boldsymbol{\zeta} \end{bmatrix} + \begin{bmatrix} \mathbf{B}_{\mathrm{NBI}} \\ \mathbf{0} \\ \mathbf{0} \end{bmatrix} \tilde{u}_{\mathrm{NBI}}, \tag{5.42}$$

for which, the LQI gains are given by $\hat{\mathbf{K}}_{LQI} = \begin{bmatrix} \hat{\mathbf{K}}_{\mathrm{P}\tilde{x}} & \hat{\mathbf{K}}_{\mathrm{P},x_c} & \hat{\mathbf{K}}_{\mathrm{I},\zeta} \end{bmatrix}$. Then the outer loop controller can be written as

$$\begin{aligned} \dot{\boldsymbol{\zeta}} =& 0\boldsymbol{\zeta} + \hat{\mathbf{K}}_{\boldsymbol{\zeta}} \tilde{\mathbf{x}}, \\ \tilde{\mathbf{u}}_{\mathrm{NBI}} =& -\hat{\mathbf{K}}_{\mathrm{P},\tilde{\mathbf{x}}} \tilde{\mathbf{x}} - \hat{\mathbf{K}}_{\mathrm{P},x_c} x_c - \hat{\mathbf{K}}_{\mathrm{I},\boldsymbol{\zeta}} \boldsymbol{\zeta}, \end{aligned} \tag{5.43}$$

which can be combined with the inner loop controller (5.40). The final feedback controller can be written in terms of the measurement $\mathbf{x}$ and the target $\mathbf{x}_{\mathrm{targ}}$ ($\tilde{\mathbf{x}} = \mathbf{x} - \mathbf{K}_{\mathrm{sg,Tr}} \mathbf{K}^{\dagger}_{\mathrm{sg,Tr}} x_{\mathrm{targ}}$) as

$$\begin{aligned} \begin{bmatrix} \dot{\boldsymbol{\zeta}} \\ \dot{x}_c \end{bmatrix} &= \begin{bmatrix} \mathbf{0} & 0 \\ \mathbf{0} & 0 \end{bmatrix} \begin{bmatrix} \boldsymbol{\zeta} \\ x_c \end{bmatrix} + \begin{bmatrix} \hat{\mathbf{K}}_\zeta \\ \mathbf{C}_{I_\mathrm{p}} \end{bmatrix} \tilde{\mathbf{x}}, \\ \begin{bmatrix} \tilde{\mathbf{u}}_{\mathrm{NBI}} \\ \tilde{\mathbf{u}}_{I_\mathrm{p}} \end{bmatrix} &= \begin{bmatrix} -\hat{\mathbf{K}}_{I,\zeta} & -\hat{\mathbf{K}}_{P,x_c} \\ \mathbf{0} & -K_{I,x_c} \end{bmatrix} \begin{bmatrix} \boldsymbol{\zeta} \\ x_c \end{bmatrix} + \begin{bmatrix} -\hat{\mathbf{K}}_{\mathrm{P},\tilde{\mathbf{x}}} \\ -\mathbf{K}_{\mathrm{P},\tilde{\mathbf{x}}} \end{bmatrix} \tilde{\mathbf{x}}. \end{aligned} \tag{5.44}$$

A SVD analysis of the linearized system's response to the NBI is shown in Figure 5.4. The analysis shows the directions in which the profile can be significantly manipulated by the NBI in steady state. The columns of input singular matrix, Figure 5.4(a), represent linear combinations of the NBI powers and the output singular vectors scaled by the singular values, $U\Sigma$, represent the response to those input

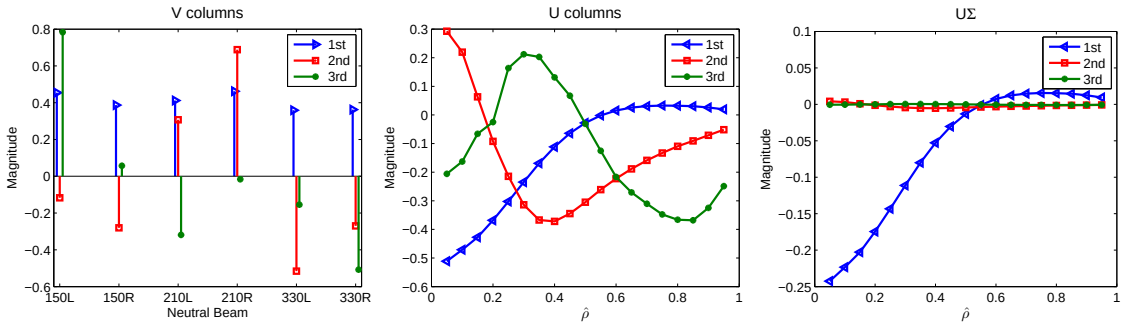


(a) **V** columns. (b) **U** columns. (c) **UΣ** columns.

**Figure 5.4:** SVD analysis of the linearized model including only the effects of the NBI. (a.) Input singular vectors, i.e. columns of **V**, which represent combinations of the NBI powers. (b.) Output singular vectors, i.e. columns of **U**, which represent deviations from the nominal profile associated with the input combinations. (c.) Output singular vectors scaled by the singular values.

combinations, Figure 5.4(c). Only the first three directions are plotted since the remaining singular values are very small. Based on the output directions shown in Figure 5.4(c), the NBI can only significantly influence the profile in two directions. Therefore two singular values are used in the truncated singular value decomposition.

### 5.3.4 Experimental Setup and Results

#### Goal of the Experiment

The goal of the experiments in this section is to obtain a certain target $q$ profile at a certain time while maintaining the plasma in a single confinement regime throughout the discharge, either L-mode or H-mode depending on the experiment. This implies the total auxiliary power must be limited from above during L-mode discharges to prevent transitions to H-mode, and limited from below during H-mode discharges to prevent back transitions to L-mode.

The primary goal of the experiments is to demonstrate reproducibility between tokamak discharges by reliably obtaining the desired $q$ target in the plasma early flattop phase or coming as close as possible. If and when the target is obtained,

control of the remainder of the discharge would be assumed by a physics studies experiment. Therefore, the goal of the experiment does not require maintaing the target in steady state. For the control tests during L-mode discharges, three target $q$ profiles were tested, each with increasing difficulty to achieve. The targets are all monotonically increasing (in $\hat{\rho}$) with varying levels of $q$ at the plasma center and plasma edge (see Figure 4.3). Essentially, it is desired to obtain a large total plasma current while also maintaining $q$ high at the center, which translates to a flat current profile or one that is not too peaked at the center and a large total plasma current. Only a few shots were available for control testing during H-mode discharges, so only one target was tested consisting of a monotonically increasing $q$ profile with a large central $q$ value and a broad flat profile at the plasma center.

### Implementation of Power Limits

To avoid L-H transitions, an upper bound on total auxiliary power was imposed during the experiments. This was accomplished by saturating the total power requested by the combined feedforward + feedback controller as follows. First, the total power requested by the controller, $P_{\text{aux}}^{\text{req}}$, is computed

$$P_{\text{aux}}^{\text{req}} = P_{\text{EC}}^{\text{req}} + \sum_{\xi=1}^{n_{\text{NBI}}} P_{\text{NBI},\xi}^{\text{req}}, \tag{5.45}$$

and if it exceeds the L-H transition power, $P_{\text{LH}}^{\text{lim}}$, then a scale factor is computed

$$P_{\text{LH}}^{\text{scale}}(t) = \frac{P_{\text{LH}}^{\text{lim}} - [P_{30L} + P_{30R}]}{P_{\text{aux}}^{\text{req}} - [P_{30L} + P_{30R}]}. \tag{5.46}$$

where the 30L and 30R NBI are not included in the scale factor because they are dedicated to diagnostics. Each of the controlled NBI and ECCD are scaled down according to

$$P_{\text{NBI},\xi} = P_{\text{LH}}^{\text{scale}} P_{\text{NBI},\xi}^{\text{req}} \quad \text{and} \quad P_{\text{EC}} = P_{\text{LH}}^{\text{scale}} P_{\text{EC}}^{\text{req}}. \tag{5.47}$$

In this fashion the total requested power is alwasys limited to prevent L-H transitions without disrupting the relative distribution of power requested by the controller for each of the controlled actuators.

For H-mode discharges a similar total auxiliary power limit is applied from below to prevent back transitions, i.e. transitions from H-mode back to L-mode. Again, the total auxiliary requested power is first computed as in (5.45), and if it is below the H-L power limit, $P_{\text{HL}}^{\text{lim}}$, then a scale factor is computed

$$P_{\text{HL}}^{\text{scale}} = P_{\text{HL}}^{\text{lim}} - P_{\text{aux}}^{\text{req}}. \tag{5.48}$$

Finally, each of the feedback controlled NBI are scaled-up additively as follows

$$P_{\text{NBI},\xi} = P_{\text{NBI},\xi} + \frac{P_{\text{HL}}^{\text{scale}}}{n_{\text{controlled}}^{\text{NBI}}}, \tag{5.49}$$

where $n_{\text{controlled}}^{\text{NBI}}$ is the number of controlled NBI. This method does not preserve the distribution of powers requested by the controller like that of the LH power scaling, but this is not very alarming since the controller is expected to very rarely request a total auxiliary power below the HL limit. In fact, generally the cases in which the HL power limit is breached only happen momentarily in practice.

### Summary of Experimental Results

First, a feedforward control solution is synthesized offline by the method described in Chapter 4. This provides an open-loop actuator waveform and an associated state evolution that evolves to the target $q$ profile at the desired time. The role of the feedback controller is to mitigate disturbances of the plasma from the optimal state evolution; it makes small updates to the feedforward control in real-time so that the $q$ profile evolves appropriately. In each case, the feedforward optimization is carried out over the time interval $t \in [0.4s, t_F]$, where $t_F$ is the time when the desired $q$ profile and $\beta_N$ value must be achieved and is employed as a design parameter (see Section 4.5).

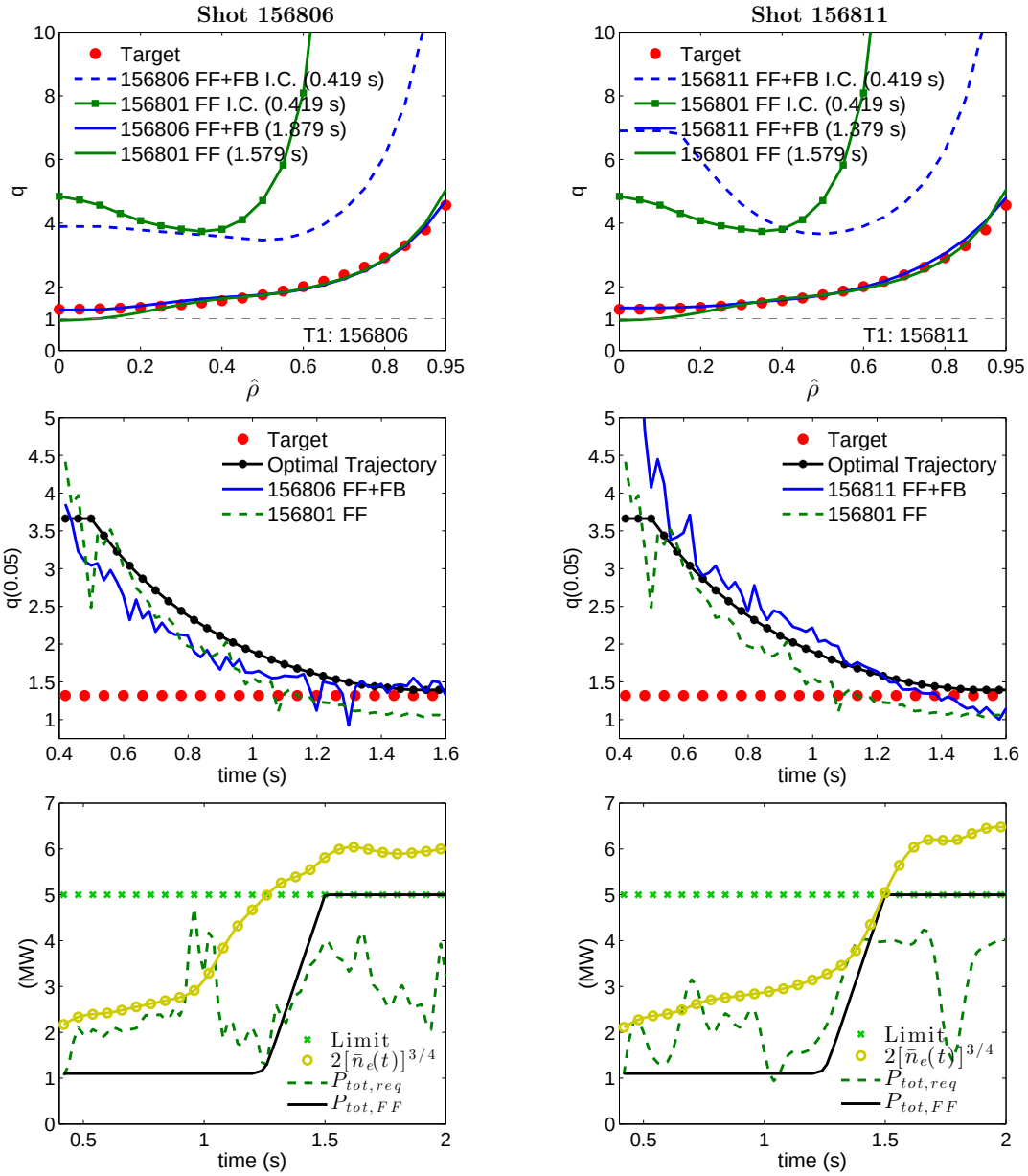


**Figure 5.5:** Target 1 tests: shot 156806 (left) and 156811 (right). The obtained $q$ profile for each shot is shown in the top plot. The red circles mark the target $q$ profile ($t_F = 1.5$ s for Target 1). Initial and final (best-matching) profiles are shown both for FF-only and FF+FB control shots. The middle plot shows $q$ at center ($\hat{\rho} = 0.05$). The black line ("Optimal Trajectory") represents the time evolution of the target profile at $\hat{\rho} = 0.05$ obtained by feedforward optimization. The bottom plot shows the total auxiliary power during the experiment including the predicted L-H power transition threshold, $2[\bar{n}_e]^{3/4}$, the imposed power limit (green stars), the feedforward auxiliary power (solid black), and the feedforward + feedback auxiliary power (dashed green).

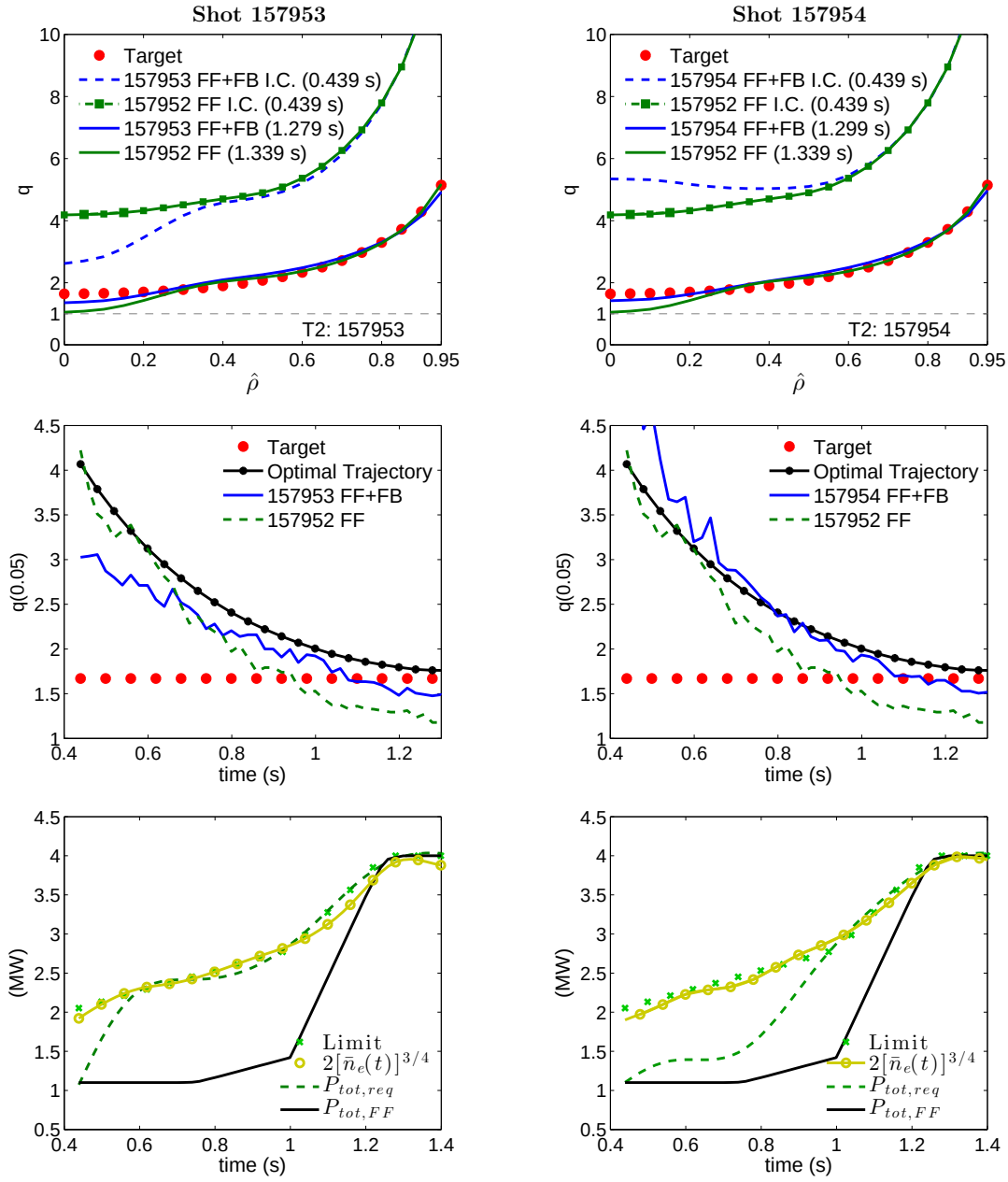


**Figure 5.6:** Target 2 tests: shot 157953 (left) and 157954 (right). The plots are configured the same as in Figure 5.5. The target time $t_F = 1.25$.

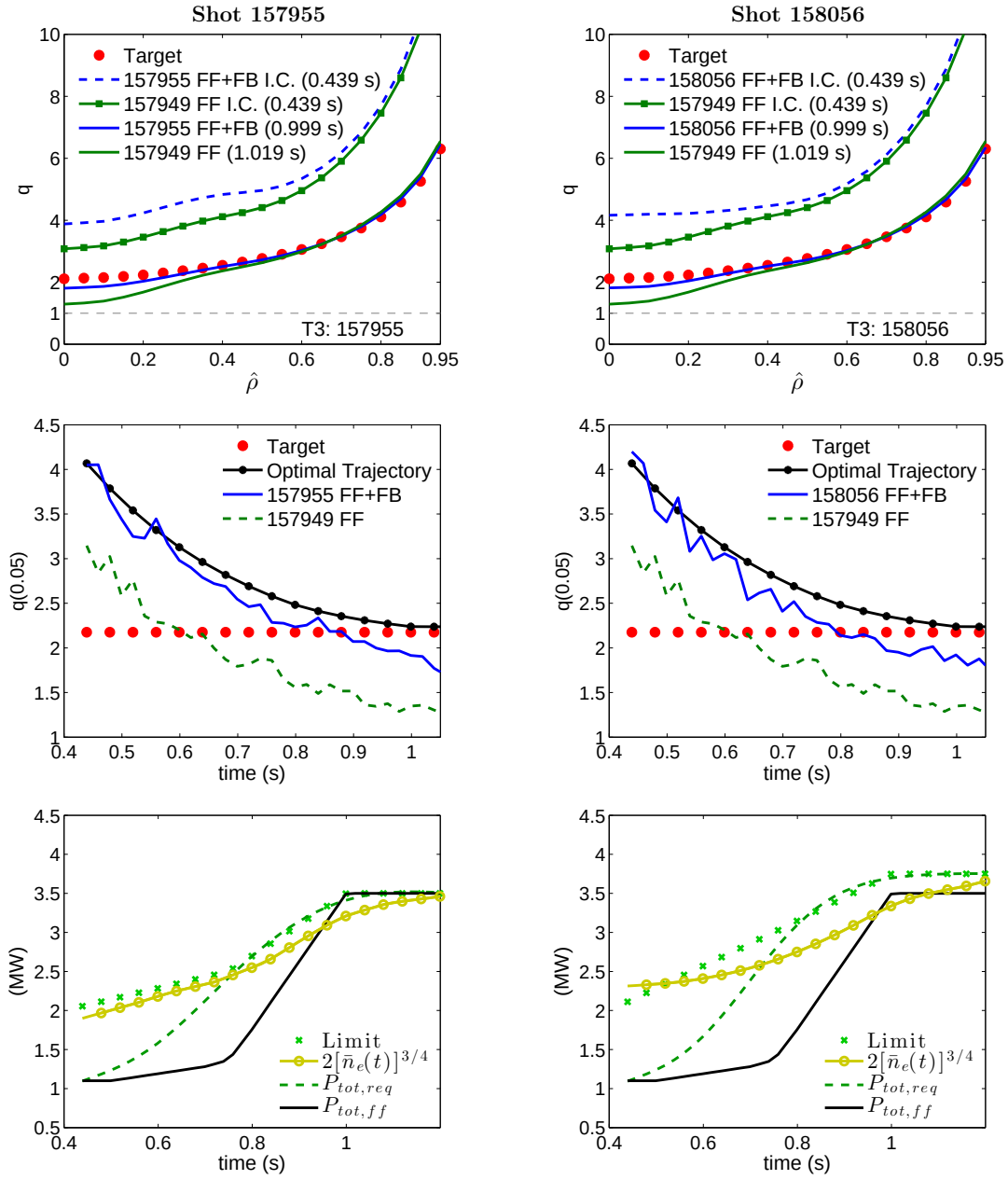


**Figure 5.7:** Target 3 tests: shot 157955 (left) and 158056 (right). The plots are configured the same as in Figure 5.5. The target time $t_F = 1.25$.

Beginning with Target 1, two control tests are shown in Figure 5.5. In the top plots are shown the obtained $q$ profile with feedforward (FF) control alone and combined feedforward and feedback (FF+FB) control at the initial and best-matching time. The target profile is shown in red dots. In the middle plots, the evolution of $q$ at the center ($\hat{\rho} = 0.05$) is shown, where the final target is plotted in red dots and the optimal evolution of $q$ at the center is plotted in black. For both shots, we can see the $q$ profile with feedforward control alone falls to one before the target time[4]. This unfortunate result is primarily due to slight modeling errors in the current diffusion rate, which lead to a nonsatisfactory feedforward control policy. This emphasizes the importance of feedback control, which is able to account for the modeling errors and to bring the $q$ profile back as close as possible to the target.

The bottom plots of Figure 5.5 show the total auxiliary power for the feedforward and feedforward+feedback cases. The imposed power limit to prevent transitions to H-mode is plotted in green stars. The experiments began with a simple power limit of $P_{\text{LH}} = 5$ MW. During testing of Target 1, the H-mode transition power was observed to approximately scale with the electron density according to

$$P_{\text{LH}} = 2\bar{n}_e^{3/4}. \tag{5.50}$$

During subsequent experiments, testing of Targets 2 and 3, the total injected power was constrained by this limit, and this limit (5.50) was also used as a constraint in the feedforward optimization as discussed in Section 4.4.

With a similar presentation of the Target 1 tests, tests of Targets 2 and 3 are plotted in Figures 5.6 and 5.7, respectively. For Target 2, $t_F = 1.25$, and for Target 3, $t_F = 1.0$. Generally, the initial conditions vary significantly from shot to shot. Again, in Figures 5.6 and 5.7, both the obtained $q$ profile with feedforward control alone and combined feedforward and feedback control at the best-matching time are shown. In all cases, feedback control improves the obtained $q$-profile matching error by about 50%, even with wildly different initial conditions.

[4]The $q$ profile is physically limited to a value greater than one; if it falls to one, an undesirable phenomenon known as saw-teeth will prevent it from falling further, essentially resetting it above one.

For both Targets 2 and 3 tests, the NBI power is almost always at the H-mode transition limit. Additional experiments involving a different type of controller showed that it was indeed possible to achieve Target 2 and Target 3 by slightly relaxing the L-H transition power limit [56]. Also, note that the obtained $q$ profiles between feedforward+feedback shots (left vs right in the top plots of Figures 5.5, 5.6, and 5.7) are nearly identical, proving to some extent the repeatability of the control approach.

The same control approach was also applied to a small number of shots during H-mode discharges. Similar results were obtained for H-mode shots as shown in Figure 5.8. The control design process is identical in both L-mode and H-mode discharges; the only differences are that the model parameters are adjusted appropriately for each case and the optimization constraints include minimum power limits to avoid the possibility of back transitions to L-mode.

## 5.4 Conclusions

Careful control of the $q$ profile evolution will be necessary to access high performance tokamak scenarios characterized by high energy confinement and high bootstrap current fraction. In practice, the desired $q$ profile cannot be reliably obtained with preprogrammed actuator waveforms alone due to variability of the plasma impurity concentration, variable wall conditions, actuator faults, and plasma drifts from external sources. This necessitates the design of a feedback control approach to actively regulate the $q$ profile evolution.

By combining feedforward optimization via nonlinear programming and linearized feedback control, target $q$ profiles were attained in both L-mode and H-mode DIII-D discharges. While results are promising, they show the sensitivity of the feedforward control solution to model mismatches. Since this solution is computed offline, the feedforward design can however be improved by increasing the complexity of the model. Feedback control remains necessary, due not only to the lack of a perfect model, but also to the existence of plasma disturbances. In the next

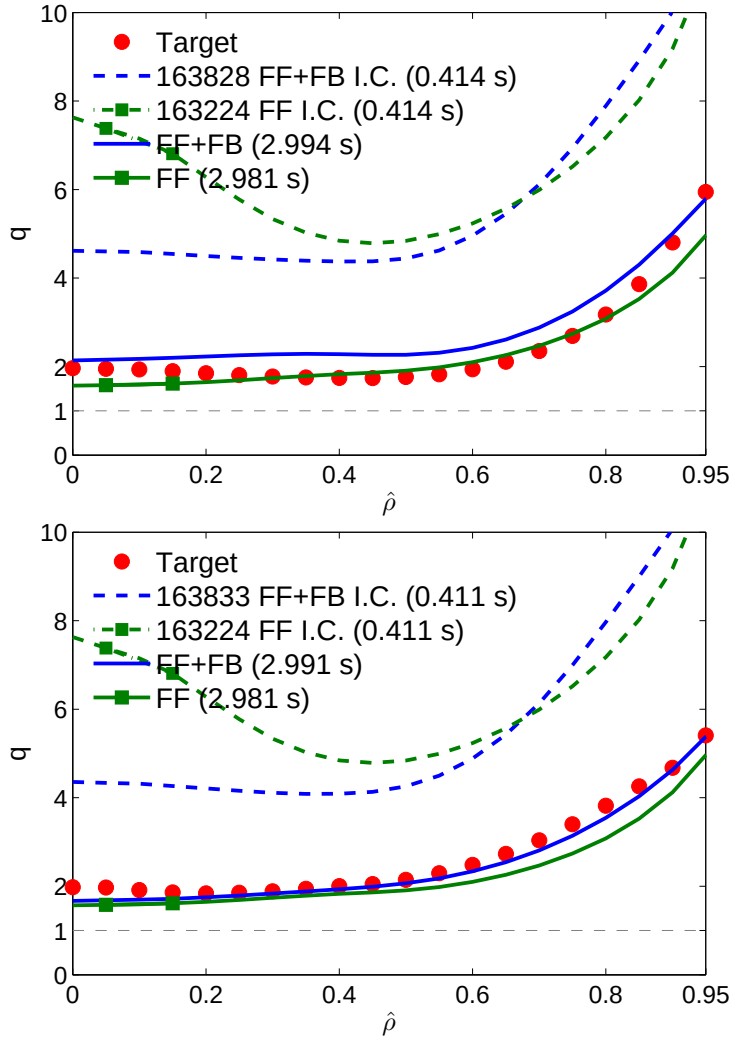


**Figure 5.8:** Obtained $q$ profiles during H-mode discharges. The results of feedforward control (shot 163224) and feedforward + feedback control (shots 163828 and 163833) at the desired target time are plotted. The red circles mark the target $q$ profiles, the dash lines mark the initial conditions and the solid lines mark the obtained $q$ profiles. Only one target tested in H-mode involving a monotonic $q$ profile with high $q_{\min} = 2.0$ and broad, flat $q$ at the plasma center.

chapter, the feedback control approach is improved with a numerical optimal control approach, which incorporates hard constraints on control actions to maintain plasma stability.

# Chapter 6

# Feedback Control Design for the Current Profile Evolution via Model Predictive Control

## 6.1 Introduction

Model predictive control of the tokamak $q$ profile has already been considered in simulations [76, 77]. By "model predictive control" we mean an explicit model of the system dynamics is used to predict the effect of present and future control actions on the system output [78]. As pointed out in [77], it is typically desired to operate tokamaks near stability limits in order to explore interesting physical phenomenon, thus, the optimal control solution for $q$ profile control often lies at the intersection of various constraints, including constraints associated with actuator limits and parameter limits to avoid deleterious MHD activity. The most effective control approach is then naturally one that anticipates constraint violations and corrects for them in a systematic way. While we do not yet include state constraints in our control implementation, we have laid the ground work in building a suitable model predictive control framework for $q$ profile control at the DIII-D tokamak that could later be expanded to include state constraints associated with the avoidance

of deleterious MHD activity.

Model predictive control has developed significantly over the last few decades [79], while originally only applicable to problems with slow time scales due to the intense computational requirements of MPC, improvements in optimization algorithms that exploit the problem structure have made MPC applicable to medium sized problems requiring fast update times between 1-5 ms [80]. We use a simple active set method [81], which combined with *warm-starting* of the optimization problem as described in Appendix D.2 allows for sufficiently fast control computation times of 1 ms. This implies the control updates can be computed sufficiently fast to allow real-time applicability for current profile control, and this is confirmed by experimental tests presented in this chapter.

This chapter is organized as follows. In Section 6.2, the feedback control approach by model predictive reference tracking is described, and in Section 6.3, the details for incorporating state constraints are described. The control system is embedded into the DIII-D plasma control system (PCS) for experimental testing, and initial tests of the proposed control method are presented in Sections 6.4 and 6.5. Initial experimental results did not consider state constraints, i.e. those constraints associated with obtaining stationary conditions in the plasma and avoidance of $\beta_N$ limits. In Section 6.6, simulations demonstrating the effect of these constraints are presented. Finally, a statement of conclusions is made in Section 6.7.

## 6.2 Current Profile Reference Tracking via Model Predictive Control

As in the previous chapter, the control objective is to reach a specified target profile shape at a specified time. Again, the control strategy involves, first, computing an open-loop control problem, which is formulated as a trajectory optimization problem to find a feasible path from the expected initial condition to the desired target. The problem involves the minimization of a scalar objective over a set of constraints associated with the dynamics of the system (model of the $q$ profile evolution), actuator

**Figure 6.1:** Model predictive control framework. The system evolution is predicted over a short horizon ($T$) in response to an applied control sequence. An optimal control sequence is determined and the first change to the control sequence is applied to the system. Then, on the next time step, the system state is sampled again and a new control sequence is computed over a receding horizon.

constraints (physical limits such as max NBI power), and bounds on the acceptable current profile shape through the ramp-up phase (see Section 4 for details). The result of the optimization procedure is an open-loop sequence of NBI powers, ECCD powers, and total plasma current and a corresponding state trajectory that reaches the target. The role of the feedback controller is to track the optimal state trajectory (desired current profile evolution).

### 6.2.1 Overview of Model Predictive Control

Upon the initial sampling time, the predicted behavior of the system in response to the control variable is considered over a short horizon, $T$. A sequence of controlled variables is selected such that the predicted response is as close as possible to some set of desired characteristics. Only the first computed change to the control variable is applied, and this process repeats at each time step.

If the model completely and accurately described all of the underlying dynamics of the system, we could simply apply the entire control sequence computed on the first time step and expect to see the same results as predicted by the model. However, since the model is only approximate, we expect to see some discrepancy between the predicted and measured state at the subsequent time step. Therefore, the common

practice is to apply the first step of the sequence, then sample the state again, and repeat the optimization procedure, which introduces feedback to the control.

### 6.2.2 Linearized Error Dynamics

Let $\mathbf{u}^{\mathrm{FF}}(t)$ represent the feedforward control sequence, and let $\boldsymbol{\theta}^{\mathrm{FF}}(t)$ and $\boldsymbol{\iota}^{\mathrm{FF}}(t)$ represent, respectively, the corresponding feedforward state and output trajectory obtained from the feedforward control optimization. In a neighborhood of the feedforward trajectory we can approximate the dynamics (4.10) with the truncated Taylor series,

$$\begin{aligned}\dot{\boldsymbol{\theta}} \approx & \boldsymbol{f}_{\theta}(\boldsymbol{\theta}^{\mathrm{FF}}(t), \mathbf{u}^{\mathrm{FF}}(t)) + \left.\frac{\partial \boldsymbol{f}_{\boldsymbol{\theta}}}{\partial \boldsymbol{\theta}}\right|_{\substack{\boldsymbol{\theta}^{\mathrm{FF}}(t) \\ \mathbf{u}^{\mathrm{FF}}(t)}} \left(\boldsymbol{\theta} - \boldsymbol{\theta}^{\mathrm{FF}}(t)\right) \\ & + \left.\frac{\partial \boldsymbol{f}_{\boldsymbol{\theta}}}{\partial \mathbf{u}}\right|_{\substack{\boldsymbol{\theta}^{\mathrm{FF}}(t) \\ \mathbf{u}^{\mathrm{FF}}(t)}} \left(\mathbf{u} - \mathbf{u}^{\mathrm{FF}}(t)\right).\end{aligned} \tag{6.1}$$

Introducing the term $\tilde{\mathbf{u}} = \mathbf{u} - \mathbf{u}^{\mathrm{FF}}$ and discretizing time derivative of the system (6.1) with a semi-implicit scheme, we can obtain the affine time-varying model,

$$\boldsymbol{\theta}_{k+1} = \mathbf{A}_k \boldsymbol{\theta}_k + \mathbf{B}_k \tilde{\mathbf{u}}_k + \mathbf{a}_k, \quad \boldsymbol{\iota}_k = \mathbf{C}\boldsymbol{\theta}_k, \tag{6.2}$$

where

$$\begin{aligned}\mathbf{A}_k &= \left(\boldsymbol{I} - T_s \left.\frac{\partial \boldsymbol{f}_{\boldsymbol{\theta}}}{\partial \boldsymbol{\theta}}\right|_{\substack{\boldsymbol{\theta}^{\mathrm{FF}}_{k+1} \\ \mathbf{u}^{\mathrm{FF}}_{k}}}\right)^{-1}, \quad \mathbf{B}_k = \mathbf{A}_k T_s \left.\frac{\partial \boldsymbol{f}_{\boldsymbol{\theta}}}{\partial \mathbf{u}}\right|_{\substack{\boldsymbol{\theta}^{\mathrm{FF}}_{k+1} \\ \mathbf{u}^{\mathrm{FF}}_{k}}}, \\ \mathbf{a}_k &= \mathbf{A}_k T_s \left(\boldsymbol{f}_{\boldsymbol{\theta}}(\boldsymbol{\theta}^{\mathrm{FF}}_{k+1}, \mathbf{u}^{\mathrm{FF}}_{k}) - \left.\frac{\partial \boldsymbol{f}_{\boldsymbol{\theta}}}{\partial \boldsymbol{\theta}}\right|_{\substack{\boldsymbol{\theta}^{\mathrm{FF}}_{k+1} \\ \mathbf{u}^{\mathrm{FF}}_{k}}} \boldsymbol{\theta}^{\mathrm{FF}}_{k+1}\right),\end{aligned}$$

(see Figure 6.2(a)) and $T_s$ is the time step. The affine term $\mathbf{a}_k$ arises due to the fact that we are writing the model in terms of the full state rather than the more common error state, i.e. the state relative to the feedforward value, for reasons discussed in the next section. Given that there is a one-to-one relationship between $\boldsymbol{\theta}$ and $\boldsymbol{\iota}$, we can eliminate $\boldsymbol{\theta}$ for simplicity of control design,

$$\boldsymbol{\iota}_{k+1} = \mathbf{A}_k \boldsymbol{\iota}_k + \mathbf{B}_k \tilde{\mathbf{u}}_k + \mathbf{a}_k, \tag{6.3}$$

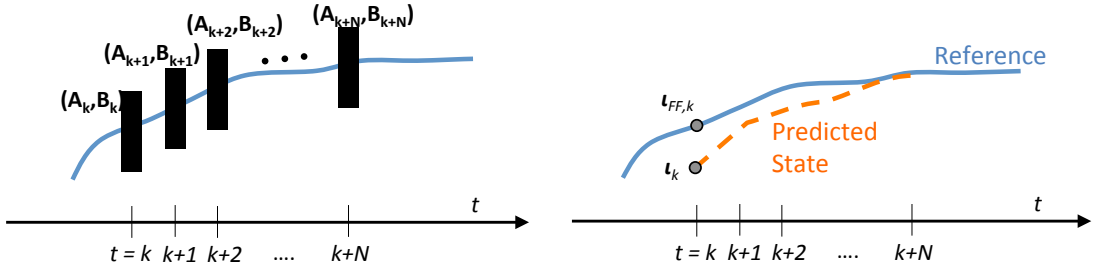


(a) Linearizations around feedforward trajectory.

(b) Finite horizon reference tracking problem.

**Figure 6.2:** Diagrams for linearization around the feedforward trajectory and reference tracking around the feedforward trajectory.

where we have overwritten $\mathbf{A}_k$, $\mathbf{B}_k$, and $\mathbf{a}_k$ with $\mathbf{A}_k \leftarrow \mathbf{C}\mathbf{A}_k\mathbf{C}^{-1}$, $\mathbf{B}_k \leftarrow \mathbf{C}\mathbf{B}_k$, $\mathbf{a}_k \leftarrow \mathbf{C}\mathbf{a}_k$.

This affine formulation has two main advantages: *i*) it allows direct inclusion of the reference value $\boldsymbol{\iota}^{\mathrm{FF}}$ in the objective function, allowing the controller to anticipate future reference changes, and *ii*) it becomes more convenient to include constraints on the state variables.

### 6.2.3 Model Predictive Reference Tracking Control Structure

We use the total plasma current to regulate the $q$ profile at the edge with a classical linear quadratic integral (LQI) controller, in the same way as Section 5.3.3. This ensures that the controller will hit the target $q$ value at the plasma edge. In the control design approach that follows, including $I_\mathrm{p}$ as a control variable is problematic because the target $q$ profile is expected to be difficult to achieve. If $I_\mathrm{p}$ were included as an actuator, the controller might attempt to reduce $I_\mathrm{p}$ to undesirably low values to minimize overall profile matching across the profile interior. While it can be advantageous to use $I_\mathrm{p}$ to control the profile shape as a boundary actuator, we elect to dedicate $I_\mathrm{p}$ towards control of the profile edge to avoid the possibility of undesirably low $I_\mathrm{p}$ values. The following design could potentially be modified to include $I_\mathrm{p}$ as an actuator with added constraints to prevent $I_\mathrm{p}$ from falling undesirably low.

To control the $q$ profile interior, we consider the trajectory tracking problem formulated as a finite-horizon, optimal control problem. As illustrated in Figure 6.2(b), the feedback controller predicts $\iota$ profile evolution over a short horizon and updates the control action to maintain $\iota$ on the feedforward evolution. At time $k$, we consider the quadratic optimization problem

$$
\begin{aligned}
\underset{\{\Delta\tilde{\mathbf{u}}^{\mathrm{c}}_{k+t}\}_{t=0}^{H_u}}{\text{minimize}} \quad & J_k = \sum_{t=1}^{H_p} \left\| \boldsymbol{\iota}_{k+t} - \boldsymbol{\iota}^{\mathrm{FF}}_{k+t} \right\|_{\mathbf{Q}} + \sum_{t=0}^{H_u} \left\| \Delta\tilde{\mathbf{u}}^{\mathrm{c}}_{k+t} \right\|_{\mathbf{R}}, \\
\text{subject to} \quad & \boldsymbol{\iota}_{k+t+1} = \mathbf{A}_{k+t}\boldsymbol{\iota}_{k+t} + \mathbf{B}^{\mathrm{c}}\tilde{\mathbf{u}}^{\mathrm{c}}_{k+t} + \mathbf{B}^{\mathrm{nc}}\tilde{\mathbf{u}}^{\mathrm{nc}}_{k+t} + \mathbf{a}_{k+t}, \\
& \boldsymbol{\iota}_k = \boldsymbol{\iota}[k] : \text{ initial condition}, \\
& \Delta\tilde{\mathbf{u}}^{\mathrm{c}}_{k+t} = \tilde{\mathbf{u}}^{\mathrm{c}}_{k+t} - \tilde{\mathbf{u}}^{\mathrm{c}}_{k+t-1}, \\
& \tilde{\mathbf{u}}^{\mathrm{c}}_{k-1} = \text{previously applied control}, \\
& \tilde{\mathbf{u}}^{\mathrm{nc}}_{k+t} = \tilde{\mathbf{u}}^{\mathrm{nc}}_{k} \text{ for } t = 0, 1, \ldots H_u, \\
& \mathbf{u}_{k+t} \in \mathcal{U}_{k+t} \text{ for } t = 0, 1, \ldots H_u, \\
& \boldsymbol{\iota}_{k+t} \in \mathcal{I}_{k+t} \text{ for } t = 1, 2 \ldots H_p.
\end{aligned}
\tag{6.4}
$$

The cost function $J_k$ includes an instantaneous cost on deviations of the $\boldsymbol{\iota}$ profile from the desired feedforward trajectory ($\boldsymbol{\iota}_{\mathrm{FF}}$) over the prediction horizon, $H_p$. Also, an instantaneous cost is applied to deviations in the control, $\Delta\tilde{\mathbf{u}}^{\mathrm{c}}_{k+t} = \tilde{\mathbf{u}}^{\mathrm{c}}_{k+t} - \tilde{\mathbf{u}}^{\mathrm{c}}_{k+t-1}$, implying no cost for the control sequence to be away from the value associated with feedforward trajectory, $\mathbf{u}_{\mathrm{FF}}$, but there is a cost for fast rate changes. The actuators have been split into controlled $\mathbf{u}^{\mathrm{c}}_k = [P_{\mathrm{NB},3}, \ldots, P_{\mathrm{NB},n_{\mathrm{NBI}}}]$ and uncontrolled $\mathbf{u}^{\mathrm{nc}}_k = [P_{\mathrm{NB},1}, P_{\mathrm{NB},2}, P_{\mathrm{EC},1}, \ldots, P_{\mathrm{EC},n_{\mathrm{EC}}}, I_{\mathrm{p}}]$. The first two NBI are dedicated to diagnostics, the total plasma current is controlled via LQI control, and the ECCD are only controlled via feedforward. We allow the prediction horizon associated with the control, $H_u$, to be less than the prediction horizon associated with the state, to reduce the complexity of the problem. We assume no further update in the control beyond the control horizon, i.e. $\mathbf{u}^{c}_{k+t+1} = \mathbf{u}^{c}_{k+t}$ for $t \geq H_u$ and we replace the future uncontrolled actuators (which are yet unknown) with their current values. Because the density is difficult to control with real accuracy in tokamaks, future density values are taken as unknown. The terms $\{\mathbf{u}_{k+t} \in \mathcal{U}_{k+t}\}_{t=0}^{H_u}$ and $\{\boldsymbol{\iota}_{k+t} \in \mathcal{I}_{k+t}\}_{t=1}^{H_p}$

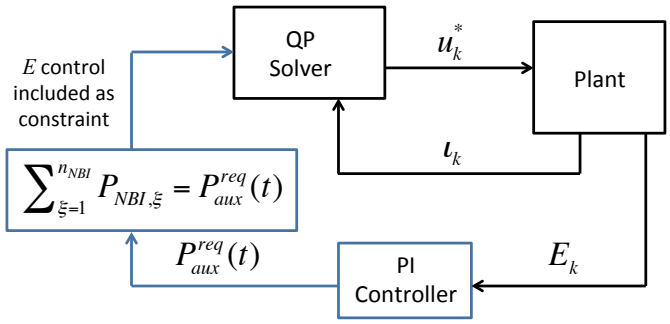


**Figure 6.3:** MPC for profile tracking with total power constraint to satisfy desired plasma stored energy.

describe linear constraints on the actuators and states to be described.

The optimal control problem (6.4) consists of the minimum of a quadratic function over a set of linear constraints. This type of quadratic optimization problem involving a positive definite cost function ($\mathbf{R} > 0$ and $\mathbf{Q} \geq 0$) can be solved efficiently using active set techniques, which take advantage of the fact that the set of active constraints on sequential control updates does not change dramatically, and thus the active set information from the previous control update can be used to warm start the solution on the next control update (see Appendix D.2).

### 6.2.4 Plasma Stored Energy Control

For control design purposes, the plasma stored energy evolution is approximated by the linear system,

$$\frac{dE}{dt} = -\frac{E}{\tau_{\mathrm{E_{eq}}}} + P_{\mathrm{aux}}(t), \tag{6.5}$$

where the contributions of ohmic power and radiative power are dropped since they are relatively small compared to the auxiliary power, and we have assumed a constant energy confinement time $\tau_{\mathrm{E_{eq}}}$, which is associated with the operating point of the target $q$ profile. The approximate energy dynamics (6.5) describe a linear first order system, therefore with a simple proportional-integral (PI) controller we can obtain acceptable closed loop performance. For a target energy $E^{\mathrm{targ}}$, the PI

controller,

$$P_{\text{aux}}^{\text{req}}(t) = k_p(E^{\text{targ}}(t) - E(t)) + k_i \int_0^t E^{\text{targ}}(\tau) - E(\tau) d\tau, \tag{6.6}$$

provides a request for total auxiliary input power, $P_{\text{aux}}^{\text{req}}(t)$, which can enter into the MPC problem (6.4) as an equality constraint on total auxiliary input power. The control design knobs $k_p$ and $k_i$ represent the proportional and integral control gains, respectively. A block diagram of the combined controller, MPC $q$ profile reference tracking plus energy control constraint, is shown in Figure 6.3. The constraint on total auxiliary input power can be written as

$$\sum_{\xi=1}^{n_{\text{NBI}}} \tilde{P}_{\text{NBI},\xi} + \tilde{P}_{\text{EC}} = P_{\text{aux}}^{\text{req}}(t) - \sum_{\xi=1}^{n_{\text{NBI}}} P_{\text{NBI},\xi}^{\text{FF}} - P_{\text{EC}}^{\text{FF}}, \tag{6.7}$$

where the NBI and EC powers have been separated into feedback components denoted by $\tilde{\cdot}$ and feedforward components. Note that (6.7) represents a linear constraint on the control variables, therefore it can be incorporated without modification into problem (6.4) over the control horizon, $H_u$. In this manner we can obtain the desired plasma stored energy, and then allow the MPC controller to find the best combination of individual NBI powers satisfying the total power constraint[1], which tracks the desired $q$ profile evolution.

### 6.2.5 Relaxing the Energy Control Constraint

The inclusion of the energy control as an input constraint is an effective strategy when the energy target is well chosen, i.e. it is consistent with the desired $q$ profile evolution. Essentially what the controller does is first specify the total NBI power necessary to maintain the desired plasma stored energy target, then selects the best combination of on-axis (330L and 330R) and off-axis (150L and 150R) NBI powers to best reach target $q$ profile. However, the possibility remains that the energy control constraint could limit the controller's freedom to obtain the desired $q$ profile target

[1]ECCD power is controlled in feedforward only for this work.

if the energy target is inappropriately selected. To address this potential outcome, we can replace the energy control constraint (6.7) with the inequalities,

$$\begin{aligned}\sum_{\xi=1}^{n_{\text{NBI}}} \tilde{P}_{\text{NBI},\xi} + \tilde{P}_{\text{EC}} &\leq P_{\text{aux}}^{\text{req}}(t) - \sum_{\xi=1}^{n_{\text{NBI}}} P_{\text{NBI},\xi}^{\text{FF}} - P_{\text{EC}}^{\text{FF}} + \epsilon_{\text{win},L}, \\ \sum_{\xi=1}^{n_{\text{NBI}}} \tilde{P}_{\text{NBI},\xi} + \tilde{P}_{\text{EC}} &\geq P_{\text{aux}}^{\text{req}}(t) - \sum_{\xi=1}^{n_{\text{NBI}}} P_{\text{NBI},\xi}^{\text{FF}} - P_{\text{EC}}^{\text{FF}} - \epsilon_{\text{win},H},\end{aligned} \tag{6.8}$$

where $\epsilon_{\text{win}}$ represents a window on forgiveness of satisfying the energy control constraint. It should be made clear, $\epsilon_{\text{win}L}$ and $\epsilon_{\text{win}H}$ are included as a control knobs to be selected during experiments not as optimization variables.

## 6.3 Additional Constraints for $q$ Profile Tracking MPC

Any constraint that can be written as a linear function of the optimization variables can be added to the problem (6.4). In this section, constraints to prevent the controller from exceeding a $\beta_N$ limit, maintenance of $q > 1$, and a constraint for achievement of stationary conditions are added to the MPC $q$ profile tracking problem.

### Enforcement of $\beta_N$ Limit

Deleterious MHD activity can be avoided by maintaining $\beta_N$ below a specified limit, $\beta_N^{\max}$. To help ensure stable plasma conditions during the discharge, we can predict changes to $\beta_N$ over the prediction horizon and enforce a constraint in the total auxiliary power to maintain $\beta_N$ below an acceptable limit. Recall from (3.18), the normalized $\beta$ can be expressed as $\beta_N = k_{\beta_N} \frac{E}{I_{\text{p}}}$, where $k_{\beta_N}$ is a constant depending on the plasma volume, plasma minor radius, and toroidal magnetic field.

At time $k$, we can take the approximate value of the energy confinement time ($\tau_{E,k} \propto I_{\text{p},k}^{0.93} \bar{n}_{\text{e},k}^{0.41} P_{\text{tot},k}^{-0.69}$) and measured energy $E_k$, to estimate the forward evolution

of $\beta_N$ according to

$$\beta_{N,k+t} = k_{\beta_N}\frac{E_{k+t}}{I_{\mathrm{p},k+t}}, \qquad \begin{aligned} E_{k+1} &= A_E E_k + B_E P_{\mathrm{aux},k}, \\ E_{k+2} &= A_E^2 E_k + A_E B_E P_{\mathrm{aux},k} + B_E P_{\mathrm{aux},k+1}, \\ E_{k+3} &= A_E^3 E_k + A_E^2 B_E P_{\mathrm{aux},k} + A_E B_E P_{\mathrm{aux},k+1} \\ &\qquad + B_E P_{\mathrm{aux},k+2}, \\ E_{k+H_p} &= A_E^{H_p} E_k + \sum_{i=0}^{H_p-1} A_E^i B_E P_{\mathrm{aux},k+H_p-1-i}, \end{aligned} \tag{6.9}$$

where $A_E = \left(1 + \frac{1}{\tau_{E,k}}T_s\right)^{-1}$ and $B_E = A_E T_s$. Since the plasma current is not included as an actuator in the MPC problem (6.4), we can assume the evolution of $I_\mathrm{p}$ is prescribed over the prediction horizon according to $I_{\mathrm{p},k+t} = I_{\mathrm{p,FF},k+t} + I_{\mathrm{p,FB},k}$, i.e. the feedforward value over the prediction horizon plus the last feedback update. Thus, the constraint on $\beta_N$ reduces to a maximum bound on total requested auxiliary power. With the prediction equations (6.9), we can transform the $\beta_N$ limit over the prediction horizon, $\beta_{N,k+t}|_{t=0,1,\ldots,H_p} \leq \beta_N^{\max}$ into a constraint on maximum auxiliary power input. In order to ensure the MPC problem remains feasible, potential conflicts between the $\beta_N$ limit and the energy control constraint (6.7) are alleviated by softening the energy control constraint with a forgiveness parameter,

$$P_{\mathrm{aux}}^{\mathrm{req}}(t) - \epsilon_\mathrm{E} \leq \left\{ \left[ \sum_{\xi=1}^{n_\mathrm{NBI}} P_{\mathrm{NBI},\xi} + P_\mathrm{EC} \right]_{k+t} \right\}_{t=0}^{H_u} \leq P_{\mathrm{aux}}^{\mathrm{req}}(t) + \epsilon_\mathrm{E}, \tag{6.10}$$

where $\epsilon_E \geq 0$ represents a window on forgiveness of satisfying the energy control constraint. The forgiveness parameter is included as an optimization variable in the MPC problem (6.4) by replacing the optimization objective with

$$J_k + W_E \epsilon_E^2, \tag{6.11}$$

the MPC problem will minimize violation of the energy control constraint, where $W_E$ is introduced as a weight.

### Constraint for Maintenance of $q > 1$

The lower bound on $q$ (4.25) can be equivalently written as the constraint $\boldsymbol{\iota} < 1$ over the prediction horizon, i.e. $\boldsymbol{\iota}_{k+t} < 1$ for $t = 1, 2, \ldots, H_p$. Given the limitations in achievable current profile shapes it is sufficient, for control purposes, to apply the constraint at only two points on $\hat{\rho}$ $(= 0.05, 0.4)$, we have

$$\mathbf{C}_q \boldsymbol{\iota}_{k+t} \leq 1.0 \quad \text{for} \quad t = 1, 2, \ldots, H_p, \tag{6.12}$$

where $(\mathbf{C}_q \boldsymbol{\iota})^T = \left[ \iota|_{\hat{\rho}=0.05} \, , \, \iota|_{\hat{\rho}=0.4} \right]$. Finally, to ensure feasibility, the above constraint can be softened with the inclusion of a forgiveness parameter, $\epsilon_q > 0$,

$$\mathbf{C}_q \boldsymbol{\iota}_k \leq 1 + \epsilon_q, \tag{6.13}$$

where, again, $\epsilon_q$ is incorporated into the cost function, $J_k$ of the MPC problem (6.4),

$$J_k \leftarrow J_k + W_E \epsilon_E^2 + W_q \epsilon_q^2, \tag{6.14}$$

so that the control will minimize violation of the constraint.

### Constraint for Achievement of Stationarity

We can attempt to control for steady-state conditions or more precisely stationarity of the plasma by applying an additional set of constraints. A stationary[2] plasma is typically described by a flat loop voltage profile, where the loop voltage is given by

$$U_{\mathrm{p}} = 2\pi \frac{\partial \psi}{\partial t}. \tag{6.15}$$

We can recognize a flat loop voltage profile when the spatial gradient of the loop voltage is identically zero,

$$\frac{\partial U_{\mathrm{p}}}{\partial \hat{\rho}} \equiv 0. \tag{6.16}$$

Since the spatial derivative of the loop voltage profile is proportional to the time derivative of the $\iota$ profile (from (4.5)), we can control for stationarity by applying the constraint $\partial \iota / \partial t = 0$, or equivalently

$$\boldsymbol{\iota}_{k+t+1} = \boldsymbol{\iota}_{k+t} \quad \text{for} \quad t = 1, 2, \ldots, H_p - 1. \tag{6.17}$$

[2]The term stationarity is used to avoid confusion with the term "steady-state" which is often used to described a loop voltage profile identically equal to zero.

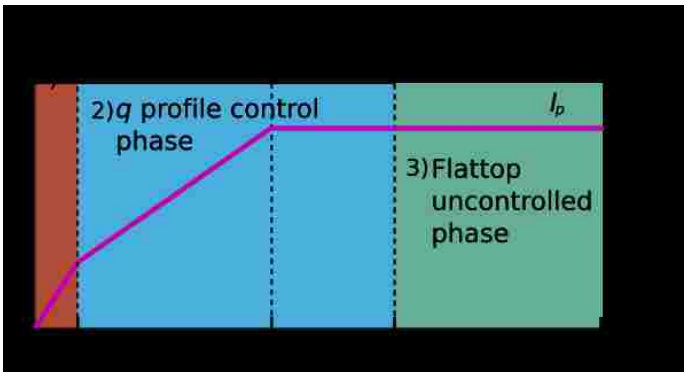


**Figure 6.4:** Each $q$ profile control test discharge is partitioned as follows: 1) EC-heated start-up and ramp-up to 0.4 kA, 2) $q$ profile control phase, 3) uncontrolled flattop phase.

in the MPC problem (6.4). However, it certainly does not make sense to apply this constraint throughout the entire control phase. Instead there should be a trigger event or a specific time during the control phase at which this constraint is applied. Again the constraint is applied only at certain points in $\hat{\rho}$ and softened with the introduction of another forgiveness parameter,

$$-\epsilon_{ss} \leq \mathbf{C}_{ss}\boldsymbol{\iota}_{k+t+1} - \mathbf{C}_{ss}\boldsymbol{\iota}_{k+t} \leq \epsilon_{ss}, \quad \epsilon_{ss} \geq 0. \tag{6.18}$$

All of the constraint forgiveness parameters are included as optimization variables in the MPC problem (6.4), and the optimization objective is replaced by,

$$J_k \leftarrow J_k + W_E\epsilon_E^2 + W_q\epsilon_q^2 + W_{ss}\epsilon_{ss}^2, \tag{6.19}$$

where $W_{ss}$ is introduced as a weight.

## 6.4 Experimental Setup

In this section we consider multiple $q$ profile control tests conducted at DIII-D demonstrating the effectiveness of the proposed control approach. As shown in Figure 6.4, the discharges were partitioned into three phases involving: an EC-heated start-up and ramp-up phase, where the plasma current is ramped to 0.4 kA,

followed by a $q$ profile control phase from time $t = 0.4$ s until $t = t_2$ (the target time), and, finally, a fixed power flattop phase for $t \geq t_2$. The first phase involved an experimental method using ECCD power to assist the plasma breakdown for more reliable access to H-mode [82]. Because the EC-assisted start-up was experimental, it created a significant degree of variability in the plasma state at the start of the $q$ profile control phase, which is useful for testing the robustness of the profile controller. After the $q$ profile control phase, the remainder of the discharge was carried out with fixed NBI power, allowing the $q$ profile to relax uncontrolled. The idea is to test different $q$ profiles for accessibility to steady-state and robustness against the development of MHD activity during the third phase, where the intent of the $q$ profile controller is to achieve the target $q$ profile.

The MPC optimization problem (6.4) combined with the constraint (6.7), is composed of the minimization of a quadratic function over a set of linear constraints, a quadratic program (QP). Defining the optimization variables as the sequence of controls and constraint relaxation parameters of (6.19), $\mathbf{z} = [\tilde{\mathbf{U}}^{\mathrm{c}}_k, \epsilon_E, \epsilon_q, \epsilon_{ss}]$ (see Appendix B.4.1), the problem can be converted to a standard form,

$$\begin{aligned} \underset{\mathbf{z}}{\text{minimize}} \quad & \frac{1}{2}\mathbf{z}^T\mathbf{H}_k\mathbf{z} + \mathbf{h}_k^T\mathbf{z}, \\ \text{subject to} \quad & \mathbf{A}_{\mathrm{eq},k}\mathbf{z} = \mathbf{b}_{\mathrm{eq},k}, \\ & \mathbf{A}_{\mathrm{in},k}\mathbf{z} \leq \mathbf{b}_{\mathrm{in},k}, \end{aligned} \tag{6.20}$$

and solved according to the active set method described in Appendix D.2. The matrices of problem (6.20) are time-varying on account of the time-varying dynamics, non-constant reference, and feedforward control. The controller work flow is summarized in Algorithm 1. First, control updates for the total plasma current and the total auxiliary power (6.6) are computed, then the QP problem (6.20) is constructed and solved. A new control update is computed every 20 ms, however, we apply a zero-order-hold on updates to the model matrices (6.3) of 100 ms, reducing the set of QP matrices to 24 for the entire tokamak discharge (control phase extends from $t = 0.4$ to $t_2 = 3.0$ s).

The controller was implemented in C and compiled with the optimized intel compiler (icc). On average, the computation time was just above 1 ms (and worst

**Algorithm 1:** $q$ profile MPC workflow

*Compute and store the pre-computable components of* $\mathbf{H}_k$, $\mathbf{f}_k$, $\mathbf{A}_{\text{eq},k}$, $\mathbf{b}_{\text{eq},k}$, $\mathbf{A}_{\text{in},k}$, $\mathbf{b}_{\text{in},k}$ of problem (6.20) (see Appendix B.4)
**for** *all* $k$ **do**
  Update $I_p$ control request to regulate $q_{95}$ with LQI controller (see Section 5.3.3)
  Update the total auxiliary power control request ($P_{\text{aux}}^{\text{req}}$) to regulate the plasma stored energy (see Section 6.2.4)
  Load the precomputed components of the QP problem matrices associated with the current time step $k$
  Get latest state measurement $\mathbf{x}_k = \begin{bmatrix} \boldsymbol{\iota}_k \\ E_k \end{bmatrix}$ and last applied control $\mathbf{u}_{k-1}^{\text{c}}$
  Construct the QP problem (6.20) with $\mathbf{x}_k$ and $\mathbf{u}_{k-1}$ (see Appendix B.4.1)
  Solve QP to compute next control update $\mathbf{u}_k$ (see Appendix D.2)
**end**

case of 4ms) during the experiments with a 3.5 Ghz processor. The efficiency of the algorithm is primarily due to the fact that the number of active constraints on sequential control updates does not change dramatically, and thus the active set information from the previous control update can be used to warm start the QP on the next control update. This allows for a significant reduction in the number of iterations, and therefore linear system solves, necessary to solve the QP. For more than 90% of control updates, the QP is solved in fewer than 3 iterations as shown in Figure 6.5.

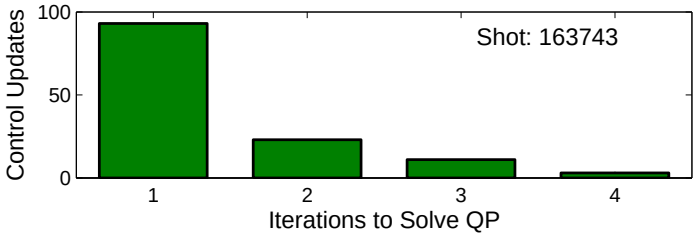


**Figure 6.5:** Number of QP solver iterations required for each control update. Results from feedback control test shot 163743.

Of the eight NBI sources available, two (30L and 30R) are dedicated to diagnostics associated with the Motional Stark Effect (MSE), which is used in the real time EFIT calculation to obtain measurements of the $q$ profile ([83]). Therefore, 30L and 30R are not available for control. Instead these two NBI contribute a constant 1 MW of power each. The two counter-current NBI (210L and 210R) were not used in past experiments because of the tendency of counter-current NBI to destabilize NTMs. This leaves four NBI sources available for control, the two on-axis, co-current NBI (330L and 330R) and the two off-axis, co-current NBI (150L and 150R) (see Figure 1.10(a)). Finally, the ECCD is only included as a feedforward control actuator, it turns on full just before the target time in an attempt to help freeze in the target profile by heating the plasma and therefore slowing the diffusion rate.

## 6.5 Experimental Results

To begin, we consider a zero shear target profile with $q_{\min} = 1.6$ and $q_{95} = 5$. A control test involving only control of the $q$ profile, i.e. no energy control constraint, is shown in Figure 6.6, and tests involving $q$ profile plus energy control are shown in Figure 6.7, where the energy control is incorporated via a constraint to the MPC problem as described in Section 6.2.4 (Figure 6.3). In all cases, the obtained $q$ profile is plotted in the upper left of the respective figures in comparison to the $q$ profile obtained with feedforward control alone. The failure of the feedforward control action to reach the target is primarily due to slight modeling errors in the resistive diffusion rate. This emphasizes the importance of feedback control, which is able to account for the modeling errors and bring the $q$ profile back on target.

In the upper right of the figures, the plasma stored energy is plotted, comparing the target value with that obtained with feedforward control only and feedforward + feedback control. Considering Figure 6.6 vs Figure 6.7, we see that controlling the $q$ profile alone leads to rather aggressive control action and therefore a choppy undesirable response in the plasma stored energy when compared to that obtained with $q$ + energy control. Note, that in Figure 6.6, the effects of the aggressive

control action are observed in the response of $\beta_N$ ($\beta$ normalized to the total plasma current), which can be problematic. If $\beta_N$ is allowed to go too high too early this can potentially seed magnetic islands that can grow and corrupt the confinement of the plasma.

Similar results are obtained for other $q$ profile targets with increased levels of $q_{\min}$ during with $q$ + energy control experiments. In Figure 6.8, targets of $q_{\min} = 1.9$ and $q_{95} = 5$ (shot 163832) $q_{\min} = 1.7$ and $q_{95} = 5$ (shot 163836) are tested.

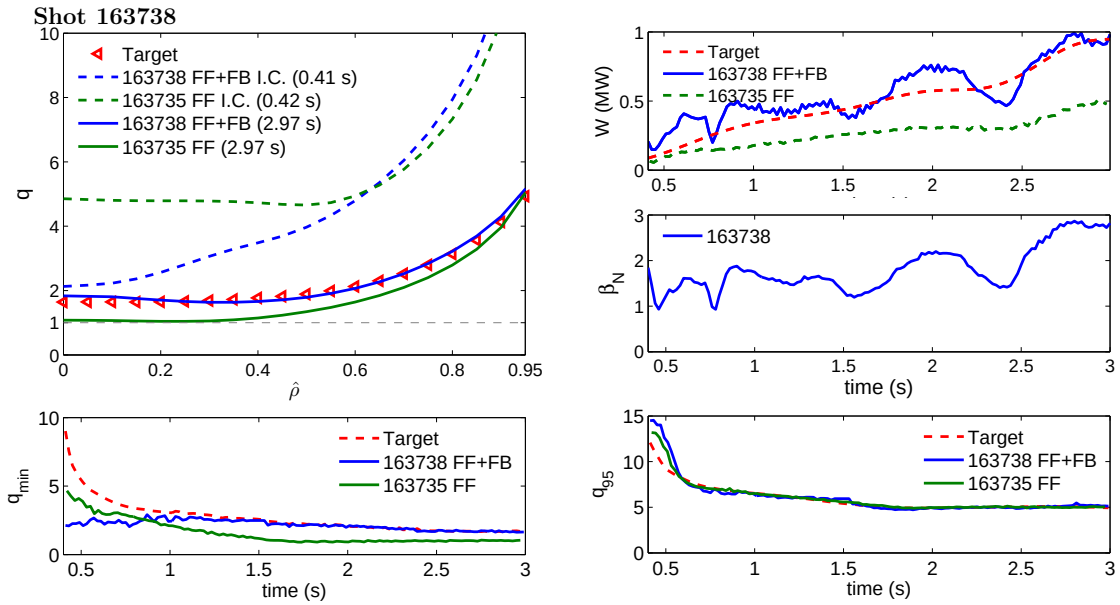


**Figure 6.6:** Shot 163738: $q$ control only. Target: $q_{\min} = 1.6$ and $q_{95} = 5$. In the left column the achieved $q$ profile at the target time for both feedforward control and feedforward + feedback control cases is displayed followed by the $q_{\min}$ value. In the right column starting from the top the plots include the plasma stored energy, $\beta_N$, and achieved $q_{95}$ for both feedforward and feedforward + feedback cases.

### 6.5.1 Experimental Results with Relaxed Energy Control Constraint

Some experiments testing the relaxed energy control constraint strategy defined by (6.8) are shown in Figure 6.9, and Figure 6.10. In the first case, Figure 6.9, the forgiveness window is chosen as $\epsilon_{\text{win}L} = 1.5$ and $\epsilon_{\text{win}H} = 0.5$ and in the second case,

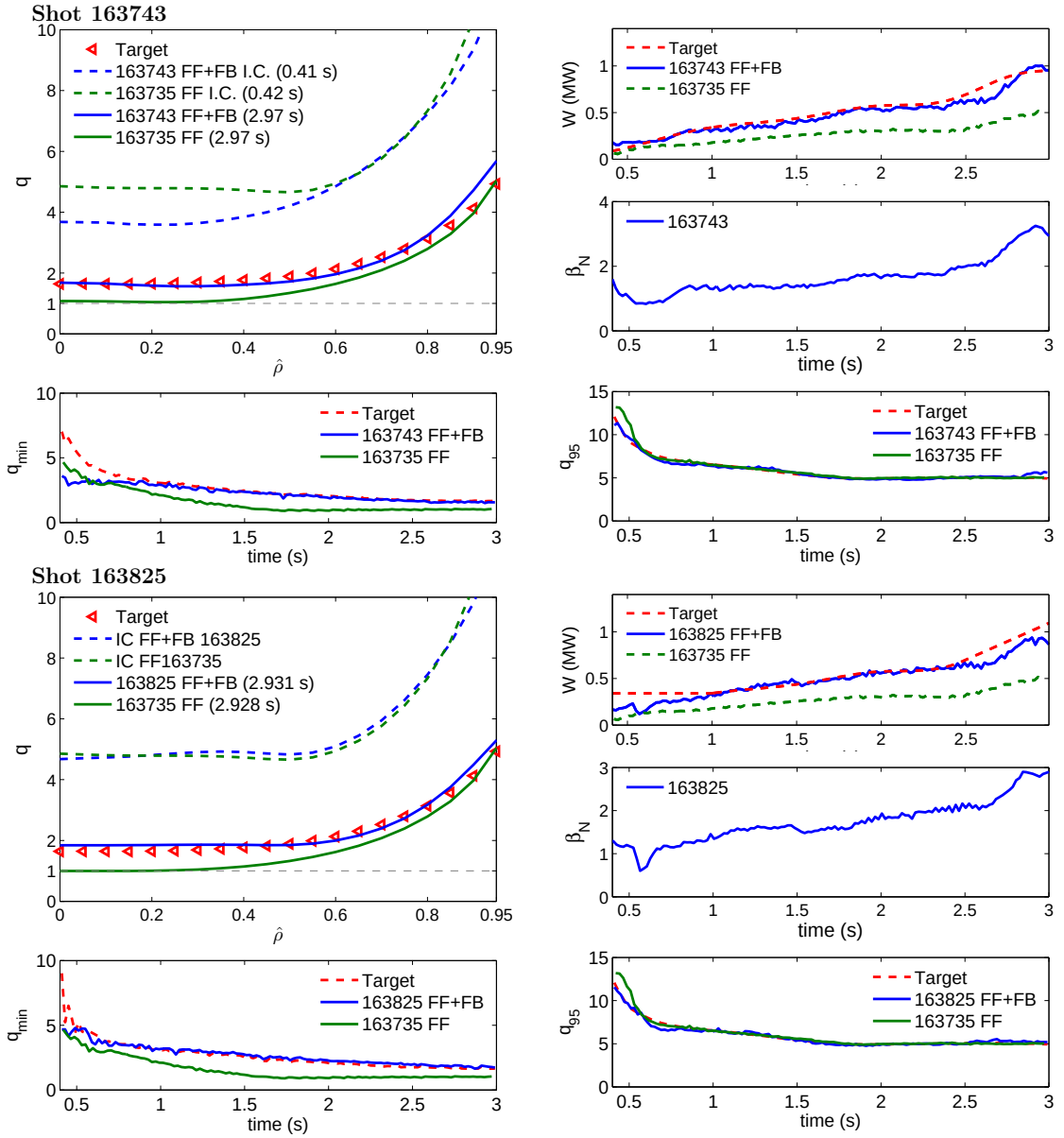


**Figure 6.7:** (Top) shot 163743: $q$ + energy control with target: $q_{\min} = 1.6$ and $q_{95} = 5$. (Bottom) shot 163832: $q$ + energy control and target: $q_{\min} = 1.6$ and $q_{95} = 5$.

Figure 6.10, the control window is chosen as $\epsilon_{\text{win}L} = 1.5$ and $\epsilon_{\text{win}H} = 0.5$. These shots also incorporate a hard lower bound on total NBI to prevent back transitions to L-mode (1.0 MW for shot 165917 in Figure 6.9 and 1.5 MW for shot 165922 in Figure 6.10). In both cases, the total injected power is usually at the limits of

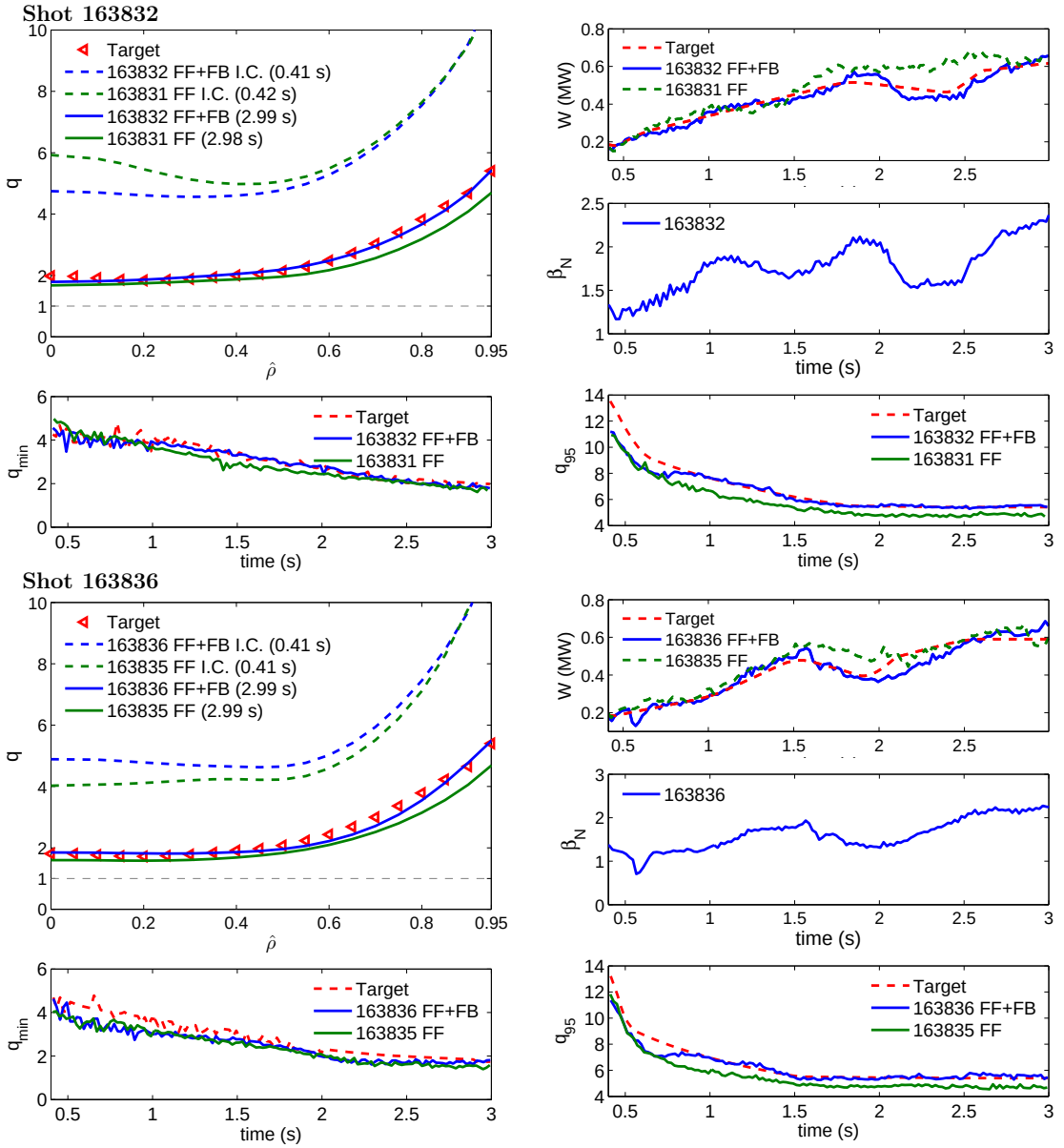


**Figure 6.8:** (Top) shot 163832: $q$ + energy control with target: $q_{\min} = 1.9$ and $q_{95} = 5$. (Bottom) shot 163836: $q$ + energy control with target: $q_{\min} = 1.7$ and $q_{95} = 5$.

window. This leads to an offset in the energy and target energy but aids control of the current profile.

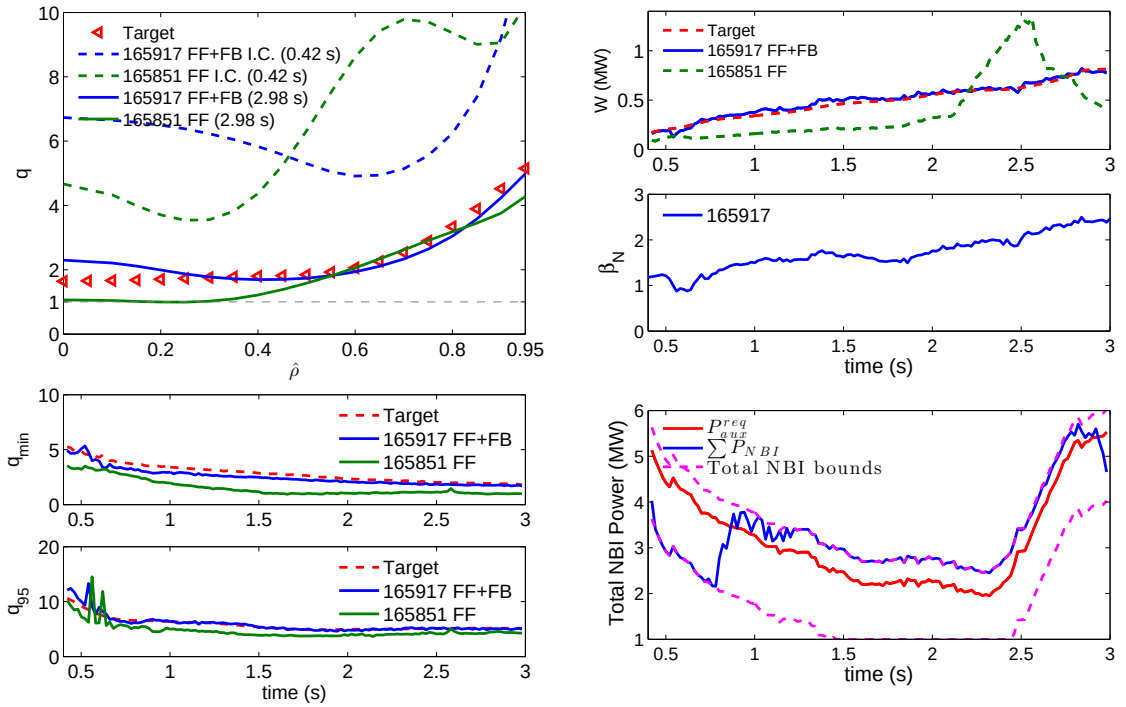


**Figure 6.9:** Shot 165917: $q$ + energy control. Target: $q_{\min} = 1.6$ and $q_{95} = 5$. A lower bound on total NBI power of 1 MW is applied to prevent back transitions to L-mode. In the left column the achieved $q$ profile at the target time for both feedforward control and feedforward + feedback control cases is displayed followed by the $q_{\min}$ and $q_{95}$ value. In the right column starting from the top the plots include the plasma stored energy, $\beta_N$, and the NBI power. The final plot includes the power requested by the energy control constraint (red), the total power window bounds (magenta) and NBI power requested by the profile controller (blue).

## 6.6 Simulations Results of MPC Tracking with Additional Constraints

In this section, simulation tests of the MPC tracking method with the additional constraints of Section 6.3 are presented. The simulations are carried out with the same setup, described in Section 6.4, of the experimental tests. To test the controller, we consider two simulations. The first, shown in Figure 6.11, includes all the constraints discussed in Section 6.3 except for the constraint associated with

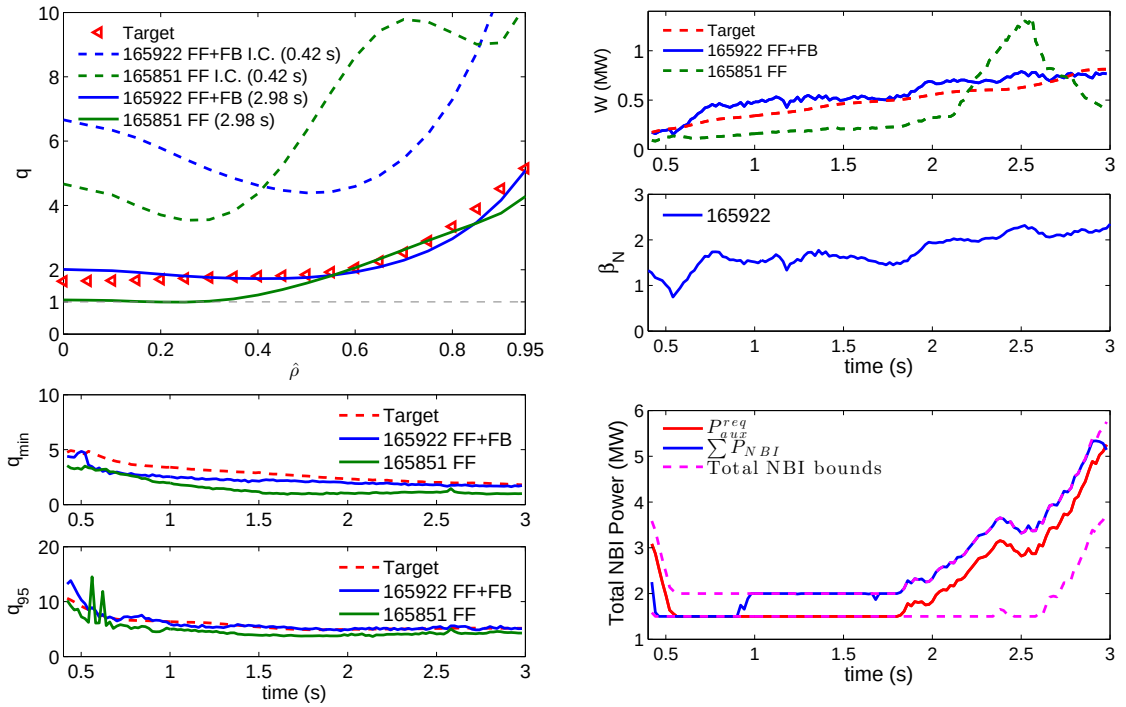


**Figure 6.10:** Shot 165922: $q$ + energy control. Target: $q_{\min} = 1.8$ and $q_{95} = 5$. A lower bound on total NBI power of 1.5 MW is applied to prevent back transitions to L-mode. In the left column the achieved $q$ profile at the target time for both feedforward control and feedforward + feedback control cases is displayed followed by the $q_{\min}$ and $q_{95}$ value. In the right column starting from the top the plots include the plasma stored energy, $\beta_N$, and the NBI power. The final plot includes the power requested by the energy control constraint (red), the total power window bounds (magenta) and NBI power requested by the profile controller (blue).

the maximum $\beta_N$ limit, and the second, shown in Figure 6.12, includes all the constraints without exception. In both simulations, the feedforward control (blue dash in the upper right plot of Figure 6.11 and Figure 6.12) is essentially deactivated by freezing the feedforward control value at 1 second. This is done to add a significant input disturbance with the objective of testing the feedback controller. Ideally, the simulations should recover the target $q$ profile at the target time of 3 seconds and hold it there. The trigger event to apply the stationarity constraint, is simply

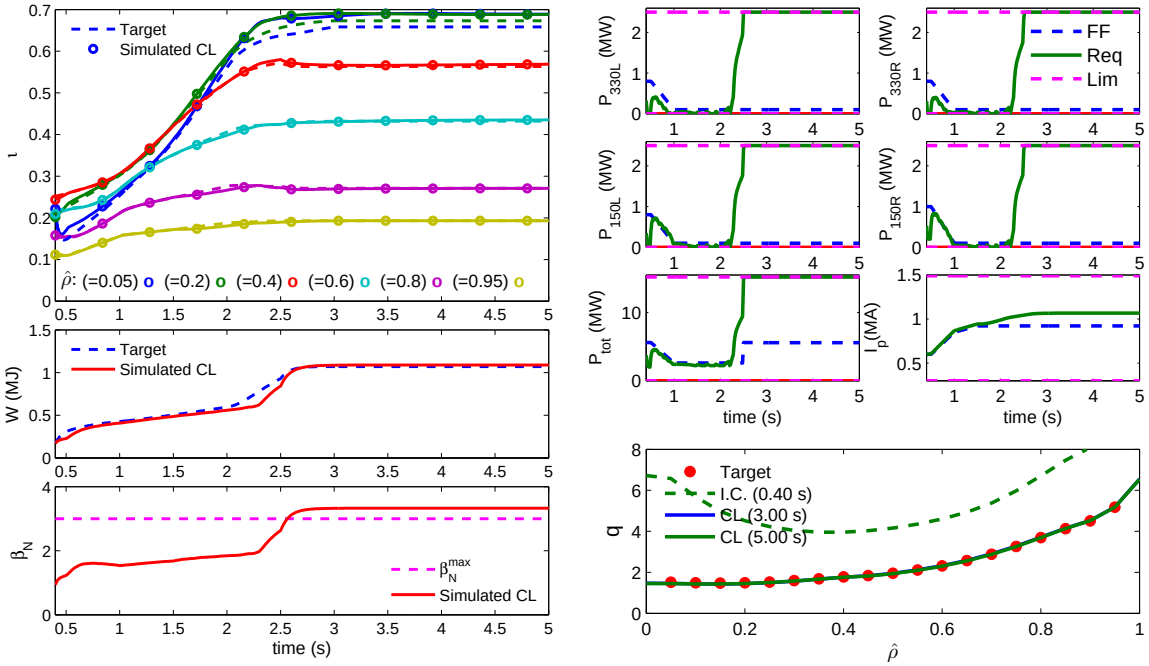


**Figure 6.11: Simulation 1:** The upper left plot shows the $\iota$ profile tracking during the closed-loop simulation. Below the upper left plot, the plasma stored energy response in closed-loop is plotted and below that the $\beta_N$ value is plotted. The $\beta_N$ constraint is not included in this simulation and as can be seen in lower left plot, the $\beta_N$ limit is violated. On the right, the controlled actuators powers plotted, showing both feedforward value and the feedforward+feedback (Req) value, and in the lower right the obtained $q$ profile is plotted at the target time of 3 s and at 5 s.

chosen as a particular time during the discharge. To aid the controller, the stationarity constraint is applied at 2.5 seconds, somewhat earlier than the target time ($t_2 = 3.0$ s).

In the first simulation, without the $\beta_N$ limit constraint, the controller is able to obtain the target $q$ profile and hold it there, but the $\beta_N$ limit is violated. The feedforward reference was designed with different model parameters than those used during the feedback simulations so as to make the target profile not achievable precisely. This is done to more closely simulate experiment conditions and explains the slight error in the profile matching at the center in the upper left plot of Figure 6.11. In the second simulation, the $\beta_N$ limit is met, but the profile begins to

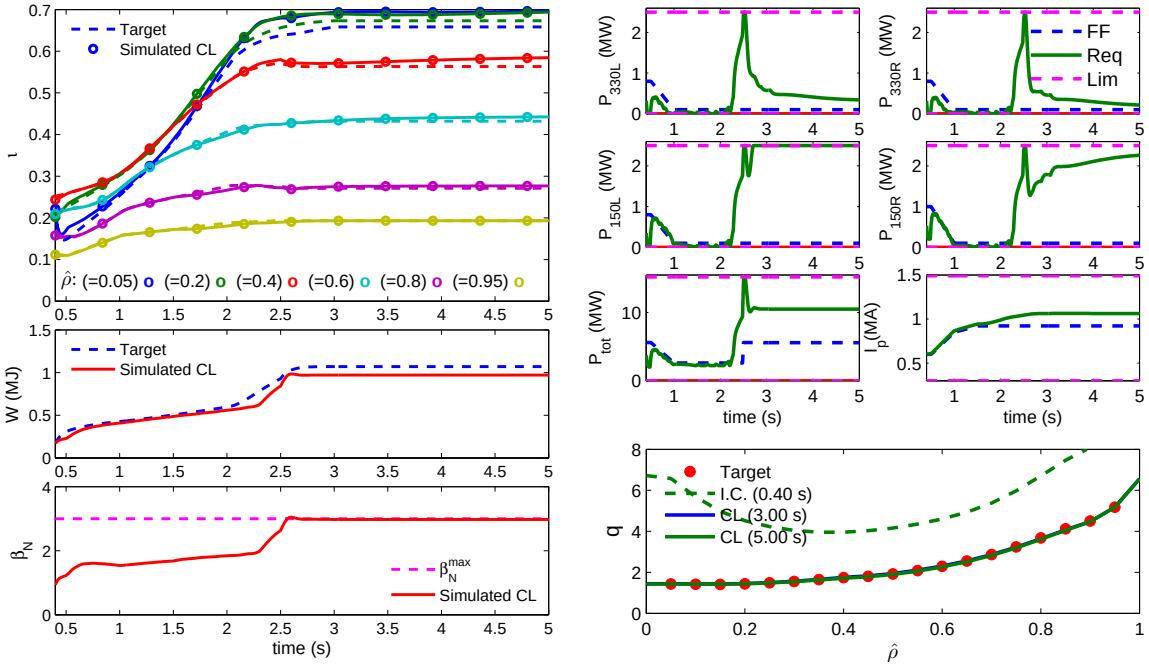


**Figure 6.12: Simulation 2:** Same as Figure 6.11 except we include the $\beta_N$ limit as a constraint. To satisfy the $\beta_N$ limit, the controller makes a trade-off in favor of off-axis NBI power (150L and 150R) over on-axis NBI (330L and 330R).

diverge slightly from the target after the target time of 3 seconds (see the red time trace of $\iota$ profile, upper left plot Figure 6.12). The $\beta_N$ limit forces the controller to make a trade-off in favor of off-axis NBI (150L and 150R) power over on-axis NBI (330L and 330R) power to meet the target $q$ profile as closely as possible while satisfying $\beta_N$ limit, which equates to an upper bound on total NBI power.

## 6.7 Conclusions

Since the high performance regimes of tokamaks operate near stability limits, active feedback controllers needs to be sufficiently sophisticated to make judicial control actions that avoid violating stability limits. The control approach developed in this chapter involves combining optimized feedforward control with constrained, predictive feedback to improve repeatability of $q$ profile target shapes. An explicit model of the underlying dynamics of the plasma is embedded into a numerical optimization

scheme to solve for the control commands. Solving the feedback control problem numerically allows for the explicit incorporation of constraints associated with actuator and plasma stability limits. This allows for the design of an aggressive profile tracking controller while maintaining avoidance of hard limits for stable plasmas such as the $\beta_N$ limit. Experiments have demonstrated the effectiveness of this approach in reaching desired $q$ profile targets as well as the real-time applicability of the numerical computation involved. With minor extensions the approach has been modified to include constraints to aid steady state achievement as opposed to the more typical control objective of profile matching. This demonstrates the flexibility of the approach which makes it a valuable physics-studies support tool.

# Chapter 7

# Feedback Control Design for the Rotation Profile Evolution

## 7.1 Introduction

This chapter describes strategies for feedback control of the rotation profile in tokamak plasmas with the purpose of building a suitable tool for aiding rotation-related physics studies. We focus specifically on the DIII-D tokamak during H-mode discharges. However, the model-based control approaches described are generally applicable, since the model can be adapted to a variety of tokamaks and scenarios only by tailoring the model parameters and not changing the model structure. We consider the first-principles-based model described in Section 3.3 for the evolution of the plasma toroidal rotation, which was simplified for applicability to real-time control design by combining the model with scenario specific correlations for the temperature, density, and torque sources.

Control of the bulk rotation with the use of neutral beam injection (NBI) is well established. Exploiting the availability of both co- and counter-current NBI at DIII-D, simultaneous control of the bulk rotation and plasma stored energy has been accomplished experimentally [84, 85], and a similar approach was considered at JET [86]. However, little work has been done to develop strategies for control of

the rotation profile shape, which will be the objective of this chapter.

We begin with a linear quadratic regulator (LQR) type control formulation for the combined regulation of the rotation profile and plasma stored energy, which is shown to be robust against the characteristically anomalous behavior of the momentum diffusivity. An LQR controller is essentially the solution to an optimal control problem, which seeks to minimize a quadratic function penalizing the discrepancy between the predicted system evolution (assuming linear dynamics) and the desired reference. In general, the optimal control sequence cannot be followed due to constraints imposed by the real plasma dynamics. For example, actuator constraints and MHD stability limits. This motivates consideration of a model-predictive control (MPC) approach, which allows for the explicit incorporation of actuator constraints into the design, and also provides the capability to avoid operation limits such as the $\beta_N$ limit. While the MPC approach is in fact much more computationally demanding because it involves solving a numerical optimization problem on every time step, it is possible to perform the computation in real-time by limiting the problem size (short prediction horizon), and employing efficient optimization techniques.

This chapter is organized as follows. In Section 7.2 the infinite dimensional PDE describing the rotation profile evolution is reduced to a finite dimensional set of ODEs by the finite element method to facilitate the design of optimal feedback controllers. In Section 7.3 simultaneous feedback control of the rotation profile and plasma stored energy evolution via LQI is considered. In Section 7.4 model predictive control of the rotation profile is considered with constraints for avoidance of unstable plasmas. Finally, conclusions are stated in Section 7.5.

## 7.2 Model Order Reduction

For convenience of control design, we can rewrite the control-oriented model (3.27) by separating the time-varying and spatially-varying parameters to obtain,

$$\begin{aligned}\frac{\partial \Omega_\phi}{\partial t} = \frac{1}{\hat{\rho}} f_1 \frac{\partial}{\partial \hat{\rho}} \left( \hat{\rho} f_2 \chi_\phi \frac{\partial \Omega_\phi}{\partial \hat{\rho}} \right) + \sum_{\xi=1}^{n_{\mathrm{NBI}}} f_{\mathrm{NBI},\xi} u_{\mathrm{NBI},\xi} \\ + (\Omega_\phi - \Omega_\phi^\star) f_{\mathrm{NRMF}} u_{\mathrm{NRMF}} - \Omega_\phi u_{\bar{n}_\mathrm{i}},\end{aligned} \tag{7.1}$$

where the functions $f_{(\cdot)}(\hat{\rho})$ incorporate constant profile shapes,

$$\begin{aligned} f_1 &= \frac{1}{m_\mathrm{i} n_\mathrm{i}^{\mathrm{prof}} \langle R^2 \rangle \hat{H}}, \\ f_2 &= \hat{H} m_\mathrm{i} n_\mathrm{i}^{\mathrm{prof}} \langle R^2 (\nabla \hat{\rho})^2 \rangle, \\ f_{\mathrm{NBI},\xi} &= \frac{k_{\mathrm{NBI},\xi}^{\mathrm{prof}} \, \eta_{\mathrm{NBI},\xi}^{\mathrm{prof}}}{m_\mathrm{i} \langle R^2 \rangle} \left( n_\mathrm{i}^{\mathrm{prof}} \right)^{\alpha_n - \alpha_T - 1} \left( k_{T_\mathrm{i}}^{\mathrm{prof}} T_\mathrm{i}^{\mathrm{prof}} \right)^{\alpha_T}, \\ f_{\mathrm{NRMF}} &= \frac{k_{\mathrm{NRMF}}^{\mathrm{prof}} \, \eta_{\mathrm{NRMF}}^{\mathrm{prof}}}{m_\mathrm{i} \langle R^2 \rangle} \left( n_\mathrm{i}^{\mathrm{prof}} \right)^{\beta_n - \beta_T - 1} \left( k_{T_\mathrm{i}}^{\mathrm{prof}} T_\mathrm{i}^{\mathrm{prof}} \right)^{\beta_T} (\omega_E^{\mathrm{prof}})^{\beta_\omega}, \end{aligned} \tag{7.2}$$

$u_{(\cdot)}(t)$ are a set of nonlinear input functions,

$$\begin{aligned} u_{\bar{n}_\mathrm{i}} = \frac{\dot{\bar{n}}_\mathrm{i}}{\bar{n}_\mathrm{i}}, \quad u_{\mathrm{NBI},\xi} = \frac{1}{\bar{n}_\mathrm{i}} \left( \frac{I_\mathrm{p} \sqrt{P_{\mathrm{tot}}}}{\bar{n}_\mathrm{i}} \right)^{\alpha_T} \bar{n}_\mathrm{i}^{\alpha_n} P_{\mathrm{NBI},\xi}, \\ u_{\mathrm{NRMF}} = \frac{1}{\bar{n}_\mathrm{i}} \left( \frac{I_\mathrm{p} \sqrt{P_{\mathrm{tot}}}}{\bar{n}_\mathrm{i}} \right)^{\beta_T} \bar{n}_\mathrm{i}^{\beta_n} I_{\mathrm{NRMF}}^2, \end{aligned} \tag{7.3}$$

and the boundary conditions (3.28) remain unchanged,

$$\frac{\partial \Omega_\phi}{\partial \hat{\rho}}(0,t) = 0, \qquad \Omega_\phi(1,t) = 0. \tag{7.4}$$

### 7.2.1 Discretization by Finite Element Method

The infinite-dimensional model (7.1) in $\hat{\rho}$ is transformed into a finite-dimensional model using the finite-element method. First, the rotation profile is approximated as

$$\Omega_\phi(\hat{\rho}, t) \approx \sum_{k=1}^{l_\omega} \omega_k(t) \phi_k(\hat{\rho}) \tag{7.5}$$

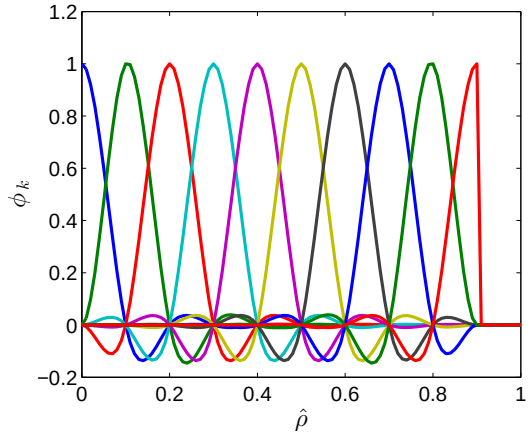


**Figure 7.1:** Cubic splines for finite element discretization of the rotation profile, $\Omega_\phi$.

where the basis $\{\phi_k \mid k = 1, 2, \ldots, l_\omega\}$, is chosen as a set of cubic splines (Figure 7.1) on a finite support that satisfy the boundary conditions (7.4). Similarly, the diffusivity profile is approximated as

$$\chi_\phi(\hat{\rho}, t) \approx \sum_{\alpha=1}^{l_\chi} \gamma_\alpha \varphi_\alpha(\hat{\rho}), \tag{7.6}$$

where the basis $\{\varphi_\alpha \mid \alpha = 1, 2, \ldots, l_\chi\}$ is obtained by the proper orthogonal decomposition (POD) method [87], summarized in Appendix A.3. The basis obtained for $\chi_\phi$ based on DIII-D shot 147634 is shown in Figure 7.2(a), as well as the expected range modeled as a linear combination of the modes in Figure 7.2(b). The POD method has the capability of obtaining a basis with relatively lower dimension than a spline basis.

Substituting (7.5) and (7.6) into (7.1), then projecting onto a set of trial basis functions as described in Appendix A.2, the PDE model is recast into a set of ordinary differential equations (ODE), which can be written as the matrix–vector equation,

$$\begin{aligned} \mathbf{M}\frac{d\boldsymbol{\omega}}{dt} &= -\mathbf{M}\boldsymbol{\omega} u_{\bar{n}_\mathrm{i}} - \mathbf{S}\boldsymbol{\omega} \\ &\quad + \sum_{\xi=1}^{n_\mathrm{NBI}} \mathbf{B}_{\mathrm{NB},\xi} u_{\mathrm{NBI},\xi} + \mathbf{B}_\mathrm{NR}\boldsymbol{\omega} u_\mathrm{NRMF} - \mathbf{B}^\star_\mathrm{NR} u_\mathrm{NRMF}, \end{aligned} \tag{7.7}$$

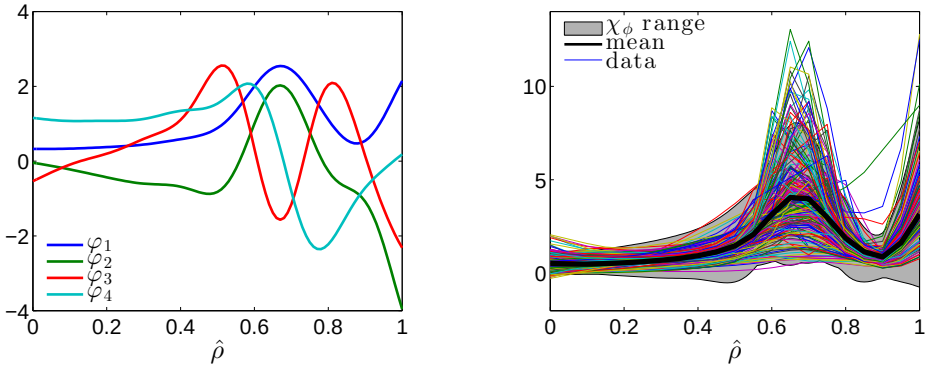


(a) POD modes $\varphi_\alpha$ (b) Diffusivity $\chi_\phi$

**Figure 7.2:** (a) POD modes that serve as a basis for $\chi_\phi$. (b) The time average of $\chi_\phi$ (black line) based on DIII-D shot 147634 over the time period $t = 2-5$ s, i.e. the current flattop phase. The lines show snapshots of $\chi_\phi$ during the current flattop phase and grey area shows the range covered by the uncertainty model.

where $\boldsymbol{\omega} = [\omega_1, \omega_2, \ldots, \omega_{l_\omega}]^T$, and the matrices are defined in Appendix A.2. From (7.7), we can see that the rotation dynamics are approximately linear, with bilinear terms associated with the density and NRMF controls.

### 7.2.2 Uncertainty Modeling for Momentum Diffusivity ($\chi_\phi$)

Since the effective diffusivity, $\chi_\phi$, is assumed to include contributions of turbulent effects which are not sufficiently understood to obtain a reliable model, we chose to represent it as an uncertainty. The parameter $\boldsymbol{\gamma} = (\gamma_1, ..., \gamma_{l_\chi})$ of (7.6) is the uncertainty vector representing a finite dimensional approximation of $\chi_\phi(\hat{\rho}, t)$ with respect to the basis $\{\varphi_\alpha \mid \alpha = 1, \ldots, l_\chi\}$. Each $\gamma_\alpha$ has the form $\gamma_\alpha = \gamma_\alpha^0 + \gamma_\alpha^1 \delta_\alpha$, where $\gamma_\alpha^0$ and $\gamma_\alpha^1$ are constants and $|\delta_\alpha| \leq 1$ for all $\alpha$. The nominal model of $\chi_\phi$ (black line of Figure 7.2(b)) is defined by $\gamma_\alpha^0$, and the uncertainty term allows the modeled value of $\chi_\phi$ to vary in the range plotted by the grey area of Figure 7.2(b).

To make the uncertainty in the state-space system explicit, the matrix $\mathbf{S}$ of (7.7) can be

$$\mathbf{S}(\boldsymbol{\delta}) = \hat{\mathbf{S}}^0 + \sum_{\alpha=1}^{l_\chi} \delta_\alpha \hat{\mathbf{S}}^\alpha, \tag{7.8}$$

where $\boldsymbol{\delta} = (\delta_1, \ldots, \delta_{l_\chi})$ (see Appendix A.2.1). Combining (7.7) and (7.8), we obtain a nonlinear, finite-dimensional, ordinary differential equation, uncertain model of the form

$$\dot{\boldsymbol{\omega}} = \boldsymbol{F}(\boldsymbol{\omega}, \mathbf{u}, \boldsymbol{\delta}) \tag{7.9}$$

where the input $\mathbf{u} = (\dot{\bar{n}}_{\mathrm{i}}, \bar{n}_{\mathrm{i}}, P_{\mathrm{EC}}, P_{\mathrm{NB},1}\,, \ \ldots, P_{\mathrm{NB},n_{\mathrm{NBI}}}, I_{\mathrm{NRMF}})$ consists of the physical actuators.

## 7.3 Feedback Control via Linear Quadratic Integrator (LQI)

In this section, we follow a linear quadratic integrator [88] approach for the simultaneous regulation of the toroidal angular rotation profile and plasma stored energy in the DIII-D tokamak during H-mode scenarios.

To begin, we separate the actuators of the system (7.9) into controlled and uncontrolled. The plasma density in tokamaks is extremely difficult to control with any real precision in large tokamaks such as DIII-D, therefore deviations of the density from the desired operating point will be treated as an input disturbance. Moreover, the first two NBI (30L and 30R) are often required for diagnostics. To account for this we split the actuators $\mathbf{u}$ into the controlled inputs $\mathbf{u}^{\mathrm{c}} = (P_{\mathrm{EC}}, P_{\mathrm{NBI},3}, \ldots, P_{\mathrm{NBI},n_{\mathrm{NBI}}}, I_{\mathrm{NRMF}})$ and the uncontrolled inputs $\mathbf{u}^{\mathrm{nc}} = (P_{\mathrm{NBI},1}, P_{\mathrm{NBI},2}, \dot{\bar{n}}_{\mathrm{i}}, \bar{n}_{\mathrm{i}})$.

By linearizing the system (7.9) with respect to the state and control around a nominal equilibrium point $(\boldsymbol{\omega}_{\mathrm{eq}}, \boldsymbol{u}_{\mathrm{eq}})$ for $\boldsymbol{\delta} = 0$, we obtain the linear time-invariant model given by

$$\dot{\boldsymbol{x}}_{\boldsymbol{\omega}} = \mathbf{A}_{\omega}\boldsymbol{x}_{\omega} + \mathbf{B}_{\boldsymbol{\omega}}\mathbf{u}_{\mathrm{FB}} + \mathbf{B}_{\omega,\mathrm{d}}\mathbf{u}_{\mathrm{d}}, \tag{7.10}$$

where $\boldsymbol{x}_{\omega} = \boldsymbol{\omega} - \boldsymbol{\omega}_{\mathrm{eq}}$, $\tilde{\mathbf{u}}(t) = \mathbf{u}^{\mathrm{c}}(t) - \mathbf{u}^{\mathrm{c}}_{\mathrm{eq}}$, $\mathbf{d}(t) = \mathbf{u}^{\mathrm{nc}}(t) - \mathbf{u}^{\mathrm{nc}}_{\mathrm{eq}}$, and the matrices are $\mathbf{A}_{\boldsymbol{\omega}} = \nabla_{\boldsymbol{\omega}}\boldsymbol{F}|_{\boldsymbol{\omega}_{eq},\mathbf{u}_{eq}}$, $\mathbf{B}_{\boldsymbol{\omega}} = \nabla_{\mathbf{u}^{\mathrm{c}}}\boldsymbol{F}|_{\boldsymbol{\omega}_{eq},\mathbf{u}_{eq}}$, and $\mathbf{B}_{\boldsymbol{\omega},\mathrm{d}} = \nabla_{\mathbf{u}^{\mathrm{nc}}}\boldsymbol{F}|_{\boldsymbol{\omega}_{eq},\mathbf{u}_{eq}}$.

Since DIII-D includes NBI aligned in both the co-current and counter-current directions as well as heating from RF waves, it provides for a partial decoupling of

the injected energy and rotation drive, enabling sufficient actuation for combined rotation and stored energy control. For control design purposes, the stored energy evolution (3.5) is approximated by

$$\frac{dE}{dt} = -\frac{E}{\tau_{\mathrm{E_{eq}}}} + P_{\mathrm{aux}}(t), \tag{7.11}$$

where the contributions of ohmic power and radiative power are dropped since they are relatively small compared to the auxiliary power for H-mode plasmas, and $\tau_{\mathrm{E_{eq}}}$ is the global energy confinement time associated with the equilibrium point $(\boldsymbol{\omega}_{\mathrm{eq}}, \mathbf{u}_{\mathrm{eq}})$. An augmented state-space system, $\boldsymbol{x} = (E, \boldsymbol{x}_{\boldsymbol{\omega}})$, is obtained by lumping the energy evolution together with the linearized rotation evolution,

$$\frac{d}{dt}\begin{bmatrix} E \\ \boldsymbol{x}_{\boldsymbol{\omega}} \end{bmatrix} = \underbrace{\begin{bmatrix} -1/\tau_{\mathrm{E_{eq}}} & 0 \\ 0 & \mathbf{A}_{\boldsymbol{\omega}} \end{bmatrix}}_{\mathbf{A}} \begin{bmatrix} E \\ \boldsymbol{x}_{\boldsymbol{\omega}} \end{bmatrix} + \underbrace{\begin{bmatrix} \mathbf{1}^T\, 0 \\ \mathbf{B}_{\boldsymbol{\omega}} \end{bmatrix}}_{\mathbf{B}} \mathbf{u}_{\mathrm{FB}}, \tag{7.12}$$

where $\mathbf{1} = [1, 1, \ldots, 1]^T$ is a column of ones[1].

### Singular Value Decomposition

For a requested target state, $\boldsymbol{x}_{\mathrm{t}}$, let $\boldsymbol{x}_{\infty}^{\mathrm{ss}}$ represent the closest stationary state achievable according to the model. This can be determined from the pseudo-inverse, $\mathbf{K}_{\mathrm{sg}}^{\dagger}$, of the model static gain matrix $\mathbf{K}_{\mathrm{sg}} = -\mathbf{A}^{-1}\mathbf{B}$. The symbol † represents the Moore-Penrose pseudo-inverse determined by singular value decomposition (SVD), i.e.

$$\mathbf{K}_{\mathrm{sg}} = \mathbf{W}\boldsymbol{\Sigma}\mathbf{V}^T, \quad \mathbf{K}_{\mathrm{sg}}^{\dagger} = \mathbf{V}\boldsymbol{\Sigma}^{\dagger}\mathbf{W}^T, \tag{7.13}$$

where $\mathbf{W}$ and $\mathbf{V}$ are unitary matrices, i.e. $\mathbf{W}\mathbf{W}^T = \mathbf{W}^T\mathbf{W} = \mathbf{I}$ and $\mathbf{V}^T\mathbf{V} = \mathbf{V}\mathbf{V}^T = \mathbf{I}$. The pseudoinverse of the diagonal matrix $\boldsymbol{\Sigma}$ is obtained by taking its transpose, $\boldsymbol{\Sigma}^T$, and then replacing each nonzero element with its reciprocal. The input associated with the desired target is determined from the pseudo-inverse of the static gain matrix, $\mathbf{u}_{\mathrm{FB},\infty}^{\mathrm{ss}} = \mathbf{K}_{\mathrm{sg}}^{\dagger}\boldsymbol{x}_{\mathrm{t}}$, which is used to determine the closest

[1]Of the controls, the ECCD and NBI contribute to the total plasma stored energy, but not the NRMF current.

achievable stationary state given by $\boldsymbol{x}_\infty^{ss} = \mathbf{K}_{\rm sg}\mathbf{u}_{\rm FB,\infty}^{\rm ss} = \mathbf{K}_{\rm sg}\mathbf{K}_{\rm sg}^{\dagger}\boldsymbol{x}_{\rm t}$. Because several of the actuators have similar effects on the profile, the matrix $\mathbf{K}_{\rm sg} = \mathbf{W}\boldsymbol{\Sigma}V^T$ is ill-conditioned, i.e. the ratio of the largest singular value to the smallest one is much larger than one. Therefore small deviations in the profile associated with the directions of the smaller singular values can result in unreasonably large control requests. Thus, we use a truncated (Tr) singular value expansion of the static gain matrix given by, $\mathbf{K}_{\rm sg,Tr} = \mathbf{W}_{\rm Tr}\boldsymbol{\Sigma}_{\rm Tr}\mathbf{V}_{\rm Tr}^T$, where the matrices $\mathbf{W}_{\rm Tr}$, $\boldsymbol{\Sigma}_{\rm Tr}$, and $\mathbf{V}_{\rm Tr}$ are the components of the SVD associated with the $n_{\rm SV}$ largest singular values,

$$\mathbf{W} = \begin{bmatrix}\mathbf{W}_{\rm Tr} & \mathbf{W}_{\rm n}\end{bmatrix},\ \boldsymbol{\Sigma} = \begin{bmatrix}\boldsymbol{\Sigma}_{\rm Tr} & \mathbf{0}\\ \mathbf{0} & \boldsymbol{\Sigma}_{\rm n}\end{bmatrix},\ \mathbf{V} = \begin{bmatrix}\mathbf{V}_{\rm Tr} & \mathbf{V}_{\rm n}\end{bmatrix}, \tag{7.14}$$

and $\mathbf{W}_n$, $\boldsymbol{\Sigma}_n$, and $\mathbf{V}_n$ are the components associated with the smaller, neglected singular values. Therefore,

$$\mathbf{u}_{\rm FB,\infty}^{\rm ss} \cong \mathbf{u}_{\rm FB,\infty} = \mathbf{K}_{\rm sg,Tr}^{\dagger}\boldsymbol{x}_{\rm t},\ \boldsymbol{x}_\infty^{ss} \cong \boldsymbol{x}_\infty = \mathbf{K}_{\rm sg,Tr}\mathbf{K}_{\rm sg,Tr}^{\dagger}\boldsymbol{x}_{\rm t}. \tag{7.15}$$

We use the theory of linear quadratic optimal control to obtain a control law which regulates the system to the closest achievable stationary state while minimizing the cost function

$$J = \int_0^\infty \left[\tilde{\boldsymbol{x}}^T(t)\ \boldsymbol{\zeta}^T(t)\right]\mathbf{Q}\begin{bmatrix}\tilde{\boldsymbol{x}}(t)\\ \boldsymbol{\zeta}(t)\end{bmatrix} + \tilde{\mathbf{u}}^T(t)\mathbf{R}\tilde{\mathbf{u}}(t)dt, \tag{7.16}$$

where $\tilde{\boldsymbol{x}} = \boldsymbol{x} - \boldsymbol{x}_\infty$, $\tilde{\mathbf{u}} = \mathbf{u}_{\rm FB} - \mathbf{u}_{\rm FB,\infty}$, $\mathbf{Q}$ positive semidefinite, $\mathbf{R}$ positive definite, and $\zeta$ represents the integral states introduced for integral control. The added integral states are expressed as $\boldsymbol{\zeta} = \mathbf{K}_\zeta\int_0^t \tilde{\boldsymbol{x}}(\tau)d\tau$, where $\mathbf{K}_\zeta$ functions as a design matrix.

### Choice of Matrix $\mathbf{K}_\zeta$

With the choice $\mathbf{K}_\zeta = \mathbf{W}_{\rm Tr}^T$, we have $\mathbf{K}_\zeta\mathbf{K}_{\rm sg,Tr}\mathbf{K}_{\rm sg,Tr}^{\dagger} = \mathbf{K}_\zeta$, since

$$\left[\mathbf{W}_{\rm Tr}^T\right]\cdot\left[\mathbf{W}_{\rm Tr}\boldsymbol{\Sigma}_{\rm Tr}\mathbf{V}_{\rm Tr}^T\right]\cdot\left[\mathbf{V}_{\rm Tr}\boldsymbol{\Sigma}_{\rm Tr}^{-1}\mathbf{W}_{\rm Tr}^T\right] = \mathbf{W}_{\rm Tr}^T = \mathbf{K}_\zeta, \tag{7.17}$$

which ensures $\mathbf{K}_\zeta\boldsymbol{x}_{\rm t} \to \mathbf{K}_\zeta\boldsymbol{x}_\infty$, since $\boldsymbol{x}_\infty = \mathbf{K}_{\rm sg,Tr}\mathbf{u}_{\rm FB,\infty} = \mathbf{K}_{\rm sg,Tr}\mathbf{K}_{\rm sg,Tr}^{\dagger}\boldsymbol{x}_{\rm t}$. Here, we have made use of the fact that $\mathbf{W}_{\rm Tr}^T\mathbf{W}_{\rm Tr} = \mathbf{I}$, and $\mathbf{V}_{\rm Tr}^T\mathbf{V}_{\rm Tr} = \mathbf{I}$, but $\mathbf{W}_{\rm Tr}\mathbf{W}_{\rm Tr}^T \neq \mathbf{I}$.

### Proportional Plus Integral Control

Written in terms of the requested target ($\tilde{\boldsymbol{x}}(t) = \boldsymbol{x}(t) - \mathbf{K}_{\text{sg,Tr}}\mathbf{K}^{\dagger}_{\text{sg,Tr}}\boldsymbol{x}_{\text{t}}(t)$), the control law that minimizes (7.16) reduces to a proportional plus integral controller of the form

$$\begin{aligned}\tilde{\mathbf{u}}(t) = &-\mathbf{K}_{\text{p}}\left[\boldsymbol{x}(t) - \mathbf{K}_{\text{sg,Tr}}\mathbf{K}^{\dagger}_{\text{sg,Tr}}\boldsymbol{x}_t(t)\right] \\ &- \mathbf{K}_{\text{i}}\mathbf{K}_{\zeta}\int_0^t \mathrm{d}\tau\left[\boldsymbol{x}(\tau) - \mathbf{K}_{\text{sg,Tr}}\mathbf{K}^{\dagger}_{\text{sg,Tr}}\boldsymbol{x}_{\text{t}}(\tau)\right],\end{aligned} \tag{7.18}$$

where the proportional gain, $\mathbf{K}_{\text{p}}$, and integral gain, $\mathbf{K}_{\text{i}}$, are given by $\begin{bmatrix}\mathbf{K}_{\text{p}} & \mathbf{K}_{\text{i}}\end{bmatrix} = \mathbf{R}^{-1}\hat{\mathbf{B}}\mathbf{Z}$, where $\mathbf{Z} = \mathbf{Z}^T$ is the unique positive semi-definite solution to the algebraic Ricatti equation, $\hat{\mathbf{A}}^T\mathbf{Z} + \mathbf{Z}\hat{\mathbf{A}} - \mathbf{Z}\hat{\mathbf{B}}\mathbf{R}^{-1}\hat{\mathbf{B}}^T\mathbf{Z} + \mathbf{Q} = 0$, and the system ($\hat{\mathbf{A}}$, $\hat{\mathbf{B}}$) is constructed by augmenting the model (7.10) with the integrator states, i.e.

$$\begin{bmatrix}\dot{\tilde{\boldsymbol{x}}} \\ \dot{\boldsymbol{\zeta}}\end{bmatrix} = \underbrace{\begin{bmatrix}\mathbf{A} & \mathbf{0} \\ \mathbf{K}_{\zeta} & \mathbf{0}\end{bmatrix}}_{\hat{\mathbf{A}}}\begin{bmatrix}\tilde{\boldsymbol{x}} \\ \boldsymbol{\zeta}\end{bmatrix} + \underbrace{\begin{bmatrix}\mathbf{B} \\ \mathbf{0}\end{bmatrix}}_{\hat{\mathbf{B}}}\tilde{\mathbf{u}}. \tag{7.19}$$

The design parameters include $\mathbf{K}_{\zeta} = \mathbf{W}^T_{\text{Tr}}$, $\mathbf{Q}$ and $\mathbf{R}$. The state weighting matrix, $\mathbf{Q}$, is chosen as $\mathbf{Q} = \begin{bmatrix}\hat{\mathbf{Q}} & \mathbf{0} \\ \mathbf{0} & \alpha^2_{\boldsymbol{\zeta}}\mathbf{I}_{n_{\text{SV}}}\end{bmatrix}$, where $\alpha_{\zeta}$ is a constant that weights the integrator states relative to the model states, $\hat{\mathbf{Q}}$ is the weighting on the model states and $\mathbf{R}$ is chosen diagonal.

## 7.3.1 Model in Robust Control Framework

The transfer function of a linear state-space system with representation $\mathbf{A}$, $\mathbf{B}$, $\mathbf{C}$, $\mathbf{D}$ can be written as an upper linear fractional transformation (LFT), $\mathbf{G}(s) = \mathbf{F}_U(\mathbf{M}_a, \frac{1}{s}\mathbf{I}) = \mathbf{D} + \mathbf{C}(s\mathbf{I} - \mathbf{A}^{-1})\mathbf{B}$, where $\mathbf{F}_U$ denotes the upper LFT, $s$ is complex variable, and the matrix $\mathbf{M}_a$ is defined as

$$\mathbf{M}_a = \begin{bmatrix}\mathbf{A} & \mathbf{B} \\ \mathbf{C} & \mathbf{D}\end{bmatrix}. \tag{7.20}$$

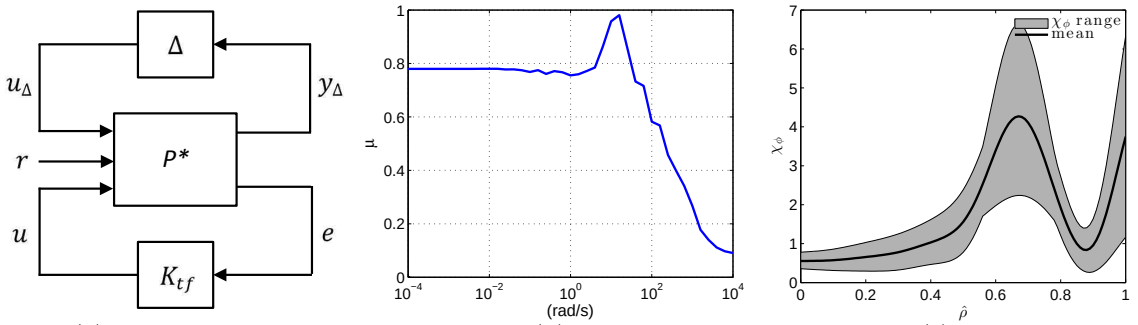


(a) $\Delta - P^* - K_{tf}$ (b) $\mu$ (c) $\chi_\phi$

**Figure 7.3:** (a) The $\Delta - P^* - K_{tf}$ robust control design framework. (b) The structured singular value $\mu$. (c) The Range of $\chi_\phi$ for which robust stability criterion is satisfied.

For robustness analysis, the linearized state space system (7.10) can be written as the general linear state-space uncertainty

$$\mathbf{M}_a = \begin{bmatrix} \mathbf{A}_0 + \sum_{\alpha=1}^{l_\chi} \delta_\alpha \mathbf{A}_\alpha & \mathbf{B}_0 + \sum_{\alpha=1}^{l_\chi} \delta_\alpha \mathbf{B}_\alpha \\ \mathbf{C}_0 + \sum_{\alpha=1}^{l_\chi} \delta_\alpha \mathbf{C}_\alpha & \mathbf{D}_0 + \sum_{\alpha=1}^{l_\chi} \delta_\alpha \mathbf{D}_\alpha \end{bmatrix}, \tag{7.21}$$

where

$$\mathbf{A}_0 = \text{diag}\left\{ -\frac{1}{\tau_{\text{E}_{\text{eq}}}}, -u_{\bar{n}_\text{i}} - \mathbf{M}^{-1}(\hat{\mathbf{S}}^0 + \mathbf{B}_{\text{NRMF}} u_{\text{NRMF}}) \Big|_{\omega_{eq}, u_{eq}} \right\},$$

$\mathbf{B}_0 = \mathbf{B}$, $\mathbf{C}_0 = \mathbf{I}$, $\mathbf{D}_0 = 0$, $\mathbf{A}_\alpha = \text{diag}\{0, -\mathbf{M}^{-1}\hat{\mathbf{S}}^\alpha\}$, and $\mathbf{B}_\alpha = \mathbf{C}_\alpha = \mathbf{D}_\alpha = 0$.

Let $\mathbf{K}_{tf}$ represent the transfer function of the controller obtained in Section 7.3 and let $\mathbf{\Delta} = \text{diag}\{\delta\}$, then we can form the standard $\mathbf{\Delta} - \mathbf{P} - \mathbf{K}_{tf}$ configuration (Figure 7.3(a)) by employing the method outlined in [89], which exploits the structure of the state matrices in (7.21). See [90] for an example of this technique. If the generalized plant is partitioned as

$$\mathbf{P}^\star = \begin{bmatrix} \bar{\mathbf{P}}^\star_{11} & \bar{\mathbf{P}}^\star_{12} \\ \bar{\mathbf{P}}^\star_{21} & \bar{\mathbf{P}}^\star_{22} \end{bmatrix} \tag{7.22}$$

where

$$\begin{aligned} \mathbf{y}_\Delta &= \bar{\mathbf{P}}^\star_{11}\mathbf{u}_{\mathbf{\Delta}} + \bar{\mathbf{P}}^\star_{12}\mathbf{u}, \\ \mathbf{e} &= \bar{\mathbf{P}}^\star_{21}\mathbf{u}_{\mathbf{\Delta}} + \bar{\mathbf{P}}^\star_{22}\mathbf{u}, \end{aligned} \tag{7.23}$$

the system can be written in the $N - \Delta$ form by using the definition of lower LFT between $\mathbf{P}^\star$ and $\mathbf{K}_{tf}$,

$$N = \mathbf{F}_L(\mathbf{P}^\star, \mathbf{K}_{tf}) = \bar{\mathbf{P}}^\star_{11} + \bar{\mathbf{P}}^\star_{12}\mathbf{K}_{tf}(I - \bar{\mathbf{P}}^\star_{22}\mathbf{K}_{tf})^{-1}\bar{\mathbf{P}}^\star_{21}. \tag{7.24}$$

We can compute the structured singular value $\mu(\mathbf{N}_{11}(j\omega))$ to determine the robust stability of the closed-loop system, where $\mathbf{N}_{11}$ is the transfer function between $\mathbf{y}_\Delta$ and $\mathbf{u}_\Delta$. The closed-loop system is robustly stable for all allowable perturbations if and only if $\mu(\mathbf{N}_{11}(j\omega)) < 1$, $\forall\omega$ [91]. To analyze the robust stability of the closed-loop system, a plot of $\mu$ versus frequency is shown in Figure 7.3(b). To obtain this $\mu$ value, the value of $\chi_\phi$ is allowed to vary throughout the range shown in Figure 7.3(c) with profile shapes equal to a linear combination of the POD modes in Figure 7.2(b).

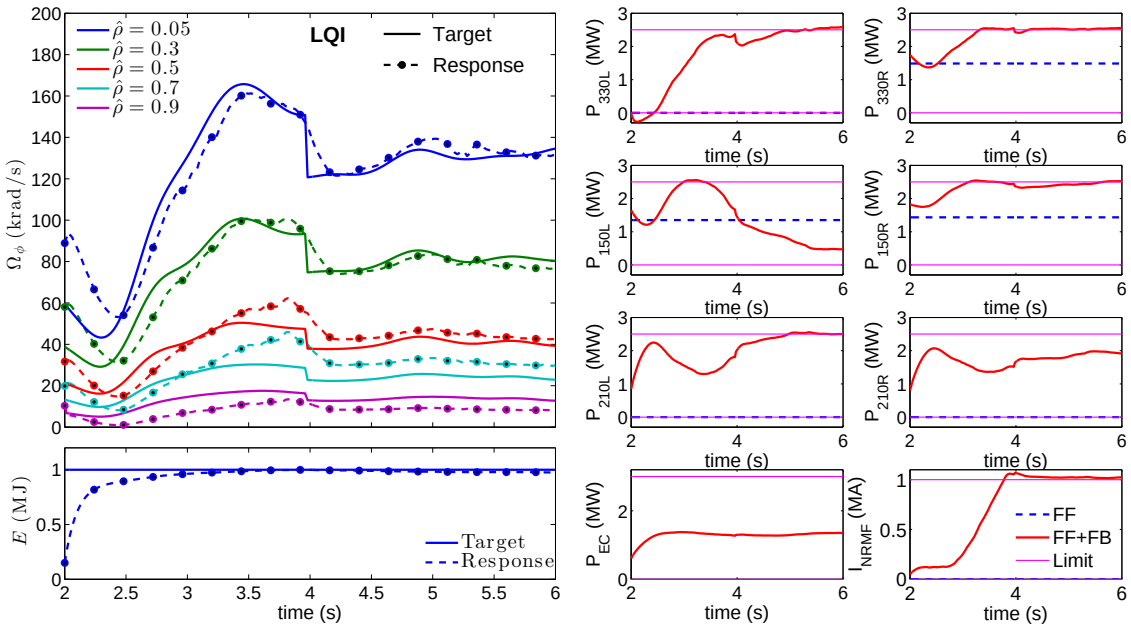


(a) $\Omega_\phi$ and $E$ (b) Inputs

**Figure 7.4:** Feedback control simulation. (a.) $\Omega_\phi$ and $E$, where the solid line is the target and the achieved profile is marked by circles. The stored energy set point is marked by the blue dashed line. (b.) Input values, where the green line marks the controller requested power, the blue dashed line marks the feedforward power, and the pink dashed line marks the actuators limits.

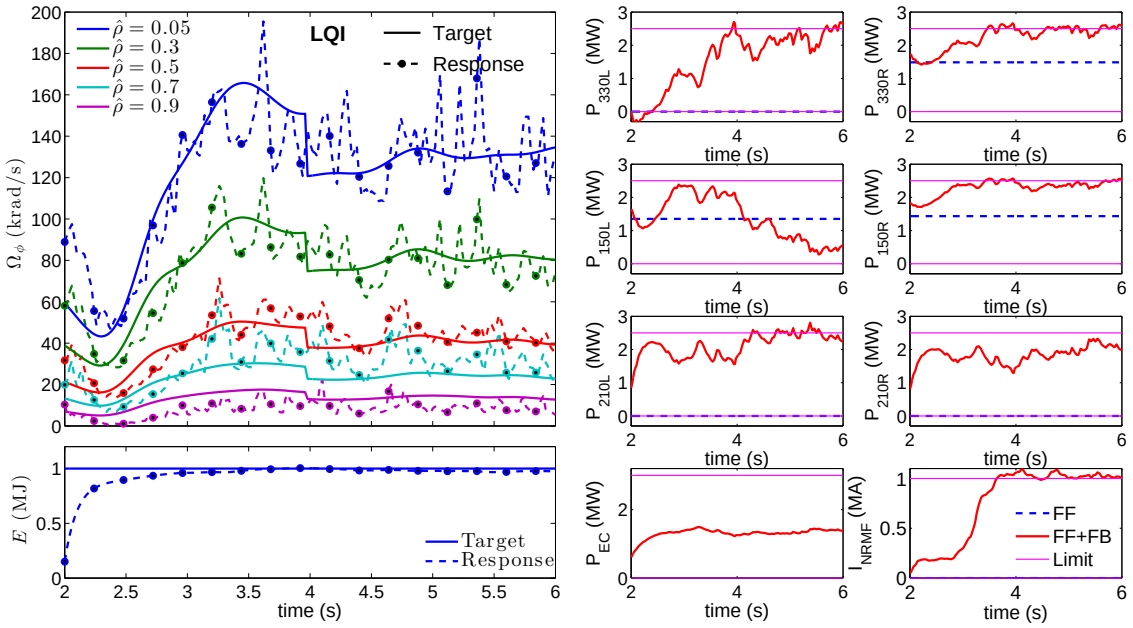


(a) $\Omega_\phi$ and $E$ (b) Inputs

**Figure 7.5:** Feedback control simulation. Same as in Figure 7.4 except the $\chi_\phi$ profile is allowed to vary randomly as a linear combination of the POD modes.

### 7.3.2 Simulation Results of the LQI Approach

In this section, we present a simulation study of the controller's effectiveness. The target for $\Omega_\phi$ is obtained from (7.9) with the input values and parameter profiles of DIII-D shot 147634, and the stored energy target is simply set to 1 MW, a typical value for H-mode plasmas. Constant feedforward values are used for the NBI, and the feedforward value of the NRMF coil current is set to a ramping function. The selected feedforward input values constitute a large input disturbance from the input values of DIII-D shot 147634 used to determine the target profile shape.

The tuning problem consists of the selection of the diagonal elements of $Q$ and $R$ and the constant $\alpha_\zeta$ to regulate the profile as close as possible to the target while maintaining constant stored energy. In Figure 7.4, we test the controller's tracking performance with feedback ON throughout the simulation. The target profile and simulated closed-loop profile response are plotted in 7.4(a), and the feedforward and

requested actuator powers are plotted in Figure 7.4(b). The controller performs well, enabling tight profile regulation while maintaining a nearly flat stored energy. At $t = 4$ s, the rotation profile target switches discretely to a lower target value. Note, the controller obtains the second, lower rotation target by increasing the counter NBI power ($P_{210\mathrm{L}}$ and $P_{210\mathrm{R}}$) while reducing the co NBI power ($P_{330\mathrm{L}}$ and $P_{150\mathrm{L}}$) to maintain the stored energy around the set point of 1 MW. The additional power from the ECRH is quite advantageous in maintaining the stored energy value and the NRMF provides some advantage over NBI in regulating the rotation at the plasma edge.

In the second simulation, Figure 7.5, the conditions are the same as the first except we allow for random perturbations in the value of $\chi_\phi$ over the range depicted in Figure 7.2(b). This simulation provides a check of robustness against the anomalous properties of $\chi_\phi$.

## 7.4 Feedback Control via Model Predictive Control (MPC)

In this section, we follow a model predictive control (MPC) [78, 79] approach for the simultaneous regulation of the toroidal angular rotation profile and plasma stored energy in the DIII-D tokamak during H-mode scenarios. The previous section considered LQI control of the combined rotation and and plasma stored energy evolution. Both control approaches are based on the first-principles-based model of sections 3.3 and 7.2, therefore a comparison will be made between the MPC approach and the LQI approach based on simulations. As will be shown, the profile control performance is similar in both cases, but the MPC approach provides an important advantage for tokamak plasma control. Because the control commands are obtained by solving a numerical optimization problem, explicit constraints for the avoidance of plasma stability limits can be incorporated.

### Model Linearization for MPC

For control design purposes, the model (7.9) is linearized with respect to the state and actuators are discretized in time. The control technique considered in this section involves solving a numerical optimization problem on each time step. It is necessary to linearize the model so that the optimal control problem is convex, which is necessary in order to ensure a solution is always attainable (see Appendix D.2). Like in Section 7.3, we split the control $\mathbf{u}$ into the controlled input $\mathbf{u}^{\mathrm{c}} = (P_{\mathrm{EC}}, P_{\mathrm{NBI},3}, \ldots, P_{\mathrm{NBI},n_{\mathrm{NBI}}}, I_{\mathrm{NRMF}})$ and the uncontrolled input $\mathbf{u}^{\mathrm{nc}} = (P_{\mathrm{NBI},1}, P_{\mathrm{NBI},2}, \dot{\bar{n}}_{\mathrm{i}}, \bar{n}_{\mathrm{i}})$, and linearize the system (7.9) with respect to the state and control around a nominal equilibrium point $(\boldsymbol{\omega}_{\mathrm{eq}}, \mathbf{u}_{\mathrm{eq}})$ for $\boldsymbol{\delta} = 0$, to obtain the linear time-invariant model given by

$$\dot{\boldsymbol{\omega}} \approx \boldsymbol{F}\Big|_{\substack{\boldsymbol{\omega}_{\mathrm{eq}} \\ \mathbf{u}_{\mathrm{eq}}}} + \frac{\partial \boldsymbol{F}}{\partial \boldsymbol{\omega}}\Big|_{\substack{\boldsymbol{\omega}_{\mathrm{eq}} \\ \mathbf{u}_{\mathrm{eq}}}} (\boldsymbol{\omega} - \boldsymbol{\omega}_{\mathrm{eq}}) + \frac{\partial \boldsymbol{F}}{\partial \mathbf{u}^{\mathrm{c}}}\Big|_{\substack{\boldsymbol{\omega}_{\mathrm{eq}} \\ \mathbf{u}_{\mathrm{eq}}}} \tilde{\mathbf{u}} + \frac{\partial \boldsymbol{F}}{\partial \mathbf{u}^{\mathrm{nc}}}\Big|_{\substack{\boldsymbol{\omega}_{\mathrm{eq}} \\ \mathbf{u}_{\mathrm{eq}}}} \mathbf{d}, \tag{7.25}$$

where $\tilde{\mathbf{u}}(t) = \mathbf{u}^{\mathrm{c}}(t) - \mathbf{u}^{\mathrm{c}}_{\mathrm{eq}}$, $\mathbf{d}(t) = \mathbf{u}^{\mathrm{nc}}(t) - \mathbf{u}^{\mathrm{nc}}_{\mathrm{eq}}$. After discretizing the linearized system with a semi-implicit scheme in time, we obtain the model,

$$\boldsymbol{\omega}_{k+1} = \mathbf{A}\boldsymbol{\omega}_k + \mathbf{B}\tilde{\mathbf{u}}_k + \mathbf{B}_d\mathbf{d}_k + \boldsymbol{f}_{\omega}, \tag{7.26}$$

where

$$\mathbf{A} = \left( \boldsymbol{I} - T_s \frac{\partial \boldsymbol{F}}{\partial \boldsymbol{\omega}}\Big|_{\substack{\boldsymbol{\omega}_{\mathrm{eq}} \\ \mathbf{u}_{\mathrm{eq}} \\ \boldsymbol{\delta}=0}} \right)^{-1}, \quad \mathbf{B} = T_s\mathbf{A} \frac{\partial \boldsymbol{F}}{\partial \mathbf{u}^{\mathrm{c}}}\Big|_{\substack{\boldsymbol{\omega}_{\mathrm{eq}} \\ \mathbf{u}_{\mathrm{eq}} \\ \boldsymbol{\delta}=0}},$$

$$\mathbf{B}_d = T_s\mathbf{A} \frac{\partial \boldsymbol{F}}{\partial \mathbf{u}^{\mathrm{nc}}}\Big|_{\substack{\boldsymbol{\omega}_{\mathrm{eq}} \\ \mathbf{u}_{\mathrm{eq}} \\ \boldsymbol{\delta}=0}}, \quad \boldsymbol{f}_{\boldsymbol{\omega}} = T_s\mathbf{A} \left( \boldsymbol{F}\Big|_{\substack{\boldsymbol{\omega}_{\mathrm{eq}} \\ \mathbf{u}_{\mathrm{eq}} \\ \boldsymbol{\delta}=0}} - \frac{\partial \boldsymbol{F}}{\partial \boldsymbol{\omega}}\Big|_{\substack{\boldsymbol{\omega}_{\mathrm{eq}} \\ \mathbf{u}_{\mathrm{eq}} \\ \boldsymbol{\delta}=0}} \boldsymbol{\omega}_{\mathrm{eq}} \right),$$

and $T_s$ is the time step. The affine term $\boldsymbol{f}_{\omega}$ arises due to the fact that we are writing the model in terms of the full state rather than the more common error state, i.e. the state relative to the equilibrium value, for reasons discussed in the next section.

## 7.4.1 Reference Tracking Problem via MPC

The reference tracking problem is formulated as a finite-horizon, optimal tracking control problem. At time $k$, consider the quadratic optimization problem

$$
\begin{aligned}
\underset{\{\Delta\tilde{\mathbf{u}}_{k+t}\}_{t=0}^{H_u}}{\text{minimize}} \quad & J_k = \sum_{t=1}^{H_p} \|\boldsymbol{\omega}_{k+t} - \mathbf{r}_{k+t}\|_{\mathbf{Q}} + \sum_{t=0}^{H_u} \|\Delta\tilde{\mathbf{u}}_{k+t}\|_{\mathbf{R}}\,, \\
\text{subject to} \quad & \boldsymbol{\omega}_{k+t+1} = \mathbf{A}\boldsymbol{\omega}_{k+t} + \mathbf{B}\tilde{\mathbf{u}}_{k+t} + \mathbf{B}_{\mathrm{d}}\mathbf{d}_{k+t} + \boldsymbol{f}_{\omega}, \\
& \boldsymbol{\omega}_k = \boldsymbol{\omega}(k) \ : \ \text{estimated state at time } k, \\
& \Delta\tilde{\mathbf{u}}_k = \tilde{\mathbf{u}}_{k+1} - \tilde{\mathbf{u}}_k, \\
& \tilde{\mathbf{u}}_{k-1} = \text{previously applied control}, \\
& \mathbf{d}_{k+t} = \mathbf{d}_k \text{ for } t = 0, 1, \ldots H_u, \\
& \tilde{\mathbf{u}}_{k+t} \in \tilde{\mathcal{U}}_{k+t} \text{ for } t = 0, 1, \ldots H_u.
\end{aligned}
\tag{7.27}
$$

The cost function $J_k$ includes an instantaneous cost on deviations of the measured outputs from the desired reference, $\mathbf{r}_k$, over the prediction horizon, $H_p$. Also, an instantaneous cost is applied to deviations in the control, $\Delta\tilde{\mathbf{u}} = \tilde{\mathbf{u}}_{k+1} - \tilde{\mathbf{u}}_k$, implying no cost for the control sequence to be away from the value associated with equilibrium operating point, $\mathbf{u}_{\mathrm{eq}}$, but there is a cost for fast rate changes. Predicting the state evolution in terms of the actual state with the use of the affine model (7.26) instead of a deviation term (error state) allows the controller to anticipate future reference changes. We allow the horizon associated with the control, $H_u$, to be less than the prediction horizon associated with the state, to reduce the complexity of the problem. We assume no further update in the control beyond the control horizon, i.e. $\tilde{\mathbf{u}}_{k+t} = \tilde{\mathbf{u}}_{k+t-1}$ for $t \geq H_u$ and we assume the uncontrolled actuators are constant ($\mathbf{d}_{k+t} = \mathbf{d}_k$). The term $\{\tilde{\mathbf{u}}_{k+t} \in \tilde{\mathcal{U}}_{k+t}\}_{t=0}^{H_u}$ describes linear constraints on the actuators to be described. The solution to this optimization problem,

$$
\Delta\tilde{\mathbf{U}}_k = \begin{bmatrix} \Delta\tilde{\mathbf{u}}_k \\ \Delta\tilde{\mathbf{u}}_{k+1} \\ \vdots \\ \Delta\tilde{\mathbf{u}}_{k+H_u} \end{bmatrix}, \tag{7.28}
$$

is a sequence of control decisions. Of course, we cannot simply apply the resulting control sequence because the model used to predict the future states is not perfectly accurate. Therefore, the common practice is to apply the first step of the sequence,

then sample the state again, and repeat the optimization procedure, which introduces feedback to the control.

### 7.4.2 Converting the Rotation Control Problem to a Standard Form Quadratic Program (QP)

The optimal control problem (7.27) consists of the minimum of a quadratic function over a set of linear constraints, i.e. a quadratic optimization problem (also known as a quadratic program (QP)). Using the shooting method transcription approach described in Appendix B.1.1, the state evolution of the MPC problem (7.27) can be written as a function of the optimization variables (7.28). Noting the model (7.26), the predicted state evolution, at time $k$, can be written in terms of the control variables and the current state estimate,

$$
\begin{aligned}
\boldsymbol{\omega}_{k+1} &= \mathbf{A}\boldsymbol{\omega}[k] + \mathbf{B}\tilde{\mathbf{u}}_k + \mathbf{B}_\mathrm{d}\mathbf{d}_k + \boldsymbol{f}_{\boldsymbol{\omega}}, \\
\boldsymbol{\omega}_{k+2} &= \mathbf{A}^2\boldsymbol{\omega}[k] + \mathbf{A}\mathbf{B}\tilde{\mathbf{u}}_k + \mathbf{B}\tilde{\mathbf{u}}_{k+1} + \mathbf{A}\mathbf{B}_\mathrm{d}\mathbf{d}_k + \mathbf{B}_\mathrm{d}\mathbf{d}_k + \mathbf{A}\boldsymbol{f}_{\boldsymbol{\omega}} + \boldsymbol{f}_{\boldsymbol{\omega}}, \\
&\vdots \\
\boldsymbol{\omega}_{k+H_p} &= \mathbf{A}^{H_p}\boldsymbol{\omega}[k] + \mathbf{A}^{H_p-1}\mathbf{B}\tilde{\mathbf{u}}_k + \mathbf{A}^{H_p-2}\mathbf{B}\tilde{\mathbf{u}}_{k+1} + \cdots + \sum_{i=0}^{H_p-1-H_u} \mathbf{A}^i\mathbf{B}\tilde{\mathbf{u}}_{k+H_u} \\
&\qquad + \sum_{i=0}^{H_p-1} \mathbf{A}^i\mathbf{B}_\mathrm{d}\mathbf{d}_k + \sum_{i=0}^{H_p-1} \mathbf{A}^i\boldsymbol{f}_{\boldsymbol{\omega}},
\end{aligned}
$$

which can be written more compactly as

$$\underbrace{\begin{bmatrix}\boldsymbol{\omega}_{k+1}\\ \boldsymbol{\omega}_{k+2}\\ \vdots\\ \boldsymbol{\omega}_{k+H_p}\end{bmatrix}}_{\mathbf{X}_k} = \underbrace{\begin{bmatrix}\mathbf{A}\\ \mathbf{A}^2\\ \vdots\\ \mathbf{A}^{H_p}\end{bmatrix}}_{\boldsymbol{\Phi}} \boldsymbol{\omega}[k] + \underbrace{\begin{bmatrix}\mathbf{B} & & & \\ \mathbf{AB} & \mathbf{B} & & \\ \vdots & & \ddots & \\ \mathbf{A}^{H_p-1}\mathbf{B} & \mathbf{A}^{H_p-2}\mathbf{B} & \dots & \sum_{i=0}^{H_p-1-H_u}\mathbf{A}^i\mathbf{B}\end{bmatrix}}_{\boldsymbol{\Gamma}_\mathbf{u}} \underbrace{\begin{bmatrix}\tilde{\mathbf{u}}_k\\ \tilde{\mathbf{u}}_{k+1}\\ \vdots\\ \tilde{\mathbf{u}}_{k+H_u}\end{bmatrix}}_{\tilde{\mathbf{U}}_k}$$
$$+ \underbrace{\begin{bmatrix}\mathbf{B}_\mathrm{d}\\ \mathbf{AB}_\mathrm{d}+\mathbf{B}_\mathrm{d}\\ \vdots\\ \sum_{i=0}^{H_p-1}\mathbf{A}^i\mathbf{B}_\mathrm{d}\end{bmatrix}}_{\boldsymbol{\Gamma}_\mathbf{d}} \mathbf{d}_k + \underbrace{\begin{bmatrix}\boldsymbol{f}_{\boldsymbol{\omega}}\\ \mathbf{A}\boldsymbol{f}_{\boldsymbol{\omega}}+\boldsymbol{f}_{\boldsymbol{\omega}}\\ \vdots\\ \sum_{i=0}^{H_p-1}\mathbf{A}^i\boldsymbol{f}_{\boldsymbol{\omega}}\end{bmatrix}}_{\boldsymbol{\Gamma}_{\boldsymbol{f}}},$$

or equivalently

$$\mathbf{X}_k = \boldsymbol{\Phi}\boldsymbol{\omega}[k] + \boldsymbol{\Gamma}_\mathbf{u}\boldsymbol{\Gamma}_\Delta^{-1}\left(\Delta\tilde{\mathbf{U}}_k + \boldsymbol{\Gamma}_{\text{last}}\tilde{\mathbf{u}}_{k-1}\right) + \boldsymbol{\Gamma}_\mathbf{d}\mathbf{d}_k + \boldsymbol{\Gamma}_{\boldsymbol{f}}, \tag{7.29}$$

where $\boldsymbol{\Gamma}_\Delta$ and $\boldsymbol{\Gamma}_{\Delta,k-1}$ are difference operators such that $\Delta\tilde{\mathbf{U}}_k = \boldsymbol{\Gamma}_\Delta\tilde{\mathbf{U}}_k - \boldsymbol{\Gamma}_{\text{last}}\tilde{\mathbf{u}}_{k-1}$ (see Section B.4). The system outputs can be obtained by

$$\mathbf{Y}_k = \begin{bmatrix}\mathbf{Y}_{k+1}\\ \mathbf{Y}_{k+2}\\ \vdots\\ \mathbf{Y}_{k+H_p}\end{bmatrix} = \underbrace{\begin{bmatrix}\mathbf{C} & & & \\ & \mathbf{C} & & \\ & & \ddots & \\ & & & \mathbf{C}\end{bmatrix}}_{\bar{\mathbf{C}}} \mathbf{X}_k, \tag{7.30}$$

where $\mathbf{C}$ can be chosen so as to control $\boldsymbol{\omega}$ at certain points in $\hat{\rho}$. With the use of the matrices defined above, we can recast the optimal control problem (7.27) into the standard quadratic programming form. Introducing the notation

$$\mathbf{T}_k = \begin{bmatrix}\mathbf{r}_{k+1}\\ \mathbf{r}_{k+2}\\ \vdots\\ \mathbf{r}_{k+H_p}\end{bmatrix} \tag{7.31}$$

we can rewrite the optimal control problem (7.27) in the form

$$\begin{aligned} \underset{\Delta\tilde{\mathbf{U}}_k}{\text{minimize}} \quad & J = (\mathbf{Y}_k - \mathbf{T}_k)^T \bar{\mathbf{Q}} (\mathbf{Y}_k - \mathbf{T}_k) + \Delta\tilde{\mathbf{U}}_k^T \bar{\mathbf{R}} \Delta\tilde{\mathbf{U}}_k \\ \text{subject to} \quad & \Delta\tilde{\mathbf{U}} \in \Delta\tilde{\mathcal{U}} \end{aligned} \tag{7.32}$$

where $\bar{\mathbf{Q}} = I_{H_p} \otimes \mathbf{Q}, \bar{\mathbf{R}} = I_{H_u} \otimes \mathbf{R}$, and the actuator constraints, $\Delta\tilde{\mathbf{U}} \in \Delta\tilde{\mathcal{U}}$ are easily transformed to linear inequality constraints.

Since the objective function is positive definite ($\bar{\mathbf{R}} > 0$ and $\bar{\mathbf{Q}} \geq 0$)[2] it can be solved efficiently using active set techniques (see Appendix D.2), which take advantage of the fact that the set of active constraints on sequential control updates does not change dramatically, and thus the active set information from the previous control update can be used to warm start the solution on the next control update.

Because of imperfections in the model due to linearization the MPC solution will not show perfect tracking. However, the model matrices of the dynamics constraints in problem (7.27) are augmented as in Appendix B.5 to allow for offset free control.

### 7.4.3 Plasma Stored Energy Control

For control design purposes the stored energy evolution is approximated by its linearized dynamics,

$$\frac{dE}{dt} = -\frac{E}{\tau_{\mathrm{E_{eq}}}} + P_{\mathrm{aux}}(t), \tag{7.33}$$

where the contributions of ohmic power and radiative power are dropped since they are relatively small compared to the auxiliary power, and $\tau_{\mathrm{E_{eq}}}$ is the global energy confinement time associated with the equilibrium point $(\boldsymbol{\omega}_{\mathrm{eq}}, \mathbf{u}_{\mathrm{eq}})$. The approximate energy dynamics (7.33) describe a linear first order system, therefore with a simple proportional-integral (PI) controller we can obtain acceptable closed loop performance. With the PI controller,

$$P_{\mathrm{aux}}^{\mathrm{req}}(t) = k_p(E^d(t) - E(t)) + k_i \int_0^t E^d(\tau) - E(\tau) d\tau, \tag{7.34}$$

[2]Strictly speaking the objective is not positive definite, since $\mathbf{Q}$ is not positive definite, but it is positive definite within the null space of the equality constraints (dynamics constraints of (7.27)).

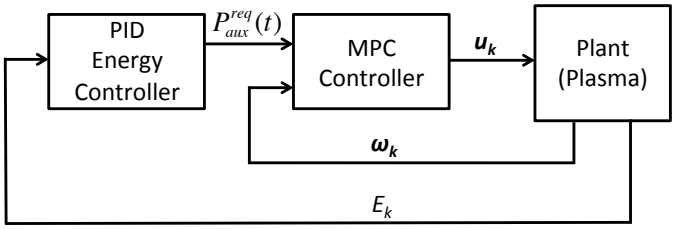


**Figure 7.6:** Rotation profile MPC with total power constraint to satisfy desired plasma stored energy.

we can obtain a request for total auxiliary input power, $P_{\text{aux}}^{\text{req}}(t)$, which can enter into the MPC problem as an equality constraint on the total auxiliary power. The combination of rotation profile MPC with energy control constraint is depicted in Figure 7.6. The constraint on total auxiliary power can be written as

$$\sum_{\xi=1}^{n_{\text{NBI}}} P_{\text{NBI},\xi} + P_{\text{EC}} = P_{\text{aux}}^{\text{req}}(t), \tag{7.35}$$

which represents a linear constraint on the control variables, therefore it can be incorporated without modification into problem (B.4) over the control horizon, $H_u$. In this manner we can obtain the desired plasma stored energy, and then allow the MPC controller to find the best combination of torque sources, NBI and NRMF, satisfying the total power constraint to match the desired rotation profile. The ECRH does not contribute any significant torque to the plasma, so it can essentially vary freely within its limits to satisfy the constraint (7.35).

### 7.4.4 Normalized Pressure Ratio ($\beta_N$) Limit

Deleterious MHD activity can be avoided by maintaing normalized $\beta_N$, $\beta$ normalized to the plasma current, below $\beta_N^{\max}$. To help ensure stable plasma conditions during the discharge, we can predict changes to $\beta_N$ over the prediction horizon and enforce a constraint in the total auxiliary power to maintain $\beta_N$ below an acceptable limit. The normalized $\beta$ can be expressed as $\beta_N = k_{\beta_N}\frac{E}{I_{\text{p}}}$, where $k_{\beta_N}$ is a constant depending on the plasma volume, plasma minor radius, and toroidal magnetic field.

At time $k$, we can take the current value of $\tau_{E,k}$ ($\tau_{E,k} \propto I_{\text{p},k}^{0.93}\bar{n}_{\text{e},k}^{0.41}P_{\text{tot},k}^{-0.69}$) and

current energy $E_k$, to estimate the forward evolution of $\beta_N$ according to

$$\begin{aligned} E_{k+1} &= A_E E_k + B_E P_{\text{aux},k}, \\ E_{k+2} &= A_E^2 E_k + A_E B_E P_{\text{aux},k} + B_E P_{\text{aux},k+1}, \\ E_{k+3} &= A_E^3 E_k + A_E^2 B_E P_{\text{aux},k} + A_E B_E P_{\text{aux},k+1} \\ &\qquad + B_E P_{\text{aux},k+2}, \end{aligned} \tag{7.36}$$

$$E_{k+t} = A_E^t E_k + \sum_{i=0}^{t-1} A_E^i B_E P_{\text{aux},k+t-i},$$

$$\beta_{N,k+t} = k_{\beta_N} \frac{E_{k+t}}{I_{\text{p},k+t}}, \tag{7.37}$$

where $A_E = \left(1 + \frac{1}{\tau_{E,k}} T_s\right)^{-1}$ and $B_E = A_E T_s$. In this work $I_\text{p}$ is assumed either constant or preprogrammed therefore the future $I_\text{p}$ evolution is known and the constraint on $\beta_N$ reduces to a maximum bound on requested auxiliary power. Combining (7.36) and (7.37), we can transform the $\beta_N$ limit over the prediction horizon, $\beta_{N,k+t}|_{t=0,1,\ldots,H_p} \leq \beta_N^{\max}$ into a constraint on maximum auxiliary power input. In order to ensure the MPC problem remains feasible, potential conflicts between the $\beta_N$ limit and the energy control constraint (7.35) are alleviated by softening the energy control constraint with a forgiveness parameter,

$$P_{\text{aux}}^{\text{req}}(t) - \epsilon_\text{E} \leq \sum_{\xi=1}^{n_\text{NBI}} P_{\text{NBI},\xi} + P_\text{EC} \leq P_{\text{aux}}^{\text{req}}(t) + \epsilon_\text{E}, \tag{7.38}$$

where $\epsilon_E \geq 0$ represents a window on forgiveness of satisfying the energy control constraint. The forgiveness parameter is included as an optimization variable in the MPC problem (B.4) by replacing the optimization objective with

$$J_k + W_E \epsilon_E^2, \tag{7.39}$$

where $W_E$ is introduced as a weight.

### 7.4.5 Simulation Results of MPC Approach

In this section, we consider a simulation study of the controller's effectiveness. The target for $\Omega_\phi$ is obtained by simulating the rotation profile evolution with the model

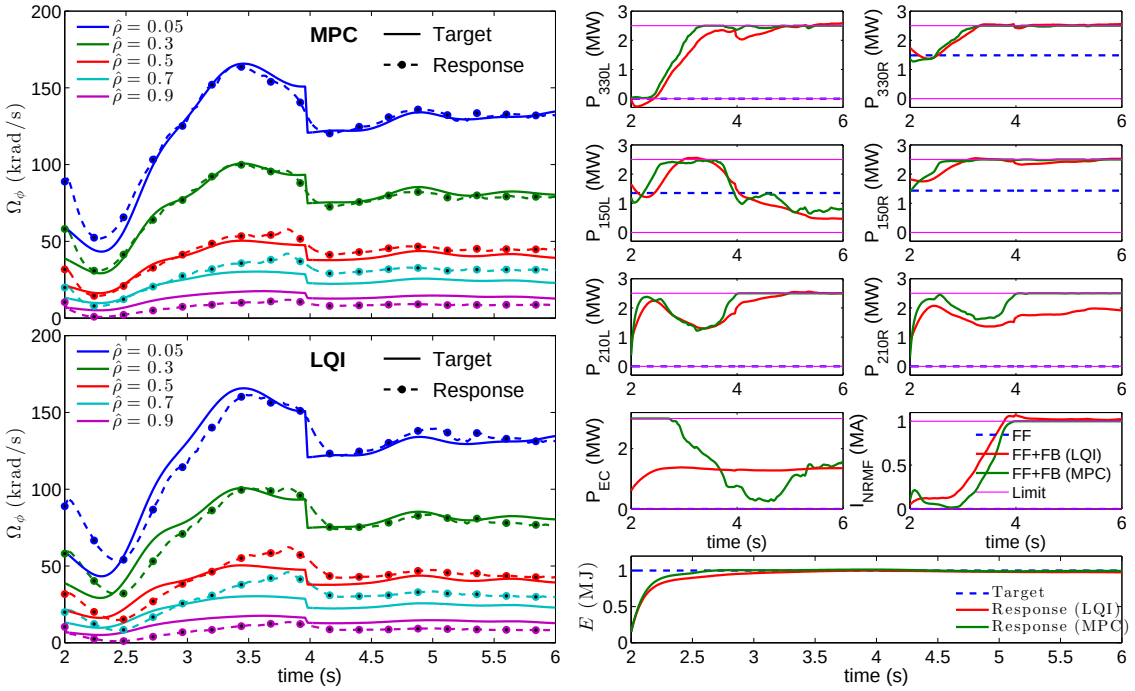


(a) $\Omega_\phi$: MPC (top) and LQI (bottom) (b) Inputs

**Figure 7.7:** Feedback control simulation. (a) $\Omega_\phi$, where the solid line is the target and the achieved profile is marked by circles. (b) Input values and $E$, where the controller requested power is in green (MPC) and red (LQI), the blue dashed line marks the feedforward power, and the pink dashed line marks the actuators limits. The stored energy set point is marked by the blue dashed line.

using the input values and parameter profiles of DIII-D shot 147634, and the stored energy set-point is simply set to 1 MJ, a typical value for H-mode plasmas. We use no feedforward control and allow the feedback controller alone to recover the target profile. The rotation evolution is modeled with equations (7.1)-(7.4).

The control-design problem consists of the selection of the diagonal elements of $\mathbf{Q}$ and $\mathbf{R}$, the prediction horizons $H_p$, and the control horizon $H_u$ of the quadratic program (QP) (7.27). To solve the QP, we use an active set algorithm, and take advantage of warm-starting (see Appendix D.2). Active set algorithms are essentially efficient methods for searching through the possible combinations of active inequality

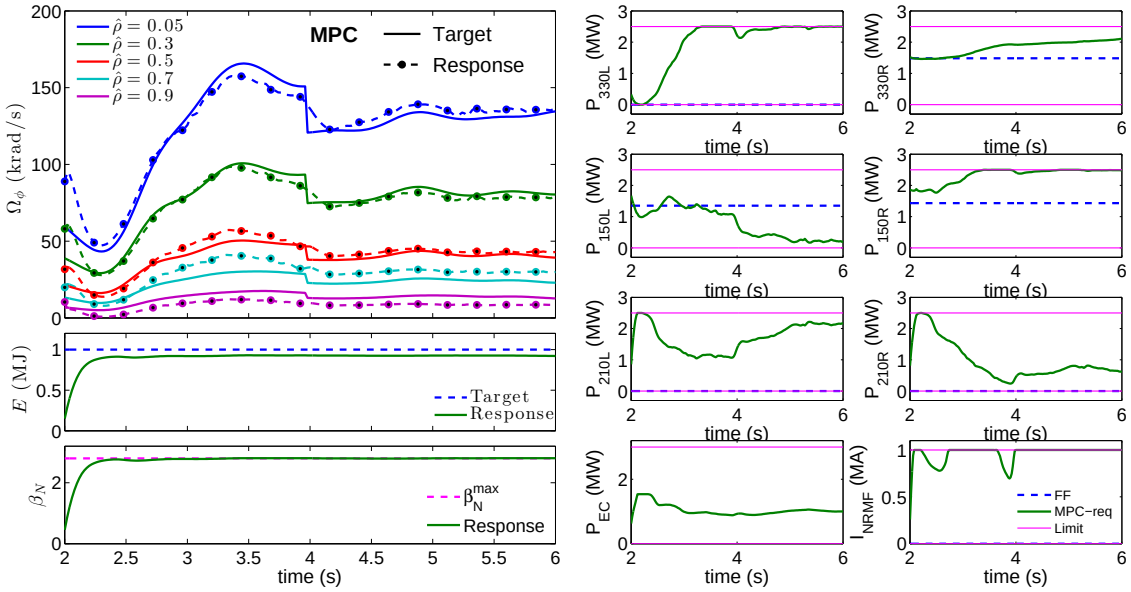


(a) $\Omega_\phi$, $E$, and $\beta_N$ for MPC (b) Inputs

**Figure 7.8:** Same simulation as in Figure 7.7 with $\beta_N$ limit imposed. The line and color configuration is also the same as in Figure 7.7.

constraints, i.e. the inequality constraints that are satisfied as equalities at the optimal solution. Once the active set is known, the solution to a strictly convex quadratic program reduces to the solution of a linear system. Therefore most of the work of an active set algorithm is associated with determining the active set. Noting the active set does not change much from one control update to the next, we can use the active set from the previous MPC solution to *warm-start* the next MPC solution. We use a short horizon time of $H_p = 10$ and $H_u = 5$, which combined with warm-starting allows for an average computation time less than 3 ms.

In Figure 7.7, we test the controller's tracking performance with feedback ON throughout the simulation. The target profile and simulated closed-loop profile response are plotted in 7.7(a), and the requested actuator powers[3] and plasma energy are plotted in Figure 7.7(b). For comparison the results of both the MPC approach

[3] $P_{330L}$ and $P_{330R}$ are co-current on-axis, $P_{150L}$ and $P_{150R}$ are co-current off-axis and $P_{210L}$ and $P_{210R}$ are counter-current on axis NBI.

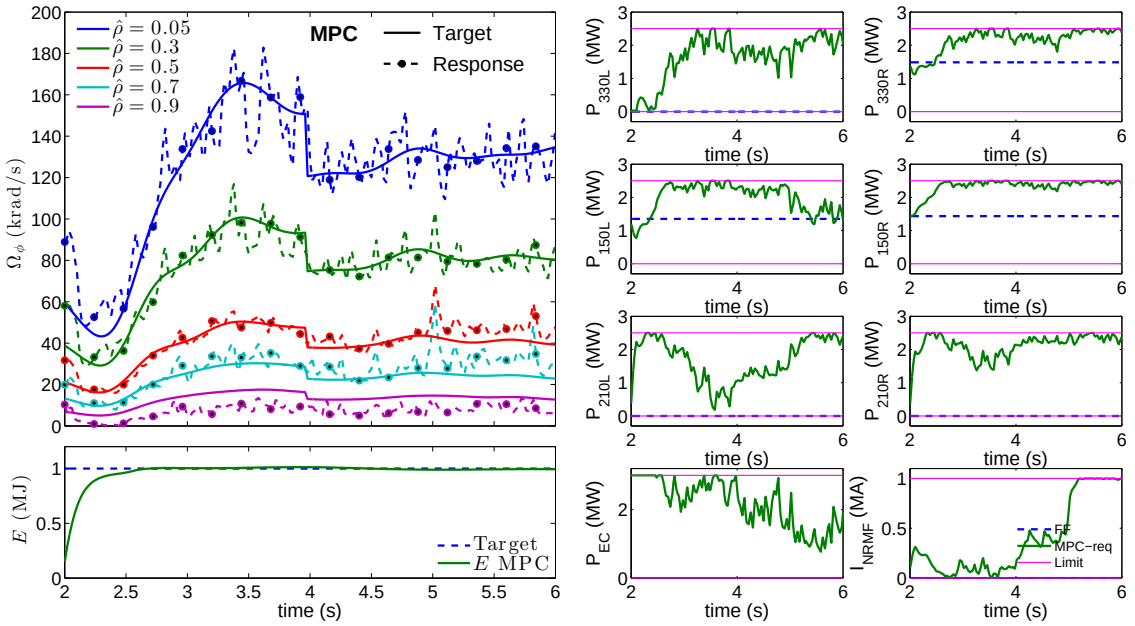


(a) $\Omega_\phi$ and $E$ for MPC (b) Inputs

**Figure 7.9:** Same simulation as Figure 7.7, except we allow $\chi_\phi$ to vary randomly in the range shown in Figure 7.2(b).

and the linear quadratic integral (LQI) approach of Section 7.3.2 are both plotted in Figure 7.7 under the same conditions (no $\beta_N$ limit). The MPC profile controller performs well, enabling tight profile regulation while maintaining a nearly flat stored energy. At $t = 4$ s, the rotation profile target switches discretely to a lower target value. Note that the controller obtains the second, lower rotation target by increasing the counter-$I_p$ NBI power ($P_{210L}$ and $P_{210R}$) while reducing the co-$I_p$ NBI power ($P_{330L}$ and $P_{150L}$) to maintain the stored energy around the set point of 1 MW. The additional power from the ECRH is quite advantageous in maintaining the stored energy value and the NRMF provides some advantage over NBI in regulating the rotation at the plasma edge. The LQI controller performs similarly to the MPC; it lags the time changing target slightly due to the fact that the MPC anticipates future target changes.

The main advantage of the MPC approach is the handling of actuator constraints,

in particular the ability to impose the $\beta_N$ limit as a variable total auxiliary power limit. In the second simulation, Figure 7.8, we consider the MPC control approach again with the $\beta_N$ limit imposed arbitrarily at $\beta_N^{\max} = 2.7$ for testing purposes. The target energy and rotation profile are met as closely possible while satisfying the $\beta_N$ limit. Comparing the simulation with $\beta_N$ limit imposed (Figure 7.8) to the simulation without the imposed $\beta_N$ limit (Figure 7.7), we can see a notable differences in the actuation. The total ECCD power is constrained in the early phase (2-3 s) of the simulation with imposed $\beta_N$ limit. After 3 s, the controller uses significantly less NBI power to maintain the $\beta_N$ limit, and a trade-off is found that exchanges NBI power for $I_{\text{NRMF}}$ actuation to maintain the target profile in the outer region ($\hat{\rho} > 0.5$).

In the third simulation, Figure 7.9, the conditions are the same as the first except we allow for random perturbations in the value of $\chi_\phi$ over the range depicted in Figure 7.2(b). It is very challenging to develop stability and robustness guarantees for numerical optimal control problems of the type defined by (7.27). This simulation provides a check of robustness against the anomalous properties of $\chi_\phi$.

## 7.5 Conclusion

Two approaches for regulation of the toroidal rotation profile and simultaneous plasma stored energy control were considered and compared. First, an LQI approach in which the rotation and plasma energy were lumped together into a single state, and, second, an MPC approach in which the energy control was incorporated via a constraint on total auxiliary power. Similar performance was found for both cases, however, the MPC controller was designed to respect limits in the kinetic to magnetic pressure ratio to improve stability against deleterious MHD activity. The simulations show promise of an effective controller for the combined control of rotation and energy using NBI, ECRH, and NRMF coils as actuators.

# Chapter 8

# TRANSP-Based Optimization for the Design of Non-inductive Ramp-up in NSTX-U

## 8.1 Introduction

One of the primary research goals of NSTX-U is to advance the spherical torus concept for a fusion nuclear science facility (FNSF), which requires developing non-inductive start-up, ramp-up, and sustainment techniques since a large scale spherical torus will have little to no room for a central solenoid[1]. Under certain plasma conditions, NSTX has been shown to sustain about 70% of the current non-inductively [92]. With recent upgrades including an additional high tangency neutral beam set and high frequency fast wave (HHFW) antenna (see Section 1.7.2), exhaustive simulations anticipate that NSTX-U [93] will be able to sustain fully non-inductive current in the flattop phase of the discharge. However, much research is still required to develop a successful approach for non-inductive start-up and ramp-up in NSTX-U.

The provisional strategy for fully non-inductive operation in NSTX-U is shown

[1]The central solenoid coil serves as the inductive current drive.

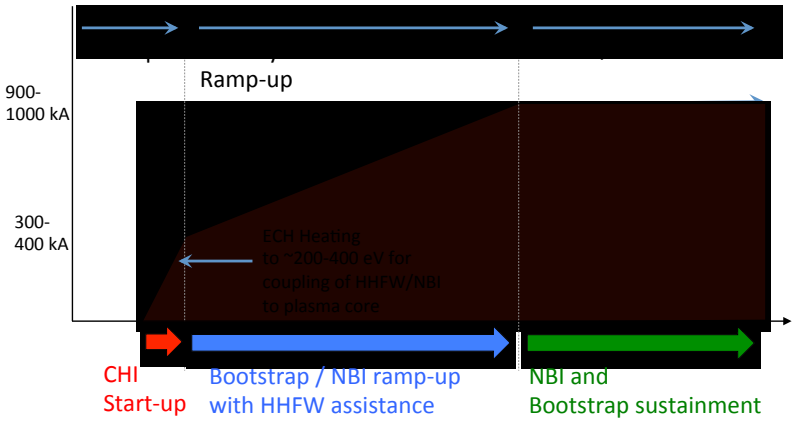


**Figure 8.1:** Non-inductive ramp-up strategy for NSTX-U.

in Figure 8.1 [94]. First, the plasma is initiated with coaxial helicity injection (CHI), and ramped to about 400 kA. The CHI initiated plasma can be heated by ECH up to several hundred eV, which is necessary in order to prime the plasma for proper coupling with the HHFW. Following the start-up and initial ramp-up from CHI, a combination of HHFW and NBI with a high bootstrap fraction can be used to ramp the plasma to a full current of around 900-1000 kA. Current drive from HHFW is necessary since the plasma density is too low to safely apply NBI in the initial phase of the discharge on account of high shine-through losses. Finally, neutral beam and a substantial bootstrap current will sustain the plasma current through the flattop phase of the discharge.

A predictive TRANSP study of the proposed non-inductive ramp-up strategy has been explored in a systematic way [40]. However, the simulations anticipate various difficulties with the start-up/ramp-up strategy. There are inherent limitations to the non-inductive current sources and their effectiveness depends strongly on the plasma conditions which change dramatically through the ramp-up. Also, without careful optimization of the plasma target, the non-inductive sources have the potential of making the plasma unstable to various undesirable magneto-hydro-dynamic (MHD) activity. During the ramp-up, the necessary contributions from NBI and HHFW were shown to cause poor plasma shape (poor elongation), large plasma-wall gap causing problems with coupling to RF sources, and low shear $q$ profiles with central $q$ falling below 1 [40].

This chapter considers an optimization-based control approach to improve on the non-inductive ramp-up strategy[2]. We combine the TRANSP code with an optimization algorithm based on sequential quadratic programming to search for time evolutions of the NBI powers that define an open-loop control strategy that maximizes the non-inductive current. This technique has the potential of playing a critical role in aiding the development of a stable non-inductive ramp-up, which will ultimately be necessary to demonstrate applicability of the spherical torus concept to larger devices without sufficient room for a central coil. Since this work is in its infancy, the chapter is brief, containing only two sections. First, in Section 8.2, the optimization approach is described, and conclusions and directions for further development are stated in Section 8.3.

## 8.2 TRANSP-Based Optimization

To begin, it is assumed that the plasma can be successfully initiated and ramped to 300 kA with CHI, therefore this work focuses only on the ramp-up phase. The objective is to obtain an open-loop control strategy, i.e. sequence of control requests parameterized by time, that could sustain the target plasma current non-inductively through the ramp-up phase while maintaining the $q$ profile within acceptable bounds for stability against deleterious MHD effects. Similar to the feedforward control design of Chapter 4, the problem is formulated as an optimal control problem, which can be passed to a numerical optimization algorithm.

Let $\boldsymbol{\alpha}$ represent the optimization variables, which could be parameterized in a variety of ways depending on the optimization goal. For example, we may consider a parameterization consisting of the turn-ON time and injected power of each NBI

[2]This work was carried out at the Princeton Plasma Physics Laboratory under the DOE Office of Science Graduate Student Research (SCGSR) Program award.

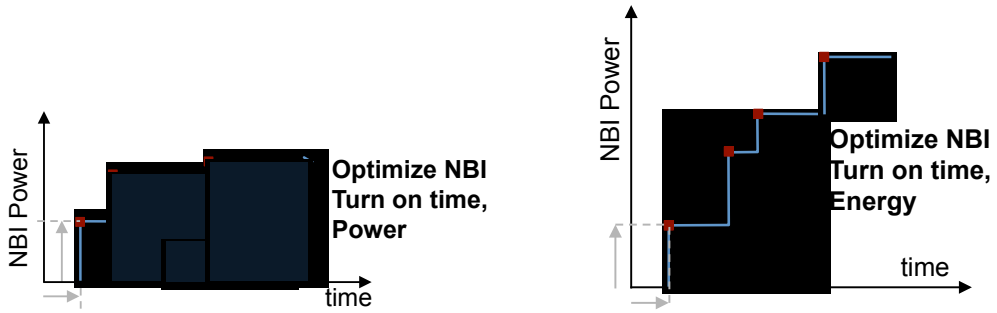


(a) Individual NBI (b) Total NBI

**Figure 8.2:** Parameterization of NBI power for TRANSP-based optimization. The parameters include the turn-ON time and the injected energy of each NBI.

as shown in Figure 8.2, in which case

$$\boldsymbol{\alpha} = \begin{bmatrix} t^{ON}_{NBI,1} \\ P_{NBI,1} \\ t^{ON}_{NBI,2} \\ P_{NBI,2} \\ \vdots \\ t^{ON}_{NBI,N} \\ P_{NBI,N} \end{bmatrix} \tag{8.1}$$

where $N$ is the number of NBI to be optimized. Now, consider the optimal control problem,

$$\underset{\boldsymbol{\alpha}}{\text{minimize}} \qquad J^{\boldsymbol{\alpha}}(I_\text{p}), \tag{8.2}$$

$$\text{subject to:} \qquad \beta_N(t) \leq \beta_{N_\text{max}}, \tag{8.3}$$

$$q \geq 1, \tag{8.4}$$

$$\boldsymbol{\alpha}_\text{min} \leq \boldsymbol{\alpha} \leq \boldsymbol{\alpha}_\text{max}. \tag{8.5}$$

The problem involves the minimization of a scalar objective over a set of constraints including actuator constraints (physical limits such as max NBI power or earliest turn-ON time), the $\beta_N$ limit, and bounds on the acceptable current profile shape through the ramp-up phase. The cost function (8.2) penalizes the difference between

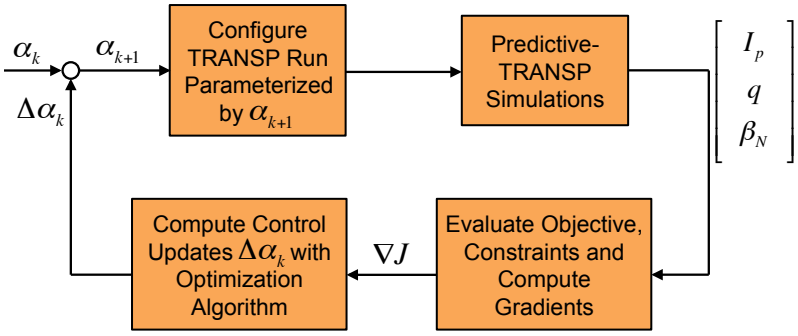


**Figure 8.3:** TRANSP-based optimization loop.

total non-inductive current drive and the current target,

$$J^{\boldsymbol{\alpha}}(I_{\mathrm{p}}) = \int_{t_i}^{t_f} \left(I_{\mathrm{p}}^{\mathrm{target}}(\tau) - I_{\mathrm{NI}}(\tau)\right)^2 d\tau = \int_{t_i}^{t_f} \left(I_{\mathrm{OHM}}(\tau)\right)^2 d\tau. \tag{8.6}$$

The TRANSP code is combined with an optimization algorithm embedded in OMFIT [95], where OMFIT acts primarily as an accessory code to automate the issuing of TRANSP runs[3]. The combined TRANSP + OMFIT routine, performs the same type of open-loop control optimization of Chapter 4, but the plasma evolution is simulated by the TRANSP code instead of a control oriented model.

This process involves coding a numerical optimization solver into the OMFIT code. We use sequential quadratic programming (SQP), which is the most widely used approach to solving constrained optimal control problems of this form (see Appendix D.1 for a description of the algorithm). Essentially, the algorithm searches for a solution by first starting with an approximate solution, call it $\boldsymbol{\alpha}_0$, and works to improve on the solution by taking steps, $\Delta\boldsymbol{\alpha}$. Sequential iterates, $\boldsymbol{\alpha}_{k+1} = \boldsymbol{\alpha}_k + \Delta\boldsymbol{\alpha}_k$, are found with the use of gradient information of the cost function and constraints.

The optimization approach treats TRANSP as a black box, as such it is impossible obtain analytic gradients as was done in Chapter 4, so instead the gradients are calculated by forward finite difference (see Section 4.3). Therefore each iteration of the optimization requires $n+1$ TRANSP runs in order to obtain gradient information, where $n$ is the dimension of $\boldsymbol{\alpha}$.

[3]OMFIT, developed and maintained by General Atomics, San Diego, is a python-based tool designed to standardize and manage the data of many plasma transport codes such as TRANSP.

The automated TRANSP + OMFIT optimization procedure is outlined in Figure 8.3. In summary, the optimization procedure works as follows:

- Choose initial, approximate solution $\boldsymbol{\alpha}_0$
- Repeat $k = 0, 1, \ldots, k_{\max}$
  - Configure the input files and initiate a TRANSP run parameterized by current iterate $\boldsymbol{\alpha}_k$
  - Configure and initiate $n$ TRANSP runs parameterized by $\boldsymbol{\alpha}_k + \epsilon \mathbf{e}_i$ for $i = 1, 2, \ldots, n$ to obtain gradients, where $\mathbf{e}_i$ is the $i^{\text{th}}$ coordinate vector, i.e. $\mathbf{e}_1 = [1, 0, \ldots, 0]^T$, $\mathbf{e}_2 = [0, 1, 0, \ldots, 0]^T$, etc. (see equation (4.20))
  - Evaluate function and constraint values and compute gradients
  - Determine search direction $\mathbf{d}_k$ (descent direction determined by SQP step)
  - Determine step length $\gamma_k$ (linesearch), $\Delta\boldsymbol{\alpha}_k = \gamma \mathbf{d}_k$
  - Check convergence, i.e. $\Delta\boldsymbol{\alpha}_k \leq$ tolerance
  - Obtain new iterate $\boldsymbol{\alpha}_{k+1} = \boldsymbol{\alpha}_k + \Delta\boldsymbol{\alpha}_k$

As a test case, we consider reproduction of the some of the work presented in [40] via the TRANSP + OMFIT optimization routine. In Figure 8.4, Figure 9 of [40] has been reproduced, in which NBI powers are optimized (by hand) to design a non-inductive ramp-up strategy. The figure shows both the results of the optimization performed by hand (figure 9 of [40]) and by the TRANSP + OMFIT optimization routine. In this case we consider optimization of the cost function (8.6) with no constraints other than NBI power bounds. Notable improvements in meeting the current target are realized, and secondarily the routine saves time associated with manually initiating TRANSP runs; the entire procedure is automatic.

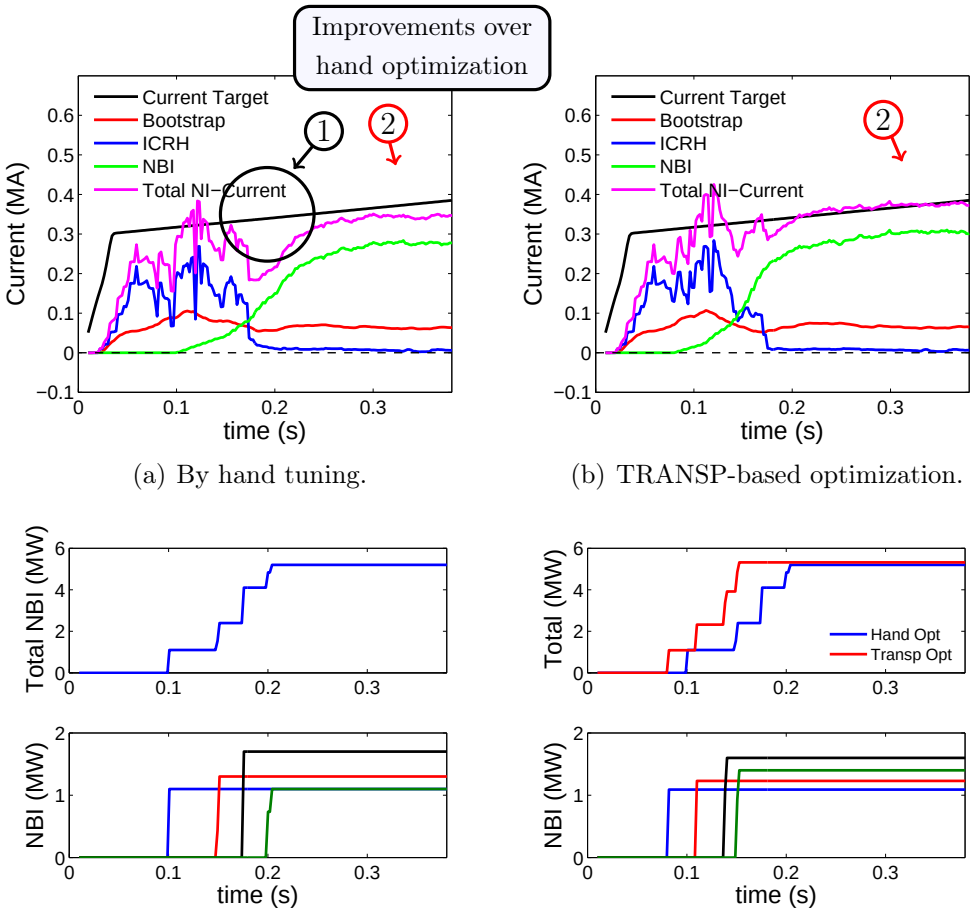


(a) By hand tuning.

(b) TRANSP-based optimization.

(c) NBI power tuned by hand.

(d) NBI power tuned by TRANSP-based optimization.

**Figure 8.4:** TRANSP-based optimization test case. (Left) NBI powers are selected by hand to best achieved the non-inductive ramp-up in NSTX-U. (Right) a reproduction of the left figure except the TRANSP-based optimization routine is used to obtain the NBI powers.

## 8.3 Conclusions and Future Work

The TRANSP + OMFIT optimization routine presented in this chapter represents a valuable tool for developing control strategies of varying objectives. The optimization algorithm written in OMFIT can accept arbitrary objective and constraint functions, and the optimization variables can include either the NBI or HHFW powers or both. It is a straight forward process to introduce other optimization variables

such as the plasma wall gap, the NBI tangency radius, or the plasma current ramp rate, to name a few relevant to current profile control in NSTX-U. Presently the code has been developed only for NSTX-U, but could be extended to other tokamaks such as DIII-D or any other device that is supported by the TRANSP code.

It is not uncommon for plasma physics researchers to use transport codes to solve engineering design problems. For example, a study considering the optimal launch location of high frequency fast waves for maximum current drive efficiency at DIII-D was carried out using GENRAY simulations [96]. These types of studies, often involving "optimization" by-hand could be aided by the tool described in this chapter. Not only does the tool provide a truly optimized result, but also automates the process, saving many hours of work.

Future work would involve addressing some shortcomings of the optimization algorithm. For example, the algorithm currently requires the iterates to remain feasible at all times during the optimization, which can be troublesome if the problem is to find a feasible point. Alternatively, we could replace the optimization algorithm altogether with a more robust commercial solver. Additionally, the code should be configured to work with other transport codes other than TRANSP, such as the previously mentioned GENRAY code.

# Chapter 9

# Conclusions and Future Work

The primary contribution of this dissertation has been the development of control algorithms to be used as tools for experimental physics studies. Control of the current profile and rotation profile enable not only improved efficiency in carrying out tokamak experiments by reducing the number of shots required to obtain the desired operating conditions in the plasma, but also enable studies designed at exploring various profile shapes in search of interesting plasma properties. In this final chapter, the contributions of the work are summarized and possible directions for further research are discussed.

## 9.1 Contributions

1. A linear plasma-response model for the combined evolution of the current profile and $\beta_N$ evolution around a reference plasma equilibrium was developed using data-driven modeling techniques. Additional simplified physics-based models were developed for the separate evolution of the current profile and rotation profile. These models, which were intended for applicability to real-time control strategies, combined first-principles laws with scenario specific correlations of the plasma temperature, density, and current drive or torque sources.

2. Feedforward control of the current profile dynamics during the ramp-up phase was formulated as a finite time optimal control problem, and solved using numerical optimization techniques. Anticipating that the un-augmented feedforward control would be insufficient to reliably obtain target current profiles due to mismatch between the model and real system, the feedforward control was combined with feedback control.

3. Numerous feedback control strategies were developed for regulation of both the current profile and rotation profile. In both cases, a focus was made on model predictive control approaches, so as to embed constraints for the avoidance of unstable plasmas. The MPC approach was combined with efficient quadratic programming techniques to enable real-time implementations. In the case of current profile control, numerous experimental tests were carried out in the DIII-D tokamak, which successfully demonstrated the effectiveness of the control approach.

4. To facilitate the development of non-inductive ramp-up strategies in NSTX-U, the TRANSP code was combined with an optimization algorithm based on sequential quadratic programming to search for time evolutions of the auxiliary current drive sources defining an open-loop control strategy that maximizes the non-inductive current fraction.

## 9.2 Future Work

One short coming to the current profile control approaches described in this work is that they are based on a control-oriented model, which lacks any spatial evolution of the electron temperature profile. Given the plasma resistivity is primarily a function of electron temperature, the model-based control approaches could be greatly benefited by incorporating, at least in some primitive form, a local model for electron energy transport. This would provide the possibility to model local changes to the resistivity profile, and thereby improve the current profile control.

For the most part, control research for tokamaks has focused on individual objectives. In reality, high-performance operation of tokamak plasmas will require a multitude of plasma control problems to be addressed simultaneously. For example, the controls associated with the suppression of NTMs, which may include localized injection of ECCD, or suppression of RWMs, which may include application of non-axisymmetric magnetic fields, introduces actuation that may conflict with the desired actuation for current profile control or rotation profile control. This necessitates the development of a supervisory control architecture that can make judicial trade-offs for the control of multiple objectives that rely on a shared actuator set. The MPC approaches that are the primary contribution of this work are well suited to be extended towards the design of a supervisory control architecture because the requirements for actuator sharing can be incorporated into the MPC profile controller as explicit actuator constraints.

# Appendix A

# Computations

## A.1 Finite Difference Discretization of the Magnetic Diffusion Equation

### A.1.1 Finite Differences Discretization for the $\psi$ model

The dynamic system describing the evolution of the poloidal magnetic flux ($\psi$) profile can be written as

$$\frac{\partial \psi}{\partial t}(\hat{\rho},t) = \frac{f_\eta u_\eta}{\hat{\rho}} \frac{\partial}{\partial \hat{\rho}} \left( \hat{\rho} D_\psi \frac{\partial \psi}{\partial \hat{\rho}} \right) + \sum_{i=1}^{n_{\mathrm{EC}}} f_{\mathrm{EC}} u_{\mathrm{EC}} + \sum_{i=1}^{n_{\mathrm{NBI}}} f_{\mathrm{NBI}} u_{\mathrm{NBI}} + \left( \frac{\partial \psi}{\partial \hat{\rho}} \right)^{-1} f_{\mathrm{BS}} u_{\mathrm{BS}}, \tag{A.1}$$

where the boundary conditions are given by

$$\frac{\partial \psi(t,0)}{\partial \hat{\rho}} = 0, \qquad \frac{\partial \psi(t,1)}{\partial \hat{\rho}} = -k_{I_{\mathrm{p}}} I_p(t), \tag{A.2}$$

the parameters $f_{(\cdot)}$ are all time-constant functions of $\hat{\rho}$, and the parameters $u_{(\cdot)}$ are a set of input functions of the form

$$\begin{aligned} u_\eta(t) &= I_{\mathrm{p}}(t)^{a_\eta} P_{\mathrm{tot}}(t)^{b_\eta} \bar{n}_{\mathrm{e}}(t)^{c_\eta}, \\ u_{\mathrm{EC},i}(t) &= I_{\mathrm{p}}(t)^{a_{ec}} P_{\mathrm{tot}}(t)^{b_{ec}} \bar{n}_{\mathrm{e}}(t)^{c_\eta} P_{\mathrm{EC},i}(t), \\ u_{\mathrm{NBI},i}(t) &= I_{\mathrm{p}}(t)^{a_{nb}} P_{\mathrm{tot}}(t)^{b_{nb}} \bar{n}_{\mathrm{e}}(t)^{c_{nb}} P_{\mathrm{NBI},i}(t), \\ u_{\mathrm{BS}}(t) &= I_{\mathrm{p}}(t)^{a_{bs}} P_{\mathrm{tot}}(t)^{b_{bs}} \bar{n}_{\mathrm{e}}(t)^{c_{bs}}. \end{aligned} \tag{A.3}$$

### Discretization in Space

To discretize the system (A.1) in space, let us divide the spatial domain ($\hat{\rho} \in [0,1]$) into $l$ evenly spaced nodes, and let $n$ represent the index of the nodes, i.e. $n = 0, 1, \ldots, l-1$. The distance between grid points (nodes) is given by $\Delta\hat{\rho} = 1/(l-1)$. For convenience, let $\hat{\rho}_n$ be the value $\hat{\rho}$ at node $n$, i.e. $\hat{\rho}_n = n\Delta\hat{\rho}$, and, similarly, let $\psi_n$ be the value of $\psi$ at node $n$, i.e. $\psi_n(t) = \psi(\hat{\rho}_n, t)$.

At the interior nodes, the spatial derivatives of (A.1) can be approximated by the central difference formulae

$$\frac{d\psi_m}{d\hat{\rho}} = \frac{\psi_{m+1} - \psi_{m-1}}{2\Delta\hat{\rho}} + O(\Delta\hat{\rho}^2), \qquad \frac{d^2\psi_m}{d\hat{\rho}^2} = \frac{\psi_{m+1} - 2\psi_m + \psi_{m-1}}{\Delta\hat{\rho}^2} + O(\Delta\hat{\rho}^2). \tag{A.4}$$

First, expand the spatial derivatives of (A.1) to obtain

$$\begin{aligned}\dot{\psi} =& \frac{f_\eta u_\eta}{\hat{\rho}}\left((\hat{\rho}\frac{dD_\psi}{d\hat{\rho}} + D_\psi)\frac{\partial\psi}{\partial\hat{\rho}} + \hat{\rho}D_\psi\frac{\partial^2\psi}{\partial\hat{\rho}^2}\right) + \sum_{i=1}^{n_{\rm EC}} f_{\rm EC}u_{\rm EC} \\ &+ \sum_{i=1}^{n_{\rm NBI}} f_{\rm NBI}u_{\rm NBI} + \left(\frac{\partial\psi}{\partial\hat{\rho}}\right)^{-1} f_{\rm BS}u_{\rm BS},\end{aligned} \tag{A.5}$$

and then replace the spatial derivatives with finite difference formulae (A.4) to obtain

$$\begin{aligned}\dot{\psi}_m = \frac{f_\eta(\hat{\rho}_m)u_\eta}{\hat{\rho}_m}&\left[\left(\hat{\rho}_m\frac{dD_\psi}{d\hat{\rho}}(\hat{\rho}_m) + D_\psi(\hat{\rho}_m)\right)\left(\frac{\psi_{m+1} - \psi_{m-1}}{2\Delta\hat{\rho}}\right)\right. \\ &\left.+\hat{\rho}_m D_\psi(\hat{\rho}_m)\left(\frac{\psi_{m+1} - 2\psi_m + \psi_{m-1}}{(\Delta\hat{\rho})^2}\right)\right] + \sum_{i=1}^{N_{\rm EC}} f_{\rm EC}(\hat{\rho}_m)u_{\rm EC} \\ &+ \sum_{i=1}^{N_{\rm NBI}} f_{\rm NBI}(\hat{\rho}_m)u_{\rm NBI} + \left(\frac{2\Delta\hat{\rho}}{\psi_{m+1} - \psi_{m-1}}\right) f_{\rm BS}(\hat{\rho}_m)u_{\rm BS},\end{aligned} \tag{A.6}$$

for $m = 1, \ldots, l-2$. To simplify notation we can introduce the terms

$$\beta_m = f_\eta(\hat{\rho}_m)\frac{D_\psi(\hat{\rho}_m)}{(\Delta\hat{\rho})^2}, \qquad \alpha_m = f_\eta(\hat{\rho}_m)\frac{\hat{\rho}_m\frac{dD_\psi(\hat{\rho}_m)}{d\hat{\rho}} + D_\psi(\hat{\rho}_m)}{\hat{\rho}_m(2\Delta\hat{\rho})}, \tag{A.7}$$

so that (A.6) can be written as

$$\dot{\psi}_m = (\psi_{m-1}(\beta_m - \alpha_m) + \psi_m(-2\beta_m) + \psi_{m+1}(\alpha_m + \beta_m))\, u_\eta + \sum_{i=1}^{n_{\rm EC}} f_{\rm EC}(\hat{\rho}_m) u_{\rm EC} + \sum_{i=1}^{n_{\rm NBI}} f_{\rm NBI}(\hat{\rho}_m) u_{\rm NBI} + 2\Delta\hat{\rho} f_{\rm BS}(\hat{\rho}_m) u_{\rm BS} \left(\frac{1}{\psi_{m+1} - \psi_{m-1}}\right), \tag{A.8}$$

for $m = 1, \ldots, l-2$. Using the following finite difference formula for the first spatial derivative at the boundary nodes

$$\frac{d\psi_0}{d\hat{\rho}} = \frac{-3\psi_0 + 4\psi_1 - \psi_2}{2\Delta\hat{\rho}} + O(\Delta\hat{\rho}^2), \tag{A.9}$$

the boundary conditions (A.2) can be used to obtain expressions for $\psi$ at the boundary nodes, i.e.

$$\psi_0 = \frac{1}{3}(4\psi_1 - \psi_2), \qquad \psi_{l-1} = \frac{1}{3}(4\psi_{l-2} - \psi_{l-3} - (2\Delta\hat{\rho}) k_{I_{\rm p}} I_{\rm p}). \tag{A.10}$$

Finally, combining the expression for interior nodes (A.6) with those for the boundary nodes (A.10), the discretized system can be written in state space form

$$\boldsymbol{\psi} = \boldsymbol{f}(\boldsymbol{\psi}, \mathbf{u}), \tag{A.11}$$

where $\boldsymbol{\psi} = [\psi_1, \psi_2, ..., \psi_{l-2}]^T$, $\mathbf{u}$ can be taken as either the input functions (A.3) or the physical actuators ($\bar{n}_e$, $P_{{\rm EC},1} \ldots, P_{{\rm EC},n_{\rm EC}}$, $P_{{\rm NBI},1}, \ldots, P_{{\rm NBI},n_{\rm NBI}}$, $I_{\rm p}$), and the nonlinear function $\boldsymbol{f}$ can be expressed as

$$\boldsymbol{f}(\boldsymbol{\psi}, \mathbf{u}) = \mathbf{F}_1 \boldsymbol{\psi} u_\eta + \mathbf{F}_2 \begin{bmatrix} u_{{\rm EC},1} \\ \vdots \\ u_{{\rm EC},n_{\rm EC}} \\ u_{{\rm NBI},1} \\ \vdots \\ u_{{\rm NBI},n_{\rm NBI}} \end{bmatrix} + \mathbf{F}_3 \begin{bmatrix} 1/(\frac{4}{3}\psi_2 - \frac{4}{3}\psi_1) \\ 1/(\psi_3 - \psi_1) \\ \vdots \\ 1/(\psi_{l-2} - \psi_{l-3}) \\ 1/\Big(\frac{4}{3}(\psi_{N-1} - \psi_{N-2}) \\ -\frac{(2\Delta\hat{\rho})}{3} k_{I_p} I_p\Big) \end{bmatrix} u_{\rm BS} + \mathbf{F}_4 u_\eta I_{\rm p}, \tag{A.12}$$

where the newly introduced matrices are given by

$$\mathbf{F}_1 = \begin{bmatrix} -\frac{2}{3}\beta_1 - \frac{4}{3}\alpha_1 & \frac{2}{3}\beta_1 + \frac{4}{3}\alpha_1 & & & \\ \beta_2 - \alpha_2 & -2\beta_2 & \alpha_2 + \beta_2 & & \\ & & \ddots & & \\ & & \beta_{l-3} - \alpha_{l-3} & -2\beta_{l-3} & \alpha_{l-3} + \beta_{l-3} \\ & & & \frac{7}{3}\beta l - 2 + \frac{4}{3}\alpha_{l-2} & -\frac{7}{3}\beta_{l-2} - \frac{1}{3}\alpha_{l-2} \end{bmatrix},$$

$$\mathbf{F}_2 = \Big[ f_{\mathrm{EC},1}(:),\ \ldots, f_{\mathrm{EC},n_{\mathrm{EC}}}(:),\ f_{\mathrm{NBI},1}(:),\ \ldots,\ f_{\mathrm{NBI},n_{\mathrm{NBI}}}(:) \Big],$$

$$\mathbf{F}_3 = \mathrm{diag}\Big[ f_{\mathrm{BS}}(\hat{\rho}_1),\ f_{\mathrm{BS}}(\hat{\rho}_2),\ \ldots,\ f_{\mathrm{BS}}(\hat{\rho}_{l-2}) \Big],$$

$$\mathbf{F}_4 = \Big[ 0,\ 0,\ \ldots,\ 0,\ \frac{1}{3}(2\Delta\hat{\rho})(\alpha_{l-2} + \beta_{l-2}) k_{I_{\mathrm{p}}} \Big]^T.$$

In the matrix $\mathbf{F}_2$, the notation $f_{\mathrm{EC},1}(:)$ has been introduced to denote the column vector $[f_{\mathrm{EC},1}(\hat{\rho}_1), f_{\mathrm{EC},1}(\hat{\rho}_2), \ldots, f_{\mathrm{EC},1}(\hat{\rho}_{l-2})]^T$, and similarly for $f_{\mathrm{EC},2}(:)$, etc.

### A.1.2 Finite Differences Discretization for the $\theta$ model

Similarly the dynamics describing the $\theta$ ($= \partial\hat{\psi}/\partial\hat{\rho}$) profile evolution can be reduced to a finite dimensional model. To begin, the infinite dimensional PDE describing the $\theta$ evolution can be written as

$$\begin{aligned} \frac{\partial\theta}{\partial t}(\hat{\rho}, t) = &\left( h_{11}(\hat{\rho}) \frac{\partial^2\theta}{\partial\hat{\rho}^2} + h_{12}(\hat{\rho}) \frac{\partial\theta}{\partial\hat{\rho}} + h_{13}(\hat{\rho})\theta \right) u_\eta(t) + \sum_{i=1}^{n_{\mathrm{EC}}} h_{\mathrm{EC},i}(\hat{\rho}) u_{\mathrm{EC},i}(t) \\ &+ \sum_{i=1}^{n_{\mathrm{NBI}}} h_{\mathrm{NBI},i}(\hat{\rho}) u_{\mathrm{NBI},i}(t) + \left( \frac{1}{\theta} \frac{dh_{\mathrm{BS}}(\hat{\rho})}{d\hat{\rho}} - \frac{h_{\mathrm{BS}}(\hat{\rho})}{\theta^2} \frac{\partial\theta}{\partial\hat{\rho}} \right) u_{\mathrm{BS}}(t), \end{aligned} \tag{A.13}$$

where the boundary conditions are given by

$$\theta(0, t) = 0, \qquad \theta(1, t) = -k_{I_{\mathrm{p}}} I_{\mathrm{p}}(t), \tag{A.14}$$

where the parameters $h_{(\cdot)}$ are functions of $\hat{\rho}$, and the parameters $u_{(\cdot)}$ are given by (A.3).

Following the same procedure as in Section A.1, we obtain the finite dimensional

model describing the $\theta$ evolution,

$$\begin{aligned}\dot{\boldsymbol{\theta}} &= \boldsymbol{g}(\boldsymbol{\theta}, \mathbf{u}) = \\ &\mathbf{G}_1\boldsymbol{\theta}u_\eta + \mathbf{G}_2\begin{bmatrix} u_{\mathrm{EC},1} \\ \vdots \\ u_{\mathrm{EC},n_{\mathrm{EC}}} \\ u_{\mathrm{NBI},1} \\ \vdots \\ u_{\mathrm{NBI},n_{\mathrm{NBI}}} \end{bmatrix} + \mathbf{G}_3\begin{bmatrix} 1/\theta_1 \\ 1/\theta_2 \\ \vdots \\ 1/\theta_m \\ \vdots \\ 1/\theta_{N-1} \end{bmatrix} u_{\mathrm{BS}} + \mathbf{G}_4\begin{bmatrix} (\theta_2-\theta_0)/\theta_1^2 \\ (\theta_3-\theta_1)/\theta_2^2 \\ \vdots \\ (\theta_{m+1}-\theta_{m-1})/\theta_m^2 \\ \vdots \\ (-\theta_{N-2})/\theta_{N-1}^2 \end{bmatrix} u_{\mathrm{BS}} \\ &\quad + \mathbf{G}_5 u_\eta I_p + \mathbf{G}_6\frac{1}{\theta_{N-1}^2}u_{\mathrm{BS}}I_p,\end{aligned} \tag{A.15}$$

where $\boldsymbol{\theta} = [\theta_1, \theta_2, ..., \theta_{l-2}]^T$, and the matrices $\mathbf{G}_i$ are given by

$$\mathbf{G}_1 = \begin{bmatrix} \gamma_1 & \beta_1 & & & & & & & \\ & \alpha_2 & \gamma_2 & \beta_2 & & & & & \\ & & & \ddots & & & & & \\ & & & & \alpha_m & \gamma_m & \beta_m & & \\ & & & & & & \ddots & & \\ & & & & & & & \alpha_{N-1} & \beta_{N-1} \end{bmatrix},$$

$$\mathbf{G}_2 = \Big[h_{\mathrm{EC},1}(:),\ \ldots,\ h_{\mathrm{EC},n_{\mathrm{EC}}}(:),\ h_{\mathrm{NBI},1}(:),\ \ldots,\ h_{\mathrm{NBI},n_{\mathrm{NBI}}}(:)\Big],$$

$$\mathbf{G}_3 = \mathrm{diag}\Big[h'_{\mathrm{BS}}(\hat{\rho}_1), h'_{\mathrm{BS}}(\hat{\rho}_2), \ldots, h'_{\mathrm{BS}}(\hat{\rho}_{l-2})\Big],$$

$$\mathbf{G}_4 = \mathrm{diag}\Big[-h_{\mathrm{BS}}(1)/2\Delta\hat{\rho}, -h_{\mathrm{BS}}(2)/2\Delta\hat{\rho}, \ldots, -h_{\mathrm{BS}}(l-2)/2\Delta\hat{\rho}\Big],$$

$$\mathbf{G}_5 = \Big[0,\ 0,\ \ldots,\ 0,\ -k_{I_{\mathrm{p}}}\beta_{N-1}\Big]^T,$$

$$\mathbf{G}_6 = \Big[0,\ 0,\ \ldots,\ 0,\ \frac{k_{I_{\mathrm{p}}}h_{\mathrm{BS}}(N-1)}{2\Delta\hat{\rho}}\Big]^T.$$

where the terms $\alpha_m$, $\beta_m$, $\gamma_m$ given by

$$\begin{aligned}\alpha_m &= \left(\frac{h_{11}(m)}{(\Delta\hat{\rho})^2} - \frac{h_{12}(m)}{2\Delta\hat{\rho}}\right), \quad \beta_m = \left(\frac{h_{11}(m)}{(\Delta\hat{\rho})^2} + \frac{h_{12}(m)}{2\Delta\hat{\rho}}\right), \\ \gamma_m &= \left(h_{13}(m) - \frac{2h_{11}(m)}{(\Delta\hat{\rho})^2}\right),\end{aligned} \tag{A.16}$$

have been introduced for notation convenience.

### A.1.3 Model Jacobians

After discretizing the systems (A.1) and (A.13) in space and reconstructing into the forms (A.12) and (A.15), respectively, it becomes straight forward to calculate the model Jacobians, which are required to construct linear approximations to the system dynamics and to compute function gradients for optimal feedforward control design of Chapter 4 (Section 4.3). For example, the model Jacobians $\frac{\partial \boldsymbol{f}(\boldsymbol{\psi},\mathbf{u})}{\partial \boldsymbol{\psi}}$ and $\frac{\partial \boldsymbol{f}(\boldsymbol{\psi},\mathbf{u})}{\partial \mathbf{u}}$ required to compute the state sensitivity equation (4.22) can be obtained by taking first derivative of (A.12),

$$
\begin{aligned}
\frac{\partial \boldsymbol{f}(\boldsymbol{\psi},\mathbf{u})}{\partial \boldsymbol{\psi}} &= \mathbf{F}_1 u_\eta \\
&+ \begin{bmatrix}
\frac{1}{\frac{4}{3}(\psi_2-\psi_1)^2} & \frac{-1}{\frac{4}{3}(\psi_2-\psi_1)^2} & & & \\
& \ddots & & & \\
& & \frac{1}{\frac{4}{3}(\psi_{l-2}-\psi_{l-3})^2} & \frac{-1}{\frac{4}{3}(\psi_{l-2}-\psi_{l-3})^2} & \\
& & & \frac{4/3}{\left(\frac{4}{3}(\psi_{N-1}-\psi_{N-2}) - (2\Delta\hat{\rho})3k_{I_p}I_p\right)^2} & \frac{-4/3}{\left(\frac{4}{3}(\psi_{N-1}-\psi_{N-2}) - (2\Delta\hat{\rho})3k_{I_p}I_p\right)^2}
\end{bmatrix} u_{\mathrm{BS}}, \\
\frac{\partial \boldsymbol{f}(\boldsymbol{\psi},\mathbf{u})}{\partial \mathbf{u}} &= \mathbf{F}_1 \boldsymbol{\psi} \frac{du_\eta}{d\mathbf{u}} + \mathbf{F}_2 \begin{bmatrix} \frac{du_{\mathrm{EC},1}}{d\mathbf{u}} \\ \vdots \\ \frac{du_{\mathrm{EC},n_{\mathrm{EC}}}}{d\mathbf{u}} \\ \frac{du_{\mathrm{NBI},1}}{d\mathbf{u}} \\ \vdots \\ \frac{du_{\mathrm{NBI},n_{\mathrm{NBI}}}}{d\mathbf{u}} \end{bmatrix} + \mathbf{F}_3 \begin{bmatrix} 1/(\frac{4}{3}\psi_2 - \frac{4}{3}\psi_1) \\ 1/(\psi_3 - \psi_1) \\ \vdots \\ 1/(\psi_{l-2} - \psi_{l-3}) \\ 1/\left(\frac{4}{3}(\psi_{N-1} - \psi_{N-2}) - \frac{(2\Delta\hat{\rho})}{3}k_{I_p}I_p\right) \end{bmatrix} \frac{du_{\mathrm{BS}}}{d\mathbf{u}} \\
&+ f_{\mathrm{BS}}(\hat{\rho}_{l-2}) \frac{\frac{(2\Delta\hat{\rho})}{3}k_{I_p}}{\left(\frac{4}{3}(\psi_{N-1} - \psi_{N-2}) - \frac{(2\Delta\hat{\rho})}{3}k_{I_p}I_p\right)^2} u_{\mathrm{BS}} \frac{dI_p}{d\mathbf{u}} + \mathbf{F}_4 I_{\mathrm{p}} \frac{du_\eta}{d\mathbf{u}} + \mathbf{F}_4 u_\eta \frac{dI_p}{d\mathbf{u}}.
\end{aligned}
\tag{A.17}
$$

## A.2 Finite Element Discretization of the Momentum Diffusion Equation

Substituting the approximations (7.5) and (7.6) into the evolution for $\Omega_\phi$ (7.1), we have

$$\begin{aligned}\sum_{k=1}^{l_\omega} \frac{d\omega_k}{dt}\phi_k = &-\sum_{k=1}^{l_\omega} \omega_k \phi_k u_{\bar{n}_\mathrm{i}} + \sum_{k=1}^{l_\omega}\sum_{\alpha=1}^{l_\chi} \omega_k \gamma_\alpha \frac{f_1}{\hat{\rho}}\frac{\partial}{\partial\hat{\rho}}\left[\hat{\rho} f_2 \varphi_\alpha \frac{\partial \phi_k}{\partial \hat{\rho}}\right] \\ &+ \sum_{\xi=1}^{n_\mathrm{NBI}} f_{\mathrm{NBI},\xi} u_{\mathrm{NBI},\xi} + \left(\sum_{k=1}^{l_\omega}\omega_k\phi_k - \Omega_\phi^\star\right) f_\mathrm{NRMF} u_\mathrm{NRMF},\end{aligned} \tag{A.18}$$

where the dependencies on $\hat{\rho}$ and $t$ have been dropped for notational convenience. Next, we construct the *weak form* by multiplying both sides by $\hat{\rho}$, projecting onto the basis functions $\phi_j$, $j = 1, \ldots, l_\omega$ and integrating over the domain $(0 \le \hat{\rho} \le 1)$, to obtain

$$\begin{aligned}&\sum_{k=1}^{l_\omega} \frac{d\omega_k}{dt}\int_0^1 \hat{\rho}\phi_j\phi_k d\hat{\rho} = -\sum_{k=1}^{l_\omega}\omega_k \int_0^1 \hat{\rho}\phi_j\phi_k d\hat{\rho} u_{\bar{n}_\mathrm{i}} \\ &+ \sum_{k=1}^{l_\omega}\sum_{\alpha=1}^{l_\chi}\omega_k\gamma_\alpha\int_0^1 f_1\phi_j\frac{\partial}{\partial\hat{\rho}}\left[\hat{\rho} f_2\varphi_\alpha\frac{\partial\phi_k}{\partial\hat{\rho}}\right]d\hat{\rho} + \sum_{\xi=1}^{n_\mathrm{NBI}}\left(\int_0^1 \hat{\rho}\phi_j f_{\mathrm{NBI},\xi} d\hat{\rho}\right) u_{\mathrm{NBI},\xi} \\ &+ \sum_{k=1}^{l_\omega}\omega_k\left(\int_0^1 \hat{\rho}\phi_j\phi_k f_\mathrm{NRMF} d\hat{\rho}\right) u_\mathrm{NRMF} - \left(\int_0^1 \hat{\rho}\phi_j\Omega_\phi^\star f_\mathrm{NRMF} d\hat{\rho}\right) u_\mathrm{NRMF},\end{aligned} \tag{A.19}$$

then integrating by parts the second part of (A.19), and taking into account the boundary conditions, we can obtain

$$\sum_{k=1}^{l_\omega} \frac{\mathrm{d}\omega_k}{\mathrm{d}t} \underbrace{\int_0^1 \hat{\rho}\phi_j\phi_k d\hat{\rho}}_{(\mathbf{M})_{jk}} = -\sum_{k=1}^{l_\omega} \omega_k \underbrace{\int_0^1 \hat{\rho}\phi_j\phi_k d\hat{\rho}}_{(\mathbf{M})_{jk}} u_{\bar{n}_\mathrm{i}} + \sum_{\xi=1}^{n_\mathrm{NBI}} \underbrace{\left[\int_0^1 \hat{\rho}\phi_j f_{\mathrm{NB},\xi} d\hat{\rho}\right]}_{(\mathbf{B}_{\mathrm{NB},\xi})_j} u_{\mathrm{NB},\xi}$$
$$- \sum_{k=1}^{l_\omega} \omega_k \underbrace{\sum_{\alpha=1}^{l_\chi} \gamma_\alpha \left[\int_0^1 \left(\phi_j' f_1 + \phi_j f_1'\right)\left(\hat{\rho} f_2 \varphi_\alpha \phi_k' - \hat{\rho} f_3 \varphi_\alpha \phi_k\right) d\hat{\rho}\right]}_{(\mathbf{S})_{jk}}$$
$$+ \sum_{k=1}^{l_\omega} \omega_k \underbrace{\left[\int_0^1 \hat{\rho}\phi_j\phi_k f_\mathrm{NR} d\hat{\rho}\right]}_{(\mathbf{B}_\mathrm{NR})_{jk}} u_\mathrm{NRMF} + \underbrace{\int_0^1 \hat{\rho}\phi_j \Omega_\phi^\star f_\mathrm{NR} d\hat{\rho}}_{(\mathbf{B}_\mathrm{NR}^\star)_j} u_\mathrm{NR}, \tag{A.20}$$

where $(\cdot)'$ denotes derivatives with respect to $\hat{\rho}$, i.e., $\frac{\partial}{\partial\hat{\rho}}$. Introducing the notation $\langle\langle g_1, \ldots, g_N\rangle\rangle \triangleq \int_0^1 g_1(\hat{\rho})\ldots g_N(\hat{\rho})\hat{\rho}d\hat{\rho}$, the matrices introduced in (A.20) can be written as

$$(\mathbf{M})_{jk} = \langle\langle \phi_j, \phi_k\rangle\rangle, \tag{A.21}$$
$$(\mathbf{B}_{\mathrm{NB},\xi})_j = \langle\langle \phi_j, f_{\mathrm{NBI},\xi}\rangle\rangle, \tag{A.22}$$
$$(\mathbf{S})_{jk} = \sum_{\alpha=1}^{l_\chi} \gamma_\alpha \left(\langle\langle f_1\phi_j', \phi_k', f_2\varphi_\alpha\rangle\rangle + \langle\langle f_1'\phi_j, \phi_k', f_2\varphi_\alpha\rangle\rangle\right), \tag{A.23}$$
$$(\mathbf{B}_\mathrm{NR})_{jk} = \langle\langle \phi_j, \phi_k, f_\mathrm{NRMF}\rangle\rangle, \quad (\mathbf{B}_\mathrm{NR}^\star)_j = \langle\langle \phi_j, \Omega_\phi^\star, f_\mathrm{NRMF}\rangle\rangle. \tag{A.24}$$

With the above matrices the system (A.20) can be written in the matrix-vector form

$$\begin{aligned}\mathbf{M}\frac{d\boldsymbol{\omega}}{dt} &= -\mathbf{M}\boldsymbol{\omega}u_{\bar{n}_\mathrm{i}} - \mathbf{S}\boldsymbol{\omega} \\ &\quad + \sum_{\xi=1}^{n_\mathrm{NBI}} \mathbf{B}_{\mathrm{NB},\xi}u_{\mathrm{NBI},\xi} + \mathbf{B}_\mathrm{NR}\boldsymbol{\omega}u_\mathrm{NRMF} - \mathbf{B}_\mathrm{NR}^\star u_\mathrm{NRMF},\end{aligned} \tag{A.25}$$

where $\boldsymbol{\omega} = [\omega_1, \omega_2, \ldots, \omega_{l_\omega}]^T$. From (A.25), we can see that the rotation dynamics are approximately linear, with bilinear terms associated with the density and NRMF controls.

### A.2.1 Incorporating Uncertainty

The uncertainty associated with the diffusivity parameter $\chi_\phi$ can be embedded into the system (A.25) by writing the multiplier $\gamma_\alpha$ of the approximation $\chi_\phi(\hat{\rho},t) \approx \sum_{\alpha=1}^{l_\chi} \gamma_\alpha \varphi_\alpha(\hat{\rho})$, as an uncertainty value. Let each $\gamma_\alpha$ take the form $\gamma_\alpha = \gamma_\alpha^0 + \gamma_\alpha^1 \delta_\alpha$, where $\gamma_\alpha^0$ is associated with the nominal $\chi_\phi$ profile (see Figure 7.2(b)) and $\gamma_\alpha^1 \delta_\alpha$ ($|\delta_\alpha| \leq 1$) quantifies the uncertainty in the value $\gamma_\alpha$. To make the uncertainty in the state-space system explicit, the matrix $\mathbf{S}$ (A.25) can be decomposed as

$$\mathbf{S}(\boldsymbol{\delta}) = \hat{\mathbf{S}}^0 + \sum_{\alpha=1}^{l_\chi} \delta_\alpha \hat{\mathbf{S}}^\alpha, \tag{A.26}$$

where

$$\begin{aligned}
\hat{\mathbf{S}}^0_{jk} &= \sum_{\alpha=1}^{l_\chi} \gamma_\alpha^0 \left( \langle\langle f_1 \phi_j', \phi_k', f_2 \varphi_\alpha \rangle\rangle + \langle\langle f_1' \phi_j, \phi_k', f_2 \varphi_\alpha \rangle\rangle \right), \\
\hat{\mathbf{S}}^\alpha_{jk} &= \gamma_\alpha^1 \left( \langle\langle f_1 \phi_j', \phi_k', f_2 \varphi_\alpha \rangle\rangle + \langle\langle f_1' \phi_j, \phi_k', f_2 \varphi_\alpha \rangle\rangle \right).
\end{aligned}$$

## A.3 Proper Orthogonal Decomposition (POD)

Let the matrix $\mathcal{A}$ comprise a data ensemble of the parameter $\chi_\phi$ discretized onto the grid $(\hat{\rho}_m, t_n)$, i.e. $\mathcal{A}_{mn} = \chi_\phi(\hat{\rho}_m, t_n)$, for integers $m$ and $n$, $1 \leq m \leq M$ and $1 \leq n \leq N$. The set $V = \text{span}\{\mathcal{A}_n \mid n = 1, 2, \ldots, N\} \subset \mathbb{R}^M$ refers to a data ensemble consisting of snapshots of $\chi_\phi$ obtained at $N$ different instants of time from the experiment. The goal of the POD method is to find an orthonormal basis $\{\phi_k \mid k = 1, \ldots, l_\omega\}$ such that for some predefined $1 \leq l_\omega \leq d$, where $d = \dim V \leq M$, the reconstruction error for the snapshots is minimized, i.e.

$$\min_{\{\phi_k \mid k=1,\ldots,l_\omega\}} \sum_{n=1}^{N} \left\| \mathcal{A}_n - \sum_{k=1}^{l_\omega} \langle \mathcal{A}_n, \phi_k \rangle \phi_k \right\|_2^2, \tag{A.27}$$

subject to

$$\langle \phi_j, \phi_k \rangle = \delta_{jk}, \quad 1 \leq j \leq l_\omega, \quad 1 \leq k \leq l_\omega \tag{A.28}$$

where $\|x\|_2 = \sqrt{x^T x}$ and $\langle \cdot, \cdot \rangle$ denotes the inner product

$$\langle f, g \rangle = \int_0^1 f g \hat{\rho} d\hat{\rho}. \tag{A.29}$$

Let $\lambda_1 > \ldots > \lambda_l > \ldots > \lambda_d > 0$ denote the eigenvalues of the correlation matrix $\mathcal{K}$, defined as $\mathcal{K}_{ij} = \langle A_j, A_i \rangle$, for $i, j = 1, \ldots, N$, and $\Lambda_1, \ldots, \Lambda_{l_\omega}, \ldots, \Lambda_d$ the associated eigenvectors, where $d = \text{rank}(\mathcal{K})$. Then, the POD basis functions take the form [87]

$$(\phi_k)_i = \frac{1}{\sqrt{\lambda_k}} \sum_{n=1}^{N} (\Lambda_k)_n \mathcal{A}_{in}, \ (k = 1, \ldots, d), \tag{A.30}$$

where $(\cdot)_i$ is the $i$-th component of the vector or simply

$$\phi_k = \frac{1}{\sqrt{\lambda_k}} \mathcal{A} \Lambda_k. \tag{A.31}$$

## A.4 Converting $\partial V/\partial\hat{\rho}$ to $\hat{H}$

The spatial derivative of volume can be expressed in terms of $\hat{H}$ in the following manner. First, express $\partial V/\partial\rho$ as a function of toroidal magnetic field strength,

$$\frac{\partial V}{\partial \rho} = \frac{\partial V}{\partial \Phi} \frac{\partial \Phi}{\partial \rho} = 2\pi B_{\phi,0} \rho \left( \frac{2\pi R}{B_\phi} \right), \tag{A.32}$$

rewriting in terms of $\hat{\rho}$

$$\frac{\partial V}{\partial \hat{\rho}} = \frac{\partial V}{\partial \rho} \frac{\rho}{\hat{\rho}} = 2\pi B_{\phi,0} \hat{\rho} \rho_b^2 \left( \frac{2\pi R}{B_\phi} \right) \tag{A.33}$$

The plasma geometric factors $\hat{F}$, $\hat{G}$, $\hat{H}$ are given by

$$\hat{F}(\hat{\rho}) = \frac{R_0 B_{\phi,0}}{R B_\phi} \qquad \hat{G}(\hat{\rho}) = \left\langle \frac{R_0^2}{R^2} |\nabla \rho|^2 \right\rangle \qquad \hat{H}(\hat{\rho}) = \frac{\hat{F}}{\langle R_0^2/R^2 \rangle} \tag{A.34}$$

rewriting $\hat{H}$ as a function of toroidal magnetic field strength

$$\hat{H} = \frac{R_0 B_{\phi,0}}{R B_\phi \langle R_0^2/R^2 \rangle} = \frac{B_{\phi,0}}{R_0} \frac{1}{\langle B_\phi / R \rangle} \tag{A.35}$$

since $RB_\phi$ is constant on a flux surface $RB_\phi = \langle RB_\phi \rangle$, thus

$$\frac{\partial V}{\partial \hat{\rho}} = 4\pi^2 \rho_b^2 \hat{\rho} R_0 \hat{H}(\hat{\rho}). \tag{A.36}$$

## A.5 Model Identification by Prediction Error Method (PEM)

After this discretization has been made, we seek a least squares fit of the discrete system to the experimental data to obtain the lumped parameter version of the state space model ignoring error signals reads:

$$\mathcal{M}: \ \dot{X}(t) = AX(t) + Bu(t),\, Y(t) = CX(t). \tag{A.37}$$

where $u(t)$ are the inputs, i.e., neutral beam injection power, total gyrotron power, and plasma current, $X(t)$ are the model states in discretized form and $Y(t)$ are the model outputs. Equation (A.37) represents the candidate model to be identified $\mathcal{M}$.

### A.5.1 Identification by Prediction Error Method

Once the candidate model has been selected it can be parameterized by some parameter vector $\theta$. Then the search for the best model within the constrictions of the candidate model (A.37) becomes a problem of determining or estimating $\theta$. We use the prediction error method [41]. Given a certain model structure $\mathcal{M}$, the objective is to find a parameter vector $\theta$ and particular model $\mathcal{M}(\theta)$ that minimizes the prediction error $\epsilon$, given by

$$\epsilon(t, \theta) = y(t) - \hat{y}(t|\theta), \tag{A.38}$$

where $y(t)$ is the measured output and $\hat{y}(t|\theta)$ is the model predicted output. The set of possible models is thus defined, for parameter vector $\theta \in D_{\mathcal{M}} \subset \mathbb{R}^d$, as

$$\mathcal{M}^* = \{\mathcal{M}(\theta) \mid \theta \ \in \ D_{\mathcal{M}}\}. \tag{A.39}$$

Considering the collected batch of data,

$$Z^N = [y(1), u(1), y(2), u(2), ..., y(N), u(N)], \tag{A.40}$$

the problem is to select a proper value $\hat{\theta}_N$ and hence a proper member $\mathcal{M}$ in the set $\mathcal{M}^*$, i.e. find the mapping

$$Z^N \ \rightarrow \ \hat{\theta}_N \ \in \ D_{\mathcal{M}}. \tag{A.41}$$

Such a mapping is called a parameter estimation method. The best model is the one that minimizes $\epsilon$. Thus we require a scalar-valued norm or criterion function that measures the size of $\epsilon$. For the case of a least squares criterion function ($\frac{1}{2}\epsilon^2$) the norm is expressed as

$$V_N(\theta, Z^N) = \frac{1}{N}\sum_{t=1}^{N}\frac{1}{2}\epsilon(t,\theta)^2, \tag{A.42}$$

which can be extended to a multi-output system with $p$ outputs by rewriting the criterion function as $\frac{1}{2}\epsilon^T\Lambda^{-1}\epsilon$ for some symmetric, positive semidefinite $p\times p$ weighting matrix $\Lambda$ that gives relative importance of the components of $\epsilon$. In this case the scalar valued norm would be

$$V_N(\theta, Z^N) = \mathrm{tr}\left(\frac{1}{N}\sum_{t=1}^{N}\frac{1}{2}\epsilon(t,\theta)^T\Lambda^{-1}\epsilon(t,\theta)\right). \tag{A.43}$$

# Appendix B

# Model Predictive Control: Definitions and Derivations

## B.1 MPC Prediction Matrices

Let $\mathbf{X} = [\mathbf{x}_0, \mathbf{x}_1, \ldots, \mathbf{x}_N]$ and $\mathbf{U} = [\mathbf{u}_0, \mathbf{u}_1, \ldots, \mathbf{u}_{N-1}]$ be, respectively, a state sequence and an input sequence. Consider Finite Horizon Optimal Control Problem (FHOCP) with quadratic cost,

$$\begin{aligned} \underset{\mathbf{X},\,\mathbf{U}}{\text{minimize}} \quad & J = \mathbf{x}_N^T \mathbf{P} \mathbf{x}_N + \sum_{n=1}^{N-1} \mathbf{x}_n^T \mathbf{Q} \mathbf{x}_n + \sum_{n=0}^{N-1} \mathbf{u}_n^T \mathbf{R} \mathbf{u}_n, \\ \text{subject to} \quad & \mathbf{x}_0 = \mathbf{x}(0), \\ & \mathbf{x}_{n+1} = \mathbf{A}\mathbf{x}_n + \mathbf{B}\mathbf{u}_n \quad \text{for} \quad n = 1, 2 \ldots N \end{aligned} \tag{B.1}$$

In order to convert the FHOCP into a standard Quadratic Program of the form

$$\begin{aligned} \underset{\mathbf{z}}{\text{minimize}} \quad & J = \mathbf{z}^T \mathbf{H} \mathbf{z} + \mathbf{f}^T \mathbf{z} \\ \text{subject to} \quad & \mathbf{A}_{\text{eq}} \mathbf{z} = \mathbf{B}_{\text{eq}} \end{aligned}$$

we need to construct prediction matrices, that is write the future states as a function of the initial condition and control sequence. The choice of decision variables $\mathbf{z}$ falls into one of two classes "shooting" and "direct transcription". In the shooting

method formulation, the decision variables consist only of the controls, and the dynamic constraints are removed from the problem by solving for the future states in terms of the controls and initial condition. In the direct transcription method formulation, the problem is over parameterized by including in the set of decision variables both the system states and controls and the system dynamics are enforced by constraints. Each of the formulations had computational advantages depending on the particular structure and size of the optimization problem (B.1). For example, the direct transcription formulation can be beneficial because it allows for a diagonal hessian matrix. The following two sections briefly introduce each approach, and then more complete descriptions follow.

### B.1.1 FHOCP via Shooting Approach

Assuming linear dynamics, $\mathbf{x}_{k+1} = \mathbf{A}\mathbf{x}_k + \mathbf{B}\mathbf{u}_k$, future states can be predicted in terms of the initial state $\mathbf{x}_0$ and the control sequence according to

$$\begin{aligned}
\mathbf{x}_0 &= \mathbf{x}(0), \\
\mathbf{x}_1 &= \mathbf{A}\mathbf{x}_0 + \mathbf{B}\mathbf{u}_0, \\
\mathbf{x}_2 &= \mathbf{A}^2\mathbf{x}_0 + \mathbf{A}\mathbf{B}\mathbf{u}_0 + \mathbf{B}\mathbf{u}_1, \\
\mathbf{x}_3 &= \mathbf{A}^3\mathbf{x}_0 + \mathbf{A}^2\mathbf{B}\mathbf{u}_0 + \mathbf{A}\mathbf{B}\mathbf{u}_1 + \mathbf{B}\mathbf{u}_2, \\
&\vdots \\
\mathbf{x}_N &= \mathbf{A}^N\mathbf{x}_0 + \mathbf{A}^{N-1}\mathbf{B}\mathbf{u}_0 + \mathbf{A}^{N-2}\mathbf{B}\mathbf{u}_1 + \cdots + \mathbf{B}\mathbf{u}_{N-1},
\end{aligned}$$

which can be rewritten as

$$\underbrace{\begin{bmatrix} \mathbf{x}_1 \\ \mathbf{x}_2 \\ \vdots \\ \mathbf{x}_N \end{bmatrix}}_{\mathbf{X}} = \underbrace{\begin{bmatrix} \mathbf{A} \\ \mathbf{A}^2 \\ \vdots \\ \mathbf{A}^N \end{bmatrix}}_{\mathbf{\Phi}} \mathbf{x}_0 + \underbrace{\begin{bmatrix} \mathbf{B} & & & \\ \mathbf{A}\mathbf{B} & \mathbf{B} & & \\ \vdots & & \ddots & \\ \mathbf{A}^{N-1}\mathbf{B} & \mathbf{A}^{N-2}\mathbf{B} & \dots & \mathbf{B} \end{bmatrix}}_{\mathbf{\Gamma}} \underbrace{\begin{bmatrix} \mathbf{u}_0 \\ \mathbf{u}_1 \\ \vdots \\ \mathbf{u}_N \end{bmatrix}}_{\mathbf{U}},$$

or equivalently

$$\mathbf{X} = \mathbf{\Phi}\mathbf{x}_0 + \mathbf{\Gamma}\mathbf{U}. \tag{B.2}$$

In this case $\mathbf{\Phi}$ and $\mathbf{\Gamma}$ represent the prediction matrices, which can be used to express all future states in terms of the control sequence $\mathbf{U}$ and initial state $\mathbf{x}_0$. We take as the optimization variables $\mathbf{z} = \mathbf{U}$, in which case the cost function of (B.1), can be written as

$$J = (\mathbf{\Phi}\mathbf{x}_0 + \mathbf{\Gamma}\mathbf{U})^T \bar{\mathbf{Q}} (\mathbf{\Phi}\mathbf{x}_0 + \mathbf{\Gamma}\mathbf{U}) + \mathbf{U}^T \bar{\mathbf{R}} \mathbf{U}$$

where $\bar{\mathbf{Q}} = \text{diag}(\mathbf{Q}, \mathbf{Q}, \ldots, \mathbf{Q}, \mathbf{P})$ and $\bar{\mathbf{R}} = \text{diag}(\mathbf{R}, \mathbf{R}, \ldots, \mathbf{R})$. In this way the dynamics constraints are implicitly satisfied by the prediction equation (B.2), and the constrained optimization problem (B.1) has been reduced to an unconstrained problem.

### B.1.2 FHOCP via Direct Transcription Approach

In the direct transcription approach we include all the future states and controls as optimization variables, i.e.

$$\mathbf{z} = [\mathbf{u}_0, \mathbf{u}_1, \ldots, \mathbf{u}_{N-1}, \mathbf{x}_1, \mathbf{x}_2, \ldots, \mathbf{x}_N],$$

in which case the cost function can be written as

$$J = \mathbf{z}^T \begin{bmatrix} \bar{\mathbf{R}} & \\ & \bar{\mathbf{Q}} \end{bmatrix} \mathbf{z},$$

and the dynamics constraints, $\mathbf{x}_{k+1} = \mathbf{A}\mathbf{x}_k + \mathbf{B}\mathbf{u}_k$ for $k = 0, 1, \ldots, N$, can be listed as

$$\begin{aligned}
\mathbf{x}_0 &= \mathbf{x}(0), \\
\mathbf{x}_1 - \mathbf{B}\mathbf{u}_0 &= \mathbf{A}\mathbf{x}_0, \\
\mathbf{x}_2 - \mathbf{A}\mathbf{x}_1 - \mathbf{B}\mathbf{u}_1 &= 0, \\
\mathbf{x}_3 - \mathbf{A}\mathbf{x}_2 - \mathbf{B}\mathbf{u}_2 &= 0, \\
&\vdots \\
\mathbf{x}_N - \mathbf{A}\mathbf{x}_{N-1} - \mathbf{B}\mathbf{u}_{N-1} &= 0.
\end{aligned}$$

In matrix form the dynamics constraints can be written as

$$\underbrace{\begin{bmatrix} -\mathbf{B} & & & \mathbf{I} & & \\ & -\mathbf{B} & & -\mathbf{A} & \mathbf{I} & \\ & & -\mathbf{B} & & -\mathbf{A} & \mathbf{I} \end{bmatrix}}_{\mathbf{\Theta}} \underbrace{\begin{bmatrix} \mathbf{u}_0 \\ \mathbf{u}_1 \\ \vdots \\ \mathbf{x}_N \end{bmatrix}}_{\mathbf{z}} = \underbrace{\begin{bmatrix} \mathbf{A} \\ 0 \\ 0 \end{bmatrix}}_{\mathbf{\Phi}} \mathbf{x}(0)$$

or equivalently

$$\mathbf{\Theta z} = \mathbf{\Phi x}_0. \tag{B.3}$$

In this case $\mathbf{\Theta}$ and $\mathbf{\Phi}$ represent the prediction matrices, and the optimization problem (B.1) can be written as

$$\begin{aligned} \underset{\mathbf{z}}{\text{minimize}} \quad & J = \mathbf{z}^T \begin{bmatrix} \bar{\mathbf{R}} & \\ & \bar{\mathbf{Q}} \end{bmatrix} \mathbf{z} \\ \text{subject to} \quad & \mathbf{\Theta z} = \mathbf{\Phi x}_0 \end{aligned} \tag{B.4}$$

This formulation has the convenient feature that additional constraints on the controls or states can be directly applied to the optimization variables. It can sometimes be more efficient to use the direct transcription formulation depending on the particular form of the optimal control problem, i.e. the size of the state, control and length of prediction horizon.

## B.2 Blocking (Incidence Points)

In some cases it can be desirable to extend the horizon time while limiting the number of the control and state variables. For example, suppose that the horizon has to be increased in order to satisfy desired closed-loop performance requirements. If the horizon time is increased, the size of the optimization problem and therefore the computation time will necessarily increase as well. To reduce computation time while maintaining the horizon length, one approach might be to update the control variable on every other time step. Additionally, it can be desirable to impose state

**Figure B.1:** Model predictive control with blocking.

constraints and matching between output and reference only at a reduced set of time points. This can be accomplished by introducing incident points, i.e. a set of future times where output and reference matching is desired. For example in Figure B.1, the control variable is updated every time step for the first two updates and then every other time step thereafter. The state incidence points occur at the first, second, and third future time steps and at the prediction horizon ($8^{\text{th}}$ time step). Let the update times for the control and incidence points be defined, respectively, by $I_u$ and $I_p$. In this case, the FHOCP (B.1) becomes

$$\begin{aligned} \underset{\substack{\{\mathbf{x}_n\}_{n\in I_p} \\ \{\mathbf{u}_n\}_{n\in I_u}}}{\text{minimize}} \quad & J = \sum_{n\in I_p} \mathbf{x}_n^T \mathbf{Q} \mathbf{x}_n + \sum_{n\in I_u} \Delta\mathbf{u}_n^T \mathbf{R} \Delta\mathbf{u}_n, \\ \text{subject to} \quad & \mathbf{x}_0 = \mathbf{x}(0), \\ & \mathbf{x}_{n+1} = \mathbf{A}\mathbf{x}_n + \mathbf{B}\mathbf{u}_n \quad \text{for} \quad n \in I_p \\ & \mathbf{x}_n \in \mathcal{X}_n \quad \text{for} \quad n \in I_p \\ & \mathbf{u}_n \in \mathcal{U}_n \quad \text{for} \quad n \in I_u \end{aligned} \tag{B.5}$$

where the cost on control has been replaced with deviations in the control term, $\Delta\mathbf{u}_n = \mathbf{u}_n - \mathbf{u}_{n-1}$.

## B.3 Shooting Formulation with Time-Varying Dynamics and Blocking

$$\prod_{t=m}^{n} \mathbf{A}_{k+t} \equiv \begin{cases} \mathbf{A}_{k+n}\mathbf{A}_{k+n-1}\dots\mathbf{A}_{k+m} & \text{if} \quad m \le n \\ \mathbf{I} & \text{if} \quad m > n \end{cases} \tag{B.6}$$

Let $H_u$ be the control horizon, where $H_u \le H_p$ implies $\mathbf{u}_{k+t} = \mathbf{u}_{k+H_u}$ for $t \ge H_u$, i.e. the control variable is only updated over the first $H_u$ time steps. Starting at time $k$, the future state trajectory can be predicted in terms of the time varying dynamics as

$$\underbrace{\begin{bmatrix} \mathbf{x}_{k+1} \\ \mathbf{x}_{k+2} \\ \vdots \\ \mathbf{x}_{k+H_p} \end{bmatrix}}_{\mathbf{x}_k} = \underbrace{\begin{bmatrix} \mathbf{A}_k \\ \mathbf{A}_{k+1}\mathbf{A}_k \\ \vdots \\ \prod_{t=0}^{H_p-1}\mathbf{A}_{k+t} \end{bmatrix}}_{\mathbf{\Phi}_k} \mathbf{x}_k \; + \underbrace{\begin{bmatrix} \mathbf{B}_k & & & \\ \mathbf{A}_{k+1}\mathbf{B}_k & \mathbf{B}_{k+1} & & \\ \vdots & & \ddots & \\ \prod_{t=1}^{H_p-1}\mathbf{A}_{k+t}\mathbf{B}_k & \prod_{t=2}^{H_p-1}\mathbf{A}_{k+t}\mathbf{B}_{k+1} & \dots & \sum_{i=H_u}^{H_p-1}\prod_{t=i+1}^{H_p-1}\mathbf{A}_{k+t}\mathbf{B}_{k+i} \end{bmatrix}}_{\mathbf{\Gamma}_k} \underbrace{\begin{bmatrix} \mathbf{u}_k \\ \mathbf{u}_{k+1} \\ \vdots \\ \mathbf{u}_{k+H_u} \end{bmatrix}}_{\mathbf{U}_k} . \tag{B.7}$$

As an alternative to the control sequence $\mathbf{U}_k$ we can take as the optimization variables

$$\Delta\mathbf{U}_k = [\Delta\mathbf{u}_k, \Delta\mathbf{u}_{k+1}, \dots, \Delta\mathbf{u}_{k+H_u}] ,$$

where $\Delta\mathbf{u}_k = \mathbf{u}(k) - \mathbf{u}(k-1)$. Now the prediction system (B.11) can be written as

$$\underbrace{\begin{bmatrix} \mathbf{x}_{k+1} \\ \mathbf{x}_{k+2} \\ \vdots \\ \mathbf{x}_{k+H_p} \end{bmatrix}}_{\mathbf{x}_k} = \underbrace{\begin{bmatrix} \mathbf{A}_k \\ \mathbf{A}_{k+1}\mathbf{A}_k \\ \vdots \\ \prod_{t=0}^{H_p-1}\mathbf{A}_{k+t} \end{bmatrix}}_{\mathbf{\Phi}_k} \mathbf{x}_k \quad + \underbrace{\begin{bmatrix} \mathbf{B}_k \\ \mathbf{A}_{k+1}\mathbf{B}_k + \mathbf{B}_{k+1} \\ \vdots \\ \sum_{i=0}^{H_p}\prod_{t=i+1}^{H_p}\mathbf{A}_{k+t}\mathbf{B}_{k+i} \end{bmatrix}}_{\mathbf{\Gamma}_k^{-1}} \mathbf{u}_{k-1} \quad + \dots \tag{B.8}$$

We can convert between the prediction systems (B.11) and (B.8) with

$$\Delta \mathbf{U}_k = \mathbf{\Gamma}_\Delta \mathbf{U}_k - \mathbf{\Gamma}_\Delta^{-1} \mathbf{u}_{k-1},$$

where difference matrix operators are given by

$$\mathbf{\Gamma}_\Delta = \begin{bmatrix} \mathbf{I} & & & \\ -\mathbf{I} & \mathbf{I} & & \\ & & \ddots & \\ & & -\mathbf{I} & \mathbf{I} \end{bmatrix}, \quad \mathbf{\Gamma}_\Delta^{-1} = \begin{bmatrix} \mathbf{I} \\ \mathbf{0} \\ \vdots \\ \mathbf{0} \end{bmatrix}. \tag{B.9}$$

The state and control blocking defined by $I_p$ and $I_u$ can be implemented by simply removing the rows of the system (B.8) that correspond to indices not present in $I_p$ and removing the columns that correspond to indices not present in $I_u$. In summation the future states predicted at time $k$ are given by

$$\mathbf{X}_k = \mathbf{\Phi}_k \mathbf{x}_k + \mathbf{\Gamma}_k^{-1} \mathbf{u}_{k-1} + \mathbf{\Gamma}_k \Delta \mathbf{U}_k,$$

and with the use of this expression, the cost function and state constraints of (B.5) can be written in terms of the optimization variables $\mathbf{z} = \mathbf{\Delta} U_k$ and the parameters $\mathbf{x}_k$ (the initial state) and $\mathbf{u}_{k-1}$ (the previously applied control).

## B.4 Converting the Current Control Problem to Standard Form Quadratic Program (QP)

With the linearized model (6.3), the predicted state evolution at time $k$ can be written in terms of the control variables and the current state estimate. Let $\boldsymbol{\iota}_k$ by the state measured at time $k$, i.e. $\boldsymbol{\iota}_k = \boldsymbol{\iota}[k]$, then the future states predicted at time

$k$ can be computed in terms of the control variables in the following fashion

$$\begin{aligned}
\boldsymbol{\iota}_{k+1} &= \mathbf{A}_k\boldsymbol{\iota}_k + \mathbf{B}_k^{\mathrm{c}}\tilde{\mathbf{u}}_k^{\mathrm{c}} + \mathbf{B}_k^{\mathrm{nc}}\tilde{\mathbf{u}}_k^{\mathrm{nc}} + \mathbf{a}_k,\\
\boldsymbol{\iota}_{k+2} &= \mathbf{A}_{k+1}\left(\mathbf{A}_k\boldsymbol{\iota}_k + \mathbf{B}_k^{\mathrm{c}}\tilde{\mathbf{u}}_k^{\mathrm{c}} + \mathbf{B}_k^{\mathrm{nc}}\tilde{\mathbf{u}}_k^{\mathrm{nc}} + \mathbf{a}_k\right)\\
&\qquad + \mathbf{B}_{k+1}^{\mathrm{c}}\tilde{\mathbf{u}}_{k+1}^{\mathrm{c}} + \mathbf{B}_{k+1}^{\mathrm{nc}}\tilde{\mathbf{u}}_{k+1}^{\mathrm{nc}} + \mathbf{a}_{k+1},\\
\boldsymbol{\iota}_{k+3} &= \mathbf{A}_{k+2}\mathbf{A}_{k+1}\left(\mathbf{A}_k\boldsymbol{\iota}_k + \mathbf{B}_k^{\mathrm{c}}\tilde{\mathbf{u}}_k^{\mathrm{c}} + \mathbf{B}_k^{\mathrm{nc}}\tilde{\mathbf{u}}_k^{\mathrm{nc}} + \mathbf{a}_k\right)\\
&\qquad + \mathbf{A}_{k+2}\left(\mathbf{B}_{k+1}^{\mathrm{c}}\tilde{\mathbf{u}}_{k+1}^{\mathrm{c}} + \mathbf{B}_{k+1}^{\mathrm{nc}}\tilde{\mathbf{u}}_{k+1}^{\mathrm{nc}} + \mathbf{a}_{k+1}\right)\\
&\qquad\quad + \mathbf{B}_{k+2}^{\mathrm{c}}\tilde{\mathbf{u}}_{k+2}^{\mathrm{c}} + \mathbf{B}_{k+2}^{\mathrm{nc}}\tilde{\mathbf{u}}_{k+2}^{\mathrm{nc}} + \mathbf{a}_{k+2}.
\end{aligned}$$

Defining the operator

$$\prod_{t=m}^{n}\mathbf{A}_{k+t} \equiv \begin{cases} \mathbf{A}_{k+n}\mathbf{A}_{k+n-1}\dots\mathbf{A}_{k+m} & \text{if} \quad m \le n \\ \mathbf{I} & \text{if} \quad m > n \end{cases} \tag{B.10}$$

the future state evolution predicted at time $k$ can be written as a matrix equation. Let $H_u$ be the control horizon, where $H_u \le H_p$ implies $\mathbf{u}_{k+t} = \mathbf{u}_{k+H_u}$ for $t \ge H_u$, i.e. the control variable is only updated over the first $H_u$ time steps. At time $k$, the predicted state trajectory can be written as

$$\underbrace{\begin{bmatrix}\boldsymbol{\iota}_{k+1}\\ \boldsymbol{\iota}_{k+2}\\ \vdots\\ \boldsymbol{\iota}_{k+H_p}\end{bmatrix}}_{\mathbf{X}_k} = \underbrace{\begin{bmatrix}\mathbf{A}_k\\ \mathbf{A}_{k+1}\mathbf{A}_k\\ \vdots\\ \prod_{t=0}^{H_p-1}\mathbf{A}_{k+t}\end{bmatrix}}_{\boldsymbol{\Phi}_k}\boldsymbol{\iota}_k + \underbrace{\begin{bmatrix}\mathbf{B}_k^{\mathrm{nc}}\\ \mathbf{A}_{k+1}\mathbf{B}_k^{\mathrm{nc}} + \mathbf{B}_{k+1}^{\mathrm{nc}}\\ \vdots\\ \sum_{i=0}^{H_p-1}\prod_{t=i+1}^{H_p-1}\mathbf{A}_{k+t}\mathbf{B}_{k+i}^{\mathrm{nc}}\end{bmatrix}}_{\boldsymbol{\Gamma}_k^{\mathrm{nc}}}\tilde{\mathbf{u}}_k^{\mathrm{nc}} + \underbrace{\begin{bmatrix}\mathbf{a}_k\\ \mathbf{A}_{k+1}\mathbf{a}_k + \mathbf{a}_{k+1}\\ \vdots\\ \sum_{i=0}^{H_p-1}\prod_{t=i+1}^{H_p-1}\mathbf{A}_{k+t}\mathbf{a}_{k+i}\end{bmatrix}}_{\boldsymbol{\Gamma}_k^{\mathrm{a}}} +$$

$$\underbrace{\begin{bmatrix}\mathbf{B}_k^{\mathrm{c}} & & & \\ \mathbf{A}_{k+1}\mathbf{B}_k^{\mathrm{c}} & \mathbf{B}_{k+1}^{\mathrm{c}} & & \\ \vdots & & \ddots & \\ \prod_{t=1}^{H_p-1}\mathbf{A}_{k+t}\mathbf{B}_k^{\mathrm{c}} & \prod_{t=2}^{H_p-1}\mathbf{A}_{k+t}\mathbf{B}_{k+1}^{\mathrm{c}} & \dots & \sum_{i=H_u}^{H_p-1}\prod_{t=i+1}^{H_p-1}\mathbf{A}_{k+t}\mathbf{B}_{k+i}^{\mathrm{c}}\end{bmatrix}}_{\boldsymbol{\Gamma}_k^{\mathrm{c}}}\underbrace{\begin{bmatrix}\tilde{\mathbf{u}}_k^{\mathrm{c}}\\ \tilde{\mathbf{u}}_{k+1}^{\mathrm{c}}\\ \vdots\\ \tilde{\mathbf{u}}_{k+H_u}^{\mathrm{c}}\end{bmatrix}}_{\tilde{\mathbf{U}}_k^{\mathrm{c}}}. \tag{B.11}$$

or equivalently

$$\mathbf{X}_k = \boldsymbol{\Phi}_k\boldsymbol{\iota}_k + \boldsymbol{\Gamma}_k^{\mathrm{c}}\tilde{\mathbf{U}}_k^{\mathrm{c}} + \boldsymbol{\Gamma}_k^{\mathrm{nc}}\tilde{\mathbf{u}}_k^{\mathrm{nc}} + \boldsymbol{\Gamma}_k^{\mathrm{a}}. \tag{B.12}$$

As an alternative to the control sequence $\tilde{\mathbf{U}}_k$, we can take as the optimization variables

$$\Delta\tilde{\mathbf{U}}_k^c = \left[\Delta\tilde{\mathbf{u}}_k^c, \Delta\tilde{\mathbf{u}}_{k+1}^c, \ldots, \Delta\tilde{\mathbf{u}}_{k+H_u}^c\right],$$

where $\Delta\tilde{\mathbf{u}}_k^c = \tilde{\mathbf{u}}_k^c - \tilde{\mathbf{u}}_{k-1}^c$ and

$$\Delta\tilde{\mathbf{U}}_k^c = \boldsymbol{\Gamma}_\Delta\tilde{\mathbf{U}}_k^c - \boldsymbol{\Gamma}_{\text{last}}\tilde{\mathbf{u}}_{k-1}^c, \tag{B.13}$$

where the difference matrix operators are given by

$$\boldsymbol{\Gamma}_\Delta = \begin{bmatrix} \mathbf{I} & & & \\ -\mathbf{I} & \mathbf{I} & & \\ & & \ddots & \\ & & -\mathbf{I} & \mathbf{I} \end{bmatrix}, \quad \boldsymbol{\Gamma}_{\text{last}} = \begin{bmatrix} \mathbf{I} \\ \mathbf{0} \\ \vdots \\ \mathbf{0} \end{bmatrix}. \tag{B.14}$$

## B.4.1 Converting the Optimal Control Problem

With the use of the prediction matrices of (B.12), we can recast the optimal control problem (6.4) into a standard form. Introducing the notation

$$\mathbf{T}_k = \begin{bmatrix} \boldsymbol{\iota}_{k+1}^{\text{FF}} \\ \boldsymbol{\iota}_{k+2}^{\text{FF}} \\ \vdots \\ \boldsymbol{\iota}_{k+H_p}^{\text{FF}} \end{bmatrix}$$

to represent the target profile over the prediction horizon, the optimal control problem (6.4) can be written as

$$\underset{\Delta\tilde{\mathbf{U}}_k^c,\, \epsilon_E,\, \epsilon_q,\, \epsilon_{ss}}{\text{minimize}} \quad J = (\mathbf{X}_k - \mathbf{T}_k)^T\bar{\mathbf{Q}}(\mathbf{X}_k - \mathbf{T}_k) + (\Delta\tilde{\mathbf{U}}_k^c)^T\bar{\mathbf{R}}\Delta\tilde{\mathbf{U}}_k^c + W_E\epsilon_E^2 + W_q\epsilon_q^2 + W_{ss}\epsilon_{ss}^2 \tag{B.15}$$

$$\text{subject to} \quad \Delta\tilde{\mathbf{U}}_k^c \in \Delta\tilde{\mathcal{U}}_k \tag{B.16}$$

$$\mathbf{X}_k \in \mathcal{X}_k \tag{B.17}$$

where $\bar{\mathbf{Q}} = I_{H_p} \otimes \mathbf{Q}, \bar{\mathbf{R}} = I_{H_u} \otimes \mathbf{R}$. Defining the entire set of optimization variables as $\mathbf{z} = (\Delta\tilde{\mathbf{U}}_k^c, \epsilon_E, \epsilon_q, \epsilon_{ss})$, and utilizing the prediction equations (B.12), it is straightforward to write the objective (B.15) and constraints (B.16)-(B.17) as functions of

the optimization variables. The standard form quadratic program (QP) is written as

$$\begin{aligned} \underset{\mathbf{z}}{\text{minimize}} \quad & \frac{1}{2}\mathbf{z}^T\mathbf{H}_k\mathbf{z} + \mathbf{h}_k^T\mathbf{z} \\ \text{subject to} \quad & \mathbf{A}_{\text{eq},k}\mathbf{z} = \mathbf{b}_{\text{eq},k} \\ & \mathbf{A}_{\text{in},k}z \leq \mathbf{b}_{\text{in},k} \end{aligned} \tag{B.18}$$

where

$$\mathbf{H}_k = \begin{bmatrix} \left(\boldsymbol{\Gamma}_k^{\text{c}}\boldsymbol{\Gamma}_{\Delta}^{-1}\right)^T \bar{\mathbf{Q}}\boldsymbol{\Gamma}_k^{\text{c}}\boldsymbol{\Gamma}_{\Delta}^{-1} + \bar{\mathbf{R}} & & & \\ & W_E & & \\ & & W_q & \\ & & & W_{ss} \end{bmatrix}, \tag{B.19}$$

$$\mathbf{h}_k = 2\left(\mathbf{E}_k - \mathbf{T}_k\right)^T \bar{\mathbf{Q}}\boldsymbol{\Gamma}_k^{\text{c}}\boldsymbol{\Gamma}_{\Delta}^{-1}, \tag{B.20}$$

and $\mathbf{E}_k$ defines the unforced dynamic evolution given by

$$\mathbf{E}_k = \boldsymbol{\Phi}_k\boldsymbol{\iota}_k + \boldsymbol{\Gamma}_k^{\text{c}}\boldsymbol{\Gamma}_{\text{last}}\tilde{\mathbf{u}}_{k-1}^{\text{c}} + \boldsymbol{\Gamma}_k^{\text{nc}}\tilde{\mathbf{u}}_k^{\text{nc}} + \boldsymbol{\Gamma}_k^{\text{a}}. \tag{B.21}$$

## B.5 MPC with Offset Free Tracking

Model predictive control uses a nominal model to predict the future state trajectory of the controlled process. If the nominal model represents perfectly the actual process and no disturbances are present, the MPC feedback scheme can be made to track reachable targets without offset. If, however, model mismatch or disturbances are present, some modifications must be made to the standard MPC algorithm to ensure offset free tracking. The most common offset free tracking methods fall into one of two categories. The disturbance model approach augments the nominal model with integrating states (called disturbances), which are estimated with an observer. Various forms of disturbance models haven been proposed, see [97] for a summary, and equivalence of the various disturbance models has been demonstrated in [98]. An alternative approach involves the so called velocity form representation [99], in which the control and state are replaced with their increment values. This formulation

permits offset free tracking by essentially correcting the target, since the target of state increments is always zero even if the plant and model are not equal. In fact, both the various disturbance and velocity form approaches have been shown to be equivalent as they are specific instances of a more general disturbance model approach [100].

In the case of full state measurement, which is the basic assumption for all the control problems considered in this thesis, the velocity form approach has the advantage that it does not require any estimator.

### B.5.1 Velocity Form Approach

Let the plant, i.e. actual system, be defined by

$$\begin{aligned} \mathbf{x}^+ &= \mathbf{A}\mathbf{x} + \mathbf{B}\mathbf{u} + \mathbf{w}, \\ \mathbf{y} &= \mathbf{C}\mathbf{x} + \mathbf{v}, \end{aligned} \tag{B.22}$$

where $\mathbf{x}^+$ is the successor state, $\mathbf{w}$ is the state disturbance, and $\mathbf{v}$ is the output disturbance. The nominal model is defined by

$$\begin{aligned} \hat{\mathbf{x}}^+ &= \mathbf{A}\hat{\mathbf{x}} + \mathbf{B}\mathbf{u}, \\ \hat{\mathbf{y}} &= \mathbf{C}\hat{\mathbf{x}}. \end{aligned} \tag{B.23}$$

Define the incremental state and control, respectively, as $\delta\mathbf{x} = \mathbf{x}(k) - \mathbf{x}(k+1)$ and $\delta\mathbf{u} = \mathbf{u}(k) - \mathbf{u}(k-1)$. The velocity form representation, in which both the state and control are replaced by their incremental counterparts, can be obtained from (B.23) as

$$\begin{aligned} \delta\hat{\mathbf{x}}^+ &= \mathbf{A}\delta\hat{\mathbf{x}} + \mathbf{B}\delta\mathbf{u}, \\ \hat{\mathbf{e}} &= \hat{\mathbf{y}}^+ - \mathbf{r} = \hat{\mathbf{y}} + \mathbf{C}\mathbf{A}\delta\hat{\mathbf{x}} + \mathbf{C}\mathbf{B}\delta\mathbf{u} - \mathbf{r}. \end{aligned}$$

Take the augmented state, $\hat{\xi} = \begin{bmatrix} \delta\hat{\mathbf{x}} \\ \hat{\mathbf{y}} - \mathbf{r} \end{bmatrix} = \begin{bmatrix} \delta\hat{\mathbf{x}} \\ \hat{\mathbf{e}} \end{bmatrix}$, as the velocity model state and the model tracking error, $\hat{\mathbf{e}}$, as the velocity model output, then

$$\begin{aligned} \hat{\xi}^+ &= \mathbf{A}_\delta\hat{\xi} + \mathbf{B}_\delta\delta\mathbf{u}, \\ \hat{\mathbf{e}} &= \mathbf{C}_\delta\hat{\xi}, \end{aligned} \tag{B.24}$$

defines the velocity model, where

$$\mathbf{A}_\delta = \begin{bmatrix} \mathbf{A} & 0 \\ \mathbf{CA} & \mathbf{I} \end{bmatrix}, \quad \mathbf{B}_\delta = \begin{bmatrix} \mathbf{B} \\ \mathbf{CB} \end{bmatrix}, \quad \mathbf{C}_\delta = \begin{bmatrix} 0 & \mathbf{I} \end{bmatrix}.$$

Letting $\xi = \begin{bmatrix} \delta\mathbf{x} \\ \mathbf{e} \end{bmatrix}$, the actual system (B.22) can also be written in velocity form as

$$\begin{aligned} \xi^+ &= \mathbf{A}_\delta \xi + \mathbf{B}_\delta \delta\mathbf{u} + \begin{bmatrix} \delta\mathbf{w} \\ \delta\mathbf{w} + \delta\mathbf{v}^+ \end{bmatrix}, \\ \hat{\mathbf{e}} &= \mathbf{C}_\delta \xi. \end{aligned} \tag{B.25}$$

Therefore the velocity form model is exact in the presence of constant state and output disturbances, i.e. $\delta\mathbf{w} = 0$ and $\delta\mathbf{v} = 0$. For this reason if we replace the prediction model of the standard MPC optimization problem with the velocity form model we can obtain offset free tracking in steady state. If full state measurement is not available, i.e. $\mathbf{C} \neq \mathbf{I}$, the augmented state of the velocity form model can be obtained from the measured tracking error by means of an observer. Note that velocity form model remains exact even if the augmented state is take as $\xi = \begin{bmatrix} \delta\mathbf{x} \\ \mathbf{y} \end{bmatrix}$, in which case the desired reference becomes a parameter of the optimization problem. This is useful for instances in which the reference is time changing it is desired for the controller to anticipate future reference changes.

# Appendix C

# Optimal Control Derivations

## C.1 Calculus of Variations

Consider a general additive cost function of the form

$$J = h(\mathbf{x}(t_f), t_f) + \int_0^{t_f} g(\mathbf{x}(t), \mathbf{u}(t), t)dt, \tag{C.1}$$

and a set of constraints consisting of the system dynamics, fixed initial condition, either fixed or free final state, and either fixed or free final time,

$$\dot{\mathbf{x}} = \mathbf{f}(\mathbf{x}, \mathbf{u}, t), \tag{C.2}$$

$$\mathbf{x}(0) = \mathbf{x}_0, \tag{C.3}$$

$$\mathbf{x}(t_f) = \mathbf{x}_f \quad \text{(optional)}. \tag{C.4}$$

The necessary conditions for an optimal control policy can be obtained from calculus of variations [69]. The process involves taking the variational of $J$, i.e. the partial derivative of $J$ with respect to each of the variables of the final cost and integrand, and setting it to zero. From the variational, the necessary conditions optimality, equivalently the conditions for the variational of $J$ to be zero, can be obtained. Defining the Hamiltonian

$$H(\mathbf{x}, \mathbf{u}, \mathbf{p}, t) = g(\mathbf{x}(t), \mathbf{u}(t), t) + \mathbf{p}(t)^T \mathbf{f}(\mathbf{x}, \mathbf{u}, t), \tag{C.5}$$

where $\mathbf{p}$ is a Lagrange multiplier (see chapter 2 of [69]), the necessary conditions for optimality can be summarized as

$$\dot{\mathbf{x}} = \mathbf{f}(\mathbf{x}, \mathbf{u}, t), \tag{C.6}$$

$$\dot{\mathbf{p}} = -H_x^T, \tag{C.7}$$

$$H_u = 0, \tag{C.8}$$

along with the boundary conditions

$$h_t(t_f) + H(t_f) = 0, \tag{C.9}$$

$$\mathbf{x}(0) = \mathbf{x}_0, \tag{C.10}$$

and depending on whether the final state is fixed of free we have the additional boundary conditions,

$$[\mathbf{x}(t_f)]_i = [\mathbf{x}_F]_i \quad \text{(for fixed final state element } i\text{)}, \tag{C.11}$$

$$[\mathbf{p}(t_f)]_i = \frac{\partial h}{\partial [\mathbf{x}]_i}(t_f) \quad \text{(for free final state element } i\text{)}. \tag{C.12}$$

### C.1.1 Example Problem: Double Integrator

Consider a brick of unit mass sliding on frictionless ice subject to a force, $u$, as shown in Figure C.1. Let $y$ be the spatial coordinate, then the dynamic evolution

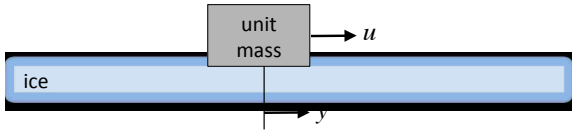


**Figure C.1:** Brick of unit mass sliding on frictionless ice.

of the brick can be described by $\ddot{y} = u$. The position of the brick is a double integral of the input over time, hence the name "double integrator". The states of the system consist of the position and velocity of the brick, i.e. $x_1 = y$ and $x_2 = \dot{y}$. Writing the

state as $\mathbf{x} = \begin{bmatrix} x_1 \\ x_2 \end{bmatrix}$, a state space description of the dynamics can be obtained

$$\dot{\mathbf{x}} = \mathbf{f}(\mathbf{x}, u) = \begin{bmatrix} x_2 \\ u \end{bmatrix}. \tag{C.13}$$

**Optimal Control Solution by Calculus of Variations**

Consider the control objective of driving the brick to the origin, $\mathbf{x}(t_f) = 0$, from an arbitrary initial condition, $\mathbf{x}(0) = [x_{10}, x_{20}]^T$, in such a way as to minimize the cost

$$J = \underbrace{\frac{1}{2} W_{t_f} t_f^2}_{h(\mathbf{x}(t_f), t_f)} + \int_0^{t_f} \underbrace{\frac{1}{2} W_u u^2}_{g(\mathbf{x}(t), u(t), t)} \, dt \tag{C.14}$$

where the final time $t_f$ is free, and $W_{t_f} > 0$, $W_u > 0$ are design weights. From the method of calculus of variations [69], we know that the optimality conditions of this problem are associated with the Hamiltonian function,

$$H = \frac{1}{2} W_u u^2 + \mathbf{p}^T \mathbf{f}(\mathbf{x}, u), \tag{C.15}$$

where $\mathbf{p}$ is a Lagrange multiplier. The necessary conditions for optimality (see Section C.1) are given by

$$\dot{\mathbf{p}} = -\mathbf{H}_x^T, \tag{C.16}$$

$$0 = \mathbf{H}_u. \tag{C.17}$$

and the boundary conditions include

$$\mathbf{x}(0) = [x_{10}, x_{20}]^T, \tag{C.18}$$

$$\mathbf{x}(t_f) = 0, \tag{C.19}$$

$$h_t(t_f) + H(t_f) = 0. \tag{C.20}$$

From (C.16), we can obtain an expressions for each $\mathbf{p}_i$:

$$\dot{p}_1 = -\frac{\partial H}{\partial x_1} \qquad \rightarrow \qquad \dot{p}_1 = 0 \qquad \rightarrow \qquad p_1 = c_1, \tag{C.21}$$

$$\dot{p}_2 = -\frac{\partial H}{\partial x_2} \qquad \rightarrow \qquad \dot{p}_2 = -p_1 \qquad \rightarrow \qquad p_2 = -c_1 t + c_2, \tag{C.22}$$

and from (C.17), we can obtain an expression for $u$:

$$H_u = 0 \qquad \rightarrow \qquad W_u u + p_2 = 0 \qquad \rightarrow \qquad u = -\frac{c_2}{W_u} + \frac{c_1}{W_u} t. \tag{C.23}$$

Imposing the boundary condition (C.20) we can obtain an expression for $t_f$:

$$\begin{aligned} H(t_f) + h_t(t_f) = 0 \quad &\rightarrow \quad \frac{1}{2} W_u u(t_f)^2 + \Big[ p_1(t_f), p_2(t_f) \Big] \begin{bmatrix} x_2(t_f) \\ u(t_f) \end{bmatrix} + W_{t_f} t_f = 0 \\ -\frac{1}{2} W_u u(t_f)^2 + W_{t_f} t_f = 0 \quad &\rightarrow \quad t_f = \frac{1}{2} \frac{1}{W_{t_f} W_u} \left( -c_2 + c_1 t_f \right)^2, \end{aligned} \tag{C.24}$$

where we have used the final state constraint $x_2(t_f) = 0$ and the expression $p_2 = -W_u u(t_f)$ from (C.23) to obtain the third equation. Returning to the state equations, we can obtain expressions for the optimal state evolution,

$$\dot{x}_2 = u \qquad \rightarrow \qquad x_2 = c_3 - \frac{c_2}{W_u} t + \frac{c_1}{2W_u} t^2, \tag{C.25}$$

$$\dot{x}_1 = x_2 \qquad \rightarrow \qquad x_1 = c_4 + c_3 t - \frac{c_2}{2W_u} t^2 + \frac{c_1}{6W_u} t^t. \tag{C.26}$$

Now, using with the boundary conditions, $\mathbf{x}(0) = [x_{10}, x_{20}]^T$ and $\mathbf{x}(t_f) = 0$, we can solve for the integration constants,

$$c_1 = \frac{12 W_u}{t_f^3} \left( x_{10} + \frac{1}{2} x_{20} t_f \right), \tag{C.27}$$

$$c_2 = \frac{6 W_u}{t_f^2} \left( x_{10} + \frac{2}{3} x_{20} t_f \right), \tag{C.28}$$

$$c_3 = x_{20}, \tag{C.29}$$

$$c_4 = x_{10}. \tag{C.30}$$

Combining the expressions for $c_1$ and $c_2$, we can obtain an expression for the optimal final time, $t_f^*$, in terms of the initial condition,

$$t_f^* = \frac{18 W_u}{W_{t_f} (t_f^*)^4} \left( x_{10} + \frac{1}{3} x_{20} t_f^* \right)^2, \tag{C.31}$$

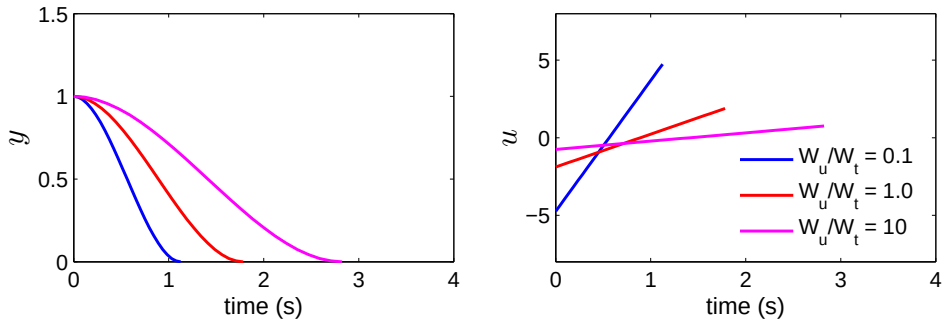


(a) Zero initial velocity: $\mathbf{x}_0 = [1, 0]^T$.

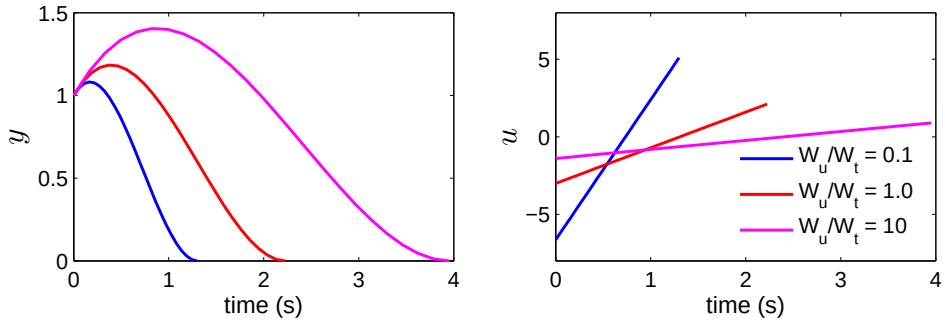


(b) Non-zero initial velocity: $\mathbf{x}_0 = [1, 1]^T$.

**Figure C.2:** Optimal state (position) and control for the brick sliding problem. Two cases shown: (a) zero initial velocity and (b) non-zero initial velocity.

which can be solved numerically by a standard Newton's method. The optimal trajectory and control policy is shown in Figure C.2 for two initial conditions, one with zero initial velocity and one with an non-zero initial velocity. Note that the control policy varies smoothly over the control time, this is a consequence of the quadratic cost applied to the control value (C.14). Also, the brick reaches the final state in finite time, which is required given the fixed final state constraint. Naturally, as the cost weight on control effort relative to cost weight on final time, $W_u/W_{t_f}$, increases, the time to reach the final state also increases. This example will be used for comparison of numerical optimization approaches described in the later sections.

### C.1.2 Derivation of Linear Quadratic Regulator (LQR) Control Policy by Calculus of Variations

While it is typically difficult to solve the optimality conditions of Section C.1 in general, there is a class of problems for which analytic solutions are very accessible, those involving linear dynamics, quadratic costs, and no other constraints. The simplest case, called the linear quadratic regulator (LQR), is derived in this section using calculus of variations. It can also be derived from dynamic programming techniques (the Hamilton Jacobi Bellman equation) [101].

#### LQR Derivation by Calculus of Variations

Consider a linear time-variant system with specified initial condition

$$\dot{\mathbf{x}} = \mathbf{A}\mathbf{x} + \mathbf{B}\mathbf{u}, \quad \mathbf{x}(0) = \mathbf{x}_0, \tag{C.32}$$

and a finite-time-horizon quadratic cost function

$$\begin{aligned} J_{\text{LQR}} =& \frac{1}{2}\mathbf{x}(t_f)^T\mathbf{Q}_f\mathbf{x}(t_f) + \int_0^{t_f} \left[\mathbf{x}^T\mathbf{Q}\mathbf{x} + \mathbf{u}^T\mathbf{R}\mathbf{u}\right] dt, \\ & \mathbf{Q}_f = \mathbf{Q}_f^T \leq 0, \quad \mathbf{Q} = \mathbf{Q}^T \leq 0, \quad \mathbf{R} = \mathbf{R}^T > 0. \end{aligned} \tag{C.33}$$

To solve for the control that optimizes the cost ($\mathbf{u}^\star$), we can use the equations defining the necessary conditions for optimality, which stem from calculus of variations. The Hamiltonian associated with this problem is obtained by augmenting the constraints (the system dynamics in this case) to the instantaneous cost (integrand),

$$H = \frac{1}{2}\left(\mathbf{x}^T\mathbf{Q}\mathbf{x} + \mathbf{u}^T\mathbf{R}\mathbf{u}\right) + \mathbf{p}^T\left(\mathbf{A}\mathbf{x} + \mathbf{B}\mathbf{u}\right), \tag{C.34}$$

where $\mathbf{p}(t)$ is the Lagrange multiplier, which is often referred to as the costate. Working from the necessary conditions for optimality, we obtain

$$\dot{\mathbf{x}} = \frac{\partial H}{\partial \mathbf{p}}^T = \mathbf{A}\mathbf{x} + \mathbf{B}\mathbf{u} \quad \text{with} \quad \mathbf{x}(0) = \mathbf{x}_0, \tag{C.35}$$

$$\tag{C.36}$$

$$\dot{\mathbf{p}} = -\frac{\partial H}{\partial \mathbf{x}}^T = -\mathbf{Q}\mathbf{x} - \mathbf{A}^T\mathbf{p} \quad \text{with} \quad \mathbf{p}(t_f) = \mathbf{Q}_f\mathbf{x}(t_f), \tag{C.37}$$

$$\frac{\partial H}{\partial \mathbf{u}} = 0 \implies \mathbf{R}\mathbf{u} + \mathbf{B}^T\mathbf{p} = 0 \implies \mathbf{u}^\star = -\mathbf{R}^{-1}\mathbf{B}^T\mathbf{p}. \tag{C.38}$$

These conditions become sufficient for optimality if $\frac{\partial^2 H}{\partial \mathbf{u}^2} \geq 0$, which is ensured for $\mathbf{R} \geq 0$.

Using the expression for $\mathbf{u}^\star$ (C.38), we can describe the optimal evolution for the state and costate by the linear system

$$\begin{bmatrix} \dot{\mathbf{x}}(t) \\ \dot{\mathbf{p}}(t) \end{bmatrix} = \begin{bmatrix} \mathbf{A} & -\mathbf{B}\mathbf{R}^{-1}\mathbf{B}^T \\ -\mathbf{Q} & -\mathbf{A}^T \end{bmatrix} \begin{bmatrix} \mathbf{x}(t) \\ \mathbf{p}(t) \end{bmatrix}. \tag{C.39}$$

The dynamics of $\mathbf{x}(t)$ and $\mathbf{p}(t)$ are coupled, where the initial state $\mathbf{x}(0) = \mathbf{x}_0$ is known and final costate $\mathbf{p}(t_f) = \mathbf{Q}_f$ is known. This represents a two point boundary value problem, which is typically difficult to solve. But in this case, the system is linear, and we can related $[\mathbf{x}(t), \mathbf{p}(t)]$ to $[\mathbf{x}(t_f), \mathbf{p}(t_f)]$ by a state transition matrix[1],

$$\begin{bmatrix} \dot{\mathbf{x}}(t) \\ \dot{\mathbf{p}}(t) \end{bmatrix} = \begin{bmatrix} \Phi_{11}(t, t_f) & \Phi_{12}(t, t_f) \\ \Phi_{21}(t, t_f) & \Phi_{22}(t, t_f) \end{bmatrix} \begin{bmatrix} \mathbf{x}(t) \\ \mathbf{p}(t) \end{bmatrix}. \tag{C.40}$$

Now solve for $\mathbf{p}(t)$ in terms of $\mathbf{x}(t)$ to obtain

$$\begin{aligned} \mathbf{p}(t) &= \left[\Phi_{21}(t, t_f) + \Phi_{22}(t, t_f)\right] \left[\Phi_{11}(t, t_f) + \Phi_{12}(t, t_f)\right]^{-1} .\mathbf{x}(t) \\ &\triangleq \mathbf{S}(t)\mathbf{x}(t) \end{aligned} \tag{C.41}$$

Differentiating (C.41) with respect to time and equating with the second equation of (C.40), we obtain

$$\dot{\mathbf{p}} = \dot{\mathbf{S}}\mathbf{x} + \mathbf{S}\dot{\mathbf{x}} = -\mathbf{Q}\mathbf{x} - \mathbf{A}^T\mathbf{p}, \tag{C.42}$$

which can be combined with the dynamics (C.32) and the optimal control (C.38),

$$-\dot{\mathbf{S}}\mathbf{x} = \mathbf{Q}\mathbf{x} + \mathbf{A}^T\mathbf{p} + \mathbf{S}\left(\mathbf{A}\mathbf{x} + \mathbf{B}\mathbf{u}\right),$$

[1] Consider the linear homogenous system $\dot{z}(t) = F(t)z(t)$ with initial condition $z(0) = z_0$. The solution is given by $z(t) = \Phi(t, t_0)z_0$, and the state transition matrix has the following properties: $\Phi(t, t) = I$, $\Phi(t_2, t_0) = \Phi(t_2, t_1)\Phi(t_1, t_0)$, and $\Phi(t_1, t_2) = \Phi(t_2, t_1)^{-1}$.

$$
\begin{aligned}
&= \mathbf{Q}\mathbf{x} + \mathbf{A}^T\mathbf{p} + \mathbf{S}\left(\mathbf{A}\mathbf{x} - \mathbf{B}\mathbf{R}^{-1}\mathbf{B}^T\mathbf{p}\right), \\
&= \left(\mathbf{Q} + \mathbf{S}\mathbf{A}\right)\mathbf{x} + \left(\mathbf{A}^T - \mathbf{S}\mathbf{B}\mathbf{R}^{-1}\mathbf{B}^T\right)\mathbf{p}, \\
&= \left(\mathbf{Q} + \mathbf{S}\mathbf{A}\right)\mathbf{x} + \left(\mathbf{A}^T - \mathbf{S}\mathbf{B}\mathbf{R}^{-1}\mathbf{B}^T\right)\mathbf{S}\mathbf{x}, \\
&= \left(\mathbf{A}^T\mathbf{S} + \mathbf{S}\mathbf{A}^T + \mathbf{Q} - \mathbf{S}\mathbf{B}\mathbf{R}^{-1}\mathbf{B}^T\mathbf{S}\right)\mathbf{x}.
\end{aligned}
$$

Since this expression must be true for all $\mathbf{x}$, $\mathbf{S}$ must satisfy

$$
-\dot{\mathbf{S}} = \mathbf{A}^T\mathbf{S} + \mathbf{S}\mathbf{A}^T + \mathbf{Q} - \mathbf{S}\mathbf{B}\mathbf{R}^{-1}\mathbf{B}^T\mathbf{S}, \tag{C.43}
$$

which is matrix differential Riccati equation. The optimal value of $\mathbf{S}$ is found by solving backwards in time from $\mathbf{S}(t_f) = \mathbf{Q}_f$. Taking $\mathbf{Q}_f = 0$, the infinite horizon case is found by the steady state solution

$$
0 = \mathbf{A}^T\mathbf{S} + \mathbf{S}\mathbf{A}^T + \mathbf{Q} - \mathbf{S}\mathbf{B}\mathbf{R}^{-1}\mathbf{B}^T\mathbf{S}, \tag{C.44}
$$

which is an algebraic Riccati equation. The solution to this equation defines the optimal control, $\mathbf{u}^\star = \mathbf{R}^{-1}\mathbf{B}^T\mathbf{S}\mathbf{x}$, which is known as the LQR control law. It is well known that the equation has a single positive-definite solution if and only if the system is controllable.

### The Optimal LQR Cost

To obtain the optimal cost, we can rewrite the cost function (C.33) as

$$
J_{\text{LQR}} = \frac{1}{2}\mathbf{x}(t_f)^T\mathbf{Q}_f\mathbf{x}(t_f) + \int_0^{t_f}\left[\mathbf{x}^T\mathbf{Q}\mathbf{x} + \mathbf{u}^T\mathbf{R}\mathbf{u} + \mathbf{p}^T\left(\mathbf{A}\mathbf{x} + \mathbf{B}\mathbf{u} - \dot{\mathbf{x}}\right)\right]dt \tag{C.45}
$$

and substitute the necessary conditions for optimality (C.35)-(C.38) to obtain

$$
\begin{aligned}
J_{\text{LQR}} &= \frac{1}{2}\mathbf{x}(t_f)^T\mathbf{Q}_f\mathbf{x}(t_f) - \frac{1}{2}\int_0^{t_f}\left[\dot{\mathbf{x}}^T\mathbf{x} + \mathbf{p}^T\dot{\mathbf{x}}\right]dt, \\
&= \frac{1}{2}\mathbf{x}(t_f)^T\mathbf{Q}_f\mathbf{x}(t_f) - \frac{1}{2}\int_0^{t_f}\left[\frac{d}{dt}(\mathbf{p}^T\mathbf{x})\right]dt, \\
&= \frac{1}{2}\mathbf{x}(t_f)^T\mathbf{Q}_f\mathbf{x}(t_f) - \frac{1}{2}\left[\mathbf{p}(t_f)^T\mathbf{x}(t_f) - \mathbf{p}(0)^T\mathbf{x}(0)\right], \\
&= \frac{1}{2}\mathbf{x}(t_f)^T\mathbf{Q}_f\mathbf{x}(t_f) - \frac{1}{2}\left[\mathbf{x}(t_f)^T\mathbf{S}(t_f)\mathbf{x}(t_f) - \mathbf{x}(0)^T\mathbf{S}(0)\mathbf{x}(0)\right],
\end{aligned}
$$

$$J_{\text{LQR}} = \frac{1}{2}\mathbf{x}(0)^T\mathbf{S}(0)\mathbf{x}(0), \tag{C.46}$$

which describes the cost to drive the system to zero starting from the initial condition at the initial time. The control action $\mathbf{u}^\star$ actuates the system so as to minimize the cost as quickly as possible. From (C.46), we can see the direction $-\mathbf{S}\mathbf{x}$ in fact represents the steepest descent of the cost function. However, not all directions are possible as the system is constrained by the available actuation. The direction $-\mathbf{B}^T\mathbf{S}\mathbf{x}$ is a projection of the steepest descent onto the controllable directions. Finally, the optimal control is scaled by the matrix $\mathbf{R}^{-1}$, $\mathbf{u}^\star = \mathbf{R}^{-1}\mathbf{B}^T\mathbf{S}$, to account for design choices which weight different control inputs. A variety of useful extensions to the LQR problem are possible [69]. For example, the results above apply even if dynamics and cost matrices are time varying $\mathbf{A} = \mathbf{A}(t)$, $\mathbf{B} = \mathbf{B}(t)$, $\mathbf{Q} = \mathbf{Q}(t)$, and $\mathbf{R} = \mathbf{R}(t)$.

## C.2 Formulating the Optimal Control Problem as Numerical Optimization Problem

Usually optimal control problems like the example of Section C.1.1 can only be solved in closed form for linear dynamical systems. For nonlinear system dynamics it is most often necessary to solve the problem numerically. There are numerous ways to transcribe an optimal control problem into a numerical optimization problem [70]. For example, in the single shooting approach described in Section 4.3, the optimization variables consist only of the controls, and the dynamic constraints are removed from the problem by solving for the future states in terms of the controls and initial condition.

Once formulated as a standard optimization problem, the optimal control problem can be solved by a commercial solver. While it is not strictly necessary, a numerical solver can benefit immensely from having the gradients of the objective and constraints computed analytically. Not only will explicit gradient calculations

greatly reduce the time necessary to solve the optimization problem, but also addresses issues associated with inaccurate finite difference approximations that creep in as the dynamics become more complicated.

As will be described in the following section, the gradient of the cost function with respect to the optimization variables depends on the sensitivity of the state evolution to the control variables. In this section, equations for the sensitivity along a trajectory are developed for various integration schemes. We consider, first, the forward Euler (explicit) integration type, then the backward Euler (implicit) integration type, and then extend the technique to general explicit and implicit Runge-Kutta integration schemes.

### C.2.1 Sensitivity

Consider the additive cost function,

$$J^{\boldsymbol{\alpha}} = h(t_0, t_F, \mathbf{x}(t_0), \mathbf{x}(t_F)) + \int_{t_0}^{t_F} g(t, \mathbf{x}(t), \mathbf{u}(t))dt, \tag{C.47}$$

for which we would like to find the gradient of $J^{\boldsymbol{\alpha}}$ with respect to some set of parameters $\boldsymbol{\alpha}$. The cost function $J^{\boldsymbol{\alpha}}$ is a function of the trajectory $(t, \mathbf{x}(t), \mathbf{u}(t))$, which is constrained by the dynamics,

$$\dot{\mathbf{x}} = \mathbf{f}(t, \mathbf{x}, \mathbf{u}), \quad \mathbf{x}(t_0) = \mathbf{x}_0, \quad t \in [t_0, t_F]. \tag{C.48}$$

The vector of free parameters, $\boldsymbol{\alpha}$, could represent a variety of things, for example it could be the initial condition $\boldsymbol{\alpha} = \mathbf{x}_0$ or it could be a control policy of the form, $\mathbf{u} = \mathbf{u}^{\boldsymbol{\alpha}}(t, \mathbf{x})$.

#### Forward Euler Integration (Explicit Integration)

In the case of explicit Euler integration of the dynamics (C.48), we have

$$\mathbf{x}[n+1] = \mathbf{x}[n] + dt\mathbf{f}(t_n, \mathbf{x}[n], \mathbf{u}[n]), \quad dt = \frac{t_F - t_0}{N}, \quad t_n = t_0 + ndt,$$

where we have defined the time step $dt$ as the difference between final time and initial time divided by a fixed number of time steps $N$, and $n$ represents the discrete

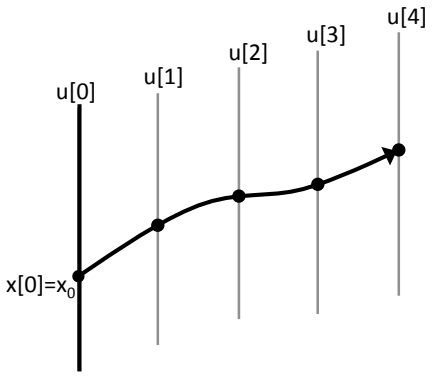


**Figure C.3:** Control parameterization for single shooting with explicit Euler integration.

time variable. Integrating the cost function (C.47) as well with the explicit Euler integration scheme, we have

$$J^{\boldsymbol{\alpha}} = h(t_0, t_F, \mathbf{x}[0], \mathbf{x}[N]) + dt \sum_{n=0}^{N-1} g(t_n, \mathbf{x}[n], \mathbf{u}[n]).$$

Consider a set of optimization variables including the initial and final time and a set of open-loop control updates along the trajectory as shown in Figure C.3, i.e. $\boldsymbol{\alpha} = [t_0, t_F, \mathbf{x}_0^T, \mathbf{u}_0^T, \mathbf{u}_1^T, \ldots, \mathbf{u}_N^T]$. Taking the partial derivative of $J^{\boldsymbol{\alpha}}$ with respect to each optimization variable the gradient of the cost function can be obtained,

$$\begin{aligned}
\frac{\partial J^{\boldsymbol{\alpha}}}{\partial \boldsymbol{\alpha}} &= \frac{\partial h(t_0, t_F, \mathbf{x}[0], \mathbf{x}[N])}{\partial t_0}\frac{\partial t_0}{\partial \boldsymbol{\alpha}} + \frac{\partial h(t_0, t_F, \mathbf{x}[0], \mathbf{x}[N])}{\partial t_F}\frac{\partial t_F}{\partial \boldsymbol{\alpha}} \\
&+ \frac{\partial h(t_0, t_F, \mathbf{x}[0], \mathbf{x}[N])}{\partial \mathbf{x}[0]}\frac{\partial \mathbf{x}[0]}{\partial \boldsymbol{\alpha}} + \frac{\partial h(t_0, t_F, \mathbf{x}[0], \mathbf{x}[N])}{\partial \mathbf{x}[N]}\frac{\partial \mathbf{x}[N]}{\partial \boldsymbol{\alpha}} + \frac{\partial dt}{\partial \boldsymbol{\alpha}} \sum_{n=0}^{N-1} g(t_n, \mathbf{x}[n], \mathbf{u}[n]) \\
&+ \sum_{n=0}^{N-1} dt \left( \frac{\partial g(t_n, \mathbf{x}[n], \mathbf{u}[n])}{\partial t_n}\frac{\partial t_n}{\partial \boldsymbol{\alpha}} + \frac{\partial g(t_n, \mathbf{x}[n], \mathbf{u}[n])}{\partial \mathbf{x}}\frac{\partial \mathbf{x}[n]}{\partial \boldsymbol{\alpha}} + \frac{\partial g(t_n, \mathbf{x}[n], \mathbf{u}[n])}{\partial \mathbf{u}}\frac{\partial \mathbf{u}[n]}{\partial \boldsymbol{\alpha}} \right)
\end{aligned}$$

The sensitivity terms, $\mathbf{S}_n = \partial \mathbf{x}[n]/\partial \boldsymbol{\alpha}$, can be obtained while integrating the dynamics forward, we have,

$$\begin{aligned}
\frac{\partial \mathbf{x}[n+1]}{\partial \boldsymbol{\alpha}} = \frac{\partial \mathbf{x}[n]}{\partial \boldsymbol{\alpha}} + dt \Bigg( & \frac{\partial \mathbf{f}(t_n, \mathbf{x}[n], \mathbf{u}[n])}{\partial t}\frac{\partial t_n}{\partial \boldsymbol{\alpha}} + \frac{\partial \mathbf{f}(t_n, \mathbf{x}[n], \mathbf{u}[n])}{\partial \mathbf{x}}\frac{\partial \mathbf{x}[n]}{\partial \boldsymbol{\alpha}} \\
& + \frac{\partial \mathbf{f}(t_n, \mathbf{x}[n], \mathbf{u}[n])}{\partial \mathbf{u}}\frac{\partial \mathbf{u}[n]}{\partial \boldsymbol{\alpha}} \Bigg) + \frac{\partial dt}{\partial \boldsymbol{\alpha}} \mathbf{f}(t_n, \mathbf{x}[n], \mathbf{u}[n]).
\end{aligned} \tag{C.49}$$

where the initial sensitivity, $\mathbf{S}_0 = \partial \mathbf{x}[0]/\partial \boldsymbol{\alpha}$, is either zero if $\mathbf{x}_0$ is fixed, or given by

$$\frac{\partial \mathbf{x}[0]}{\partial \boldsymbol{\alpha}} = \begin{bmatrix} \mathbf{0} & \mathbf{0} & \mathbf{I} & \mathbf{0} & \dots & \mathbf{0} \end{bmatrix}, \tag{C.50}$$

if $\mathbf{x}_0$ is taken as an optimization variable. The remaining terms, $\partial \mathbf{u}[n]/\partial \boldsymbol{\alpha}$, $\partial t_0/\partial \boldsymbol{\alpha}$, etc. are given by

$$\frac{\partial \mathbf{u}[0]}{\partial \boldsymbol{\alpha}} = \begin{bmatrix} \mathbf{0} & \mathbf{0} & \mathbf{0} & \mathbf{I} & \mathbf{0} & \dots & \mathbf{0} \end{bmatrix}, \quad \frac{\partial t_0}{\partial \boldsymbol{\alpha}} = \begin{bmatrix} 1 & 0 & \dots & 0 \end{bmatrix}, \quad \text{etc.}$$

**Backward Euler Integration**

Consider a cost function including only a time independent path cost,

$$J^{\boldsymbol{\alpha}} = \int_{t_0}^{t_F} g(\mathbf{x}(t), \mathbf{u}(t)) dt. \tag{C.51}$$

The boundary cost and time dependency of the dynamics which was included in the previous section has been omitted for simplicity. Employ a backward Euler (implicit Euler) scheme for integration of both the dynamics and cost function[2],

$$J^{\boldsymbol{\alpha}} = dt \sum_{n=0}^{N-1} g(\mathbf{x}[n+1], \mathbf{u}[n]), \qquad \mathbf{x}[n+1] = \mathbf{x}[n] + dt\mathbf{f}(\mathbf{x}[n+1], \mathbf{u}[n]).$$

In this case, the gradient of the cost function can be written as

$$\begin{aligned} \frac{\partial J^{\boldsymbol{\alpha}}}{\partial \boldsymbol{\alpha}} = dt \sum_{n=0}^{N-1} \left( \frac{\partial g(\mathbf{x}[n+1], \mathbf{u}[n])}{\partial \mathbf{x}} \frac{\partial \mathbf{x}[n+1]}{\partial \boldsymbol{\alpha}} + \frac{\partial g(\mathbf{x}[n], \mathbf{u}[n])}{\partial \mathbf{u}} \frac{\partial \mathbf{u}[n]}{\partial \boldsymbol{\alpha}} \right) \\ + \frac{\partial dt}{\partial \boldsymbol{\alpha}} \sum_{n=0}^{N-1} g(\mathbf{x}[n+1], \mathbf{u}[n]) \end{aligned} \tag{C.52}$$

and the sensitivity, $\mathbf{S}_n = \partial \mathbf{x}[n]/\partial \boldsymbol{\alpha}$, is given by

$$\frac{\partial \mathbf{x}[n+1]}{\partial \boldsymbol{\alpha}} = \left( \mathbf{I}_{n_x} - dt \frac{\partial \mathbf{f}(\mathbf{x}[n+1], \mathbf{u}[n])}{\partial \mathbf{x}} \right)^{-1} \left( \frac{\partial \mathbf{x}[n]}{\partial \boldsymbol{\alpha}} + dt \frac{\partial \mathbf{f}(\mathbf{x}[n+1], \mathbf{u}[n])}{\partial \mathbf{u}} \frac{\partial \mathbf{u}[n]}{\partial \boldsymbol{\alpha}} \right). \tag{C.53}$$

If the dynamics or cost are also a function time or the cost function $J^{\boldsymbol{\alpha}}$ includes a boundary cost, the additional terms can be easily incorporated in the same fashion as the explicit Euler integration scheme.

[2]It is important for the cost to be integrated under the same integration scheme as the dynamics in order to minimize noise in the calculation of gradients [70].

## C.3 General Runge-Kutta Methods

The explicit and implicit Euler integration schemes described above are particular forms of the Runge-Kutta methods. For a general dynamical system, $\dot{\mathbf{x}} = \mathbf{f}(t, \mathbf{x}, \mathbf{u})$, the general $s$-stage explicit Runge-Kutta (ERK) [70, 102] method is given by

$$\mathbf{x}_{n+1} = \mathbf{x}_n + dt \sum_{i=1}^{s} b_i \mathbf{k}_i \tag{C.54}$$

where

$$\begin{aligned}
\mathbf{k}_1 &= \mathbf{f}(t_n, \mathbf{x}_n, \mathbf{u}_1), \\
\mathbf{k}_2 &= \mathbf{f}(t_n + c_2 dt, \mathbf{x}_n + a_{21} dt \mathbf{k}_1, \mathbf{u}_2), \\
\mathbf{k}_3 &= \mathbf{f}(t_n + c_3 dt, \mathbf{x}_n + a_{31} dt \mathbf{k}_1 + a_{32} dt \mathbf{k}_2, \mathbf{u}_3), \\
&\vdots \\
\mathbf{k}_s &= \mathbf{f}(t_n + c_s dt, \mathbf{x}_n + a_{s1} dt \mathbf{k}_1 + a_{s2} dt \mathbf{k}_2 + \cdots + a_{s,s-1} dt \mathbf{k}_{s-1}, \mathbf{u}_s).
\end{aligned} \tag{C.55}$$

Independent control values, $\mathbf{u}_i$, have been included for each unique value $c_i$. For example, a four-stage ERK method with uniformly spaced $c_i$ is shown in Figure C.4 The particular ERK method is specified by the number of stages, $s$, the Runge-Kutta matrix given by $a_{ij}$, and the weights $c_i$ and $b_i$. Typically, this data is tabulated in the convenient form called a Butcher Tableau as shown in Figure C.5(a) for the ERK methods, which are characterized by a strictly lower triangular Runge-Kutta matrix, $\mathbf{A}_{RK} = \{a_{ij}\}$ for $i, j = 1, 2, \ldots, s$. Implicit Runge-Kutta (IRK) methods differ from explicit methods in that the Runge-Kutta matrix may contain nonzero terms in or above the main diagonal (see Figures C.5(b) and C.5(c)). For implicit methods the $\mathbf{k}_i$ terms of (C.54) are given by

$$\begin{aligned}
\mathbf{k}_1 &= \mathbf{f}(t_n, \mathbf{x}_n + a_{11} dt \mathbf{k}_1 + a_{12} dt \mathbf{k}_2 + \cdots + a_{1,s} dt \mathbf{k}_s, \mathbf{u}_1), \\
\mathbf{k}_2 &= \mathbf{f}(t_n + c_2 dt, \mathbf{x}_n + a_{21} dt \mathbf{k}_1 + a_{22} dt \mathbf{k}_2 + \ldots a_{2,s} dt \mathbf{k}_s, \mathbf{u}_2), \\
\mathbf{k}_3 &= \mathbf{f}(t_n + c_3 dt, \mathbf{x}_n + a_{31} dt \mathbf{k}_1 + a_{32} dt \mathbf{k}_2 + \ldots a_{3,s} dt \mathbf{k}_s, \mathbf{u}_3), \\
&\vdots \\
\mathbf{k}_s &= \mathbf{f}(t_n + c_s dt, \mathbf{x}_n + a_{s1} dt \mathbf{k}_1 + a_{s2} dt \mathbf{k}_2 + \ldots a_{s,s} dt \mathbf{k}_s, \mathbf{u}_s).
\end{aligned} \tag{C.56}$$

Note that $\mathbf{k}_i$ of earlier stages may be functions of $\mathbf{k}_i$ at later stages for implicit methods implying they must be solved numerically if the dynamics are nonlinear.

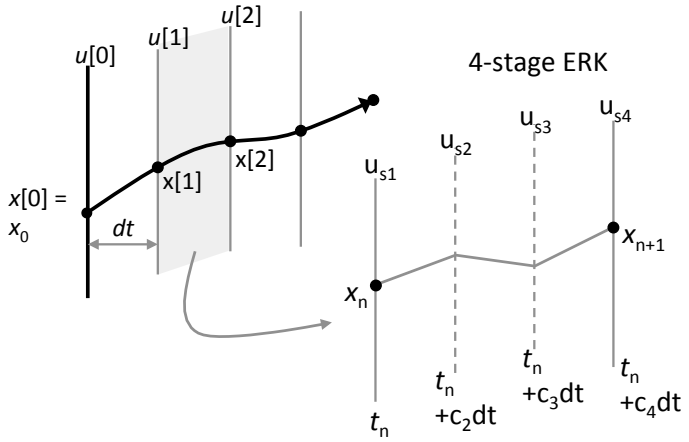


**Figure C.4:** Four-stage ERK method. The control value is allowed to be independent at each Runge-Kutta stage.

| | | | | | |
|---|---|---|---|---|---|
| 0 | | | | | |
| $c_2$ | $a_{21}$ | | | | |
| $c_3$ | $a_{31}$ | $a_{32}$ | | | |
| $\vdots$ | $\vdots$ | | $\ddots$ | | |
| $c_s$ | $a_{s,1}$ | $a_{s,2}$ | $\dots$ | $a_{s,s-1}$ | |
| | $b_1$ | $b_2$ | $\dots$ | $b_{s-1}$ | $b_s$ |

(a) ERK Butcher Tableau

| | | | | |
|---|---|---|---|---|
| $c_1$ | $a_{11}$ | $a_{12}$ | $\dots$ | $a_{1s}$ |
| $c_2$ | $a_{21}$ | $a_{22}$ | $\dots$ | $a_{2s}$ |
| $c_3$ | $a_{31}$ | $a_{32}$ | $\dots$ | $a_{3s}$ |
| $\vdots$ | $\vdots$ | | $\ddots$ | |
| $c_s$ | $a_{s,1}$ | $a_{s,2}$ | $\dots$ | $a_{s,s}$ |
| | $b_1$ | $b_2$ | $\dots$ | $b_s$ |

(b) IRK Butcher Tableau

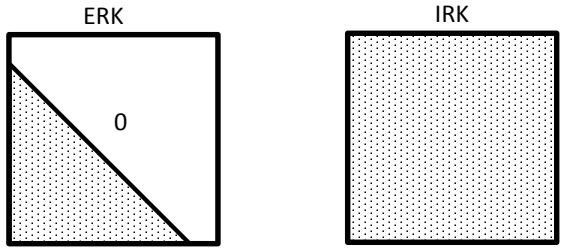


(c) $\mathbf{A}_{RK}$ for ERK vs. IRK.

**Figure C.5:** Butcher Tableau for explicit (ERK) and implicit (IRK) methods.

The Butcher Tableau provides a convenient way to program the sensitivity equations for arbitrary Runge-Kutta methods as described in the following sections.

### C.3.1 Sensitivity for General Explicit Runge-Kutta (ERK) Methods

Let $\mathbf{S}_n$ be the sensitivity of the state $\mathbf{x}_n$, i.e. $\mathbf{S}_n = \partial \mathbf{x}_n / \partial \boldsymbol{\alpha}$, and for simplicity assume $t_0$ and $t_F$ are fixed and the dynamics are not time dependent, then an update equation for the sensitivity can be obtained by differentiating (C.54) with respect to the optimization variables, which gives

$$\mathbf{S}_{n+1} = \mathbf{S}_n + dt \sum_{i=1}^{s} b_i \mathbf{k}'_i \tag{C.57}$$

where $\mathbf{k}'_i = \partial \mathbf{k}_i / \partial \boldsymbol{\alpha}$ are given by

$$\mathbf{k}'_1 = \mathbf{k}_{1,\mathbf{u}} \frac{\partial \mathbf{u}_1}{\partial \boldsymbol{\alpha}} + \mathbf{k}_{1,\mathbf{x}} \mathbf{S}_n, \tag{C.58}$$

$$\mathbf{k}'_2 = \mathbf{k}_{2,\mathbf{u}} \frac{\partial \mathbf{u}_2}{\partial \boldsymbol{\alpha}} + \mathbf{k}_{2,\mathbf{x}} \left( \mathbf{S}_n + a_{21} dt \mathbf{k}'_1 \right), \tag{C.59}$$

$$\mathbf{k}'_3 = \mathbf{k}_{3,\mathbf{u}} \frac{\partial \mathbf{u}_3}{\partial \boldsymbol{\alpha}} + \mathbf{k}_{3,\mathbf{x}} \left( \mathbf{S}_n + a_{31} dt \mathbf{k}'_1 + a_{32} dt \mathbf{k}'_2 \right), \tag{C.60}$$

$$\vdots \tag{C.61}$$

$$\mathbf{k}'_s = \mathbf{k}_{s,\mathbf{u}} \frac{\partial \mathbf{u}_s}{\partial \boldsymbol{\alpha}} + \mathbf{k}_{s,\mathbf{x}} \left( \mathbf{S}_n + a_{s1} dt \mathbf{k}'_1 + a_{s2} dt \mathbf{k}'_2 + \cdots + a_{s,s-1} dt \mathbf{k}'_{s-1} \right), \tag{C.62}$$

where the terms $\mathbf{k}_{i,\mathbf{u}}$ and $\mathbf{k}_{i,\mathbf{x}}$, which have been introduced for notational simplicity are given by

$$\mathbf{k}_{i,\mathbf{u}} = \frac{\partial \mathbf{k}_i}{\partial \mathbf{u}_i}, \qquad \mathbf{k}_{i,\mathbf{x}} = \frac{\partial \mathbf{k}_i}{\partial \mathbf{x}}. \tag{C.63}$$

The recursive characteristics of the $2^{\text{nd}}$ term on right side of (C.58)-(C.62) allows $\mathbf{S}_n$ to be written as

$$\mathbf{S}_{n+1} = \mathcal{S} \mathbf{S}_n + dt \sum_{i=1}^{s} b_i \mathbf{k}_{i,\mathbf{u}} \frac{\partial \mathbf{u}_i}{\partial \boldsymbol{\alpha}} \tag{C.64}$$

where $\mathcal{S}$ is a matrix given by

$$\begin{aligned}\mathcal{S} = \mathbf{I} + dt\,\{&b_1\mathbf{k}_{1,\mathbf{x}} + b_2\mathbf{k}_{2,\mathbf{x}}\left(\mathbf{I} + a_{21}dt\mathbf{k}_{1,\mathbf{x}}\right)\\ &+ b_3\mathbf{k}_{3,\mathbf{x}}\left[\mathbf{I} + a_{31}dt\mathbf{k}_{1,\mathbf{x}} + a_{32}dt\mathbf{k}_{2,\mathbf{x}}\left(\mathbf{I} + a_{21}dt\mathbf{k}_{1,\mathbf{x}}\right)\right] + \dots\\ &+ b_s\mathbf{k}_{s,\mathbf{x}}\left[\mathbf{I} + a_{s1}dt\mathbf{k}_{1,\mathbf{x}} + a_{s2}dt\mathbf{k}_{2,x}\left(\mathbf{I} + a_{21}dt\mathbf{k}_{1,\mathbf{x}}\right) + \dots\right.\\ &\qquad \left.+a_{s,s-1}dt\mathbf{k}_{s-1,\mathbf{x}}\left(\mathbf{I} + a_{s-1,1}dt\mathbf{k}_{1,\mathbf{x}} + \cdots + a_{s-1,s-2}dt\mathbf{k}_{s-2,\mathbf{x}}\left(\mathbf{I} + \dots\right)\right)\right]\}\end{aligned} \tag{C.65}$$

### C.3.2 Sensitivity for General Implicit Runge-Kutta (IRK) Methods

In the implicit Runge-Kutta schemes, we can consider a two stage scheme, and straightforward extensions can be made to extend the method for the two stage scheme to general implicit Runge-Kutta schemes defined by the Butcher Tableau of Table C.5(b). The two stage implicit scheme Butcher Tableau is given by

| | | |
|---|---|---|
| $c_1$ | $a_{11}$ | $a_{12}$ |
| $c_2$ | $a_{21}$ | $a_{22}$ |
| | $b_1$ | $b_2$ |

from which $\mathbf{k}_1$ and $\mathbf{k}_2$ can be obtained

$$\begin{aligned}\mathbf{k}_1 &= \mathbf{f}(t_n + c_1dt, \mathbf{x}_n + dt(a_{11}\mathbf{k}_1 + a_{12}\mathbf{k}_2)),\\ \mathbf{k}_2 &= \mathbf{f}(t_n + c_2dt, \mathbf{x}_n + dt(a_{21}\mathbf{k}_1 + a_{22}\mathbf{k}_2)).\end{aligned} \tag{C.66}$$

Like the explicit Runge-Kutta case, $\mathbf{S}_n$ is again defined by (C.57), where $\mathbf{k}'_1$ and $\mathbf{k}'_2$ can be written as

$$\begin{aligned}\mathbf{k}'_1 &= \mathbf{k}_{1,x}\left(\mathbf{I} + dta_{11}\mathbf{k}'_1 + dta_{12}\mathbf{k}'_2\right) + \mathbf{k}_{1,u},\\ \mathbf{k}'_2 &= \mathbf{k}_{2,x}\left(\mathbf{I} + dta_{21}\mathbf{k}'_1 + dta_{22}\mathbf{k}'_2\right) + \mathbf{k}_{2,u},\end{aligned} \tag{C.67}$$

where $\mathbf{k}_{i,x} = \partial\mathbf{k}_i/\partial\mathbf{x}$ and $\mathbf{k}_{i,u} = \partial\mathbf{k}_i/\partial\mathbf{u}$. In the implicit case the $\mathbf{k}$ terms at earlier stages depend on $\mathbf{k}$ terms at later stages, therefore we must solve the system

$$\begin{bmatrix}\mathbf{I} - a_{11}dt\mathbf{k}_{1,x} & -a_{12}dt\mathbf{k}_{1,x}\\ -a_{21}dt\mathbf{k}_{2,x} & -a_{22}dt\mathbf{k}_{2,x}\end{bmatrix}\begin{bmatrix}\mathbf{k}'_1\\ \mathbf{k}'_2\end{bmatrix} = \begin{bmatrix}\mathbf{k}_{1,x} + \mathbf{k}_{1,u}\\ \mathbf{k}_{2,x} + \mathbf{k}_{2,u}\end{bmatrix} \tag{C.68}$$

to obtain each $\mathbf{k}'_i$.

## C.4 Multiple-Shooting Formulation

So far we have only considered only the single shooting approach, in which the entire state trajectory is expressed as an integral function of the controls and initial state (see Section 4.3). However, the single shooting approach will break down for long trajectories with complicated dynamics because the gradients of the objective and constraints will become highly sensitive to small changes in the inputs. In the multiple shooting approach, the trajectory is divided into multiple segments as shown in Figure C.6. Discrepancies between the endpoints of the segments are accounted for by defect constraints. While the multiple shooting approach does increase the size of the optimization problem it becomes easier to solve because the sensitivity, $\mathbf{S}_n$, becomes more linear [70].

If the trajectory is divided into $N_S$ segments, this requires the introduction of the optimization parameters $\mathbf{x}_1$, $\mathbf{x}_2$, $\ldots$, $\mathbf{x}_{N_S-1}$, and the addition of $N_s - 1$ defect constraints to the optimization problem. The sensitivity, $\mathbf{S}_n$, can be calculated separately for each shooting segment in the same fashion as Section C.2.1.

The multiple shooting approach can also speed up the optimization process because the shooting segments can be integrated simultaneously. This can be valuable for dynamics that require implicit integrations schemes.

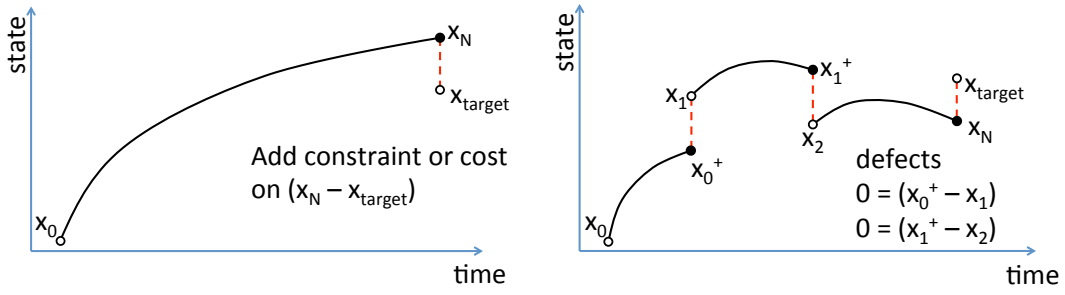


(a) Single shooting.

(b) Multiple shooting with three shooting segments.

**Figure C.6:** Single shooting vs. multiple shooting.

# Appendix D

# General Nonlinear Optimization Problem

Consider the general optimization problem

$$\begin{aligned} \underset{\mathbf{x}}{\text{minimize}} \quad & f(\mathbf{x}) \\ \text{subject to} \quad & \mathbf{c}_{\text{eq}}(\mathbf{x}) = 0 \\ & \mathbf{c}_{\text{in}}(\mathbf{x}) \leq 0 \end{aligned} \tag{D.1}$$

where $f : \mathbb{R}^n \to \mathbb{R}$, $\mathbf{c}_{\text{eq}} : \mathbb{R}^n \to \mathbb{R}^{n_{\text{eq}}}$, and $\mathbf{c}_{\text{in}} : \mathbb{R}^n \to \mathbb{R}^{n_{\text{in}}}$ are smooth functions which may be nonlinear and non convex. First-order necessary conditions for optimality require solutions to the problem (D.1) to be feasible, i.e. to satisfy all the constraints, and to be a stationary point to the Lagrangian

$$\mathcal{L}(\mathbf{x}, \lambda_{\text{eq}}, \lambda_{\text{in}}) = f(\mathbf{x}) - \lambda_{\text{eq}}^T \mathbf{c}_{\text{eq}}(\mathbf{x}) - \lambda_{\text{in}}^T \mathbf{c}_{\text{in}}(\mathbf{x}). \tag{D.2}$$

Potential solutions, labeled $(\mathbf{x}^\star, \lambda^\star)$, must satisfy the Karush-Kuhn-Tucker (KKT) conditions, which are essentially first-order necessary conditions for optimality[1],

$$\nabla_{\mathbf{x}} \mathcal{L}(\mathbf{x}^\star, \lambda_{\text{eq}}^\star, \lambda_{\text{in}}^\star) = 0, \tag{D.3}$$

$$\mathbf{c}_{\text{eq}}(\mathbf{x}^\star) = 0, \tag{D.4}$$

[1] In all cases vector inequalities denote component-wise comparisons

$$\mathbf{c}_{\text{in}}(\mathbf{x}^\star) \leq 0, \tag{D.5}$$

$$\lambda^\star_{\text{in}} \geq 0, \tag{D.6}$$

$$\lambda^\star_{\text{in},i}\mathbf{c}_{\text{in},i}(\mathbf{x}^\star) = 0, \quad \text{for } i = 1, 2, \ldots, n_{\text{in}}. \tag{D.7}$$

where $\nabla$ represents $\partial/\partial\mathbf{x}$. The conditions (D.7) are known as complimentarily conditions, they imply that either constraint $i$ is active ($c_{\text{in},i}(\mathbf{x}^\star) = 0$) or $\lambda^\star_{\text{in},i} = 0$, or possibly both. Typically, algorithms search for a solution to problems of this type by first starting with an approximate solution, call it $\mathbf{x}_0$, and work to improve on the solution by taking steps, $\Delta\mathbf{x}$, resulting in a sequence of iterates $\mathbf{x}_0, \mathbf{x}_1, \mathbf{x}_2, \ldots$, which converges to a solution. The general procedure is outlined in Algorithm 2.

**Algorithm 2:** General Optimization

Choose initial approximate solution $\mathbf{x}_0$
Evaluate $f_0 = f(x_0)$, $\nabla f_0$, initial constraints and constraint gradients
**for** $k = 0, 1, \ldots, k_{\max}$ **do**
    Check convergence criteria
    Determine search direction $\mathbf{p}_k$ (descent in some sense)
    Determine step length / step acceptance ($\alpha_k$)
    Set new iterate $\mathbf{x}_{k+1} = \mathbf{x}_k + \alpha_k\mathbf{p}_k$
    Set $f_{k+1} = f(\mathbf{x}_{k+1})$, $\nabla f_{k+1} = \nabla f(\mathbf{x}_{k+1})$, etc.
**end for**

## D.1 Sequential Quadratic Programming

Sequential Quadratic Programming (SQP) is a numerical optimization approach that has proven successful at solving medium scale problems such as those associated with optimal control. The SQP method generates a sequence of quadratic programming subproblems which are to be solved successively, hence the nomenclature sequential quadratic programming. Originally proposed in the doctoral work by Wilson [103], SQP was further developed into a globally convergent method by Han [104] and Powell [105]. The basic SQP algorithm described below is the same as that implemented in MATLAB's method for constrained optimization [74].

### D.1.1 Computing the SQP Search Direction

Sequential quadratic programming is essentially based on Newton's method. Consider the general equality constrained optimization problem

$$\begin{aligned} \underset{\mathbf{x}}{\text{minimize}} \quad & f(\mathbf{x}) \\ \text{subject to} \quad & \mathbf{c}_{\text{eq}}(\mathbf{x}) = 0 \end{aligned} \tag{D.8}$$

SQP arises by applying Newton's method to the KKT conditions relevant to this problem (D.3)-(D.4), i.e.

$$\begin{bmatrix} \nabla_{\mathbf{x}} \mathcal{L}(\mathbf{x}^\star, \boldsymbol{\lambda}^\star) \\ \mathbf{c}_{\text{eq}}(\mathbf{x}^\star) \end{bmatrix} = 0. \tag{D.9}$$

We can proceed to search for a minimizer to the problem (D.8) by searching for points that solve the system (D.9). The natural approach is to solve the root finding problem with Newton's method. Roughly speaking, we start with an initial "guess" solution, linearize the system (D.9) around the guess solution, and solve the linear system to improve on the guess.

Assume we have an approximate solution, $(\mathbf{x}_k, \boldsymbol{\lambda}_k)$. Linearizing (D.9), around $(\mathbf{x}_k, \boldsymbol{\lambda}_k)$, we obtain

$$\begin{aligned} \nabla_{\mathbf{x}} \mathcal{L}(\mathbf{x}_k, \boldsymbol{\lambda}_k) + \nabla^2_{\mathbf{x}} \mathcal{L}(\mathbf{x}_k, \lambda_k) \Delta \mathbf{x}_k - \nabla \mathbf{c}_{\text{eq}}(\mathbf{x}_k) \Delta \boldsymbol{\lambda}_k &= 0, \\ \mathbf{c}_{\text{eq}}(\mathbf{x}_k) + \nabla \mathbf{c}_{\text{eq}}(\mathbf{x}_k)^T \Delta \mathbf{x}_k &= 0, \end{aligned}$$

where $\Delta \mathbf{x}_k$ and $\Delta \boldsymbol{\lambda}_k$ represent steps away from $\mathbf{x}_k$ and $\boldsymbol{\lambda}_k$. Noting that $\nabla_{\mathbf{x}} \mathcal{L}(\mathbf{x}_k, \boldsymbol{\lambda}_k) = \nabla f(\mathbf{x}_k) - \nabla c_{\text{eq}}(\mathbf{x}_k) \lambda_k$ and introducing the shorthand $\boldsymbol{\lambda}^+ = \boldsymbol{\lambda}_k + \Delta \boldsymbol{\lambda}_k$, we can rewrite the linearized system as

$$\begin{bmatrix} \nabla^2_{\mathbf{x}} \mathcal{L}(\mathbf{x}_k) & -\nabla \mathbf{c}_{\text{eq}}(\mathbf{x}_k) \\ -\nabla \mathbf{c}_{\text{eq}}(\mathbf{x}_k)^T & 0 \end{bmatrix} \begin{bmatrix} \Delta \mathbf{x}_k \\ \boldsymbol{\lambda}^+ \end{bmatrix} = \begin{bmatrix} -\nabla f(\mathbf{x}_k) \\ -\mathbf{c}_{\text{eq}}(\mathbf{x}_k) \end{bmatrix}. \tag{D.10}$$

It can be shown that the conditions (D.10) are precisely the optimality conditions of the following quadratic program (QP) [74],

$$\begin{aligned} \underset{\Delta \mathbf{x}_k}{\text{minimize}} \quad & \nabla f(\mathbf{x}_k)^T \Delta \mathbf{x}_k + \frac{1}{2} \Delta \mathbf{x}_k^T \left( \nabla^2_{\mathbf{x}} \mathcal{L}(\mathbf{x}_k, \boldsymbol{\lambda}_k) \right) \Delta \mathbf{x}_k, \\ \text{subject to} \quad & \mathbf{c}_{\text{eq}}(\mathbf{x}_k) + \nabla \mathbf{c}_{\text{eq}}{}^T(\mathbf{x}_k) \Delta \mathbf{x}_k = 0. \end{aligned} \tag{D.11}$$

A full step Newton's method solves QPs of the form (D.11) on each iteration and updates the approximate solution according to

$$\begin{aligned}\mathbf{x}_{k+1} &= \mathbf{x}_k + \Delta\mathbf{x}_k,\\ \boldsymbol{\lambda}_{k+1} &= \boldsymbol{\lambda}_k + \Delta\boldsymbol{\lambda}_k = \boldsymbol{\lambda}^+.\end{aligned}$$

While it is not possible to apply Newton's method to the KKT conditions associated with inequality constrained problems because the complimentarily conditions (D.4) are non smooth, we can incorporate inequality constraints into QP subproblem (D.11) in the same fashion as the equality constraints. For the mixed constraint problem (D.1), the QP subproblem becomes

$$\begin{aligned}\underset{\Delta\mathbf{x}_k}{\text{minimize}} \quad & \nabla f(\mathbf{x}_k)^T\Delta\mathbf{x}_k + \frac{1}{2}\Delta\mathbf{x}_k^T\mathbf{B}_k\Delta\mathbf{x}_k,\\ \text{subject to} \quad & \mathbf{c}_{\text{eq}}(\mathbf{x}_k) + \nabla\mathbf{c}_{\text{eq}}{}^T(\mathbf{x}_k)\Delta\mathbf{x}_k = 0,\\ & \mathbf{c}_{\text{in}}(\mathbf{x}_k) + \nabla\mathbf{c}_{\text{in}}{}^T(\mathbf{x}_k)\Delta\mathbf{x}_k = 0,\end{aligned} \tag{D.12}$$

which has a solution $(\Delta\mathbf{x}_{k+1}, \boldsymbol{\lambda}_{\text{eq}}^+, \boldsymbol{\lambda}_{\text{in}}^+)$ and the Hessian matrix is

$$\mathbf{B}_k = \nabla^2_{\mathbf{x}}\mathcal{L}(\mathbf{x}_k, \boldsymbol{\lambda}_{\text{eq},k}, \boldsymbol{\lambda}_{\text{in},k}). \tag{D.13}$$

Methods for solving the QP subproblem are described in Appendix D.2.

### D.1.2 Computing the SQP Step Size

The SQP method described above (Section D.1.1) is only locally convergent. When starting far from a solution, it can generate an erratic sequence of iterates that may by chance enter the neighborhood of a solution and then converge, but more likely the sequence will not converge. The two main approaches to globalizing the SQP method, i.e. modifying the algorithm so that it is convergent from any starting point, include trust region and line search. The latter is considered in this work.

The line search method adapts a change in the iterate by a step size $\alpha_k \in [0, 1]$, i.e.

$$\mathbf{x}_{k+1} = \mathbf{x}_k + \alpha_k\mathbf{p}_k$$

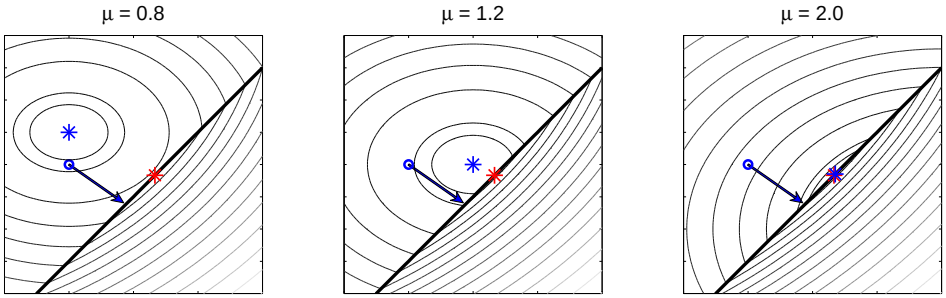


**Figure D.1:** Exactness of the merit function. As $\mu$ is increased, the search direction goes from an ascent direction of the merit function ($\mu = 0.8$) to a descent direction ($\mu = 1.2$) to exact ($\mu \geq 2.0$).

where $\mathbf{p}_k$ is the step direction computed by the method in the previous section. The step size parameter is important because it forces convergence from poor starting approximations. However, the choice of step size is complicated by the necessary trade off between reducing the objective function and moving towards feasibility. The issue of balancing both goals with the preference towards satisfying constraints can be addressed with a "merit-function". The most common general merit function is of the form:

$$\phi(\mathbf{x};\mu) = f(\mathbf{x}) + \mu\left(\|c(\mathbf{x})\|_1 + \max\{0, h(\mathbf{x})\}\right), \tag{D.14}$$

where the positive scalar $\mu$ is the *penalty parameter* which weights constraint satisfaction relative to minimization of the objective. This merit function is not differentiable but it has the important property of being *exact* meaning there is a positive scalar $\mu^\star$ such that for any $\mu > \mu^\star$ any local solution of the original nonlinear optimization problem is a local minimizer of $\phi(\mathbf{x};\mu)$.

An example of exactness is depicted in Figure D.1. The thin lines draw the contours of the merit function (D.14) and the dark black line draws feasible points. The blue star denotes minimizer of the merit function and red star denotes minimizer of the optimization problem. As $\mu$ is increased, the search direction computed from the QP subproblem denoted by the blue arrow becomes a descent direction for the merit function. For $\mu \geq 2$ the merit function is exact.

Ideally we would like choose $\alpha_k$ such that

$$\alpha_k = \arg\min_{\alpha_k \in [0,1]} \phi(\mathbf{x}_k + \alpha_k \mathbf{p}_k, ; \mu)$$

but in general this is expensive to calculate and instead it is more common to accept a step if it produces a *sufficient decrease* in the merit function. While the above merit function is not differentiable because of the 1-norm and max terms, it does have a direction derivative. Let $D(\phi(\mathbf{x};\mu) : \mathbf{p})$ represent the directional derivative of $\phi(\mathbf{x};\mu)$ in the direction $\mathbf{p}$. In a line search method, the sufficient decrease condition requires the step size parameter $\alpha > 0$ be small enough that the inequality

$$\phi(\mathbf{x} + \alpha\mathbf{p};\mu) \leq \phi(\mathbf{x};\mu) + \eta\alpha(\phi(\mathbf{x};\mu) : \mathbf{p}),$$

is satisfied for some $\eta \in (0,1)$. The next two sections discuss how to compute the directional derivative and how to choose the penalty parameter $\mu$.

### Directional Derivative of the Composite Merit Function

While the merit function discussed in Section D.1.2 is not differentiable, it does have a directional derivative. Consider the the function

$$v(\mathbf{x}) = \|c(\mathbf{x})\|_1 + \max\{0, h(\mathbf{x})\} \tag{D.15}$$

where $c(\mathbf{x})$ and $h(\mathbf{x})$ are scalar functions. The directional derivative of the function $\mathbf{f}(\mathbf{x})$ in direction $\mathbf{p}$ is defined as

$$D(\mathbf{f}(\mathbf{x});\mathbf{p}) \equiv \lim_{\epsilon \to 0} \frac{\mathbf{f}(\mathbf{x} + \epsilon\mathbf{p}) - \mathbf{f}(\mathbf{x})}{\epsilon} \tag{D.16}$$

To obtain the directional derivative of $\|c(\mathbf{x})\|$, first consider the the function $c(\mathbf{x}) = \mathbf{x}$. We have from the definition (D.16)

$$D(\|\mathbf{x}\|_1;\mathbf{p}) = \lim_{\epsilon \to 0} \frac{\|\mathbf{x} + \epsilon\mathbf{p}\|_1 - \|\mathbf{x}\|_1}{\epsilon} = \lim_{\epsilon \to 0} \frac{\sum_{i=1}^n |x_i + \epsilon p_i| - \sum_{i=1}^n |x_i|}{\epsilon} \tag{D.17}$$

If $x_i > 0$, we have $|x_i + \epsilon p_i| = |x_i| + \epsilon p_i$ for all $\epsilon$ sufficiently small. If $x_i < 0$, we have $|x_i + \epsilon p_i| = |x_i| - \epsilon p_i$ for all $\epsilon$ sufficiently small, while if $x_i = 0$, we have

$|x_i + \epsilon p_i| = \epsilon p_i$. Thus,

$$D(\|\mathbf{x}\|_1; \mathbf{p}) = \sum_{i|x_i<0} -p_i + \sum_{i|x_i>0} p_i + \sum_{i|x_i=0} |p_i|. \tag{D.18}$$

In summation, for the scalar $x$, the directional derivative depends on the sign of $x$ and the direction $p$

1. If $x < 0$, then $D = p$
2. If $x > 0$, then $D = -p$
3. If $x = 0$, then $D = |d|$ (Note, it's always positive, which makes sense since $x = 0$ is a minimizer of $|x|$.)

More generally, for $\|c(\mathbf{x})\|_1$, the result is the same except $x$ is replaced by $c(\mathbf{x})$ and $d$ is replaced by $\nabla c(\mathbf{x})^T\mathbf{d}$

1. If $c(\mathbf{x}) < 0$, then $D = \nabla c(\mathbf{x})^T\mathbf{d}$
2. If $c(\mathbf{x}) > 0$, then $D = -\nabla c(\mathbf{x})^T\mathbf{d}$
3. If $c(\mathbf{x}) = 0$, then $D = |\nabla c(\mathbf{x})^T\mathbf{d}|$

For the function $\max\{0, h(\mathbf{x})\}$, the only differences is that now the directional derivative is always zero when $h(\mathbf{x}) < 0$ because the max function will remain zero for small deviations in $\mathbf{x}$.

1. If $h(\mathbf{x}) < 0$, then $D = \nabla h(\mathbf{x})^T\mathbf{d}$
2. If $h(\mathbf{x}) > 0$, then $D = 0$
3. If $h(\mathbf{x}) = 0$, then $D = \max\{0, h(\mathbf{x})^T\mathbf{d}\}$

Here, we've used the property of directional derivatives

$$D(\max\{f_1, f_2\}, \mathbf{d}) = \max\{\nabla f_1^T\mathbf{d}, \nabla f_2^T\mathbf{d}\}. \tag{D.19}$$

### D.1.3 Approximating the Hessian

The Hessian of the Lagrangian $\nabla^2_{\mathbf{x}}\mathcal{L}(\mathbf{x}_k, \lambda_k)$ required in the QP subproblem (D.12) is made of up of second derivatives of the objective function and constraints. For optimal control applications, this information is not easy to compute so it is necessary to replace the exact Hessian by some approximation. Various formulae have been developed for generating Hessian approximations based solely on the first derivative information of pervious iterates (D.12). The most popular form of Hessian approximation for SQP methods is the BFGS method [74] because it ensures superlinear convergence when near a solution. The BFGS update for constrained problems is given by

$$\mathbf{B}_{k+1} = \mathbf{B}_k - \frac{\mathbf{B}_k \mathbf{s}_k \mathbf{s}_k^T \mathbf{B}_k}{\mathbf{s}_k^T \mathbf{B}_k \mathbf{s}_k} + \frac{\mathbf{y}_k \mathbf{y}_k^T}{\mathbf{y}_k^T \mathbf{s}_k},$$

where $\mathbf{s}_k = \mathbf{x}_{k+1} - \mathbf{x}_k$ and $\mathbf{y}_k = \nabla_{\mathbf{x}}\mathcal{L}(\mathbf{x}_{k+1}, \lambda_{k+1}) - \nabla_{\mathbf{x}}\mathcal{L}(\mathbf{x}_k, \lambda_{k+1})$.

### D.1.4 The SQP Algorithm

In summation the general SQP framework can be broken down into the following steps:

**Step 1: Initial Guess.** Obtain some working guess solution, $\mathbf{x}_k$ and multipliers $\boldsymbol{\lambda}_{\text{eq},k}$ and $\boldsymbol{\lambda}_{\text{in},k}$

**Step 2: Construct QP Subproblem.** Use $\mathbf{x}_k$, $\boldsymbol{\lambda}_{\text{eq},k}$, and $\boldsymbol{\lambda}_{\text{in},k}$ to construct the QP subproblem as in (D.12).

**Step 3: Solve QP Subproblem.** Solve the QP subproblem to obtain the search direction, $\mathbf{p}_k = \Delta\mathbf{x}_k$ and new multipliers $\boldsymbol{\lambda}^+_{\text{eq}}$, and $\boldsymbol{\lambda}^+_{\text{in}}$. Set $\Delta\boldsymbol{\lambda}_{\text{in},k} = \boldsymbol{\lambda}^+_{\text{in}} - \boldsymbol{\lambda}_{\text{in},k}$ and $\Delta\boldsymbol{\lambda}_{\text{eq},k} = \boldsymbol{\lambda}^+_{\text{eq}} - \boldsymbol{\lambda}_{\text{eq},k}$.

**Step 4: Compute Step-size and Update.** Compute the step size

$$\alpha_k \coloneqq \underset{\alpha\in[0,1]}{\arg\min}\, \phi(\mathbf{x}_k + \alpha_k \boldsymbol{\Delta} x_k).$$

Update iterates $(\mathbf{x}_{k+1}, \boldsymbol{\lambda}_{\text{eq},k+1}) \leftarrow (\mathbf{x}_k, \boldsymbol{\lambda}_{\text{eq},k}) + \alpha_k(\Delta\mathbf{x}_{k+1}, \Delta\boldsymbol{\lambda}_{\text{eq},k})$ and return to Step 2.

The line search SQP algorithm is formally written in Algorithm 3.

**Algorithm 3:** SQP line search algorithm

Choose initial approximate solution $\mathbf{x}_0$ and initial multipliers $\boldsymbol{\lambda}_{\text{eq},0}$ and $\boldsymbol{\lambda}_{\text{in},0}$;
Evaluate $f_0$, $\nabla f_0$, $\mathbf{c}_{\text{eq},0}$, $\nabla \mathbf{c}_{\text{eq},0}$, $\mathbf{c}_{\text{in},0}$, and $\nabla \mathbf{c}_{\text{in},0}$;
Choose an initial Hessian approximation $\mathbf{B}_0 > 0$;
**for** $k = 0, 1, \ldots, k_{\max}$ **do**
  Check convergence criteria: $\|\mathbf{p}_k\| \leq \text{tol}$ or $\|\nabla_x \mathcal{L}\| \leq \text{tol}$;
  Compute the search direction $\mathbf{p}_k = \Delta \mathbf{x}_k$ and updated multipliers $\boldsymbol{\lambda}_{\text{eq}}^+$, and $\boldsymbol{\lambda}_{\text{in}}^+$ by solving the QP subproblem (D.12);
  Set step size $\alpha_k \leftarrow 1$;
  **while** $\phi_1(\mathbf{x}_k + \alpha_k \mathbf{p}_k; \mu_k) > \phi_1(\mathbf{x}_k; \mu_k) + \eta \alpha_k D_1(\phi(\mathbf{x}_k; \mu_k)\mathbf{p}_k)$ **do**
    Reset $\alpha_k \leftarrow \tau_\alpha \alpha_k$ for some $\tau_\alpha \in (0, \tau]$;
  **end while**
  Set $\mathbf{x}_{k+1} \leftarrow \mathbf{x}_k + \alpha_k \mathbf{p}_k$
  Evaluate $f_{k+1}$, $\nabla f_{k+1}$, etc.
  Set $s_k \leftarrow \alpha_k p_k$ and $y_k \leftarrow \nabla_x \mathcal{L}(x_{k+1}, \lambda_{k+1}) - \nabla_x \mathcal{L}(x_k, \lambda_{k+1})$
  Compute $B_{k+1}$ by updating $B_k$ according to BFGS formula
**end for**

# D.2 Quadratic Programming Solutions

A quadratic program is defined as the optimization of a quadratic objective function over a polytope, i.e. the intersection of a finite number of linear equality and inequality constraints [74], for example see Figure D.2.

## D.2.1 Quadratic Program Reduced to General Form

Consider an equality and inequality constrained QP written in the standard form,

$$\begin{aligned} \underset{\mathbf{z}}{\text{minimize}} \quad & \frac{1}{2}\mathbf{z}^T \mathbf{H} \mathbf{z} + \mathbf{g}^T \mathbf{z} \\ \text{subject to} \quad & \mathbf{A}\mathbf{z} = \mathbf{b} \\ & \mathbf{C}\mathbf{z} \leq \mathbf{d} \end{aligned} \tag{D.20}$$

for which we want to find the optimizer $\mathbf{z}^\star$.

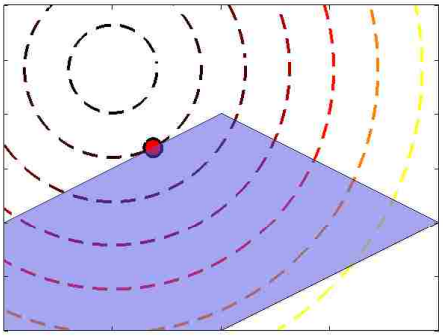

**Figure D.2:** Example QP problem: the purple area represents the feasible set and the red dot represents the optimal point.

At the optimal solution, some of the inequalities will be *active*, i.e. the solution resides at the boundary of the inequality. If the set of active inequalities at the optimal solution, the *active set*, were known apriori, the remaining inactive inequalities could be dropped from the problem and the optimal solution could be found by solving the equality constrained problem

$$\begin{aligned} \underset{\mathbf{z}}{\text{minimize}} \quad & \frac{1}{2}\mathbf{z}^T\mathbf{H}\mathbf{z} + \mathbf{g}^T\mathbf{z} \\ \text{subject to} \quad & \mathbf{A}\mathbf{z} = \mathbf{b} \\ & \mathbf{c}_i^T\mathbf{z} = \mathbf{d}_i \;\; \forall i \in \mathcal{A} \end{aligned} \tag{D.21}$$

where $\mathcal{A}$ is set of indices representing the active inequalities. Assuming $\mathbf{H}$ is positive definite, i.e. the problem is strictly convex then there is a unique optimizer which can be found from the single stationary point of the Lagrangian

$$\mathcal{L}(\mathbf{z}, \alpha, \lambda) = \frac{1}{2}\mathbf{z}^T\mathbf{H}\mathbf{z} + \mathbf{g}^T\mathbf{z} + \boldsymbol{\alpha}^T(\mathbf{A}\mathbf{z} - \mathbf{b}) + \sum_{i \in \mathcal{A}} \lambda_i(c_i^T\boldsymbol{z} - d_i) \tag{D.22}$$

where $\alpha$ and $\lambda$ have been introduced as Lagrange multipliers. The stationarity point of D.22 can be found by solution of the linear system

$$\begin{bmatrix} \mathbf{H} & \mathbf{A}^T & \mathbf{C}_{\text{act}}^T \\ \mathbf{A} & 0 & 0 \\ \mathbf{C}_{\text{act}} & 0 & 0 \end{bmatrix} \begin{bmatrix} \mathbf{z} \\ \alpha \\ \lambda \end{bmatrix} = \begin{bmatrix} -\mathbf{g} \\ \mathbf{b} \\ \mathbf{d}_{\text{act}} \end{bmatrix}. \tag{D.23}$$

An efficient approach to finding the solution to the equality constrained problem is discussed below. An active set algorithm is a procedure to determine the active set $\mathcal{A}$. Numerous possibilities exists for finding $\mathcal{A}$, one such possibility is described in the next subsection [81].

### D.2.2 Simple Active Set Algorithm For Solving Inequality Constrained Quadratic Program

Consider the general equality constrained problem

$$\begin{aligned} \underset{\mathbf{z}}{\text{minimize}} \quad & \frac{1}{2}\mathbf{z}^T\mathbf{H}\mathbf{z} + \mathbf{g}^T\mathbf{z} \\ \text{subject to} \quad & \mathbf{A}\mathbf{z} = \mathbf{b} \\ & \mathbf{C}\mathbf{z} \leq \mathbf{d} \end{aligned}$$

and let $\mathcal{W}$ represent a guess of the optimal active set $\mathcal{A}$. For a strictly convex QP, there is a single optimizer that must satisfy the KKT conditions (equivalent to stationary point of , which can be summarized as follows

$$\left.\begin{aligned} \mathbf{H}\mathbf{z} + \boldsymbol{\alpha}^T\mathbf{A} + \sum_{i\in\mathcal{W}} \lambda_i \mathbf{c_i} &= -\mathbf{g} \\ \mathbf{A}\mathbf{z} &= \mathbf{b} \\ \forall i \in \mathcal{W} \quad {c_i}^T\mathbf{z} &= d_i \end{aligned}\right\} \text{KKT(1)}$$

$$\left.\begin{aligned} \mathbf{C}\mathbf{z} &\leq \mathbf{d} \\ \forall i \in \mathcal{W} \quad \lambda_i &\geq 0 \end{aligned}\right\} \text{KKT(2)}$$

With a guess of the active set $\mathcal{W}$ the solution to the problem determined by solving (D.23) will satisfy KKT(1), but will not necessarily satisfy KKT(2) unless $\mathcal{W}$ is equal to the optimal active set $\mathcal{A}$. The procedure to determine the active set starts by first taking a guess to the active set, call it the working set $\mathcal{W}$. From the working set, we construct an equality constrained QP and obtain a candidate solution, $\hat{\mathbf{z}}$. With the candidate solution, we can check the conditions KKT(2), any violated inequality constraints are added to the working set and any constraint $i$ for

$\lambda_i < 0$ currently in the working set is removed.[2] The process is repeated until no constraints are added or removed from the working set. The active set algorithm is formally summarized in Algorithm 1 [81].

**Algorithm 4:** Active Set Method for Quadratic Programming

```
iter ← 0
repeat
  Compute z satisfying KKT(1)
  if c_i^T z > d_i|_{i∉W} then
    add i to W
  end if
  if λ_i < 0|_{i∈W} then
    remove i from W
  end if
  iter ← iter + 1
  if iter > MAXITER then
    return Fail
  end if
until z satisfies KKT(2)
A ← W
return A, z
```

### D.2.3 Efficient solution of equality constrained problem

If $\mathbf{H}$ is positive definite, the solution to the equality constrained QP (D.21) can be efficiently solved via the Schur complement method [74]. Let $\bar{\mathbf{A}} = \begin{bmatrix}\mathbf{A}^T & \mathbf{C}_{\text{act}}^T\end{bmatrix}^T$ and $\bar{\mathbf{b}} = [\mathbf{b}^T \;\; \mathbf{d}_{\text{act}}^T]^T$, then a solution to the system (D.23) rewritten here as

$$\begin{bmatrix}\mathbf{H} & \bar{\mathbf{A}}^T \\ \bar{\mathbf{A}} & 0\end{bmatrix} \begin{bmatrix}\mathbf{z} \\ \begin{bmatrix}\boldsymbol{\alpha} \\ \boldsymbol{\lambda}\end{bmatrix}\end{bmatrix} = \begin{bmatrix}-\mathbf{g} \\ \bar{\mathbf{b}}\end{bmatrix}$$

can be found by first solving for $\alpha$ and $\lambda$

$$\left(\bar{\mathbf{A}}\mathbf{H}^{-1}\bar{\mathbf{A}}^T\right) \begin{bmatrix}\boldsymbol{\alpha} \\ \boldsymbol{\lambda}\end{bmatrix} = \left(\bar{\mathbf{A}}\mathbf{H}^{-1}\mathbf{g} - \bar{\mathbf{b}}\right).$$

[2] A negative multiplier implies the optimal solution lies within this inequality constraint.

After obtaining $\alpha$ and $\lambda$, recover $\mathbf{z}$

$$\mathbf{z} = -\mathbf{H}^{-1}\left(\mathbf{g} + \bar{\mathbf{A}}^T \begin{bmatrix} \boldsymbol{\alpha} \\ \boldsymbol{\lambda} \end{bmatrix}\right)$$

This method requires $\mathbf{H}^{-1}$ and factorization of matrix $\bar{\mathbf{A}}^T\mathbf{H}^{-1}\bar{\mathbf{A}}$, therefore it is most efficient when the inverse of $\mathbf{H}^{-1}$ can be easily computed, i.e. is diagonal, or can be precomputed, which is the case in the MPC approaches described in this document.

# Bibliography

[1] J. Wesson, *Tokamaks*, ser. International Series of Monographs on Physics. New York: Oxford University Press Inc., Third Edition, 2004, vol. 118.

[2] J. Ongena and Y. Ogawa, "Nuclear fusion: Status report and future prospects," *Energy Policy*, vol. 96, pp. 770 – 778, 2016. [Online]

[3] L. Grisham *et al.*, "Recent improvements to the ITER neutral beam system design," *Fusion Engineering and Design*, vol. 87, no. 11, pp. 1805 – 1815, 2012. [Online]

[4] F. Troyon, R. Gruber, H. Saurenmann, S. Semenzato, and S. Succi, "MHD-Limits to Plasma Confinement," *Plasma Physics and Controlled Fusion*, vol. 26, no. 1A, p. 209, 1984. [Online]

[5] T. M. A. Jr., J. F. Drake, P. N. Guzdar, A. B. Hassam, Y. T. Lau, C. S. Liu, and S. V. Novakovskii, "Physical mechanism of enhanced stability from negative shear in tokamaks: Implications for edge transport and the L-H transition," *Physics of Plasmas*, vol. 3, no. 6, pp. 2221–2223, 1996. [Online]

[6] C. Gormezano *et al.*, "Internal Transport Barriers in JET Deuterium-Tritium Plasmas," *Phys. Rev. Lett.*, vol. 80, pp. 5544–5547, Jun 1998. [Online]

[7] O. Gruber *et al.*, "Stationary H-Mode Discharges with Internal Transport Barrier on ASDEX Upgrade," *Phys. Rev. Lett.*, vol. 83, pp. 1787–1790, Aug 1999. [Online]

[8] A. Garofalo, G. Jackson, R. La Haye, M. Okabayashi, H. Reimerdes, E. Strait, J. Ferron, R. Groebner, Y. In, M. Lanctot, G. Matsunaga, G. Navratil, W. Solomon, H. Takahashi, M. Takechi, A. Turnbull, and the DIII-D Team, "Stability and control of resistive wall modes in high beta, low rotation DIII-D plasmas," *Nuclear Fusion*, vol. 47, no. 9, p. 1121, 2007. [Online]

[9] C. Gormezano *et al.*, "Progress in the ITER Physics Basis, Chapter 6: Steady state operation," *Nuclear Fusion*, vol. 47, no. 6, p. S285, 2007. [Online]

[10] T. Hender *et al.*, "Chapter 3: MHD stability, operational limits and disruptions," *Nuclear Fusion*, vol. 47, no. 6, p. S128, 2007. [Online]

[11] M. Kikuchi, "A Review of Fusion and Tokamak Research Towards Steady-State Operation: A JAEA Contribution," *Energies*, vol. 3, pp. 1741–1789, 2010. [Online]

[12] The JET Team (presented by F X Söldner), "Shear optimization experiments with current profile control on JET," *Plasma Physics and Controlled Fusion*, vol. 39, no. 12B, p. B353, 1997. [Online]

[13] M. D. Bock, "Understanding and controlling plasma rotation in tokamaks," Ph.D. dissertation, Technische Universiteit Eindhoven, 2007.

[14] T. H. Stix, "Decay of poloidal rotation in a tokamak plasma," *The Physics of Fluids*, vol. 16, no. 8, pp. 1260–1267, 1973. [Online]

[15] T. S. Taylor, "Suppression of turbulence and transport by sheared flow," *Rev. of Modern Physics*, vol. 72, no. 1, pp. 109–165, Jan 2000.

[16] K. H. Burrell, M. E. Austin, C. M. Greenfield, L. L. Lao, B. W. Rice, G. M. Staebler, and B. W. Stallard, "Effects of $E \times B$ velocity shear and magnetic shear in the formation of core transport barriers in the DIII-D tokamak," *Plasma Physics and Controlled Fusion*, vol. 40, no. 9, p. 1585, 1998. [Online]

[17] R. J. La Haye, D. P. Brennan, R. J. Buttery, and S. P. Gerhardt, "Islands in the stream: The effect of plasma flow on tearing stability," *Physics of Plasmas*, vol. 17, no. 5, p. 056110, 2010. [Online]

[18] R. J. Buttery, R. J. La Haye, P. Gohil, G. L. Jackson, H. Reimerdes, E. J. Strait, and the DIII-D Team, "The influence of rotation on the $\beta_N$ threshold for the 2/1 neoclassical tearing mode in DIII-D," *Physics of Plasmas*, vol. 15, no. 5, p. 056115, 2008. [Online]

[19] P.A. Politzer and C.C. Petty and R.J. Jayakumar and T.C. Luce and M.R. Wade and J.C. DeBoo and J.R. Ferron and P. Gohil and C.T. Holcomb and A.W. Hyatt and J. Kinsey and R.J. La Haye and M.A. Makowski and T.W. Petrie, "Influence of toroidal rotation on transport and stability in hybrid scenario plasmas in DIII-D," *Nuclear Fusion*, vol. 48, no. 7, p. 075001, 2008. [Online]

[20] A. M. Garofalo, E. J. Strait, L. C. Johnson, R. J. La Haye, E. A. Lazarus, G. A. Navratil, M. Okabayashi, J. T. Scoville, T. S. Taylor, and A. D. Turnbull, "Sustained Stabilization of the Resistive-Wall Mode by Plasma Rotation in the DIII-D Tokamak," *Phys. Rev. Lett.*, vol. 89, p. 235001, Nov 2002. [Online]

[21] S. Sabbagh, A. Sontag, J. Bialek, D. Gates, A. Glasser, J. Menard, W. Zhu, M. Bell, R. Bell, A. Bondeson, C. Bush, J. Callen, M. Chu, C. Hegna, S. Kaye, L. Lao, B. LeBlanc, Y. Liu, R. Maingi, D. Mueller, K. Shaing, D. Stutman, K. Tritz, and C. Zhang, "Resistive wall stabilized operation in rotating high beta NSTX plasmas," *Nuclear Fusion*, vol. 46, no. 5, p. 635, 2006. [Online]

[22] A. Sontag, S. Sabbagh, W. Zhu, J. Menard, R. Bell, J. Bialek, M. Bell, D. Gates, A. Glasser, B. LeBlanc, K. Shaing, D. Stutman, and K. Tritz, "Investigation of resistive wall mode stabilization physics in high-beta

plasmas using applied non-axisymmetric fields in NSTX," *Nuclear Fusion*, vol. 47, no. 8, p. 1005, 2007. [Online]

[23] F. Hinton and M. Rosenbluth, "The mechanism for toroidal momentum input to Tokamak plasmas from neutral beams," *Physics Letters A*, vol. 259, no. 3, pp. 267 – 275, 1999. [Online]

[24] S. Suckewer, H. P. Eubank, R. J. Goldston, E. Hinnov, and N. R. Sauthoff, "Toroidal Plasma Rotation in the Princeton Large Torus Induced by Neutral-Beam Injection," *Phys. Rev. Lett.*, vol. 43, pp. 207–210, Jul 1979. [Online]

[25] A. Pankin, D. McCune, R. Andre, G. Bateman, and A. Kritz, "The tokamak Monte Carlo fast ion module NUBEAM in the National Transport Code Collaboration library," *Computer Physics Communications*, vol. 159, no. 3, pp. 157 – 184, 2004. [Online]

[26] R. C. Isler, "A Review of Charge-Exchange Spectroscopy and Applications to Fusion Plasmas," *Physica Scripta*, vol. 35, no. 5, p. 650, 1987. [Online]

[27] A. H. Boozer, "Error Field Amplification and Rotation Damping in Tokamak Plasmas," *Phys. Rev. Lett.*, vol. 86, pp. 5059–5061, May 2001. [Online]

[28] W. Zhu, S. A. Sabbagh, R. E. Bell, J. M. Bialek, M. G. Bell, B. P. LeBlanc, S. M. Kaye, F. M. Levinton, J. E. Menard, K. C. Shaing, A. C. Sontag, and H. Yuh, "Observation of Plasma Toroidal-Momentum Dissipation by Neoclassical Toroidal Viscosity," *Phys. Rev. Lett.*, vol. 96, p. 225002, Jun 2006. [Online]

[29] K. C. Shiang *et al.*, "Neoclassical transport fluxes in the plateau regime in nonaxisymmetric toroidal plasmas," *Physics of Fluids*, vol. 29, no. 521, 1986.

[30] A. J. Cole, J. D. Callen, W. M. Solomon, A. M. Garofalo, C. C. Hegna, M. J. Lanctot, and H. Reimerdes, "Observation of Peak Neoclassical Toroidal

Viscous Force in the DIII-D Tokamak," *Phys. Rev. Lett.*, vol. 106, p. 225002, Jun 2011. [Online]

[31] A. M. Garofalo, W. M. Solomon, M. Lanctot, K. H. Burrell, J. C. DeBoo, J. S. deGrassie, G. L. Jackson, J.-K. Park, H. Reimerdes, M. J. Schaffer, and E. J. Strait, "Plasma rotation driven by static nonresonant magnetic fields," *Physics of Plasmas*, vol. 16, no. 5, p. 056119, 2009. [Online]

[32] K. H. Finken *et al.*, "Toroidal Plasma Rotation Induced by the Dynamic Ergodic Divertor in the TEXTOR Tokamak," *Phys. Rev. Lett.*, vol. 94, p. 015003, Jan 2005. [Online]

[33] Y.-K. Peng and D. Strickler, "Features of spherical torus plasmas," *Nuclear Fusion*, vol. 26, no. 6, p. 769, 1986. [Online]

[34] Y.-K. M. Peng, "The physics of spherical torus plasmas," *Physics of Plasmas*, vol. 7, no. 5, pp. 1681–1692, 2000. [Online]

[35] A. Sykes, "Progress on spherical tokamaks," *Plasma Physics and Controlled Fusion*, vol. 36, no. 12B, p. B93, 1994. [Online]

[36] J. Freidberg, *Plasma Physics and Fusion Energy.* Cambridge University Press, NY, p. 412, 2007.

[37] T. Shinya, Y. Takase, T. Wakatsuki, A. Ejiri, H. Furui, J. Hiratsuka, K. Imamura, T. Inada, H. Kakuda, H. Kasahara, R. Kumazawa, C. Moeller, T. Mutoh, Y. Nagashima, K. Nakamura, A. Nakanishi, T. Oosako, K. Saito, T. Seki, M. Sonehara, H. Togashi, S. Tsuda, N. Tsujii, and T. Yamaguchi, "Non-inductive plasma start-up experiments on the TST-2 spherical tokamak using waves in the lower-hybrid frequency range," *Nuclear Fusion*, vol. 55, no. 7, p. 073003, 2015. [Online]

[38] Y. Takase, A. Ejiri, H. Kakuda, T. Oosako, T. Shinya, T. Wakatsuki, T. Ambo, H. Furui, T. Hashimoto, J. Hiratsuka, H. Kasahara, K. Kato, R. Kumazawa, C. Moeller, T. Mutoh, A. Nakanishi, Y. Nagashima, K. Saito,

T. Sakamoto, T. Seki, M. Sonehara, R. Shino, H. Togashi, O. Watanabe, and T. Yamaguchi, "Non-inductive plasma initiation and plasma current ramp-up on the TST-2 spherical tokamak," *Nuclear Fusion*, vol. 53, no. 6, p. 063006, 2013. [Online]

[39] R. Raman, T. Jarboe, D. Mueller, M. Schaffer, R. Maqueda, B. Nelson, S. Sabbagh, M. Bell, R. Ewig, E. Fredrickson, D. Gates, J. Hosea, S. Jardin, H. Ji, R. Kaita, S. Kaye, H. Kugel, L. Lao, R. Maingi, J. Menard, M. Ono, D. Orvis, F. Paoletti, S. Paul, Y.-K. Peng, C. Skinner, J. Wilgen, S. Zweben, and N. R. Team, "Non-inductive current generation in NSTX using coaxial helicity injection," *Nuclear Fusion*, vol. 41, no. 8, p. 1081, 2001. [Online]

[40] F. Poli, R. Andre, N. Bertelli, S. Gerhardt, D. Mueller, and G. Taylor, "Simulations towards the achievement of non-inductive current ramp-up and sustainment in the National Spherical Torus Experiment Upgrade," *Nuclear Fusion*, vol. 55, no. 12, p. 123011, 2015. [Online]

[41] L. Ljung, *System Identification: Theory for the User*. Prentice Hall PTR, 1999.

[42] B. Anderson and J. Moore, *Optimal Filtering*. Prentice Hall, 1979.

[43] P. Wang, *Distributed Parameter Systems: Modelling and Identification*. Berlin, Germany: Springer-Verlag, 1978.

[44] Y. S. Na, "Modelling of current profile control in tokamak plasmas," Ph.D. dissertation, Fakultat fur Physik: Technische Universitat Munchen, Munich, Germany, 2003.

[45] D. Moreau, D. Mazon, M. Ariola, G. D. Tommasi, L. Laborde, F. Piccolo, F. Sartori, T. Tala, L. Zabeo, A. Boboc, E. Bouvier, M. Brix, J. Brzozowski, C. Challis, V. Cocilovo, V. Cordoliani, F. Crisanti, E. D. L. Luna, R. Felton, N. Hawkes, R. King, X. Litaudon, T. Loarer, J. Mailloux, M. Mayoral, I. Nunes, E. Surrey, O. Zimmerman, and J. E. Contributors,

"A two-time-scale dynamic-model approach for magnetic and kinetic profile control in advanced tokamak scenarios on JET," *Nuclear Fusion*, vol. 48, no. 10, p. 106001, 2008. [Online]

[46] M. Yoshida, Y. Koide, H. Takenaga, H. Urano, N. Oyama, K. Kamiya, Y. Sakamoto, G. Matsunaga, Y. Kamada, and the JT-60 Team, "Momentum transport and plasma rotation profile in toroidal direction in JT-60U L-mode plasmas," *Nuclear Fusion*, vol. 47, no. 8, p. 856, 2007. [Online]

[47] F. Hinton and R. Hazeltine, "Theory of plasma transport in toroidal confinement systems," *Rev. Mod. Phys.*, vol. 48, pp. 239–308, 1976.

[48] J. Blum, *Numerical Simulation and Optimal Control in Plasma Physics: With Applications to Tokamaks*. Wiley, Paris, 1989.

[49] E. Witrant, E. Joffrin, S. Brémond, G. Giruzzi, D. Mazon, O. Barana, and P. Moreau, "A control-oriented model of the current profile in tokamak plasma," *Plasma Physics and Controlled Fusion*, vol. 49, no. 7, p. 1075, 2007. [Online]

[50] V. Basiuk, J. Artaud, F. Imbeaux, X. Litaudon, A. Bécoulet, L.-G. Eriksson, G. Hoang, G. Huysmans, D. Mazon, D. Moreau, and Y. Peysson, "Simulations of steady-state scenarios for Tore Supra using the CRONOS code," *Nuclear Fusion*, vol. 43, no. 9, p. 822, 2003. [Online]

[51] C. A. J. Fletcher, *Computational Galerkin Methods*. Berlin, Heidelberg: Springer Berlin Heidelberg, 1984, pp. 72–85. [Online]

[52] C. T. Holcomb, J. R. Ferron, T. C. Luce, T. W. Petrie, P. A. Politzer, C. Challis, J. C. DeBoo, E. J. Doyle, C. M. Greenfield, R. J. Groebner, M. Groth, A. W. Hyatt, G. L. Jackson, C. Kessel, R. J. La Haye, M. A. Makowski, G. R. McKee, M. Murakami, T. H. Osborne, J.-M. Park, R. Prater, G. D. Porter, H. Reimerdes, T. L. Rhodes, M. W. Shafer, P. B. Snyder, A. D. Turnbull, and W. P. West, "Optimizing stability, transport,

and divertor operation through plasma shaping for steady-state scenario development in DIII-D," *Physics of Plasmas*, vol. 16, no. 5, p. 056116, 2009. [Online]

[53] W. W. Heidbrink, M. Murakami, J. M. Park, C. C. Petty, M. A. V. Zeeland, J. H. Yu, and G. R. McKee, "Beam-ion confinement for different injection geometries," *Plasma Physics and Controlled Fusion*, vol. 51, no. 12, p. 125001, 2009. [Online]

[54] W. Shi, W. Wehner, J. Barton, M. Boyer, E. Schuster *et al.*, "PTRANSP Simulation and Experimental Test of a Robust Current Profile and $\beta_N$ Controller for Off-axis Current Drive Scenarios in the DIII-D Tokamak," in *Proceeding of the 2013 American Control Conference*, 2013.

[55] W. Wehner, W. Shi, E. Schuster *et al.*, "Identification and Control of Magneto-Kinetic Response During Advanced Tokamak Scenarios in DIII-D," in *Proceeding of the 2013 American Control Conference*, 2013.

[56] J. Barton, "Physics-model-based optimization and feedback control of the current profile dynamics in fusion tokamak reactors," PhD Thesis, Lehigh University, USA, 2015. [Online]

[57] Y. Ou, T. Luce, E. Schuster *et al.*, "Towards model-based current profile control at DIII-D," *Fusion Engineering and Design*, vol. 82, pp. 1153–1160, 2007.

[58] J. Barton *et al.*, "Physics-based Control-oriented Modeling of the Current Density Profile Dynamics in High-performance Tokamak Plasmas," in *52nd IEEE Conference on Decision and Control*, 2013.

[59] H. S. John, "Equations and associated definitions used in onetwo," p. 8, Nov 2005. [Online]

[60] R. J. Goldston, "Basic physical processes of toroidal fusion plasmas," *Proc. Course and Workshop Varenna, 1985*, vol. 1, pp. 165–186, 1986.

[61] ITER Physics Basis Editors and ITER Physics Expert Group Chairs and Co-Chairs and ITER Joint Central Team and Physics Integration Unit, "Chapteră1: Overview and summary," *Nuclear Fusion*, vol. 39, no. 12, p. 2137, 1999. [Online]

[62] R. J. Goldston, "Energy confinement scaling in Tokamaks: some implications of recent experiments with Ohmic and strong auxiliary heating," *Plasma Physics and Controlled Fusion*, vol. 26, no. 1A, p. 87, 1984. [Online]

[63] O. Sauter, C. Angioni, and Y. R. Lin-Liu, "Neoclassical conductivity and bootstrap current formulas for general axisymmetric equilibria and arbitrary collisionality regime," *Physics of Plasmas*, vol. 6, no. 7, pp. 2834–2839, 1999. [Online]

[64] ——, "Neoclassical conductivity and bootstrap current formulas for general axisymmetric equilibria and arbitrary collisionality regime," *Physics of Plasmas*, vol. 6, no. 7, pp. 2834–2839, 1999. [Online]

[65] G. V. Pereverzev *et al.*, "ASTRA Automated System for Transport Analysis in a Tokamak," in *Technical Report 5/98 IPP Report*, 2002.

[66] P. Politzer and G. Porter, "Power threshold for neutral beam current drive," *Nuclear Fusion*, vol. 30, no. 8, p. 1605, 1990. [Online]

[67] J. Callen, A. Cole, and C. Hegna, "Toroidal rotation in tokamak plasmas," *Nuclear Fusion*, vol. 49, no. 8, p. 085021, 2009. [Online]

[68] W. Solomon, K. Burrell, A. Garofalo, A. Cole, R. Budny, J. deGrassie, W. Heidbrink, G. Jackson, M. Lanctot, R. Nazikian, H. Reimerdes, E. Strait, M. V. Zeeland, and the DIII-D Rotation Physics Task Force, "Advances in understanding the generation and evolution of the toroidal rotation profile on DIII-D," *Nuclear Fusion*, vol. 49, no. 8, p. 085005, 2009. [Online]

[69] A. E. Bryson and Y. C. Ho, *Applied Optimal Control*, New York.

[70] J. T. Betts, *Practical Methods for Optimal Control and Estimation Using Nonlinear Programming*, 2nd ed. New York, NY, USA: Cambridge University Press, 2009.

[71] ——, "Survey of numerical methods for trajectory optimization. Journal of Guidance, Control, and Dynamics," *Nucl. Fusion*, vol. 21, no. 2, pp. 193–207, 1998. [Online]

[72] C. Xu, Y. Ou, J. Dalessio, E. Schuster, T. C. Luce, J. R. Ferron, M. L. Walker, and D. A. Humphreys, "Ramp-Up Phase Current Profile Control of Tokamak Plasmas via Nonlinear Programming," *IEEE Transactions on Plasma Science*, vol. 38, no. 2, pp. 163–173, 2010. [Online]

[73] Y. Ou, C. Xu, E. Schuster, T. C. Luce, J. R. Ferron, M. L. Walker, and D. A. Humphreys, "Design and simulation of extremum-seeking open-loop optimal control of current profile in the DIII-D tokamak," *Plasma Physics and Controlled Fusion*, vol. 50, no. 11, p. 115001, 2008. [Online]

[74] J. Nocedal and S. J. Wright, *Numerical Optimization 2nd edn.* Berlin: Springer, 2006.

[75] B. Sengupta, K. Friston, and W. Penny, "Efficient gradient computation for dynamical models," *NeuroImage*, vol. 98, pp. 521 – 527, 2014. [Online]

[76] H. Ouarit, "Validation of plasma current profile model predictive control in tokamaks via simulation," *Fusion Engr. and Design*, vol. 86, pp. 1018–1021, 2011.

[77] E. Maljaars, F. Felici, M. de Baar, J. van Dongen, G. Hogeweij, P. Geelen, and M. Steinbuch, "Control of the tokamak safety factor profile with time-varying constraints using MPC," *Nuclear Fusion*, vol. 55, no. 2, p. 023001, 2015. [Online]

[78] C. E. Garcia, D. M. Prett, and M. Morari, "Model Predictive Control: Theory and Practice – a Survey," *Automatica*, vol. 25, no. 3, pp. 335 – 348, 1989. [Online]

[79] J. H. Lee, "Model predictive control: Review of the three decades of development," *International Journal of Control, Automation and Systems*, vol. 9, no. 3, p. 415, Jun 2011. [Online]

[80] Y. Wang and S. Boyd, "Fast model predictive control using online optimization," *IEEE Transactions on Control Systems Technology*, vol. 18, no. 2, pp. 267–278, March 2010. [Online]

[81] S. Kuindersma, F. Permenter, and R. Tedrake, "An Efficiently Solvable Quadratic Program for Stabilizing Dynamic Locomotion," in *International Conference on Robotics and Automation (ICRA)*, 2014.

[82] A. C. C. Sips, G. Giruzzi, S. Ide, C. Kessel, T. C. Luce, J. A. Snipes, and J. K. Stober, "Progress in preparing scenarios for operation of the international thermonuclear experimental reactor," *Physics of Plasmas*, vol. 22, no. 2, p. 021804, 2015. [Online]

[83] J. Ferron, M. Walker, L. Lao, H. S. John, D. Humphreys, and J. Leuer, "Real time equilibrium reconstruction for tokamak discharge control," *Nuclear Fusion*, vol. 38, no. 7, p. 1055, 1998. [Online]

[84] J. Scoville, "Simultaneous feedback control of plasma rotation and stored energy on the DIII-D tokamak," in *Proceedings of the 24th Symposium on Fusion Technology, Warsaw, Poland*, 2006.

[85] M. Wade, "Development in the DIII-D tokamak of advanced operating scenarios and associated control techniques for ITER," *Nuclear Fusion*, vol. 47, no. 10, p. S543, 2007. [Online]

[86] M. Yoshida, Y. Sakamoto, M. Sueoka, Y. Kawamata, N. Oyama, T. Suzuki, and Y. Kamada, "Real-time measurement and feedback control of ion

temperature profile and toroidal rotation using fast CXRS system in JT-60U," *Fusion Engineering and Design*, vol. 84, no. 12, pp. 2206 – 2213, 2009. [Online]

[87] K. Kunisch and S. Volkwein, "Galerkin proper orthogonal decomposition methods for parabolic problems," *Numerische Mathematik*, vol. 90, pp. 117–148, 2001.

[88] B. Anderson and J. Moore, *Optimal Control: Linear Quadratic Methods*. Dover Books on Engr., 2007.

[89] A. Packard, "What News with $\mu$: Structured Uncertainty in Multivariable Control," Ph.D. dissertation, UC Berkeley, 1988.

[90] J. Barton, M. Boyer, W. Shi, E. Schuster *et al.*, "Toroidal Current Profile Control During Low Confinement Mode Plasma Discharges in DIII-D via First-Principles-Driven Model-based Robust Control Synthesis," *Nuclear Fusion*, vol. 52, no. 123018, 2012.

[91] S. Skogested and I. Postlethwaite, *Multivariable Feedback Control*. New York: John Wiley and Sons, Ltd, 2003.

[92] S. Gerhardt, E. Fredrickson, D. Gates, S. Kaye, J. Menard, M. Bell, R. Bell, B. L. Blanc, H. Kugel, S. Sabbagh, and H. Yuh, "Calculation of the non-inductive current profile in high-performance NSTX plasmas," *Nuclear Fusion*, vol. 51, no. 3, p. 033004, 2011. [Online]

[93] S. Gerhardt, R. Andre, and J. Menard, "Exploration of the equilibrium operating space for NSTX-Upgrade," *Nuclear Fusion*, vol. 52, no. 8, p. 083020, 2012. [Online]

[94] S. Kaye *et al.*, "An overview of recent physics results from NSTX," *Nuclear Fusion*, vol. 55, no. 10, p. 104002, 2015. [Online]

[95] O. Meneghini, S. Smith, L. Lao *et al.*, "Integrated modeling applications for tokamak experiments with OMFIT," *Nuclear Fusion*, vol. 55, no. 8, p. 083008, 2015. [Online]

[96] R. Prater, C. Moeller, R. Pinsker, M. Porkolab, O. Meneghini, and V. Vdovin, "Application of very high harmonic fast waves for off-axis current drive in the DIII-D and FNSF-AT tokamaks," *Nuclear Fusion*, vol. 54, no. 8, p. 083024, 2014. [Online]

[97] G. Pannocchia and J. B. Rawlings, "Disturbance models for offset-free model-predictive control," *AIChE Journal*, vol. 49, no. 2, pp. 426–437, 2003. [Online]

[98] M. R. Rajamani, J. B. Rawlings, and S. J. Qin, "Achieving state estimation equivalence for misassigned disturbances in offset-free model predictive control," *AIChE Journal*, vol. 55, no. 2, pp. 396–407, 2009. [Online]

[99] A. Gonzalez, E. Adam, and J. Marchetti, "Conditions for offset elimination in state space receding horizon controllers: A tutorial analysis," *Chemical Engineering and Processing: Process Intensification*, vol. 47, no. 12, pp. 2184 – 2194, 2008. [Online]

[100] G. Pannocchia, "Offset-free tracking MPC: A tutorial review and comparison of different formulations," in *2015 European Control Conference (ECC)*, July 2015, pp. 527–532.

[101] D. P. Bertsekas, *Dynamic Programming and Optimal Control*, 2nd ed. Athena Scientific, 2000.

[102] E. Hairer, S. P. Nørsett, and G. Wanner, *Solving Ordinary Differential Equations I (2Nd Revised. Ed.): Nonstiff Problems*. New York, NY, USA: Springer-Verlag New York, Inc., 1993.

[103] R. B. Wilson, "A simplicial algorithm for concave programming," Ph.D. dissertation, Graduate School of Business Administration, Harvard University, Boston, 1963.

[104] S. P. Han, "A globally convergent method for nonlinear programming," *Journal of Optimization Theory and Applications*, vol. 22, no. 3, pp. 297–309, 1977. [Online]

[105] M.J.D. Powell, "A fast algorithm for nonlinearly constrained optimization calculations," *Numerical Analysis*, vol. 630, 1978.

# Vita

Mr. William Pennock Wehner was born on August 22, 1984 in Boston Massachusetts. He received the B.S., M.S., and Ph.D. degrees in mechanical engineering from Lehigh University, Bethlehem, PA, in 2007, 2009, and 2017, respectively. Through his M.S. and Ph.D. degrees he was a member of the Lehigh University Plasma Controls Group, where he participated in numerous experiments involving the development of plasma control solutions for the DIII-D tokamak. Upon completion of his Ph.D. degree he is moving to a post-doctoral position stationed at General Atomics, San Diego, CA, to continue development of control solutions for high performance plasmas operation in the DIII-D tokamak.